UNIVERSIDADE TÉCNICA DE LISBOA

INSTITUTO SUPERIOR TÉCNICO

Charge and velocity reconstruction with the RICH detector of the AMS experiment

Analysis of the RICH prototype data

Maria Luísa Ferreira da Gama Velho Arruda

(Mestre)

Dissertação para obtenção do Grau de Doutor em Física

Orientador: Doutor Fernando José de Carvalho Barão

Júri:

Presidente:

Reitor da Universidade Técnica de Lisboa

Vogais:

Doutor Jorge Venceslau Comprido Dias de Deus
Doutor Michel Buenerd
Doutor Mário João Martins Pimenta
Doutor Alessandro de Angelis
Doutor Fernando José de Carvalho Barão
Doutor António Joaquim Onofre de Abreu Ribeiro Gonçalves

Janeiro de 2008

UNIVERSIDADE TÉCNICA DE LISBOA

INSTITUTO SUPERIOR TÉCNICO

Charge and velocity reconstruction with the RICH detector of the AMS experiment

Analysis of the RICH prototype data

Maria Luísa Ferreira da Gama Velho Arruda

(Mestre)

Dissertação para obtenção do Grau de Doutor em Física

Orientador: Doutor Fernando José de Carvalho Barão

Júri:

Presidente:

Reitor da Universidade Técnica de Lisboa

Vogais:

Doutor Jorge Venceslau Comprido Dias de Deus
Doutor Michel Buenerd
Doutor Mário João Martins Pimenta
Doutor Alessandro de Angelis
Doutor Fernando José de Carvalho Barão
Doutor António Joaquim Onofre de Abreu Ribeiro Gonçalves

Janeiro de 2008

To my beloved grandparents

João and Zulmira

"In my end is my beginning."

from Four Quartets, "East Coker" T. S. Eliot

Resumo

O Espectrómetro Magnético Alfa (AMS), a ser instalado na Estação Espacial Internacional (ISS) será equipado com um detector de Čerenkov de imagem anelar (RICH) para medir a velocidade e a carga eléctrica de partículas cósmicas carregadas. Este detector irá contribuir para um elevado nível de redundância nas medições conforme o requerido por AMS, bem como para rejeição de partículas de albedo. Espera-se uma separação de carga até ao ferro e uma resolução de velocidade da ordem de 0.1% para partículas de carga unitária.

Foi contruído um protótipo do RICH que consiste numa matriz de detecção com 96 fotomultiplicadores e guias de luz, um segmento do espelho cónico e amostras dos materiais do radiador. O desempenho do mesmo detector foi avaliado. Serão apresentados resultados detalhados do teste de feixe de 2003 usando fragmentos iónicos produzidos na colisão de um feixe primário de iões de índio (CERN SPS) com 158 GeV/c/nucleão num alvo de chumbo. A grande quantidade de dados coligidos permitiu testar e caracterizar diferentes amostras de aerogel e fluoreto de sódio para o radiador. As capacidades de reconstrução de velocidade e carga eléctrica deste subdetector foram confirmadas. Adicionalmente, a reflectividade do espelho foi avaliada. A análise dos dados confirma os objectivos do projecto.

Por outro lado, a precisão requerida na reconstrução de velocidade e carga baseia-se num preciso conhecimento de certos parâmetros do detector. A resposta da célula unitária de detecção deverá ser conhecida ao nível do 1% para não degradar a capacidade de determinação de carga. Uma exaustiva caracterização de todos os elementos de detecção foi efectuada antes e durante a montagem do detector.

Palavras Chave: RICH/AMS, Ângulo de Čerenkov, Carga eléctrica, Protótipo do RICH, Teste de feixe de 2003, Testes de funcionalidade das células unitárias de detecção

Abstract

The Alpha Magnetic Spectrometer (AMS) to be installed in the International Space Station (ISS) will be equipped with a proximity Ring Imaging Cherenkov (RICH) detector for measuring the velocity and electric charge of the charged cosmic particles. This detector will contribute to the high level of redundancy required for AMS as well as to the rejection of albedo particles. Charge separation up to iron and a velocity resolution of the order of 0.1% for singly charged particles are expected.

A RICH prototype consisting of a detection matrix with 96 photomultiplier units, a segment of a conical mirror and samples of the radiator materials was built and its performance was evaluated. Results from the 2003 beam test performed with ion fragments originated from the collision of a 158 GeV/c/nucleon primary beam of indium ions (CERN SPS) on a lead target are thoroughly presented. The large amount of collected data allowed to test and characterize different aerogel samples and the sodium fluoride radiator. The velocity and electric charge reconstruction capabilities of this subdetector were confirmed. In addition, the reflectivity of the mirror was evaluated. The data analysis confirms the design goals.

On the other hand, the accuracy of the charge reconstruction requires that the single detection cell response must be known at the percent level. Extensive characterization of all the detection elements was performed prior to and during the detector assembly.

Keywords: RICH/AMS, Čerenkov Angle, Electric Charge, RICH Prototype, 2003 Beam Test, Detection Cell Functionality Tests

Acknowledgments

No man is an island.
John Donne
in Devotions Upon Emergent Occasions,
Meditation XVII

The work presented in this thesis corresponds a joint effort in the context of the participation of LIP (Laboratório de Instrumentação e Física Experimental de Partículas) in the AMS experiment. The contributions from many made its accomplishment possible. In some lines I would like to thank everyone involved in the development of this work, helping me in this enterprise.

Firstly, I would like to thank Professor Fernando Barão, my supervisor, for all the support and availability for all the fruitful discussions and for having introduced me to this challenging area: Astroparticle Physics. My sincere thanks for his professional attitude.

A very special thanks to Rui Pereira for the daily brainstormings, for all the availability, friendship and for all the delighting conversations soaked in his witty humour.

Thanks to Patrícia for the knowledge and scientific attitude she transferred me in such an enthusiastic way. Thanks for all the good times after the most stressful tasks overcome.

I am very grateful to Professor Mário Pimenta for the all the suggestions, for the enthusiastic way he conducted all our discussions and encouraged me.

I also express my acknowledgments to João for the fruitful discussions on physics and on technical questions. Thanks for his co-operation at the beginning and for his sincere friendship.

I would like to thank Grenoble people and Madrid group for the good reception within their institutes. Thanks to RICH collaboration of Grenoble for the prototype construction and for the first calibration tests in which I had opportunity to take part. Thanks to Madrid people for the strong collaboration in data analysis and calibration tests. My special thank for the joint effort during the beam test periods not only to the former groups as well as to the other institutes within the RICH collaboration.

Thanks also to David Maurin whose work gave me the first boost in the propagation models study. Thanks for the corrections suggested to this manuscript.

I thanks Fundação para a Ciência e a Tecnologia for the financial support provided.

I also thank Catarina, Gonçalo, Pedro and Andreia for the friendship and help offered to overcome technical questions. Thanks for the pleasant lunch times and refreshing coffee breaks.

I would like to express my extreme gratitude to my parents and grandparents for all the unconditional love, support and constant attention in all the steps of this period of my life. My sincere thanks to Ana, my beloved sister, for her company in several occasions. Thanks also to my parents-in-law for the company and for several times having watched over me as a daughter. To little Mariana I want to thank for her sweet intelligence and unforgettable good playtimes.

My special thanks to Rui whose constant presence, love and tenderness, helped me to endure such a demanding task.

To my friends Paula, Alberto and Bruno I would like to thank for the thrilling discussions on Physics and sincere friendship. Thanks for proving the quote: "Real friends are never apart, maybe in distance, but not in heart". Thanks also to Srª Dª Elvina for the friendship, contagious good mood and bright smile.

Finally I express my recognition to all the people in LIP and people from the AMS collaboration that in any way contributed to the birth of this work, a very grateful experience. Thanks to LIP which embraced me in such a good way!

Contents

List of Figures

List of Tables

Introduction

Scientists love a mystery, because solving a mystery in nature means the opportunity to learn something new about the universe.
High-energy cosmic rays are just such a mystery.

Pierre Auger Observatory homepage

The recent technological advances in the capacity of detecting cosmic rays strengthened the establishment of a new interface field between particle physics and astrophysics: astroparticle physics. In this interdisciplinary research field several fundamental issues regarding the origin of matter in the universe are being explored. The subjects being addressed include: high energy and very high energy cosmic rays, dark matter, gravitation and neutrinos. In particular the study of cosmic rays has traditionally been an important tool for understanding the high energy processes. The existence of ionizing particles falling into the Earth's atmosphere was first noticed in 1912 by Victor Hess through a series of balloon-flight measurements. Hess shared the 1936 Nobel prize with Carl D. Anderson, who discovered the positron in cosmic rays, confirming Dirac's first prediction of the existence of antimatter through its quantum-relativistic formulation for the electron. Cosmic rays have historically been very important for the development of particle physics. Before the emergence of man-made high energy particle accelerators, they were the only means of studying energetic collision and decay processes. The muon (1937), the pion (1947), the positron (1932) and particles containing strange quarks were first discovered in cosmic-ray induced reactions.

Interest in cosmic rays has been recovered recently because a precise knowledge of its spectrum can enlight several fundamental issues like the apparent absence of primordial antimatter and the origin of dark matter.

During the last decade an intensive experimental program has been established and will keep on taking place for the forthcoming years motivated by the previous outstanding quests. The region of ultra-high energy of the spectrum ($E \gtrsim 10^{18}$ eV/nucleon) has been studied with experiments like AGASA [1], HiRes [2], and AUGER [3], indirectly detecting cosmic rays on the surface of the earth by observing the showers of particles they produce in the air. An air shower occurs when a fast-moving cosmic-ray particle strikes an air molecule high in the atmosphere, creating a violent collision. Fragments fly out from this collision and collide with more air molecules, in a cascade that continues until the energy of the original particle is spread among millions of particles raining down upon the earth. By studying the air showers, scientists can measure the properties of the original cosmic-ray particles.

The extensive air showers induced by primary cosmic rays in the energy range $10^{14} - 10^{18}$ eV have been probed by experiments like KASCADE [4] and recently by KASCADE-Grande [5].

The measurement of cosmic rays in the region of medium and lower energy ($E \lesssim 10^{13}$ eV/nucleon) is made directly and requires sending detectors to heights above most of the earth's atmosphere, using high-flying balloons (e.g. HEAT [6], ISOMAX [7], CAPRICE [8], BESS [9] and more recently ATIC [10], TRACER [11] and CREAM [12] all taking advantage of NASA's long-duration balloon program), satellites (e.g. PAMELA [13]) or the International Space Station (ISS) like AMS.

As the first magnetic spectrometer in space, the Alpha Magnetic Spectrometer (AMS) will collect information from cosmic sources emanating from stars and galaxies millions of light years away from the Milky Way. A precursor flight on board of the U.S. Space Shuttle Discovery, STS-91 took place in June 1998 for a 10 day period, at a mean altitude of 370 km, completing 152 orbits at $\pm 52^{\circ}$ of latitude, in order to test the design principles. This was achieved as well as about 100 million cosmic-ray events were collected enabling precise measurements of the spectra of high energy protons, electrons, positrons and helium nuclei [14]. This first stage of the experiment is known as AMS-01. For the second phase an improved version of the detector, with the inclusion of new subdetectors and the completion of those from the experimental flight, will be installed in the International Space Station and will take data for at least three years.

The detector was designed and is being constructed by an international team of physicists and engineers from 37 universities and research institutes located in

Switzerland, France, Russia, China, Taiwan, Italy, Germany, Spain, Portugal, Romania, Finland and the United States. Important technical challenges have been faced to build such a detector for use in space in accordance with strict space qualification standards and safety parameters requested by **N**ational **A**eronautics and **S**pace **A**dministration (NASA). Not only the international support of the experiment but also the joint effort of the U.S. **D**epartment **o**f **E**nergy (DOE) and NASA are making it become true.

Specifically, AMS has been designed to study the origin and composition of cosmic rays; the physical origin and structure of dark matter; to probe the existence or absence of cosmological antimatter and to understand the overwhelming majority of matter over antimatter in the visible Universe through the detection of anti-carbon, anti-helium or heavier nuclei with a sensitivity $\sim 10^4$ better then the current experimental limits, for example for helium nuclei the upper limit is of the order of 10^{-9} ($\overline{\mathrm{He}}/\mathrm{He} < 10^{-9}$). These characteristics overwhelm the capacity of the previous stratospheric balloon experiments which have been limited by their short duration, resulting in low statistics, and affected by the absorption power of Earth's atmosphere. AMS will be able to detect cosmic rays with kinetic energies in the range $\sim$0.3$-$0.5 GeV to $\sim$1 TeV.

This thesis is dedicated to one of the subdetectors of AMS, the Ring Imaging Čerenkov detector (RICH) whose purpose is to perform a highly accurate measurement of particle's velocity. A relative resolution of 0.1% is expected for unitary charges. The RICH detector will also give a measurement of the absolute value of the charge, identifying nuclei at least up to iron ($Z = 26$). Besides, the measurement of the isotopic abundances of light nuclei (up to $A \sim 10$), essentially secondarily produced, AMS isotopic measurements will also provide information about the galactic halo, cosmic-ray time confinement and will help to distinguish different propagation models. The RICH detector will play a key role in this framework providing a velocity measurement whose resolution evolutes with charge with a law like $\sim 0.1\%/Z$.

The device will have a dual radiator composed of a central square of sodium fluoride surrounded by aerogel tiles with a refractive index of 1.05. The detection matrix will have 680 photomultipliers coupled to light guides. The whole detector will be involved by a high reflectivity conical mirror.

In this thesis my research activity, during a period of four years as a PhD student in AMS is presented.

The AMS research group of LIP (Laboratório de Instrumentção e Física Experimental de Partículas) had an active participation in the ion beam tests performed with a prototype of the RICH detector at CERN (European Organization for Nuclear Research) in 2002 and 2003, as well as in the tests with cosmic rays, participating in the data analysis. LIP also had an important participation in the aerogel tile optical characterization that took place at LPSC (Laboratoire de Physique Subatomique et de Cosmologie), Grenoble, as well as in the functional tests and full characterization of the final detection unit-cells performed at CIEMAT (Centro de Investigaciones Energéticas, Medioambientales y Tecnológicas), Madrid. From the point of view of the software, LIP is partially responsible for the Monte Carlo simulation programs, for the charge and velocity reconstruction programs and for the analysis of some physics channels with the AMS full simulation. LIP is also simulating the optical surface roughness effects within the GEANT4 collaboration, implementing new tools for a better description of photon propagation. LIP was responsible for several optimization studies for the RICH radiator like the dual radiator configuration, the aerogel radiator thickness and aerogel tiles' spaces.

As already referred, in order to test the measurement capabilities and design goals of RICH, a prototype was built with 1/10 of the detection matrix of the final detector. The goal of this work is, on one hand, to evaluate the behaviour of the RICH prototype during the ion beam test in 2003 and on the other hand to show the results of the functionality tests with the final unit cells grid. In the former studies three different tiles of aerogel were used which allowed their complete characterization. The data from the tracker were also available which gave a very precise measurement of the track and allowed an external measurement of charge.

My contribution to the activity of the AMS group during my PhD includes the participation in the RICH prototype beam tests at CERN and the data analysis to estimate the prototype performance. I also did a comparative study with Monte Carlo simulation. I studied and implemented the velocity algorithm optimization. This algorithm is based on a likelihood approach for the Čerenkov angle reconstruction and therefore for the particle velocity reconstruction. I also took part in the functional tests of the RICH detection unit cells at CIEMAT and analyzed the data.

This thesis is organised in nine chapters. In the first some topics in cosmic-ray physics are presented: present knowledge about their origin, acceleration mechanisms and propagation. The matter-antimatter problem with its theoretical and experimental features is established, with an emphasis on the observational part: its manifestations, difficulties in detection and the recent experimental efforts, in particular AMS-01 results. The dark matter problem is also approached.

The next chapter is dedicated to a description of the AMS-02 detector, where each subdetector is introduced. Here the aims of the AMS experiment are exposed. The third chapter starts with some brief considerations on the Čerenkov radiation and then the RICH detector, the detector in this current study, is introduced. The RICH standalone simulation is briefly described and the simulation studies for the effects of the radiator black PORON walls on photon ring acceptance are presented.

Chapter 4 introduces the Čerenkov angle reconstruction method as well as its optimization studies. The charge reconstruction method is also thoroughly explained.

Chapter 5 describes the RICH prototype and all the other subdetectors present at the experimental setup for the 2003 beam test. The analysis of the data acquired is the core of this thesis and it is described in the following chapters.

Chapter 6 is dedicated to the analysis of the runs with the aerogel radiator in different configurations: vertical runs, inclined runs, tile scan runs and wide beam runs. A complete characterization of each aerogel radiator was possible. The comparison with Monte Carlo is showed and discussed.

Chapter 7 is devoted to the sodium fluoride runs analysis and to the light guide standalone simulation to explain the disagreement between the signal observed in data and Monte Carlo.

Chapter 8 presents the analysis of the runs with a prototype of the RICH mirror together with the evaluation of the mirror reflectivity. A comparison with the manufacturer measurement in laboratory is done.

Chapter 9 presents the status of the RICH assembly. The functionality tests with the detection unit-cells of the grid G and the aerogel tile characterization are described.

Finally the conclusions obtained from this work are shown.

Chapter 1

Cosmic Rays

The ability to reduce everything to simple fundamental laws does not imply the ability to start from those laws and reconstruct the universe.
Philip W. Anderson

1.1 Introduction to Cosmic Rays

Cosmic Rays (CR) are high energy particles originated in space that reach the top of the atmosphere. The incoming flux is mainly formed by ionized nuclei and protons (98%) and by a small percentage of electrons and a detectable flux of photons and neutrinos (2%).

Cosmic rays are divided in three different categories: Galactic Cosmic Rays (GCR), Solar Cosmic Rays (SCR) and Anomalous Cosmic Rays (ACR).

Galactic cosmic rays are originated and accelerated far outside our solar system. Their composition is 90% protons, 9% α particles, 1% electrons and heavier nuclei fully ionized, as well as, antiprotons and positrons essentially produced in secondary reactions. GCR are the most typical cosmic rays with energies extending up to 10^{20} eV.

Solar cosmic rays or Solar Energetic Particles (SEP) have their origin in the Sun mostly originated from solar flares, coronal mass ejections and shocks in the interplanetary medium. Their composition is roughly similar to the GCR with energies up to several hundred MeV/nucleon.

Anomalous cosmic rays [15] are mainly singly charged low energy particles ($<$

100 MeV/nucleon) resulting from interstellar neutral particles that are photoionized by solar UV photons or by charge-exchange collisions with solar wind protons when they penetrate the heliosphere and are carried by the solar wind. They have more helium than protons and much more oxygen than carbon. This unusual composition reflects the fact that only atoms with high first-ionization potentials (above 13.6 eV) are abundant as interstellar neutrals. These cosmic rays are below the detection range of AMS. AMS will detect cosmic rays in the energy range above few hundred MeV and below 1 TeV and these cosmic particles are thought to be originated by galactic sources.

The discovery of CR dates from the beginning of the 20th century when in 1900, Wilson discovered the continuous atmospheric ionization by measuring the accumulated static charge. It was believed to be due to the natural radioactivity of the Earth. In order to check that, Victor Hess (Nobel Prize 1936) from the University of Vienna launched in 1912 an electrometer aboard a balloon to an altitude of 5 km. He discovered that the ionization rate first decreased up to about 700 m as expected, but then increased with altitude showing thus an outer space origin for ionization rather than from natural radioactivity coming from the Earth. During the following experiments, Hess showed that the ionizing radiation was not of solar origin since it was similar for day and night time. In 1928 J. Clay discovered that the ionization rate increased with latitude thus showing that the ionization sources were charged particles deflected by the geomagnetic field.

D. Skobelzyn (1929), using a newly invented cloud chamber, observed the first ghostly tracks left by cosmic rays. In the same year Bothe and Kolhörster had the experimental proof that CR are charged particles assuming to be only composed of electrons. Later on, in 1937, S. Neddermeyer and Carl Anderson discovered muons in cosmic rays. Cosmic rays were used for particle physics research until the appearance of particle accelerators in the fifties.

In 1938 T.H. Johnson *et al.* discovered that the ionization rate increases from east to west, indicating that the ionization was due to positively charged particles correctly assumed to be protons. In the same year, P. Auger discovered extensive air showers, showers of secondary nuclei produced by the collision of primary high-energy particles with air molecules. Using two cloud chambers in the Alps located many meters apart and performing coincidence measurements, he indirectly measured the cosmic-ray energy up to 10^{15} eV. In 1948 P. Frier *et al.* discovered helium and heavier elements in CR.

In 1950 the U.S. Naval Research Laboratory fired the Viking research rocket at the intersection of the geographic and geomagnetic equators in order to study the correlation between the cosmic ray intensity and the pressure and atmospheric temperature. Nine years later, the Russian K. Gringauz flew 'ion traps' on the Soviet Luna 2 and 3 missions. Explorer VII was launched into Earth orbit with a particle detector. Later, in 1977, Voyager I and II were launched to the interstellar medium (ISM). In the period from 1977 until 1982 a series of balloon experiments took place. The data collected allowed Bogomolov *et al.* to found antiprotons in CR. In 1990 the Ulysses mission was launched to obtain a tridimensional map of the solar wind and cosmic rays.

Simultaneously a great effort to understand the origin and nature of this radiation was done by the theorists. In particular, the understanding of the origin of the most energetic component of the cosmic rays has made a great influence on the study of novas and supernovas and on the theory of plasmas in astrophysics.

1.1.1 Cosmic-ray spectra

The most striking feature of the cosmic rays is the fact that their energy spectra span a very wide range of energies indeed. From the left-hand plot of Figure 1.1 it is visible that the energies are between 10^9 eV and 10^{20} eV. Below 10^9 eV the interaction between the Earth's magnetic field and the outflowing solar wind forbids any measurement. This phenomenon is known as solar modulation of the flux of cosmic rays. It appears that the greater the solar activity, the greater the disturbances in the interplanetary magnetic field which impede the propagation of particle with energies less than 1 GeV/nucleon.

The spectra extends over 32 decades in flux between some millions of particles per m^2 per second at low energies and of the order of one particle per km^2 per century for the most energetics. Another important aspect of the spectra is that its

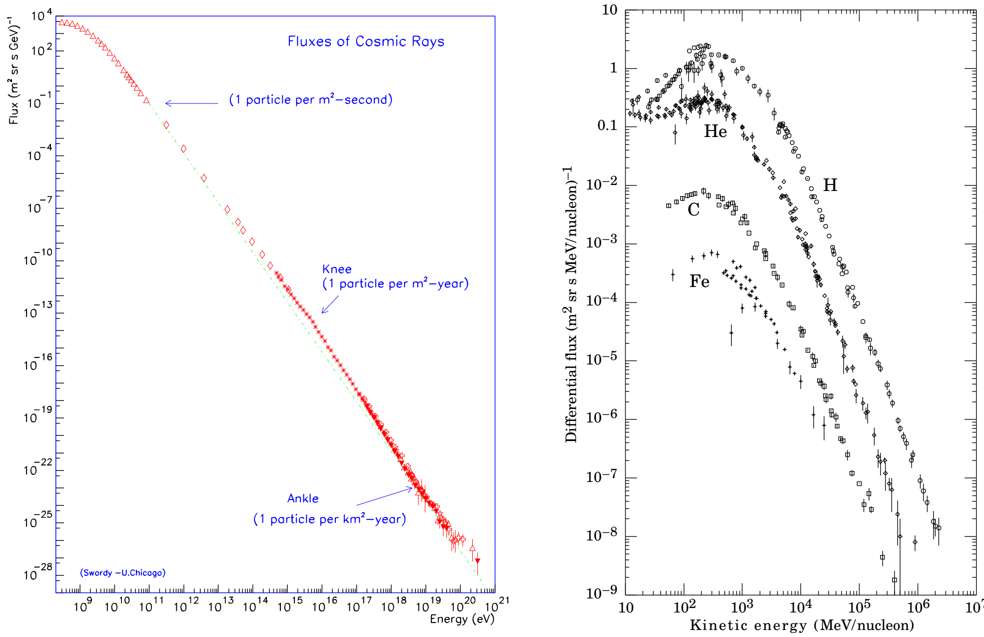

Figure 1.1: *The spectrum of cosmic radiation. Left: the total flux* [16]*. The dotted line shows an* E^{-3} *power-law for comparison. Right: the differential fluxes of different species of GCR near the Earth* [17].

form can be approximately represented by a simple power law of the form

$$\frac{dN}{dE} \sim E^{-\gamma} \tag{1.1}$$

where γ is the spectral index.

The right-hand plot of Figure 1.1 shows the differential energy spectra for different species of CR. One can see that the spectra are fairly similar to each other which indicates that the particles were generated/accelerated with similar processes. Up to values around 10^{15} eV (1 PeV), $\gamma \simeq 2.7$. From here on the spectrum becomes steeper with $\gamma \simeq 3$ ('knee'), which could point to a different origin for the two regions. From around 3×10^{18} eV the spectrum becomes less steep again ('ankle'). The behaviour at 10^{20} eV has been an important issue. The questions are: if an energy maximum has been reached at 5×10^{19} eV because of the interaction of cosmic rays with the cosmic background radiation (Greisen-Zatsepin-Kuzmin cut-off), or if a plateau is forming, or whether the flux simply becomes too small to be reliably measured. The observation of events at energies higher than 10^{20} eV has given rise to speculative ideas about their origin [18]. The question of whether the spectrum extends beyond

10^{20} eV is currently the foremost problem in high-energy particle astrophysics.

The changes in the spectral index reflect the different origin and the propagation history of cosmic rays with different energy: below the 'knee' their curvature radius is smaller than the galactic disk thickness, hence their sources must belong to our Galaxy. Above the 'knee' ($E > 10^{18}$ eV), due to the fact that particles can not be magnetically bound efficiently by the Galaxy, the curvature radius becomes greater than the disk thickness, and cosmic rays may escape into the galactic halo.

Another possibility is that the 'knee' is associated with the upper limit of acceleration by galactic supernovae, while the ankle is associated with the onset of an extragalactic population that is less intense but has a harder spectrum that dominates at sufficiently high energy. The limiting energy is defined by the size and magnetic field strength of the acceleration region ($E_{max} < Z \times (B \times L)$).

Primary and secondary cosmic rays

The elemental composition of cosmic rays can be measured at energies ranging from MeV to TeV and is similar in good approach to the solar system values (see Figure 1.2). This points to a similarity in the production processes, i.e. both of stellar nature.

There is a pronounced odd-Z versus even-Z variation in the abundance and there is an abundance peak at iron for both. The first can be understood as being due to the relative stability of the nuclei according to their atomic numbers. Nevertheless, differences are observed, especially for the most abundant nuclei: H and He, which are relatively less abundant in cosmic rays. This is not fully understood and it could be either due to their ionization potential and consequently to the greater difficulty in accelerating those particles or due to a different birth mechanism. The *spallation* products of C and O (Li, Be, B) and those of Fe (Sc, Ti, V, Cr, Mn, known as sub-Fe elements) in the hydrogen nuclei of the interstellar medium are more abundant in cosmic rays since they are not produced in stellar nucleosynthesis. From the experimental point of view, the B/C ratio is the most significant quantity of the relation between primaries and secondaries. Information on the density of the interstellar medium can be obtained comparing the relative abundance of primaries and secon-

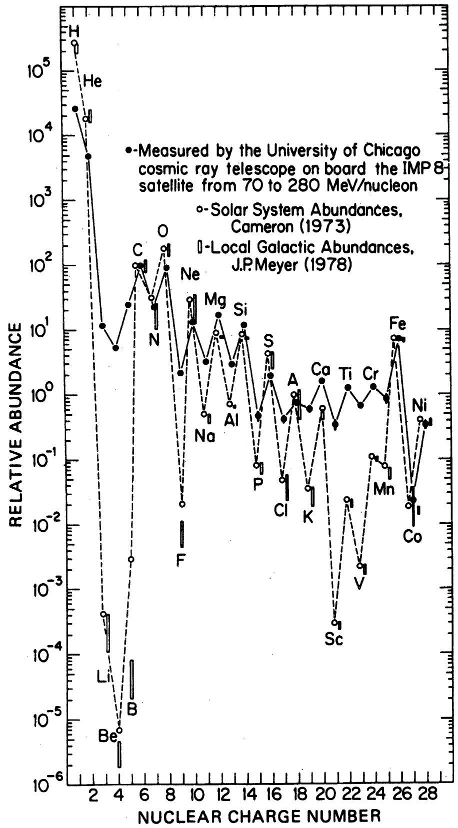

Figure 1.2: *The cosmic ray elemental abundance (H-Ni) measured on board of cosmic-ray satellite (closed circles) compared to solar system abundances (open circles) and to local galactic abundances (open boxes)* [19].

daries. An estimate of the amount of matter traversed based on ratios of secondary spallative products gives a value ranging from 5 to 10 g/cm^2 between the injection and the observation. Being the average density in the Galaxy of 1 proton/cm^3, the amount of matter traversed comes several times the thickness of the Galaxy which proves that the propagation is by diffusion [16].

1.1.2 Origin and acceleration mechanisms for cosmic rays

Using the cosmic ray energy requirements and the nonthermal radiation as a guideline, then the most powerful accelerators of relativistic particles in the Galaxy should be supernovae (SN) and supernova remnants (SNR); pulsars; compact accreting systems, like neutron stars or black holes in close binary systems; stars and winds of young massive stars. It is commonly assumed that cosmic rays with the highest detected energies, $E > 10^{19}$ eV, have an extragalactic origin. They might be generated in active galactic nuclei, relativistic jets, interacting galaxies, or result from the decays of hypothetical topological defects [20].

Concerning the energy, supernovae with its remnants, which may include neutron stars, are the most probable cosmic ray sources in the Galaxy [21] for energies at least up to the 'knee' at $\sim 10^{15}$ eV and probably up to the 'ankle' at $\sim 10^{18}$ eV. The data on cosmic rays at the Earth and the observations of nonthermal radiation from supernova remnants testify that the particles are accelerated with high efficiency and in a wide range of energies. The total power of galactic cosmic ray sources necessary to maintain the observed cosmic ray density is estimated as $L_{cr} \sim 10^{41}$ erg/s that implies the release of energy in the form of cosmic rays of approximately 10^{50} erg per supernovae if the supernovae rate in the Galaxy is 1 every 30 years [20]. This value comes to about 10% of the kinetic energy of the ejects which is in agreement with the prediction of the theory of diffusive shock acceleration for supernovae [22] discussed below.

Diffusive shock acceleration is the most generally accepted process for the investigation of cosmic ray acceleration in the Galaxy and it assumes the acceleration of cosmic rays by the outward propagating shock, which results from the supernova explosion and propagates in the interstellar medium or in the wind of the progenitor star.

A description of Fermi's original theory explaining acceleration is given, followed by its modification in the context of astrophysical shocks into the more efficient 1$^{\text{st}}$ order Fermi mechanism, known as diffusive shock acceleration.

The rotational energy of a young pulsar with period P that remains after the supernova explosion is estimated to be 2×10^{50} $(10\,\mathrm{ms}/P)^2$ erg and may provide an additional energy reservoir for the acceleration of cosmic rays. Binary star systems could also be a source. If one of the participating partners is a compact object such as a neutron star or a black hole it accretes mass, which is strongly accelerated, from its companion. The candidates discussed above are sources as well as accelerators and are of very small size, they are therefore called *point sources*.

Fermi acceleration

In order to explain the origin of cosmic rays, Enrico Fermi in 1949 [23] suggested an effective mechanism of particle acceleration. He explored the possibility of a charged particle interacting with a moving magnetic cloud in the interstellar medium (ISM) and acquiring part of its kinetic energy. These clouds are rather large, several light years, occupying several percent of ISM, with a density 10−100 times higher than the average ISM density. In the original Fermi's theory charged particles are reflected from 'magnetic mirrors' associated with irregularities in the Galactic magnetic field. Mirrors are assumed to move randomly with typical velocity V, and Fermi showed that particles gain energy statically in these reflections. If particles only remain within the acceleration region for some characteristic time τ a power-law distribution of particles is found.

In the frame of the cloud:

- there is no change in energy because the scattering is elastic, the cloud as a whole is much more massive than the cosmic ray;
- the cosmic ray's direction is randomized by the scattering.

Assuming that θ_1 is the angle between the initial direction of the particle and the normal to the surface of the mirror, the change of particle energy in a single collision written in the cloud's frame is:

$$E_1' = \gamma E_1 \left(1 - \beta \cos\theta_1\right) \tag{1.2}$$

where $\beta = V/c$ and $\gamma = 1/\sqrt{1-\beta^2}$. Going back to the laboratory frame:

$$E_2 = \gamma E_2' \left(1 + \beta \cos\theta_2'\right) \tag{1.3}$$

Since the magnetic field is tied to the cloud and this is very massive, in the cloud's rest frame there is no change in energy, $E_2' = E_1'$, and hence we obtain the fractional change in the laboratory frame energy $(E_2 - E_1)/E_1$,

$$\frac{\Delta E}{E} = \frac{1 - \beta\cos\theta_1 + \beta\cos\theta_2' - \beta^2\cos\theta_1\cos\theta_2'}{1-\beta^2} - 1 \tag{1.4}$$

Inside the cloud, the direction is random, $<\cos\theta_2'> = 0$. The $<\cos\theta_1>$ depends on the rate at which cosmic rays collide with clouds at different angles. The rate of collision is proportional to the relative velocity between the cloud and the particle so that the probability per unit solid angle of having a collision at angle θ_1 is proportional to $(v - V\cos\theta_1)$. So

$$<\cos\theta_1>=\frac{\int \cos\theta_1 \frac{dP}{d\Omega_1} d\Omega_1}{\int \frac{dP}{d\Omega_1} d\Omega_1} = -\frac{\beta}{3}, \tag{1.5}$$

giving

$$\frac{\Delta E}{E} = \frac{1+\beta^2/3}{1-\beta^2} - 1 \simeq \frac{4}{3}\beta^2 \tag{1.6}$$

since $\beta \ll 1$.

Thus, the net energy gain (averaged per collision) is

$$dE \propto \beta^2 E \tag{1.7}$$

and the energy attained by the particle after n collisions is

$$E = E_i \mathrm{exp}(\beta^2 n) \tag{1.8}$$

where E_i is the initial 'injection' energy of the particle.

This mechanism has to compete with ionization losses. Effectively the Fermi acceleration mechanism has a threshold energy. For protons this energy is about 200 MeV, for oxygen about 20 GeV and 300 GeV for iron because of higher ionization losses. Thus, this mechanism cannot produce the similar shape of differential spectra for different nuclei as discussed in subsection 1.1.1.

First order Fermi acceleration at SN or other shocks

Bell (1978) [24] and Blandford and Ostriker (1978) [25] independently showed that Fermi acceleration by supernova remnant shocks is particularly efficient because the motions are not random. A charged particle ahead of the shock front can pass through the shock and then be scattered by magnetic inhomogeneities behind the shock (see Figure 1.3). Here a large plane shock front moves with velocity $-u_1$. The shocked gas flows away from the shock with a velocity u_2 relative to the shock front and $|u_2| < |u_1|$. Thus, in the laboratory the gas behind the shock moves to the left with velocity $V = -u_1 + u_2$. Equation 1.4 applies to this situation

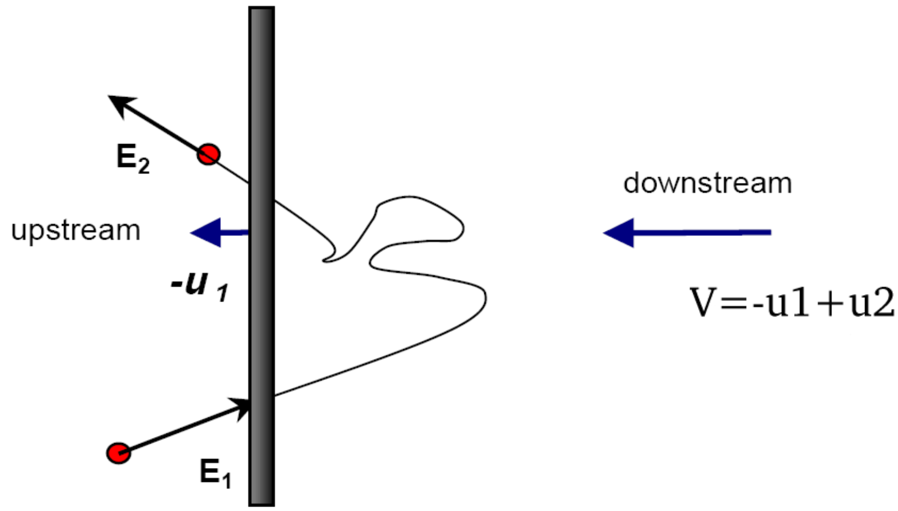

Figure 1.3: *Sketch of a collision of a charged particle with a moving shock.*

with β interpreted as the velocity of the shocked gas ('downstream') relative to the unshocked gas ('upstream'). Since the shock is planar, $<\cos\theta_1>$ = -2/3 e $<\cos\theta_2'>$ = 2/3. Therefore,

$$\frac{\Delta E}{E} = \frac{1 + \frac{4}{3}\beta + \frac{4}{9}\beta^2}{1-\beta^2} - 1 \approx \frac{4}{3}\beta \tag{1.9}$$

This acceleration is more effective ($\beta \ll 1$) than the previous mechanism. The particle gains energy from this 'bounce' and flies back across the shock, where it can be scattered by magnetic inhomogeneities ahead of the shock. This enables the particle to bounce back and forth gaining energy each time. This process is now called the 1$^{\text{st}}$ order Fermi acceleration (also known as Fermi shock acceleration) because the mean energy gain is dependent on the shock velocity only to the first power. The previous process is the 2$^{\text{nd}}$ order Fermi acceleration.

Evidences for shock acceleration from supernova

The characteristic spectrum of synchrotron radiation is featureless, following a more or less straight line. This is in contrast to a spectrum from a hot radiating gas, which has many bumps and peaks corresponding to emission from particular atoms at particular energies.

The analysis of synchrotron emission, which occurs when high energy electrons spiral around magnetic field lines, in Cas A [26] showed the presence of electrons with energies up to 200 GeV at the strength of a magnetic field arount 500 μG in the young supernova remnant. The interpretation of nonthermal radio emission from external galaxies confirms that supernova remnants are the locals of acceleration of relativistic electrons with the same efficiency which is needed to provide the observed intensity of galactic cosmic-ray electrons [27].

Gamma-ray emission associated with few bright supernova remnants has been found using the EGRET[1] catalogue of gamma-ray sources at $E > 30$ MeV [28]. The gamma-ray fluxes from the two most prominent sources, gamma-Cygni and IC443, indicate an energy of about $3{\times}10^{49}$ erg for relativistic protons and nuclei confined in each envelope, assuming that gamma rays are generated through $\pi^0 \to 2\gamma$ decay.

The nonthermal X-rays radiation with a characteristic power law tail at energies more than few keV from the bright rims in supernova remnants including SN1006 [29, 30], RX J1713.7-3946 [31, 32], IC443, RCW 86 [32], and Cas A [33] was found in experiments done by the X-ray observatoires ASCA, RXTE, ROSAT, Chandra, XMM/Newton. It was interpreted as synchrotron emission by electrons accelerated up to energies as high as 100 TeV. The inverse Compton scattering of background photons by these electrons and/or gamma rays generated via π^0 decays is the most probable mechanism of the emission of TeV gamma-ray flux detected from RX J1713.7-3946 [34] and Cas A [35].

1.2 Propagation Models

When the cosmic ray beam, which resembles an accelerated sample of galactic matter, propagates through ISM it interacts in various ways depending on the type of cosmic ray particle and the constituents of this interstellar environment such as gas, magnetic fields or photons [36].

In our galaxy cosmic rays spend more than 10^7 years before they escape into the intergalactic space. This suggests a diffusive process for their transport, since the confinement time along a line through the disk of our galaxy would only be about 10^3 years.

The distribution of synchrotron radio emission can be observed from edge-on

[1]Energetic Gamma Ray Experiment Telescope.

spiral galaxies such as NGC 891 implying that high energy particles do not strictly restrain to the thin galactic disk but propagate out into the halo. Thus the volume in which cosmic rays can be found is larger than that given by the thin galactic disk where most of the stars and energetic processes take place. Cosmic ray sources are probably located in the same region.

Any model whose purpose is describing the transport of CR in the galaxy has to reproduce the observational data of many kinds which are related to cosmic-ray origin and propagation. All these various observational data provide many independent constraints and should be used to develop a realistic physical picture of CR propagation.

The general equation of diffusion can be written as [37, 38, 21, 39]

$$\frac{\partial N_j}{\partial t} - \vec{\nabla} \cdot (D\vec{\nabla}N_j - \vec{V}_c N_j) - \frac{\partial}{\partial E}\left(\frac{\vec{\nabla} \cdot \vec{V}_c}{3} E_k \left(\frac{2m + E_k}{m + E_k}\right) N_j\right) + \frac{\partial}{\partial E}(b(E)N_i) - \frac{1}{2}\frac{\partial^2}{\partial E^2}(d_j N_j) + nv\sigma_j N_j = q_j + \sum_{k=j+1}^{n_{max}} nv\sigma_{kj} N_k \quad (1.10)$$

where the terms are

- $\vec{\nabla} \cdot \left(D\vec{\nabla}N_j\right)$: the diffusion term. D is the diffusion tensor;
- $\vec{\nabla} \cdot \left(\vec{V}_c N_j\right)$: the convection term originated by the galactic wind;
- $\frac{\partial}{\partial E}\left(\frac{\vec{\nabla}\cdot\vec{V}_c}{3} E_k \left(\frac{2m+E_k}{m+E_k}\right) N_j\right)$ is the adiabatic expansion term;
- q_j is the source term;
- $\frac{\partial}{\partial E}(b(E)N_i)$ is the term of losses by ionization and Coulombian interaction in the interstellar medium and $b(E) \equiv dE/dt$ is the energy loss rate which is only important for energies $\lesssim$500 MeV/nucleon;
- $\sum_{k=j+1}^{n_{max}} nv\sigma_{kj}N_j$; represents the secondary particle j production per interaction of the species k in the ISM with the density n;
- $nv\sigma_j N_j$ is the scattering term for particles j in the ISM with density n;

- $\frac{1}{2}\frac{\partial^2}{\partial E^2}(d_j N_j)$ where $d_j(E) = \frac{\Delta E}{\Delta t}$ is the stochastic reaccelleration term due to the scattering of charged particles in the magnetic turbulence in the interstellar hydrodynamical plasma, this mechanism is a Fermi mechanism of second order.

It has been pointed out many years ago that the relevant physical propagation model to be used is the diffusion model [38, 21]. According to that the sources of CR should be distributed within the thin galactic disk and the escape from the disk into the halo and finally into the intergalactic space is determined by diffusion. In this Diffusion Halo Model (DHM) a gradient of CR density away from the galactic disk is expected, implying a constant streaming of CR particles away from the galactic disk into the halo.

The DHM competes with the very popular Leaky Box Model (LBM). The LBM describes an equilibrium model in which cosmic-ray sources and primary and secondary cosmic ray particles are homogeneously distributed in a confinement volume (box, galaxy) and constant in time with no gradient of CR density. Thus the transport of CR is not controlled by diffusion but by a hypothetic leakage process at the imaginary boundaries.

The DHM is a more realistic propagation model. However, the LBM has been often preferred for its mathematical simplicity [38].

1.2.1 The Leaky Box model

In a certain sense, the Leaky Box model can be considered as an extremely simplified version of the diffusion model. In the LBM particles propagate freely in the containment volume and production and loss of particles are balanced in time, thus the mathematical description of the LBM is given by a continuity equation. In this case it is assumed that the diffusion takes place rather rapidly and that, therefore, the density of cosmic rays in the Galaxy is constant. Of course, it is necessary to wait a certain escape time from the system. Under such conditions the term $\vec{\nabla} \cdot (D\vec{\nabla} N_j)$ can be replaced by $\frac{N_j}{\tau_{esc}}$, where τ_{esc} is the escape time of CR from the confinement volume (Galaxy), often called the age of cosmic rays. By ignoring energy changing processes and radioactive particles the equation becomes the following [38] at the stationary case ($\partial/\partial t = 0$)

$$\frac{N_j}{\tau_{esc}} + \bar{n}v\sigma_j N_j = \bar{q}_j + \sum_{k=j+1}^{n_{max}} \bar{n}v\sigma_{kj}N_k \tag{1.11}$$

where all the quantities are now averaged $n \leftrightarrow \bar{n}$, $q_j \leftrightarrow \bar{q}_j$.

Consequently, this leads to a system of algebraic equations for the various kinds of nuclei j which allows to obtain $N_j = f(\bar{q}_j, \sigma_j, \sigma_{kj}; k = j...n_{max})$. For the first nucleus

$$N^{n_{max}} = \frac{\bar{q}^{n_{max}}}{(1/\tau_{esc} + \bar{n}v\sigma^{n_{max}})} \tag{1.12}$$

where τ_{esc} appears as a parameter determined by experimental data. From a statistical point of view there is an exponential distribution which governs the escape of an individual particle and τ_{esc} is the mean of it. The exponential distribution works since the probability of a particle escaping from the box in time dt is given by $dt/\tau_{esc}(E)$.

In order to calculate the ratios of secondaries over primaries (s/p) τ_{esc} is replaced by λ_{esc} which characterizes the matter traversed in [g/cm^2]. The relation is

$$\lambda_{esc}(E) =< m > \cdot\bar{n}(\mathrm{cm}^{-3}) \cdot c \cdot \beta \cdot \tau_{esc}(E) \tag{1.13}$$

where $<m>$ denotes the mean mass of gas and $c \cdot \beta$ the particle velocity.

λ_{esc} determination

The determination of λ_{esc} [39] can be done considering a primary P_1 and a secondary S_1 from P_1 ($q^{S_1} = 0$, only *spallation* origin with the production term being given by $\bar{n}v\sigma^{ps}P_1$). The ratio S_1/P_1 only depends on the parameter $\tilde{\lambda}_{esc} = \lambda_{esc}/ < m >$ and is written as

$$\frac{S_1}{P_1} = \frac{\sigma^{ps}}{\sigma^s + 1/\tilde{\lambda}_{esc}}. \tag{1.14}$$

Through the comparison of calculated s/p ratios, such as B/C and sub-Fe/Fe, with the measured ratio, λ_{esc} can be extracted from the fit to data since it is the only free parameter. Data for B/C are used because this is the most accurately measured ratio covering a wide energy range and having well-established cross sections. Figure 1.4 [40] shows such a fit to a compilation of measured B/C ratios. As the ratio B/C depends on the energy λ_{esc} is expected to have an energy dependence.

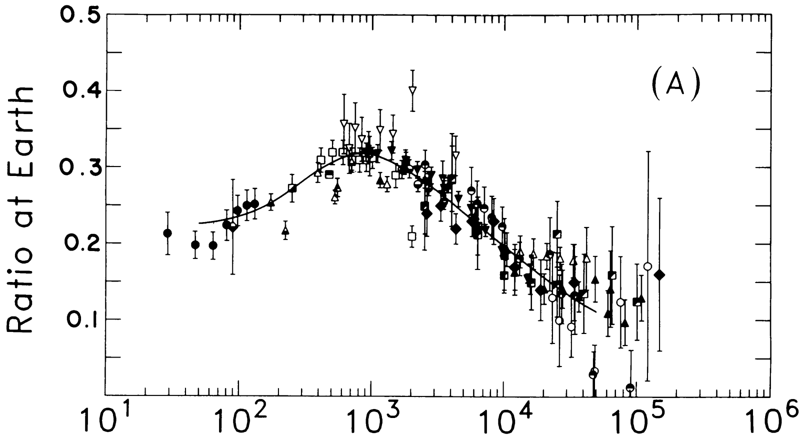

Figure 1.4: *Collection of measured B/C ratios at different energies* [40]. *The curve represents a fit to the data. The fit determines the λ_{esc} dependence in the LBM. Measured values are from the following:*

- ● Garcia-Munoz and Simpson (1979)
- Caldwell and Meyer (1977)
- Dwyer (1978)
- ◑ Dwyer and Meyer (1981)
- ○ Juliusson (1974)
- ◇ Buffington, Orth, and Mast (1978)
- Mewaldt *et al.* (1981)
- ◆ Orth *et al.* (1978)
- Fisher *et al.* (1976)
- Hagen, Fisher, and Ormes (1977)
- □ Maehl *et al.* (1977)
- Simon *et al.* (1980)
- ▲ Chappell and Webber (1981)
- △ Lezniak and Webber (1978*a*)
- Webber, Damle, and Kish (1972)
- Webber *et al.* (1977)
- Webber (1982)
- ▼ Engelmann *et al.* (1981)
- ▽ Lund *et al.* (1975)
- Julliot, Koch, and Petrou (1975)

$$\lambda_{esc} = \begin{cases} \lambda_0 \left[\mathrm{g/cm^2}\right] \left(\frac{R}{4.7\,\mathrm{GV}}\right)^{0.8} & \text{for } R < 4.7\,\mathrm{GV} \\ \lambda_0 \left[\mathrm{g/cm^2}\right] \left(\frac{R}{4.7\,\mathrm{GV}}\right)^{0.57} & \text{for } R > 4.7\,\mathrm{GV} \end{cases} \tag{1.15}$$

Equation 1.15 describes the dependence of λ_{esc} as function of rigidity [$R = pc/|Z|e$ (GV)] with $\lambda_0 = 12.8\,\mathrm{gcm^{-2}}$ [41]. Similar calculations have been done by many authors and Figure 1.5 shows some of the published curves on the rigidity dependence of $\lambda_{esc}(R)$, which are used by the various authors to fit the data on cosmic rays. Despite the visible differences existing between these curves, particularly at low energies, which may be partly due to cross-section uncertainties, they agree in their general shape. They all have the maximum around some GeV/nucleon and fall off to higher and lower energies.

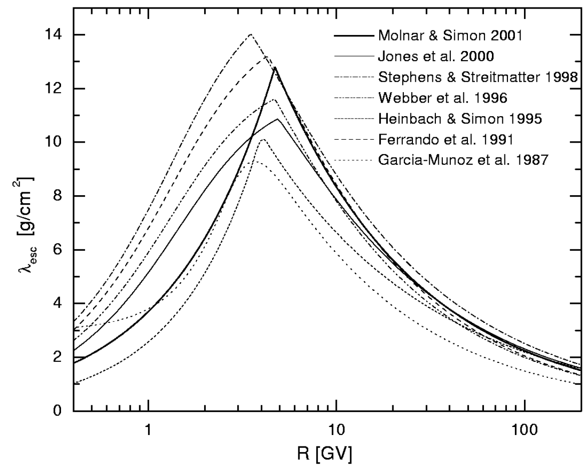

Figure 1.5: *Rigidity dependences of the mean escape lenght λ_{esc} as published by different authors [41]. This quantity is a free parameter in the LBM and results by fitting measured secondary/primary ratios, such as B/C.*

Mean density of the interstellar medium ($\bar{n}\,[\mathrm{cm}^{-3}]$)

As it was stated above in equation 1.13, the LBM uses the derived λ_{esc} values to obtain the mean age or escape time τ_{esc} of cosmic rays. To proceed like that it is necessary to previously determine $\bar{n}$, the mean density of the interstellar medium.

A test particle is needed which is not only sensitive to the total matter traversed in units of g/cm^2 but also to the gas density through which it traverses. Secondary radioactive isotopes are such test particles since they are not only produced along the mean path of λ_{esc}, but can also decay on their journey, and the number of actually survived isotopes depends on the gas density around them. Good candidates are those nuclei with decay times τ_{dec} at rest comparable to the expected escape time τ_{esc} such as: ^{10}Be (2.3×10^6 yr), ^{26}Al (1.0×10^6 yr), ^{36}Cl (4.5×10^5 yr), ^{53}Mn (5.4×10^5 yr). They are known as cosmic-ray clocks.

Thus, considering two isotopes originating from the same primary, like ^{10}Be and ^{9}Be, and comparing the measured surviving fraction of ^{10}Be which is the radioactive isotope, or the ^{10}Be/^{9}Be ratio (^{9}Be is a stable isotope), the mean gas density $\bar{n}$ (cm^{-3}) can be calculated. Making the following substitution in equation 1.14

$$\left[\sigma^s + 1/\tilde{\lambda}_{esc}\right] \longleftrightarrow \left[\sigma^s + 1/\tilde{\lambda}_{esc} + 1/(\gamma\tau^{\beta}_{I_i} \cdot \bar{n}v)\right], \tag{1.16}$$

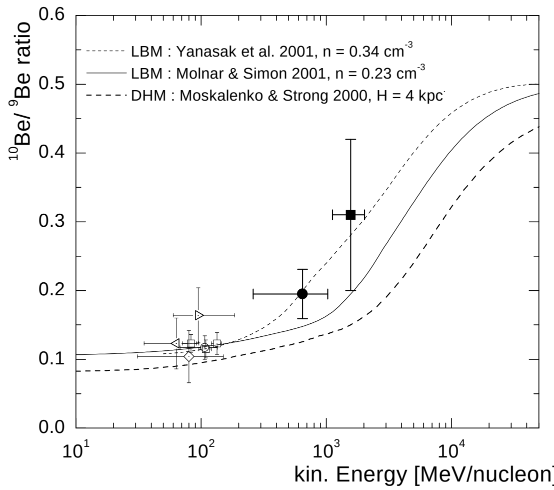

Figure 1.6: *Comparison between the calculated* $^{10}Be/^{9}Be$ *ratio and data* [42]. Measurements at the top of the atmosphere by ISOMAX (● Hams *et al.*, 2001 [42] and ■ de Nolfo *et al.*, 2001 [7]) *compared with space measurements:* □ *ACE* [43], ○ *Ulysses* [44], ◁ *Voyager 1-2* [45], ▷ *ISEE-3* [46], *and* ◇ *IMP 7/8* [40, 47]. *The lines show the expected beryllium ratio in different propagation models. The two upper lines are leaky-box model (LBM) the lower one is a diffusive-halo model (DHM).*

where the approximations $\sigma^{pI_1} = \sigma^{pI_2} \equiv \sigma^{ps}$ and $\sigma^{I_1} = \sigma^{I_2} \equiv \sigma^{s}$ were done assuming I_1 as the unstable isotope, the ratio of the two isotopes is:

$$\frac{S_{I_1}}{S_{I_2}} = \frac{\sigma^s + 1/\tilde{\lambda}_{esc}}{\sigma^s + 1/\tilde{\lambda}_{esc} + 1/(\gamma\tau_{I_i}^{\beta} \cdot \bar{n}v)}. \tag{1.17}$$

Determining $\tilde{\lambda}_{esc}$ from B/C and having data from the isotopic ratio in the conditions defined above, it is straightforward to invert the relation 1.17. The two upper curves in Figure 1.6 are different leaky-box models. The top dashed curve by Yanasak *et al.* (2001) assumes an average density of 0.34 atoms/cm^3 for the interstellar medium. The solid curve by Molnar & Simon (2001) takes a density of 0.23 atoms/cm^3 into account. A mean gas density of $\sim$0.34 cm^{-3} with a mean mass of $<m> = 2\times10^{-24}$ g and assuming the escape length to be $\lambda_{esc} = 10\,\mathrm{g/cm^2}$ for cosmic rays around some GeV/nucleon leads to an escape time $\tau_{esc} \sim 15$ My.

Model limitations

This simple, linear model that neglects energetic phenomena and consequently loses validity at the high-energy regime does not explain some measurements for the radioactive nuclei. The mean density of the interstellar medium given by the radioactive nuclei is of the order of $\bar{n} \sim 0.34\,[\mathrm{cm}^{-3}]$, while the observations of the galactic disk give $\sim 1\,[\mathrm{cm}^{-3}]$. This is usually interpreted as the proof of the existence of a large, diffusive halo empty of matter.

In fact a description in terms of Leaky Box may lead to wrong results for radioactive species in a realistic Galaxy [48].

1.2.2 The Diffusion Halo model

To solve the equation 1.10 a cylindrical geometry composed of two regions as shown in Figure 1.7 is used [39]. The inner area illustrates the thin Galactic disk of half-height $h = 0.1\,\mathrm{kpc}$ and the outer part is the halo. The radius of the cylinder is assumed to be $R = 20\,\mathrm{kpc}$ and the half-height L, whose numerical value is to be determined, is probably greater than a few kpc ($L \sim 3 - 10\,\mathrm{kpc}$). The half-heights satisfy $h \ll L$ so the disk is usually considered as infinitely thin for all practical purposes. The solar system is located in the galactic disk ($z = 0$) and rotates around the dense center at a distance $d = 8\,\mathrm{kpc}$ [50, 51].

It is assumed that cosmic ray sources are placed in the thin galactic disk, where the stars and most of the interstellar gas is located and homogeneously distributed but the cosmic rays themselves diffuse out and may spend appreciable portions of their lifetime in the halo. The gas is mostly composed of hydrogen (90%), neutral and ionized, and helium (10%), heavier nuclei being present but at a negligible amount. The density of interstellar matter is observed to be about $\bar{n} \sim 1\ \mathrm{cm}^{-3}$ for all radius, so $n(r, z) = 2h\delta(z)\bar{n}$. Particles escape freely through the halo boundaries into intergalactic space where the density of cosmic rays is negligible. Consequently, the diffusion model assumes a gradient in the density of cosmic rays with a maximum value in the Galactic disk decreasing as a function of distance from the Galactic plane; the escape of particles from the halo to the intergalactic space is done by diffusion.

The study of the transport of cosmic-ray nuclear component requires a consideration of nuclear *spallation* and ionization energy losses. Hundreds of isotopes are included in the calculations of nuclear fragmentation and transformation of energetic nuclei in the course of their interaction with interstellar gas. There is a powerful

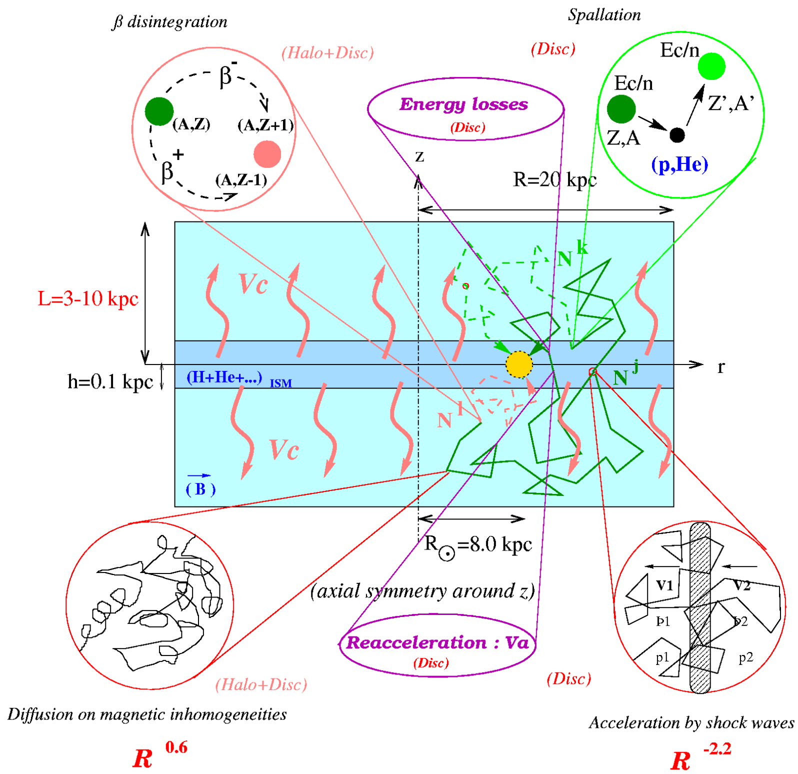

Figure 1.7: *Schematic view of our Galaxy and of cosmic-ray propagation according to a diffusion model* [49].

method to solve a set of transport equations for generations of nuclei linked by nuclear fragmentation of parent isotopes into lighter progenitors [20]. This method, the weighted slab technique, consists in splitting the problem into astrophysical and nuclear parts [21, 52]. The nuclear fragmentation problem is solved using the weighted slab [38, 39, 53] where the cosmic ray beam is allowed to traverse a thickness, $x\,\mathrm{g/cm^2}$, of the interstellar gas and these solutions are integrated over all the values of x weighted with a distribution function $G(x)$, the path length distribution (PLD), that is derived from an astrophysical propagation model.

The alternative way is the direct numerical solution of the diffusion transport equations for the entire Galaxy and for all successive generations of nuclei [54]. The numerical method is based on a Crank-Nicholson implicit second order scheme.

The analytical and numerical solutions for this model show that in the first approximation the cosmic ray propagation for not very heavy stable primary and secondary nuclei is characterized by only one main parameter, the escape length, X_e (g/cm^2) [21]. For an observer in the Galactic disk the relation between the parameters of diffusion model and the escape length is $X_e = \mu v H/(2D)$, where μ is the surface gas density of the Galactic disk ($\mu = 2.4$ mg/cm^2, at the Sun location in the Galaxy), v is the particle velocity, H is the scale height of the cosmic-ray halo, and D is the cosmic-ray diffusion coefficient [20]. The previous expression for the escape length is valid for nuclei with total *spallation* cross sections $\sigma \ll (mH)/(X_e h_g)$ where m is the average mass of an atom in the interstellar gas and h_g is the characteristic height of the gas distribution above the Galactic plane. The path length distribution in this case is approximated by the exponential form $G = \exp(-x/X_e)$ with the mean matter thickness, X_e.

The value of the escape length can be found from the data on abundance of secondary nuclei in cosmic rays like B/C and sub-Fe/Fe ((Sc+Ti+V)/Fe) so it allows to determine the ratio H/D. In order to disentangle this correlation it is necessary to look at measurements of radioactive secondaries, so a fit to ^{10}Be/^{9}Be leads to an independent evaluation of the diffusion coefficient D and the cosmic-ray effective halo size H. From Figure 1.6 a diffusion coefficient of $D = (2-5) \times 10^{28}$ cm^2/s is found. Combining this result on D with the H/D ratio as obtained by fitting the B/C ratio leads to an effective size of the cosmic halo of $H \sim 4\,$kpc which is in agreement with the radio-astronomical observations [55]. The characteristic time of cosmic-ray diffusion from the Galaxy calculated as the mean time which particles spend in the volume which is bounded by the full size of the halo is $H^2/2D \sim 7 \times 10^7\,$yr.

Thus this value is 10 times greater than the one deduced in the LBM. The explanation relies on the fact that on the basis of the physical picture of the DHM the ^{10}Be isotopes cannot probe the full halo volume which the stable particles pervade because they decay on their way out from the galactic disk where they are physically produced. Any attempt to deduce the mean gas density from the ^{10}Be isotopes, as one does in the LB approach, will overestimate this number. The true mean gas density which stable particles encounter is much smaller since they fill a larger volume. That is the reason of the underestimation of the escape time in the LBM.

Figure 1.6 illustrates that the LBM and the DHM provide different dependences on the ^{10}Be/^{9}Be ratio. These quantities are model-dependent and their measurement over a larger energy range can actually tell what model describes cosmic-ray propagation and better constrains the propagation parameters. Wider energetic measurements are needed as well as with higher statistics as will be discussed next.

1.3 AMS-02 expected performance on cosmic-ray fluxes measurements

The expected performances of AMS-02 concerning relevant measurements for constraining CR production, acceleration and propagation models can be separated in three main categories. First, precise measurements of the fluxes of H, He and CR species which are believed to have a primary origin (CNO) in a broad energy range are related to the injection spectra and can constrain the primary acceleration mechanisms of CR. The fluxes of secondary nuclei (absent near the sources) and the ratio of these secondary species to the primaries which produce them by *spallation* in the ISM define the amount of material traversed by CR since their acceleration. Finally, the ratio of radioactive to stable secondary nuclei can be used to determine the cosmic ray confinement time in the Galaxy and, in diffusion models, the effective thickness of the galactic halo as explained in section 1.2.2.

AMS-02 will accurately measure the fluxes of individual elements with electric charges $1 \leq Z \leq 26$ in the energy range $0.1\,\mathrm{GeV/nucleon} \lesssim E \lesssim 1\,\mathrm{TeV/nucleon}$. After 3 years of data taking AMS-02 will detect $\sim 10^8$ H, $\sim 10^7$ He and $\sim 10^5$ C with energies above 100 GeV/nucleon. In addition, AMS-02 will identify 10^4 B with energies above 100 GeV/nucleon and B/C measurements up to 1 TeV/nucleon [56]. Panel (a) of Figure 1.8 shows the expected B/C sensitivity after 6 months of data taking.

Regarding the stable light isotope measurements, AMS-02 with the RICH detector will be able to separate deuterons, D, from protons, p, from 0.9 GeV/nucleon in sodium fluoride radiator up to $\sim$6 GeV/nucleon in aerogel. The foreseen result, extracted using the simulation of D and p fluxes in the RICH detector, is shown in panel (b) of Figure 1.8, together with previous measurements from other experiments. The simulated statistics corresponds to one day of data taking for the aerogel

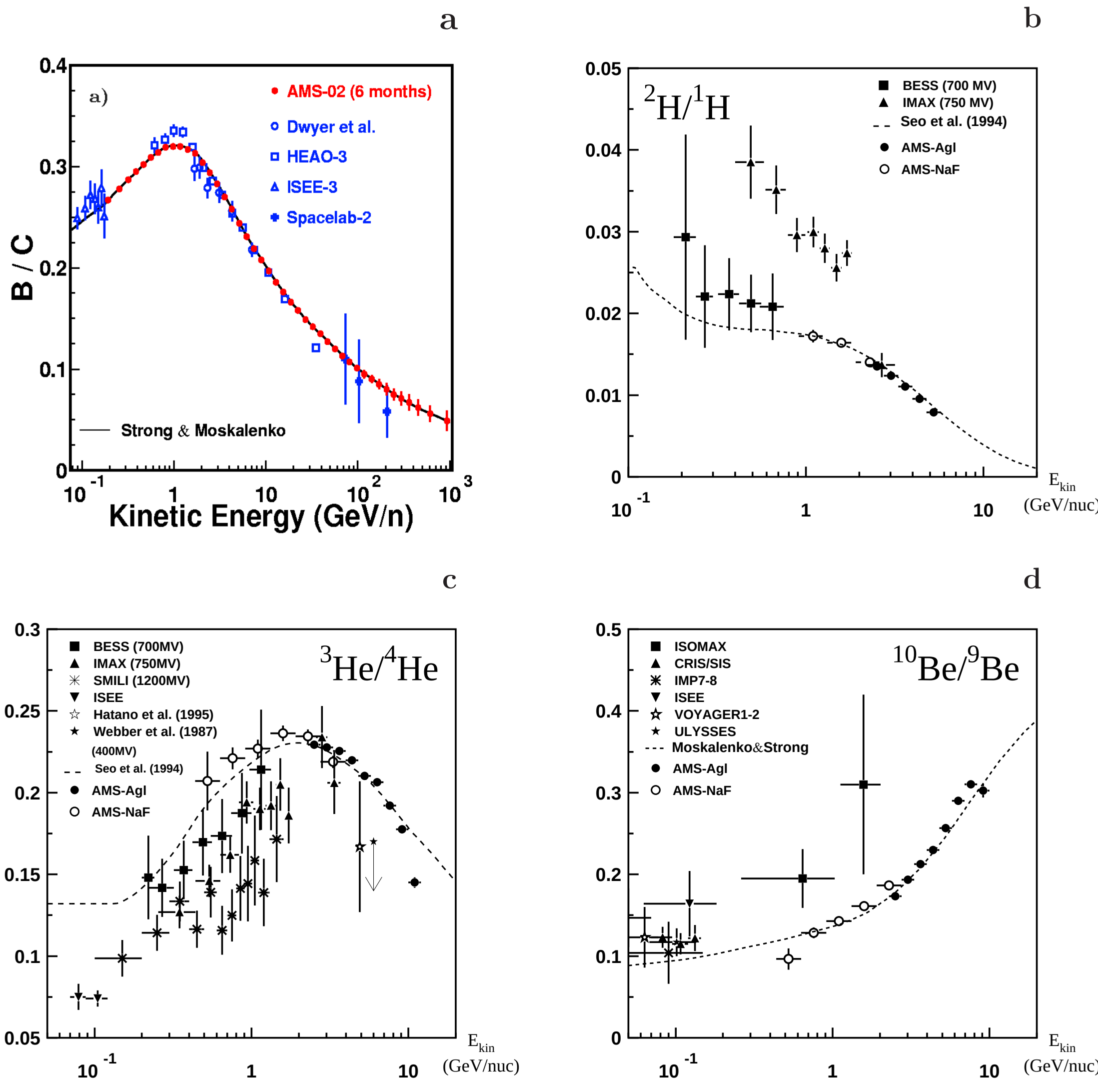

Figure 1.8: (a) *AMS-02 expected performance on B/C ratio after 6 months of data taking together with data from other experiments* [56]; (b) *AMS-02 RICH expected measurements for D/p ratio after 1 day of data taking for the aerogel radiator and one week of data taking for the sodium fluoride radiator compared with previous experiments;* (c) *AMS-02 RICH expected measurements for* $^{3}He/^{4}He$ *ratio after 1 day of data taking compared with previous experiments* and (d) *AMS-02 RICH expected measurements for* $^{10}Be/^{9}Be$ *ratio after one year of data taking compared with previous experiments* [57].

radiator and one week of data taking for the sodium fluoride radiator. For helium isotopes (^{3}He/^{4}He) the separation will start at ~0.5 GeV/nucleon with the sodium fluoride contribution and will be extended up to ~10 GeV/nucleon with aerogel data. This is visible in plot (c) of Figure 1.8, which shows the expected results for one day of data taking, together with measurements acquired by other experiments. AMS-02 time-of-flight measurements will extended down these measurements to energies ~0.1 GeV/nucleon.

Among the β-radioactive secondary nuclei in cosmic rays, ^{10}Be is the lightest isotope having a half-life comparable with the confinement time of cosmic rays in the Galaxy, as mentioned before. AMS-02, equipped with the RICH detector, will be able to separate ^{10}Be from the stable ^{9}Be in the range $0.5 \lesssim E \lesssim 8$ GeV/nucleon. This is depicted in panel (d) together with measurements from other experiments. The simulated statistics corresponds to one year of data taking. AMS-02 time-of-flight measurements will extended down these measurements to energies ~0.15 GeV/nucleon. After 3 years, AMS-02 will have collected around 10^5 ^{10}Be in this energy range.

Separation power, defined as $\Delta m/m$ where Δm is the separation between mass peaks, is higher for lighter elements, suggesting isotope separation should be possible up to higher energies in the case of D/p. However, the huge difference between proton and deutoron statistics (D/p $\sim 10^{-2}$) compared to the He and Be isotopes case eventually leads to the separation being only feasible up to ~6 GeV/nucleon compared to $\sim 8-10$ GeV/nucleon [57]. For more details on isotopic separation see reference [58].

These figures clearly show that even a small fraction of the expected AMS statistics will represent a major improvement on existing results for any of the nuclei. Present measurements suffer from lack of statistics which is notorious in the large error bars and they are also limited in the energy range. AMS will cover a wider energy range with unprecedented accuracy.

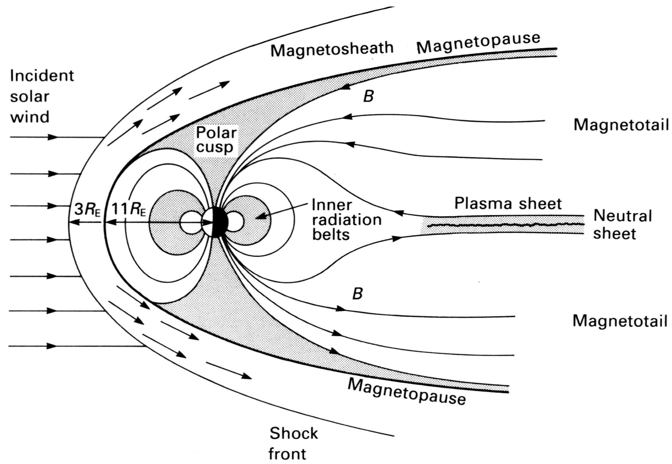

Figure 1.9: *The interaction of the solar wind with the Earth's magnetosphere* [59].

1.4 Solar Modulation

The continuous expansion of the solar corona produces drift of the interstellar plasma with a velocity around 300 Km/s which conducts 10 protons per cm^3 to the terrestrial orbit. This is the solar wind which transports the lines of the solar magnetic field producing the interplanetary magnetic field. Due to the solar rotation, with a period of 27 days, the strength lines get a spiral form with the radial direction and making 45^o with the terrestrial orbit. At distances from the sun greater than the astronomical unit, the field becomes more disordered due to the thermal anisotropy of the medium and due to irregular expansions of the solar corona.

The terrestrial magnetic field offers a barrier to the solar wind, see Figure 1.9.

In 1967 Gleeson and Axford [60] proved that the influence of the solar flux in cosmic rays could be parametrized by the so-called Force Field model which has only one parameter: the modulated flux of a particle with energy E_k is obtained considering the interstellar flux of cosmic rays with energy E_k, plus the energy lost when they reach the Earth ($Ze\Phi$), multiplied by a factor less than 1, which only depends on the initial energy $E_k + Ze\Phi$ and the final E_k. The parameter Φ only depends on the solar activity and has the dimension of a potential (usually measured in MV):

$$\phi(E_k) = \frac{E_k^2 + 2mE_k}{(E_k + Ze\Phi)^2 + 2m(E_k + Ze\Phi)}\phi(E_k + Ze\Phi) \tag{1.18}$$

where Φ ranges from 350 MV up to 1500 MV in the maximum of solar activity. So the flux is maximal when the solar activity is minimal and follows the solar activity cycles of around 11 years.

Drift models predict a clear charge-sign dependence for the heliospheric modulation of charged particle however the simple Force Field model will not be good enough to take full advantage of low energy measurements. Drift models predict a clear charge-sign dependence for the heliospheric modulation of charged particle. Cosmic rays of opposite charge drift in opposite directions, taking different routes to arrive at Earth, depending on the solar activity level. A drift has to be included, as shown in p, $\bar{p}$ measurements performed by the BESS flights [61].

1.5 The Geomagnetic Field and Geomagnetic Cut-off

The magnetic field of Earth can be approximated by a dipole, whose orientation and strength are chosen in agreement with experimental data. A more detailed model is given by the International Geomagnetic Reference Field (IGRF) [62].

The geomagnetic latitude (λ) is the angle measured from the geomagnetic equator, defined as the plane normal to the dipole axis, to the point considered and containing the Earth's center. Figure 1.10 shows the geomagnetic field at an Earth altitude of 370 Km, the altitude of the first AMS flight (AMS-01) and the mean altitude of the ISS. The region close to the South America where the magnetic field sinks is known as the South Atlantic anomaly. Here, high fluxes of low energy particles are observed.

The geomagnetic cut-off is the minimal rigidity a charged cosmic ray should have to reach a point located at an altitude h above the surface and at the geomagnetic latitude λ. This cut-off will also depend on the polar angle θ between the direction of arrival of the particle and the tangent to circle of latitude. It is given by the

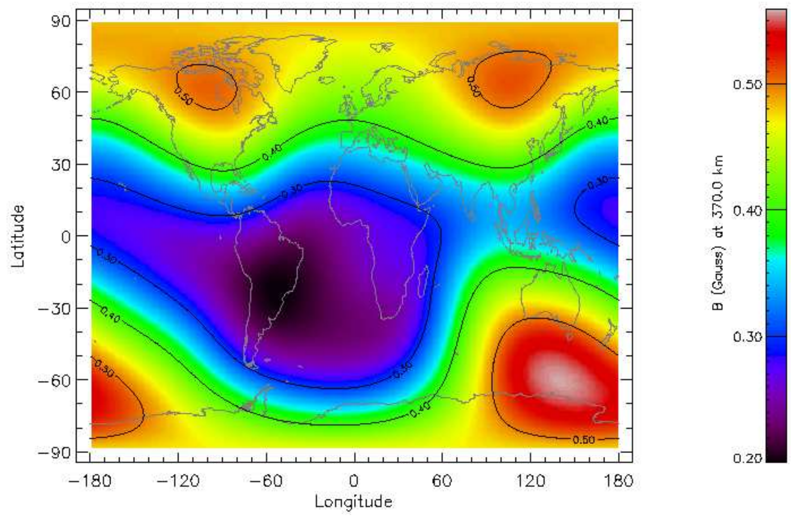

Figure 1.10: *Isointensity of geomagnetic field lines (in Gauss units) at an altitude of 370 Km* [62].

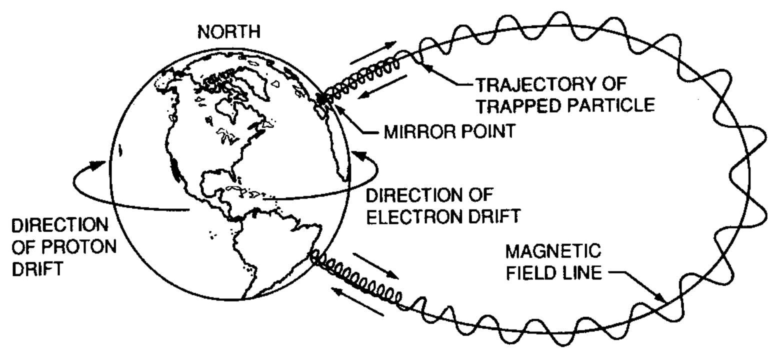

Figure 1.11: *Particle motion in geomagnetic field* [63].

following expression:

$$R_{cut} = \frac{60}{\left(1 + \frac{h}{R_E}\right)^2} \frac{\cos^4 \lambda}{\left[(1 + \cos\theta \cos^3 \lambda)^{1/2} + 1\right]^2} \; [GV] \tag{1.19}$$

where R_E is the Earth radius.

Another side effect of the geomagnetic field is the existence of charged particles trapped in the field. These particles follow a spiral motion along the field lines, bouncing between two mirror points and drifting east-west (see Figure 1.11). Positive particles will drift to West and negative to East.

1.6 Antimatter

1.6.1 Antimatter in astroparticle physics

Proving that antimatter exists in cosmic rays is part of a wider problem of matter-antimatter symmetry of the Universe. This issue and more generally the antimatter problem in space has become apparent after Dirac (1928) had predicted the existence of the positron, and Anderson had experimentally confirmed it in 1932. In fact, Dirac put forward the idea of the matter-antimatter symmetric universe, with the existence of anti-stars made of antiprotons and positrons.

The Big-Bang model assumes that at the first instants of creation, half of the Universe was made out of antimatter. The validity of this model is based on three main experimental observations: the recession of galaxies with a velocity proportional to their relative distance (Hubble expansion) [64]; the highly isotropic **C**osmic **M**icrowave **B**ackground (CMB) [65] which is a diffusive radiation described by a blackbody spectrum corresponding to a temperature of $(2.725 \pm 0.002)\,\mathrm{K}$ [66] and the relative abundance of light isotopes (He, Li and B) formed in the first stages of the Universe [67]. However, the presence of cosmological antimatter somewhere is missing.

Particle-antiparticle symmetry means that not only parity (P) and electric charge (C) are conserved but also the baryon number, B, which distinguishes baryons (e.g. protons and neutrons) from leptons (e.g. electrons, μ -mesons and neutrinos), and the lepton number, L, which is a principal lepton characteristic. This means that particles are always produced in pairs of particle and antiparticle, being produced from neutral states (B=0, C=0, L=0). According to the Big-Bang theory an equal number of particles and antiparticles should be produced in the Universe. However, no trace of antimatter has been observed so far. How did particle-antiparticle symmetric interactions end up in the strongly asymmetric Universe known today? There are three main directions which intend to provide an answer:

(a) *Observations:* Cosmic rays are the most promising objects for the antimatter search: antimatter may manifest through annihilation products which would contribute to the diffused γ-ray spectrum.

(b)*A Symmetric Universe*: Theorists have come up with the idea that matter and antimatter have been separated at an early stage of the universe and formed domains out of either one of them [68]. The existence of macroscopic regions of antistars in a globally asymmetric Universe has been also studied [69, 70]. However, observations do not support this and more complicated and consequently less elegant, symmetric Universe models are introduced. In fact, if the current theoretical estimates of the expected Cosmic Diffuse Gamma ray (CDG) spectrum are not incorrect by an order of magnitude, the model of a baryon symmetric Universe is neither in agreement with the observed uniformity of the CMB nor with the measured diffuse γ-ray spectrum [71].

(c) *Theory-antimatter-free Universe:* An initially symmetric Universe evolved dynamically to a completely asymmetric one where all the antimatter disappeared by some 'annihilation catastrophe', which was inevitable when the Universe cooled down. The baryons that had survived formed the Universe as it is known. This is called baryogenesis. This is the most reliable theory until now, despite the absence of an explanation for the way the baryon asymmetry had survived within the inflation scenario, and for complications like *preheating* and *reheating* after the inflation. This implies a violation in baryon number and a CP violation. The baryon number violation has not been experimentally verified until now, the present lower limit on the proton lifetime determined by the partial width of the decay $p \to e^+\pi$ is set at $\tau_p > 1.6 \times 10^{33}$ years [72]. CP violation was first measured in the kaon system and experiments like Belle, BaBar, experiments at LHC and Tevatron to observe $B^0 - \bar{B}^0$ oscillations are in progress. It should be noted, however, that the strength of the observed CP violation is far too small to account for the baryon asymmetry of the Universe.

1.6.2 Experimental search for antimatter

<u>Direct Antimatter Search</u>: observation of antinuclei in cosmic rays.

Antimatter does not exist on Earth in macroscopic amounts, otherwise it would have been annihilated releasing tremendous amounts of energy. The constant flux of charged particles emitted by the Sun and propagated throughout the Solar System (Solar wind) allows to exclude antimatter planets since they would constantly emit very bright γ-rays. Photons emitted by other stars do not probe directly the sign of the baryon number of the object from where they are emitted. Fortunately cosmic rays do!

Some distant antimatter objects (anti-stars, anti-galaxies) would provide space with cosmic antimatter particles, primarily antiprotons and positrons but also antinuclei. Antimatter particles would diffuse through space and eventually reach the vicinity of the Earth.

Positrons and antiprotons are measured in cosmic rays, but they do not provide a clear evidence for such existence of antimatter in the Universe since the measured flux is compatible with secondary production. Antiprotons can be produced in interactions of primary cosmic ray protons with the interstellar medium by the reaction:

$$p + p \rightarrow p + p + p + \bar{p}. \tag{1.20}$$

Different propagation models are used to evaluate the secondary antiprotons production [73, 74]. The energy spectrum of these secondary antiprotons should have a peak around 2 GeV, with a sharp decrease of the flux below and above the peak, as consequence of the reaction kinematics. This is visible in Figure 1.12. Further measurements reported a $\bar{p}/p$ flux above the expected for a purely secondary process (see [75, 76]). Different explanations are considered:

- antimatter reaching the Galaxy from antimatter galaxies in a baryon-antibaryon symmetric Universe [77], [78];
- production by dark matter particle annihilation (see eq. 1.21);
- production by primordial black hole evaporation [79].

Several experiments were done in the energy range 100 MeV to 10 GeV which show a good agreement in the peak. The discrepancy observed at low energy can not be related with primordial antimatter because of the solar modulation effect which shifts the energy spectrum towards lower energy values. So the present data

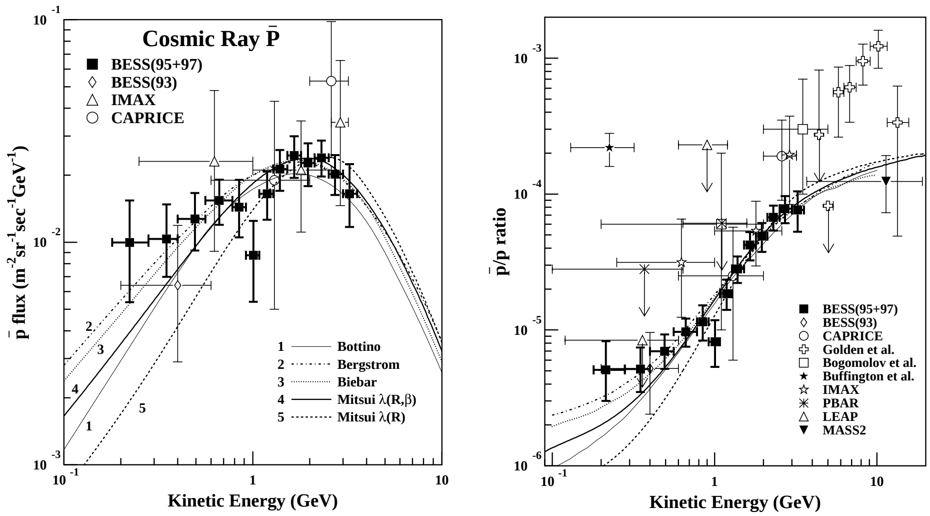

Figure 1.12: *Cosmic-ray $\bar{p}$ flux in the energy spectrum from 0.1 GeV to 10 GeV, different models and flux measurements by different balloon experiments* (left). *$\bar{p}/p$ ratio for the same energies as expected by different models and with the corresponding measurements by different experiments* (right) [80].

are not sufficient to provide a clear answer on the search for primordial antimatter in the Universe.

A few years ago, the BESS balloon experiment detected antiprotons at low energies below 1 GeV [81]. The size of the signal was slightly above estimations available at the time, from the interaction of cosmic rays with interstellar gas. Bergström, Edsjö and Ullio [82, 83], and Bieber et al [84] in 1999 have evaluated the effect of helium interactions, as well as collective nuclear effects and proton and antiproton secondary interactions. The consequences were an increase of the expectations of antiprotons in the energy range below 1 GeV, with the main uncertainty coming from the parametrization of the primary proton spectrum. In parallel, the BESS experiment also improved its measurements, and the measured antiproton yields are now smaller. With those developments, there is today no indication for new physics in the antiproton signal.

Other experiments have been carried out on balloons or satellites for direct search of antinuclei in cosmic rays. The most promising is antihelium, once it is expected to be the most abundant antinucleus. It would constitute an evidence for cosmologically significant amounts of antimatter. Heavier antinuclei, like $\bar{\mathrm{C}}$, would have even more profound consequences because they would point to an antinucleosynthesis and consequently to the existence of antistars which burnt antihelium.

In addition, the detection of an antinucleus would be a clear signal of the existence of antimatter since antinuclei production from matter collisions is strongly suppressed $\left(p + ISM \rightarrow \bar{N} + \ldots\right)$ $\bar{N}/p \propto \exp\left(\frac{M_N - m_p}{80}\right)$.

Indirect Antimatter Search:

This can be performed by observation of the γ-ray spectrum. When hadronic matter and antimatter interact, they annihilate mainly by the processes:

$$N + \bar{N} \rightarrow \begin{cases} \pi^0 \rightarrow \gamma + \gamma \\ \pi^{\pm} \rightarrow \mu^{\pm} + \upsilon_\mu(\bar{\upsilon_\mu}) \quad\quad \mu^{\pm} \rightarrow e^{\pm} + \bar{\upsilon_\mu}(\upsilon_\mu). \end{cases}$$

In such processes both neutral and charged pions would be produced with similar multiplicities and energy distributions. Half of the total energy would be carried away by the neutrinos and consequently not measured due to the difficulty in detecting neutrinos.

Annihilation photons, whose spectrum is peaked around E $\sim$ 70 MeV, have an average energy of 180 MeV and could be detected at a somewhat redshifted value in the cosmic diffuse gamma spectrum. In 1971, Stecker *et al.* came up with the idea of using distant redshift annihilations, $z \sim 100$, to explain the γ spectra at $\sim$1 MeV as originated from the decay of pions produced in baryon-antibaryon annihilations. The diffuse γ-ray spectra was recently measured on-board the satellite-borne Compton Gamma Ray Observatory (CGRO) by two groups: the Compton telescope (COMPTEL) [85] and the Energetic Gamma Ray-Experiment Telescope (EGRET) [86]. The COMPTEL measurements covered the energy range from 0.8 to 30 MeV and EGRET the energy range from 30 MeV to 100 GeV. Taking into account the contributions to this spectrum from different astrophysical objects (quasars, supernovae, blazars, etc.), the spectrum can be consistently reproduced and no sign of annihilation was found.

A sharp spectral line in X-rays at 0.36 keV observed by the ROSAT satellite was recently ascribed to the highly redshifted products of direct leptonic annihilations

[87]. More powerful detectors are needed to explore this region.

Studying the possibility of a universal matter-antimatter symmetry, it was concluded that the electrons produced in the annihilation of different baryonic signed particles should induce a distortion of the Cosmic Microwave Background (CMB) spectrum: photons would suffer scattering to higher energies due to the Compton effect, and electrons could heat the ambient plasma [71]. The predicted signal is yet lower than the limit established by COBE on departures from a thermal spectrum.

Difficulties in the observation of antimatter

Antinuclei from distant sources necessarily pass through extragalactic magnetic fields. If the fields are too high they limit the distance from which antinuclei could approach the Earth. However, with a poor knowledge of the magnetic fields of the Universe [88], the estimation of the distance the antinuclei are from Earth is not very accurate: the range would vary from a fraction of Mpc to the distance of the horizon of the Universe.

After an antinucleus reached our planet the problem would be to detect it. Ground-based detection techniques are not very efficient:

- There is the atmosphere shielding and the consequent several interactions;
- At the time the shower produced by the antinucleus is detected the information about the nature of the primary particle is practically lost.

Balloon detectors are still affected by the residual atmosphere, and they have low statistics once they normally collect data for a period ranging from a few days to a few weeks. A more efficient measure would be to install detectors on space for some years. The detector should be equipped with a system to clearly identify the negative charge of the detected particle. This implies a magnetic spectrometer with the capacity to minimize any background imitating the antinuclei.

Until now, the conclusions are that at least within our local supercluster of galaxies (tens of Mpc) there is no antimatter. There were several balloon flights of an instrument called BESS [9] as well as the AMS-01 flight Figure 1.13 [14]. Both were magnetic spectrometers and used technologies developed for particle physics accelerator experiments. The upper limit for antihelium search with AMS-01 was obtained

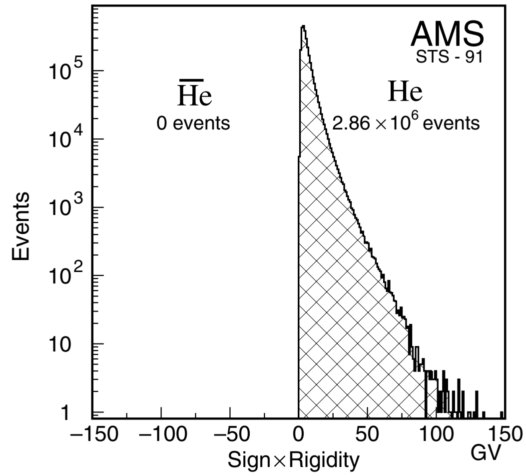

Figure 1.13: *Distribution of rigidity times sign of charge for* $|Z| = 2$ *particles in AMS-01. No antihelium candidates were found in the range* $1 - 140\,GV$ [89].

assuming that the He and $\overline{\mathrm{He}}$ energy spectrum were identical: $\overline{\mathrm{He}}/\mathrm{He} < 1.1 \times 10^{-6}$. The antihelium search result is illustrated in Figure 1.13. The AMS-02 results for the search of $\overline{\mathrm{He}}$ on the ISS is illustrated in Figure 1.14 (left). The expected upper limit after 3 years of exposure is $\overline{\mathrm{He}}/\mathrm{He} < 10^{-9}$. If no antimatter is found with AMS-02 it can be concluded that there is no antimatter to the edge of 1000 Mpc in the Universe. A comparison between experiments on the limits of antimatter detection are presented in Figure 1.14.

1.7 Dark Matter

Rotational velocities in spiral galaxies (see Figure 1.15) and dynamical effects in galactic clusters provide convincing evidence that either Newton laws completely fail at scales of galaxies or, more likely, most of our Universe is made of non-luminous (dark) matter.

From the Newton theory of gravitation the orbital velocity of star in the edges of a group of galaxies, at a distance R would be $v = \sqrt{G\frac{M}{R}}$, where M is the mass within the orbit of radius R, and G is the gravitational constant. The velocity does not depend on the mass of the star, but only on the mass of the galaxies in the

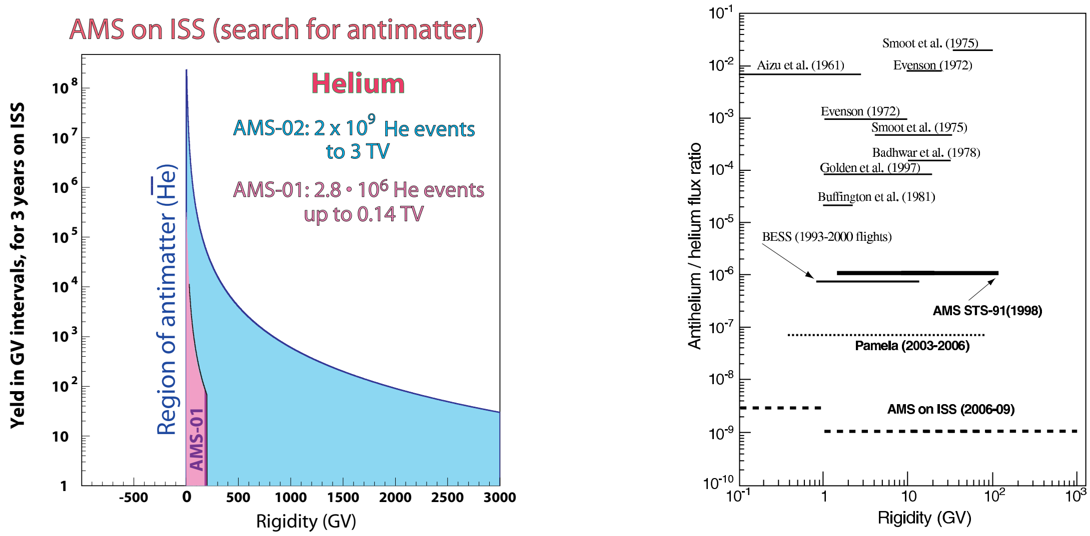

Figure 1.14: *Monte Carlo simulation of the three-year exposure of the AMS detector on the ISS to search for antihelium. The region studied by AMS-01 is also illustrated* [88] (left)*. Antimatter limits for different experiments before AMS-02 including AMS-02* [90] *and Pamela* (right).

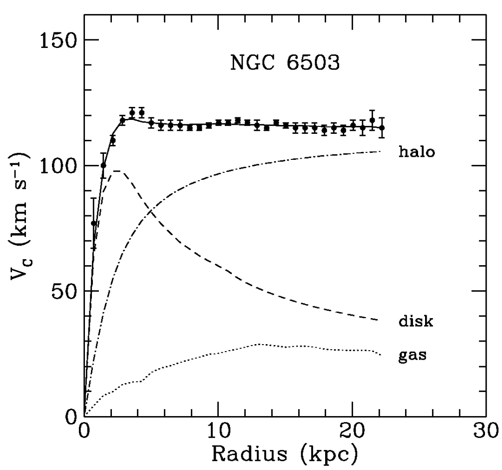

Figure 1.15: *Rotational curve of the spiral galaxy NGC 6503, determined by radio measurements of the 21 cm line emission of neutral hydrogen in the disk. The dashed line shows the rotation curve expected from the disk material alone, the dot-shaded line is from the dark matter halo alone* [91].

interior of the orbit and on its radius. To have a velocity independent of R, as the astronomical measures point to, it is necessary that the mass M grows linearly with R. The luminosity of galaxies does not behave like this with R. If only the mass corresponding to the luminosity was considered, the stars in the edge would have an orbital velocity much lower than the observed one. To explain these observations, it is necessary to evoke the existence of a quantity of dark matter more abundant than visible matter.

A similar value is supported by the measurement of the abundance of deuterium in the Universe. Deuterium, ^{2}H (or D), as well as ^{4}He, was produced during the primordial nucleosynthesis, although in small quantities. Being a relatively unstable nucleus, the amount produced is highly dependent of the photon/nucleon ratio. From the fraction of deuterium such estimation is obtained and, knowing the density of photons in the CMB, the density of nucleons is deduced. This value is lower than the expected one.

There are several dark matter candidates [92], [93]:

Baryonic matter

- Neutrons and protons;
- Among the proposed candidates are MACHOs (Massive Astrophysical Compact Halo Objects), i.e. astronomical objects which do not emit electromagnetic waves and can be observed by means of *gravitational lensing*:
  - Primordial black holes;
  - White dwarfs, which represent the final stage of a star in the main sequence, with a mass between 0.1 and $3M_{\odot}$[2];
  - Brown dwarfs, that are compact objects with a mass below the ignition threshold (mass $\approx 0.08\ M_{\odot}$), that is the minimum mass needed to start the full thermonuclear fusion cycle in the core of the object;
  - Jupiters, which are hypothetical big planets with a mass of the order of Jupiter's mass.

[2] $M_{\odot}$ is the Solar mass.

  - Neutron stars, that are the final states of core collapse of supernovae.

- Cold H_2 gas, a halo surrounding the spiral galaxies, is another candidate.

The recent results from the WMAP[3] collaboration [94] confirm that baryon matter density ($\Omega_b h^2 = 0.0223^{+0.0007}_{-0.0009}$) is largely insufficient to saturate the total matter density ($\Omega_m h^2 = 0.127^{+0.007}_{-0.013}$) ($h = H_0/100 = 0.73^{+0.03}_{-0.03}$, where H_0 is the Hubble constant). In addition, baryonic dark matter itself is only responsible for 1/10 of all the dark matter.

Non-baryonic matter:

- Thermal Relics: 'hot' and 'cold' dark matter, depending on their relativistic properties at the time of decoupling from ordinary matter in the early Universe, which means particles that in a first stage were in thermal equilibrium with radiation and then decoupled and were relativistic particles (Hot Dark Matter), from particles which have never been in the same equilibrium, and were not relativistic (Cold Dark Matter).

  - 'Hot' Dark Matter (HDM) is required to explain the formation of big structures (clusters of galaxies and so on). Light neutrinos whose mass upper limit is $m_\nu < 2.2\,\mathrm{eV}$ are obvious candidates but this mass value implies a limit of 0.1% for their contribution to dark matter.
  - 'Cold' Dark Matter (CDM) is required to explain the formation of small structures (galaxies). Candidates are Weakly Interacting Massive Particles (WIMP's): these can be massive neutrinos of either Dirac or Majorana type ($m \geq 20$ GeV); supersymmetric (SUSY) particles: s-neutrino, neutralino (χ) which is the lightest supersymmetric particle (LSP) [95]; and the lightest Kaluza-Klein particle (LKP) [96] of certain extra-dimensions models.

- Non-Thermal relics: axions, that are bosons coupled to photons with mass $\approx 10^{-5}$ eV; monopoles, that are topological defects of very large mass $\approx 10^{16}$ GeV predicted by Grand Unified Theories (GUTs).

[3] Wilkinson Microwave Anisotropy Probe

<table>
<tr><td rowspan="5">$\Omega_{\text{TOT}} = 1$</td><td rowspan="4">$\Omega_{\text{Matter}} \approx 0.24$</td><td rowspan="2">$\Omega_{\text{Baryonic}} \approx 0.04$</td><td>$\Omega_{\text{Luminous}} \approx 0.006$</td></tr>
<tr><td>$\Omega_{\text{Baryonic DM}} \approx 0.04$</td></tr>
<tr><td rowspan="2">$\Omega_{\text{Non-Baryon}} \approx 0.2$</td><td>$\Omega_{\text{Hot DM}} \lessapprox 0.04 \rightarrow$
light ν's</td></tr>
<tr><td>$\Omega_{\text{Cold DM}} \approx 0.2 \rightarrow$
WIMP's
(SUSY LSP=neutralino)</td></tr>
<tr><td colspan="3">$\Omega_{\text{Vacuum energy}}(\Omega_\Lambda) \approx 0.76$</td></tr>
</table>

Table 1.1: *Universe composition taking into account both experimental observations and theoretical predictions and assuming that cold dark matter component is justified in a SUSY scenario.*

Taking into account both experimental observations and theoretical predictions, the presently mostly supported scenario is roughly described by the one shown in Table 1.1.

The formation of structures in the Universe tells us that early after the Big Bang dark matter particles must have been cold rather than hot. In fact, if the dark matter had been hot, then these fast-moving particles would have smoothed out the smaller density irregularities (the seeds for the formation of galaxies and clusters) by streaming from high-density regions to low-density regions. The first objects to form would have been the largest structures (the super-clusters) and small objects (galaxies) would only have formed later by fragmentation. However, this is inconsistent with observations. The deep image of the sky obtained by the Hubble Deep Field in 1995, together with other observations by ground-based telescopes, identified the epoch when most galaxies formed as a few billion years after the Big Bang. The Sloan Digital Sky Survey (SDSS), as well as X-ray observations, have shown that clusters form later. Finally super-clusters are forming just today. This sequence is inconsistent with hot dark matter.

The present knowledge gives the following picture for the evolution of the Universe: immediately after the Big Bang all the matter is hot, the cooling down happens during the expansion until it reaches the temperature at which SUSY symmetry is broken ($\sim$1 TeV): particles decouple from s-particles and, the latter being heavy, become quickly non-relativistic and begin to arrange themselves in structures due to gravity. Interacting as a self-gravitating isothermic gas, the s-particles form relatively small structures: the future galactic halos. During the expansion of the Universe, at a given temperature, baryons decouple from radiation and are attracted inside the cold dark matter objects to form galaxies.

Neutralinos can be detected directly through its elastic scattering on nuclei [97] or indirectly looking for anomalies in the expected spectra of primary cosmic rays due to $\chi - \chi$ annihilation in the galactic halo. The second option implies searching for greater abundance of rare components in cosmic rays like γ-rays, e^+ and $\bar{p}$.

1.7.1 AMS detection of dark matter

AMS intends to indirectly search for dark matter performing high statistics precision measurements of $\bar{p}$, e^+, γ and $\bar{\mathrm{D}}$ spectra and looking for anomalies on those spectra. Neutralinos can annihilate in the galactic halo in different channels:

$$\chi + \chi \rightarrow \bar{p} + X, e^+ + X, 2\gamma \tag{1.21}$$

$$\chi, \chi \rightarrow \gamma \upsilon \tag{1.22}$$

There are also predictions that antideuterons, which AMS will detect, can be produced from the collision of SUSY particles.

e^+ spectrum

AMS-01 measured the positron fraction $e^+/(e^+ + e^-)$ from 1-50 GeV [98]. Positrons were identified by conversion of *bremsstrahlung* photons, an approach that yields an overall background proton rejection of more than 10^5, and allows to extend the energy range accessible to the experiment far beyond its design goals constrained by the performance of the aerogel threshold counter which allowed e^+/p discrimination only up to 3 GeV. The left-hand plot of Figure 1.16 illustrates these measurements and shows that the positron fraction measured by AMS-01 is consistent with previous measurements. However AMS-01 can not identify the possible positron signal from neutralino annihilation at higher energies. AMS-02 with the Transition Radiation Detector (TRD), the RICH detector and the electromagnetic calorimeter will improve the capabilities of detecting such dark matter signal extending the

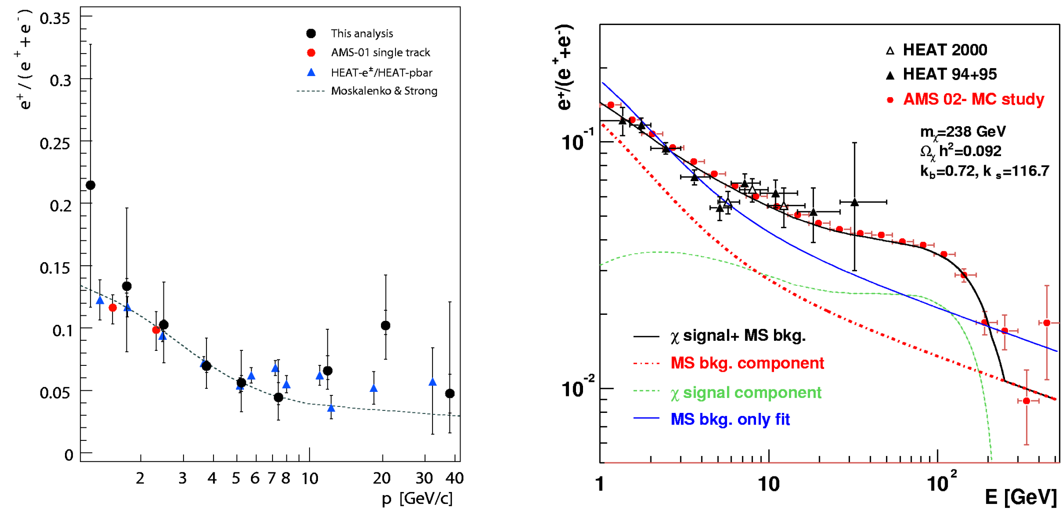

Figure 1.16: *The positron fraction $e^+/(e^+ + e^-)$ of primary cosmic rays measured by AMS-01* [98] *compared with HEAT-$e^{\pm}$* [100], *HEAT-pbar* [101] *and AMS-01 earlier results* [102] *together with a model calculation for purely secondary production (dashed line). The total error is given by the outer error bars, while the inner bars represent the systematic contribution to the total error* (left). *Statistical accuracy on AMS-02 positron fraction measurement in 3 years in case of neutralino annihilation (m_χ=238 GeV, boost factor=166)* (right).

detection range up to ∼300 GeV and collecting around 50 e^+/year/GeV with an energy of ∼50 GeV. The background, essentially composed of misidentified protons ($\Phi_p/\Phi_{e^+} \sim 10^3$) and electrons ($\Phi_{e^-}/\Phi_{e^+} \sim 10$), is rejected by factors of respectively 10^6 and 10^4. The mean acceptance for positrons in the energy range from 3 to 300 GeV is 0.045 m^{2}sr, with a proton contamination of ∼4% [99].

The positrons coming from neutralino annihilation will generate an increase in the flux. The signal is easier to identify if the neutralino is in a pure higgsino state [103].[4] In fact, the annihilation of this neutralino can increase the positron flux in two ways. The first mode is through direct decay of gauge bosons:

$$\chi, \chi \to W^+ \quad W^- \qquad \chi, \chi \to Z^0 Z^0 \tag{1.23}$$

$$W^+ \to e^+ \nu \qquad Z^0 \to e^+ e^- \tag{1.24}$$

(the branching ratio for the W^+ decay in e^+ is ∼11%, while for the Z^0 is ∼3%).

[4]Neutralinos are Majorana particles formed by a superposition of *photino*, *higgsino* and *zino*; the relative weights of these particles depend on three parameters of the SUSY model and as they are changed neutralinos can annihilate in different channels.

Since neutralinos in the galactic halo have a velocity $\sim 10^{-3} \cdot c$, annihilations can be considered at rest. In this case, positrons coming from direct decays of gauge bosons will have an energy equal to half the neutralino mass ($m_\chi/2$). Their spectrum will show a steep drop when the energy increases and reaches zero at an energy value equal to the neutralino mass. The steep descent should provide a strong signature for this signal providing an easy identification. The signal should appear as a peak in the positron fraction. The second production channel via annihilations of Higgsino-kind neutralinos is given by secondary decays of gauge bosons:

$$W^+ \rightarrow \mu^+ \rightarrow e^+ \qquad W^+ \rightarrow (\text{b and c quarks}) \rightarrow e^+$$

or, the final products of a cascade of charged pions resulting from the hadronization of quarks coming from decays of gauge bosons ($\pi^+ \rightarrow \mu^+ \rightarrow e^+$). Positrons produced from pions are ten times more abundant than those from decays of gauge bosons; this fact however would not hide the possible signal discussed above because the energies of secondary positrons are lower. In fact, this second channel contributes with a wider spectrum peaked at an energy corresponding to $m_\chi/20$.

The right-hand plot of Figure 1.16 shows an example of the foreseen results for the positron fraction measurement made by AMS-02 if the excess on the HEAT data in the energy region from 7 to 10 GeV were due to the annihilation of 238 GeV neutralinos: a signal boost factor of 166 has been used to fit the HEAT data [104]. Significantly lower boost factors are required if the anomaly is due to LKPs with masses of few hundred GeV [105]. Clumpiness of dark matter is taken into account by a general, energy-independent multiplicative number called *boost factor*, by which the signal computed from a smooth dark matter distribution should be multiplied. However, this is not correct and the clumpiness effects cannot be described by a unique number because it depends on energy. The exact distribution of the clumps in the Galactic halo is unknown and the expected signal from some types of WIMPs can be quite sensitive to it. Several statistical studies on the effect of halo clumpiness on the annnihalation signal were done [106]. According to these studies the boost factor was considered as a random variable and different assumptions on the clumps distribution were done. The boost factor was proved to strongly depend on the clumpy halo we are living in.

All the analysis of the HEAT data allowed to conclude that fits taking into account SUSY predictions together with the expected background lead to a better agreement with data than background-only fits, although not excellent.

As can be seen from the previous figures, data currently available do not allow to establish the presence, and possibly the type of signal with confidence. One of the main purposes of AMS-02 is to study the positron fraction with greater resolution and at higher energies, i.e. in the region where a potential signal should be stronger.

$\bar{p}$ spectrum

AMS-02 will detect antiproton fluxes up to $\sim$400 GeV and $\sim 10^6$ antiprotons will be detected with E $\leqslant$ 5 GeV. Antiprotons will be identified as negative single charged tracks reconstructed by TRD and tracker. The acceptance for this signal is $\sim$0.16 sr m^2 between 1 and 16 GeV and $\sim$0.033 sr m^2 between 16 and 300 GeV [107]. The main backgound sources are misreconstructed proton interactions and misidentified electrons. For proton rejection a good control of charge confusion, interaction with the detector and misreconstructed tracks is necessary. For electron rejection it is necessary to use Time-of-flight (TOF) and RICH velocity measurements at low energies and TRD and Electromagnetic calorimeter (ECAL) rejection capability at high energy. The rejection factors are better than 10^6 against protons and around $10^3 - 10^4$ against electrons.

Figure 1.17 shows the expected profile after 3 years together with the existing measurements of the antiproton flux.

However, as explained before for the antimatter case, extracting a signal from the spectrum of antiprotons is a very difficult task. It was realized that a few processes add up together to flatten out at low energy the spectrum of secondary antiprotons. The antiproton signal of supersymmetric dark matter is masked in this region. The most interesting region is the one between 10 and 400 GeV where, assuming that large boost factors ($\sim 10^3$) enhance the process, a dark matter annihilation could be revealed [109].

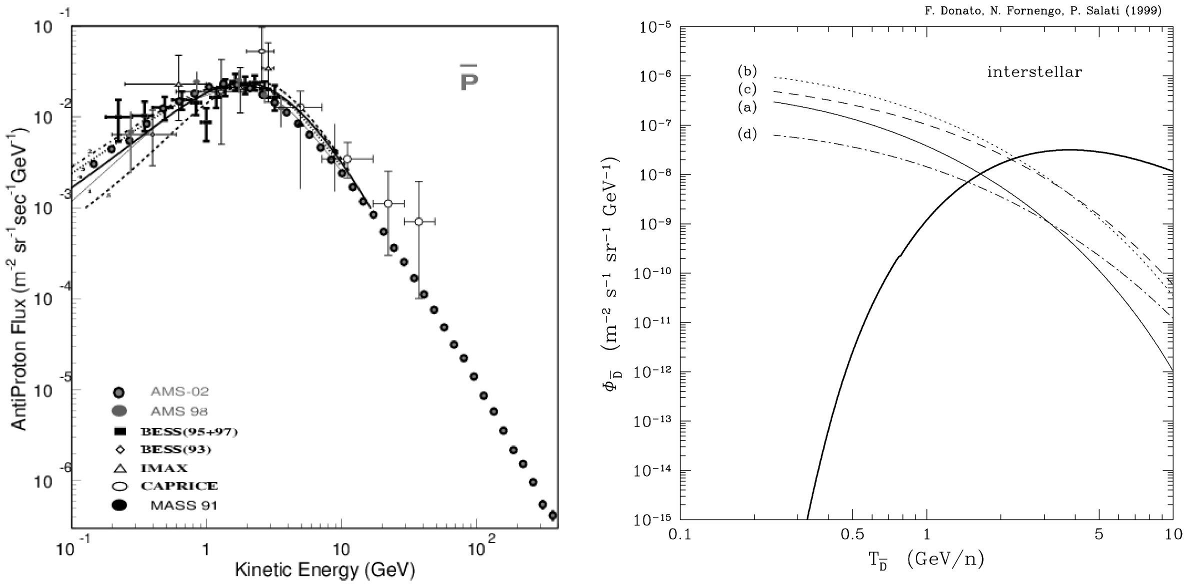

Figure 1.17: *Expected precision on the antiproton spectrum measurement by AMS-02 in 3 years* (left). *Antideuteron flux due to secondary production (heavier solid line) and fluxes due to antideuterons of supersymmetric origin* [108] (right).

$\bar{\mathrm{D}}$ spectrum

Searches for low-energy antideuterons appear in the meantime as a plausible alternative worth being explored [108]. They form when an antiproton and an antineutron merge together [110]. The two antinucleons must be almost at rest with respect to each other in order for fusion to happen. For kinematic reasons, a spallation reaction creates few low-energy particles. Low-energy secondary antideuterons are even further suppressed. Energy loss mechanisms are also less efficient in shifting the antideuteron energy spectrum towards low energies. A maximum of $2-5\times10^{-8}\bar{\mathrm{D}}\mathrm{m}^{-2}\mathrm{sr}^{-1}\mathrm{GeV}^{-1}$ appears for a kinetic energy of $\sim$4 GeV/nucleon. AMS-02 should collect a dozen of secondary antideuterons.

On the other hand, antinucleons are produced in neutralino annihilations with low energies. Subsequently the fusion into antideuterons happens, giving origin to a fairly flat spectrum for supersymmetric antideuterium nuclei. Below a few GeV/nucleon, secondary antideuterons are quite suppressed with respect to their supersymmetric partners. The right-hand plot of Figure 1.17 shows the flux of $\bar{\mathrm{D}}$

foreseen by some supersymmetric theories. This low-energy suppression is orders of magnitude more effective for antideuterons than for antiprotons which makes the former signal a much more promising probe of SUSY dark matter than the latter one. Unfortunately, antideuteron fluxes are quite small (four orders of magnitude smaller) with respect to the antiprotons considering both originated from $\chi - \chi$ annihilation. However, if a few low-energy antideutrons are discovered, this should be seriously taken as a clue for the existence of massive neutralinos in the Milky Way.

AMS should reach a sensitivity of 4.8×10^{-8} $\bar{\mathrm{D}}\mathrm{m}^{-2}\mathrm{sr}^{-1}\mathrm{GeV}^{-1}$ at solar minimum activity, pushing it down to 3.2×10^{-8} $\bar{\mathrm{D}}\mathrm{m}^{-2}\mathrm{sr}^{-1}\mathrm{GeV}^{-1}$ at solar maximum, for a modulated energy of 0.24 GeV/nucleon.

γ spectrum

Gamma rays might be a possible signature of dark matter through the golden process $\chi\chi \to \gamma\gamma$ and $\chi\chi \to Z^0\gamma$ or through the γ continuum coming from other decay channels during hadronisation.

The most distinctive feature of the γ-ray spectrum that can be observed as a consequence of neutralino annihilation is certainly the presence of sharp spectral lines. The annihilation processes $\chi\chi \to \gamma\gamma$ and $\chi\chi \to Z\gamma$ [111] should produce nearly monoenergetic photons, since WIMP's move in the galaxy with nonrelativistic velocities and almost at rest. The energy of the photons is then $E_\gamma \approx m_\chi$ and $E_\gamma \approx m_\chi \left(1 - m_Z^2/4m_\chi^2\right)$ respectively.

The rates of these processes are difficult to estimate because of uncertainties in the supersymmetric parameters, cross sections and halo density profile. However they give a direct measurement of the neutralino mass.

In practice the monochromatic spectral lines will suffer a smearing due to redshift that can turn them in features of the continuum annihilation spectrum. As redshift only streches the observed wavelength of the photons, the smear is assymetric and looks like a cutoff at about the value of the neutralino mass (for $\chi\chi \to \gamma\gamma$) [112].

A second signature may be found in the continuum γ-ray spectrum in the form of a smooth bump at about 1/10 m_χ. This signal is very low compared with the flux measured by EGRET [113] (about 5 orders of magnitude), though there is a possibility that the bulk of EGRET flux may be due to unresolved AGN. In this case AMS, which will explore a quite complementary energy range, would have good chances to pick this kind of signal. Moreover it is possible that clumpy distributions of dark matter enhance the signal itself.

The EGRET measurements of gamma-ray fluxes done in the 1990s are the most precise data available until now from the 20 MeV up to ∼20 GeV energy range. More accurate measurements are needed not only to perform dark matter searches but also to analyse emissions from gamma sources (pulsars, blazars, AGNs), diffusive gamma background emission and gamma ray bursts (GRB).

GLAST (Gamma-ray Large Area Space Telescope) [114],[115] is the next great step beyond EGRET, providing a huge leap in capabilities. It is equipped with two different instruments: a Gamma Ray Burst Monitor, working in the energy range from 20 keV to 20 MeV, mainly dedicated to the detection of GRBs, and the Large Area Telescope (LAT), able to reconstruct γ-ray directions and energies in the range 20 MeV up to at least 300 GeV, which includes the unexplored region $E > 10$ GeV. This detector is beased on silicon strip sensors with a total peak effective area larger than 8000 cm^2 (factor > 5 better than EGRET). GLAST will cover ∼20% of the sky (about 2.4 sr), a factor 4 greater than EGRET and it offers a sensitivity to the point like sources $< 6 \times 10^{-9}\,\mathrm{cm}^{-2} s^{-1}$ which is improved by a factor 30 with respect to EGRET. The GLAST satellite is planned to be launched in May 2008 in a circular orbit at 565 km of altitude and it will operate for $5 - 10$ years.

AMS-02 is also planned to do gamma-ray physics. Cosmic photons may be detected in AMS using two complementary techniques: photon conversions in e^+e^- pairs in the material upstream of the first layer of silicon sensors in the tracker[5] [116, 117, 118] and direct photon measurements in the ECAL [119]. For a *converted photon* the energy range of detection is limited by the upper energy value reachable for double track reconstruction ($E \sim 200$ GeV).

The *conversion mode* ensures an excellent photon angle resolution of 1^o at 100 GeV, an excellent energy resolution (3% up to 20 GeV, 6% at 100 GeV), a good acceptance (0.06 m^2 sr at 100 GeV) and a large field of view (∼43^o). The back-

[5]The material in front of the first silicon tracker plane consists of the TRD, the first two layers of TOF scintillators and mechanical supports. It represents $\simeq 0.23 X_0$.

ground is mainly due to p and e^- which interact in the AMS detector, producing secondaries, mainly δ-rays[6], which result in double-track events associated with a common origin at the interaction point. This background can be strongly reduced (rejection factor 5×10^4 [120]) by identifying events with interactions, vetoing with the TRD and cutting on the pair invariant mass.

The ECAL measures photons with a large energy range from 3 GeV up to 10^3 GeV. The measurement with this subdetector has an angular resolution of 1° at 100 GeV, an excellent energy resolution (3% at 100 GeV), a large acceptance at high energies ($\sim$0.1 m^2 sr above 100 GeV), but a reduced field of view of $\sim 23^{\circ}$. The main background is due to charged particles (mainly p, e^- and He) either passing undetected in the gaps of the AMS active tracking volume or entering the ECAL from the side. To reject background it is necessary to identify p, He by analysing the 3-dimensional shower development in the ECAL and to identify charged particles by requiring the trajectory direction of the reconstructed ECAL to pass inside the AMS fiducial region. A rejection factor better than 6×10^4 is obtained for $e^{\pm}$ and better than $1.7{\times}10^6$ for He nuclei. For protons a rejection factor of $(2.5 \pm 1) \times 10^6$ is expected [120].

The left-hand plots of Figure 1.18 show the acceptance and the effective area for the two detection modes. The corresponding energy and angular resolutions are shown in the right-hand plots of the same figure. It is interesting to observe that the silicon tracker of AMS-02 will perform measurements with a comparable or even better angular and energetic resolution than the GLAST telescope. For a deeper comparison see thesis [121].

In three years the exposure to the galactic center will amount to 40 days for the conversion mode and to 15 days for the direct photon mode; the integrated acceptance will be practically the same for the two methods: $\sim 1.5 \times 10^5\,\mathrm{m^2 s}$ [122].

The expected *gamma* spectrum in the direction of the Galactic Center measured by the ECAL-AMS-02 (*single photon*) after one year of data taken is shown in the left-hand plot of Figure 1.19. The supersymmetric signal is due to a 207 GeV neutralino annihilation. The superposition with the expected diffusive galactic gamma

[6] A δ-ray is characterized by very fast electrons produced by alpha particles or other fast energetic charged particles knocking orbiting electrons out of the medium atoms.

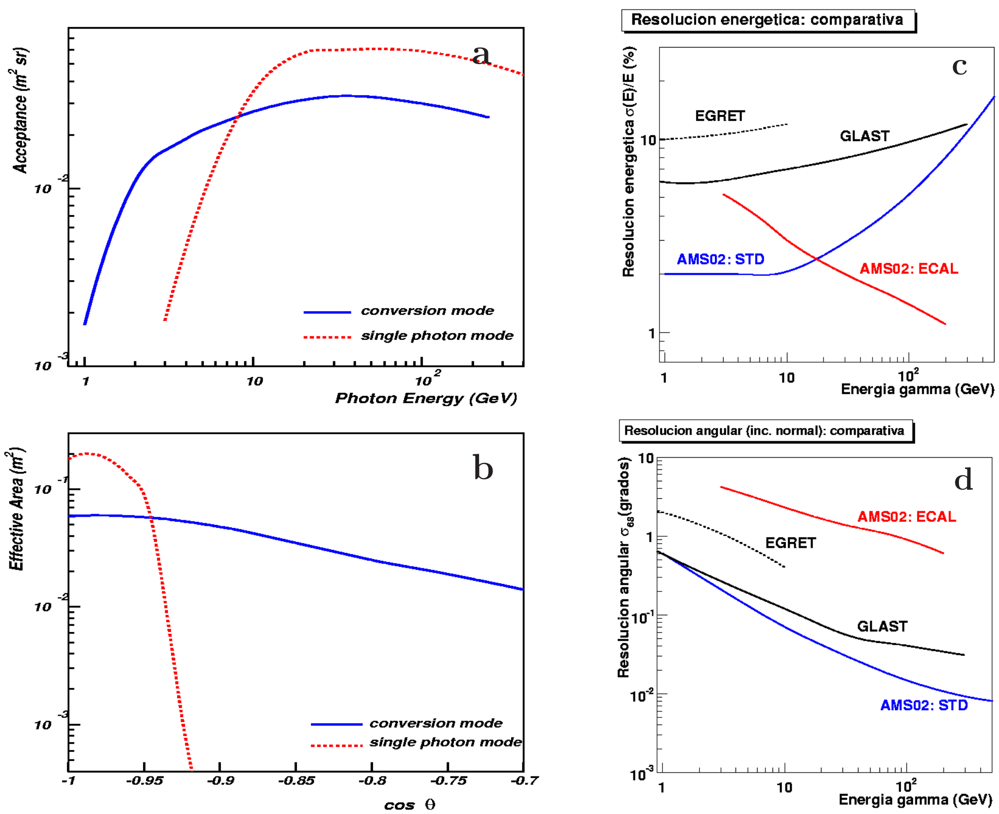

Figure 1.18: *AMS-02 γ detection capabilities.* (a) *The AMS-02 acceptance as function of γ-ray energy for the two detection modes* [120]. (b) *The effective areas versus zenith angle at 50 GeV γ-ray energy* [120]. (c) *Energy resoltion as a function of original γ-ray energy* [121]. (d) *The 68% containement angular resolution for both complementary detection modes as a function of energy* [121].

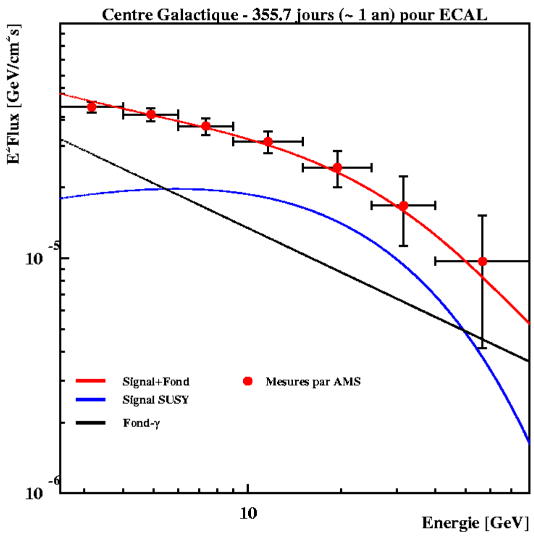

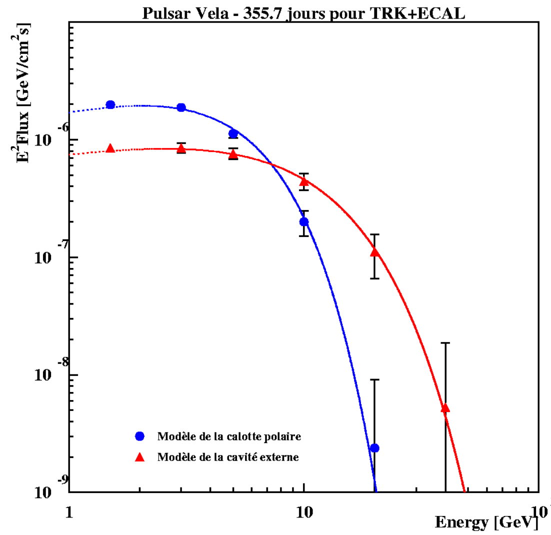

Figure 1.19: *Gamma ray flux expected from the Galactic Center for a chosen SUSY model after one year of data taking with AMS-02 and measured by the ECAL* (left). *Expectation from Outer Gap and Polar Cap models of gamma ray emission from the Vela pulsar. AMS-02 will be able do distinguish between these two models* (right) [123].

spectrum is also shown.

Precise measurement of diffusive gamma ray fluxes may reveal the origin of dark matter, while gamma rays originating from different sources such as active galactic nuclei (AGN) and gamma ray bursts may provide information about possible quantum gravity effects.

AMS-02 will be able to measure the galactic and extragalactic diffusive gamma ray spectra up to 10^3 GeV. In addition, up to 10 gamma ray bursts and about 500 AGN per year will be recorded. This means more information on unidentified gamma sources as well as on known objects and discovery of new sources. For example a possible AMS-02 measurement is presented on the right-hand plot of Figure 1.19. Two different models of gamma emission from the Vela pulsar [124, 125] can be distinguished with AMS-02 gamma measurements in the energy range from 5 to 50 GeV where there is not enough statistics from EGRET measurements.

1.8 Conclusions

From the previous overview it is clear that to perform antimatter and dark matter searches and the foreseen astrophysics studies it is necessary an experiment with a high sensitivity and very good charge identification, rigidity and velocity measurements, with good e/p separation and albedo rejection. In addition it is required to have a strong system redundancy with a large acceptance and long duration measurements to reduce the statistical errors as much as possible. AMS-02 with its large acceptance ($\sim 0.5\,\mathrm{m}^2\,\mathrm{sr}$) and large exposure period of at least 3 years will collect close to three orders of magnitude more statistics than AMS-01 under much better instrumental conditions which will allow to extend by orders of magnitude the sensitivity reachead by previous experiments. In addition its privileged location on the ISS will avoid any secondaries produced in the Earth's atmosphere. Due to its large rigidity range, energy, velocity and electric charge redundant measurements, as will be shown in the next chapters, due to its good e/p separation and albedo rejection, AMS-02 will allow to do a rich, diversified and unprecedented physics program.

AMS-02 expected measurements

Table 1.2 shows the AMS-02 expected measurements after 3 years of data taking.

Measurement	statistics	energy range	physics goals
e^+	10^7	1-400 GeV	**Dark Matter**
$\bar{p}$	10^6	0.5-200 GeV	
$\overline{\mathrm{D}}$	$\sim$10	0.1-8 GeV/A	
γ-ray	10^5	1-10^3 GeV	
D	10^8	0.1-8 GeV/A	**Astrophysics**
^{3}He	10^8	0.1-8 GeV/A	
^{10}Be	10^5	0.1-7 GeV/A	
Measurement	sensitivity	rigidity range	physics goals
$\overline{\mathrm{He}}$/He	10^{-9}	0.5-10^3 GV	**Antimatter**
$\overline{\mathrm{C}}$/C	10^{-8}	0.5-10^3 GV	

Table 1.2: *AMS-02 expected measurements after 3 years on the ISS.*

Chapter 2

The Alpha Magnetic Spectrometer

God wills, Man dreams, the Work is born.

Fernando Pessoa in Mensagem

2.1 Physics Goals

The **A**lpha **M**agnetic **S**pectrometer (AMS) is a particle detector that will be installed on the **I**nternational **S**pace **S**tation (ISS) for three to five years to measure cosmic ray fluxes, at an altitude of 430 km, on a 51^{o} orbit (see Figure 2.1). It is a large acceptance ($\sim$0.5 m^2 sr) superconducting magnetic spectrometer that due to its long exposure time will allow AMS to collect an unprecedented large data sample and extend by orders of magnitude the sensitivity reached by previous experiments. It is a large international collaboration with around 500 collaborators from institutes in America, Europe and Asia.

Figure 2.1: *Artistic view of the International Space Station with the AMS detector on the left arm.*

The physics aims of AMS, already explored in the previous chapter, will be:

- Search for cosmic antimatter, through the detection of antinuclei with $|Z| \geqslant 2$;
- Search for non-baryonic dark matter through the detection of annihilation products appearing as anomalies of the cosmic-ray spectra (e^+, $\bar{p}$, γ and $\bar{\mathrm{D}}$);
- Measurement of cosmic ray spectra from few hundred MeV up to 1 TeV, in particular:
  - hydrogen, helium and beryllium isotopes (D/p, ^{3}He/^{4}He, ^{10}Be/^{9}Be);
  - secondary to primary spectrum (B/C and sub-Fe/Fe)
  - cosmic gamma-ray spectrum.

Events nominally will occur at a rate of about 100 to 2000 per second [126] depending on orbital location and solar flare activity. A total statistics above 10^{10} events is expected.

2.2 The AMS-01 detector and its test flight

A 'scaled-down' version of the final AMS detector, AMS-01, was built and successfully flown on the space shuttle Discovery (STS-91) from 2$^{\text{th}}$ June until 12$^{\text{th}}$ June 1998 at a mean altitude of 370 km including a Mir docking period of about four days. The purpose was to guarantee that:

- The AMS experiment can function properly in space; in vacuum with orbital temperature changes from $-65\,^{\circ}$C to $+50\,^{\circ}$C and bombarded by the intense radiation background;
- The detector can withstand the vibration (150 dB) and acceleration (3 g) at launch and the deceleration (6.5 g) at landing.

In addition, the similarity between the flight orbit and the ISS orbit allowed studying the expected backgrounds in the weak signals being searched and 100 million events were acquired during the first 100 effective hours of data taking and along a total of 154 orbits inclined at $51.7\,^{\circ}$. The AMS data acquisition system had

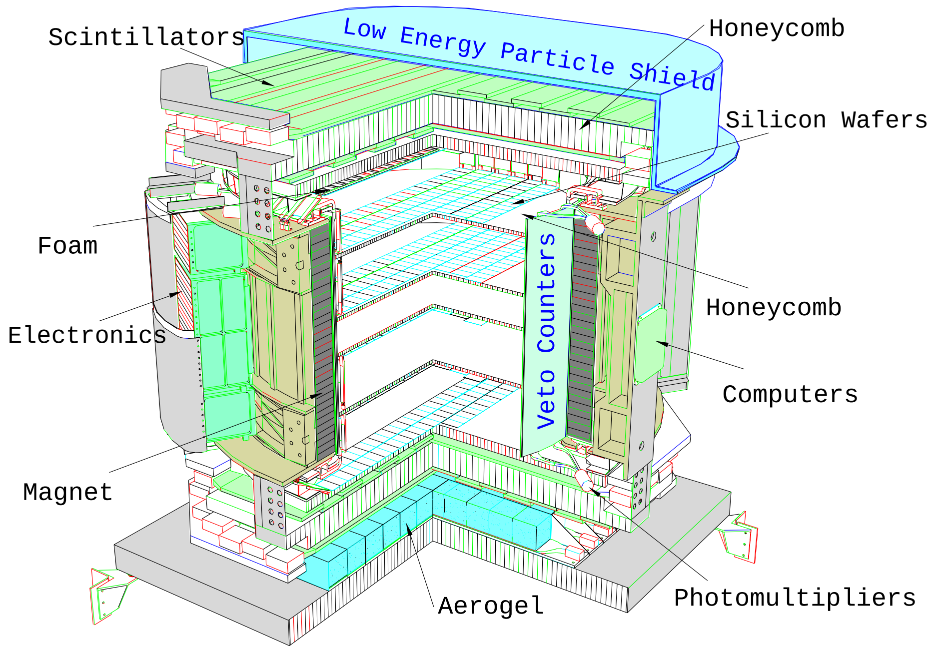

Figure 2.2: *Scheme of the AMS detector sent on a ten days flight during June 1998.*

lifetimes varying from 40 to 95% with recorded event rates of 700 to 100 Hz. The large majority of events were essentially collected at zenith inclinations of 0, 20 and 45 degrees. Albedo data was taken on the last day when the detector faced the Earth.

2.2.1 Detector description

The detailed experimental setup of AMS-01 is shown in Figure 2.2. The apparatus was about 1.6 m high and its horizontal cross section was about 2.6 m^2.

The experimental flight apparatus was composed of a permanent magnet, a Time-Of-Flight system (TOF), a silicon Tracker (TRK), Veto Counters and an Aerogel Threshold counter (ATC).

Charged particles crossing the AMS spectrometer within a geometrical acceptance of $\sim$0.3 m^2 sr were bended in a Nd-Fe-B permanent magnet with an analyzing power, BL^2, of 0.14 Tm^2. The magnet had a cylindrical shape with an inner diameter of 1.1 m and 0.8 m high. Particle identification relied on a set of measurements performed by the following subdetectors.

The TOF detector was composed of four scintillator planes 1 mm thick placed at the magnet end-caps. It measured particle energy loss and transit time with a resolution for singly charged particles of 120 ps. Therefore the velocity relative resolution was $\Delta\beta/\beta \sim 3\%$ for $Z = 1$ particles, the direction of incidence was obtained allowing to distinguish inward from upward particles and the charge magnitude (Z) and a fast trigger signal were extracted.

The tracker was made of six double sided silicon planes inserted inside the magnet. The accuracy of the position measurement was $\sim$10 μm and $\sim$30μm respectively in the bending (Y) and non-bending (X) planes. The particle rigidity, $R = pc/|Z|e$ (GV), was derived from the track curvature. A resolution of $\sim$8% for momenta ranging from around 2 to 8 GeV/c/nucleon was attained. Charge was also measured by energy sampling in the six planes.

The veto (ACC, Anti-Coincidence Counter) consisted on a layer of anti-coincidence scintillation counters used to tag events interacting inside the magnet.

The ATC detector was made of 11 modules superimposed in two layers of 5 and 6 modules, respectively from top to bottom and placed below the TOF counter. The granularity of this detector was defined by the elemental cell of 10 cm^3, having an aerogel radiator ($n = 1.035$) inside coupled to a photomultiplier. Its signal relied on the Čerenkov photons emitted by charged particles crossing the radiator material. This detector performed velocity measurements and was sensitive to the charge magnitude. It contributed to particle identification, namely e/p separation.

Events were triggered by the coincidence of signals in the four TOF planes consistent with the passage of a charged particle through the active tracker volume with no signal from the ACC.

Physics results

A detailed description of the data analysis as well as the obtained results can be found in [14] and in its references. A summary of them is presented hereafter.

Antimatter search

The antihelium data sample was selected requiring particles with a charge $Z = -2$. Background particles are mainly protons with a wrong charge determination (magnitude and sign) and helium nuclei reconstructed with a negative sign. Wrong charge magnitude reconstruction was reduced to a 10^{-7} level by combining the TOF and tracker independent measurements of the particle energy loss. The background coming from wrong sign reconstructed events due to interactions inside the tracker (e.g. δ rays and nuclear scattering) was suppressed by demanding a large accuracy on the measured rigidity and an isolation cut.

A total of 2.86×10^6 helium events were selected up to a rigidity of 140 GV. No antihelium nuclei were detected at any rigidity. The upper limit with 95% confidence level on the relative flux of antihelium to helium, assuming similar rigidity spectra was established at $\frac{N_{\overline{He}}}{N_{He}} < 1.1 \times 10^{-6}$ [127].

Particles spectra

Precise knowledge of proton and helium fluxes is important for the determination of secondary particle fluxes ($\bar{p}$, e^+) and has strong implications on the prediction of atmospheric neutrino fluxes. Based on a proton sample of 5.6×10^6 events in the kinetic energy range from 0.2 to 200 GeV, a proton spectral index $\gamma = 2.78 \pm 0.025$ was obtained [128].

The helium spectrum from 0.1 to 100 GeV/nucleon was measured accumulating 10^6 events. The spectral index obtained was $\gamma = 2.74 \pm 0.02$.

Below the geomagnetic cutoff ($R < 3$ GV) a second spectra of protons and helium nuclei was observed [129, 130]. Most of the second spectrum protons follow a complicated trajectory and originate from a restricted geographic region. In the second helium spectrum over the energy range 0.1 to 1.2 GeV/nucleon, in the geomagnetic latitude from -0.4 to $+0.4$ rad, the flux was measured to be $(6.3 \pm 0.9) \times 10^{-3} / (\mathrm{m}^2\,\mathrm{sec}\,\mathrm{sr})$ and, contrary to expectations, more than 90% of helium was ^{3}He (at the 90% confidence level).

Lepton spectra in the kinetic energy ranges 0.2 to 40 GeV for e^- and 0.2 to 3 GeV for e^+ were measured. From the origin of the leptons two distinct spectra were registered: a higher energy spectrum and a substantial second spectrum with positrons much more abundant than electrons. Tracing leptons from the second spectrum shows that most of these leptons travel for an extended period of time in the geomagnetic field and that the e^+ and e^- originate from two complementary geographic regions [102].

A total of 10^4 deuterium nuclei in the energy range 0.1 to 1.0 GeV/nucleon were observed allowing the first accurate test of galactic confinement models.

In a total of 10^4 deuterium nuclei in the momentum range 1 to 3 GeV/c no antideuterium nuclei were detected. The most precise limit on the flux of antideuterium of less than 10^{-4} has been obtained [126].

Beyond the primary spectrum, data obtained showed a particle flux below the geomagnetic cutoff that could not come from outer space. A detailed study of the trajectories showed that those particles arise from the interaction of primary particles with the top layers of the atmosphere [126].

2.3 The AMS-02 Detector

The AMS spectrometer capabilities were reviewed and extended with respect to those of the STS-91 experimental flight through the inclusion of new subdetector systems and the completion of others constructed with the state of the art of particle identification techniques.

AMS-02 will have a larger acceptance ($0.5\,\mathrm{m}^2\,\mathrm{sr}$) and the magnetic field will be produced by a superconducting magnet providing a $\sim$6 times stronger bending power. The silicon tracker will have the number of double sided layers extended from six to eight in order to reduce bad charge sign reconstructions and to improve the reconstruction efficiency. The momentum resolution will be improved by a factor $\sim$10. New detector systems will be included: a Transition Radiation Detector (TRD), a new Čerenkov detector - the Ring Imaging Čerenkov detector (RICH) - and an Electromagnetic Calorimeter (ECAL).

A schematic view of all the subdetectors is shown in Figure 2.3. The maximum dimensions of the AMS detector are $3\times3\times3\ \mathrm{m}^3$ and it weighs around 7 tons, a figure which is strictly controlled due to the shuttle and space station restrictions. It will be subject to several other constraints during the complete mission. The detector will suffer vibration (150 dB) and acceleration (3 g) at launch and deceleration (6.5 g) at landing. AMS will operate in vacuum (pressure less than 10^{-10} Torr) with orbital temperature changes from $-65\,^\circ\mathrm{C}$ to $+40\,^\circ\mathrm{C}$ and will be hit by an intense ionizing radiation ($\sim 1000\,\mathrm{cm}^{-2}\mathrm{s}^{-1}$) background and orbital debris and micrometeorites [126].

It will operate with limited power (2 kW) supplied by the ISS and must operate reliably for three or more years with no human intervention since beyond the payload lift into space no further access is foreseen to the device, which implies a strongly redundant measurement system. The challenge is to build AMS in a space-qualified way with several strict limits imposed by NASA.

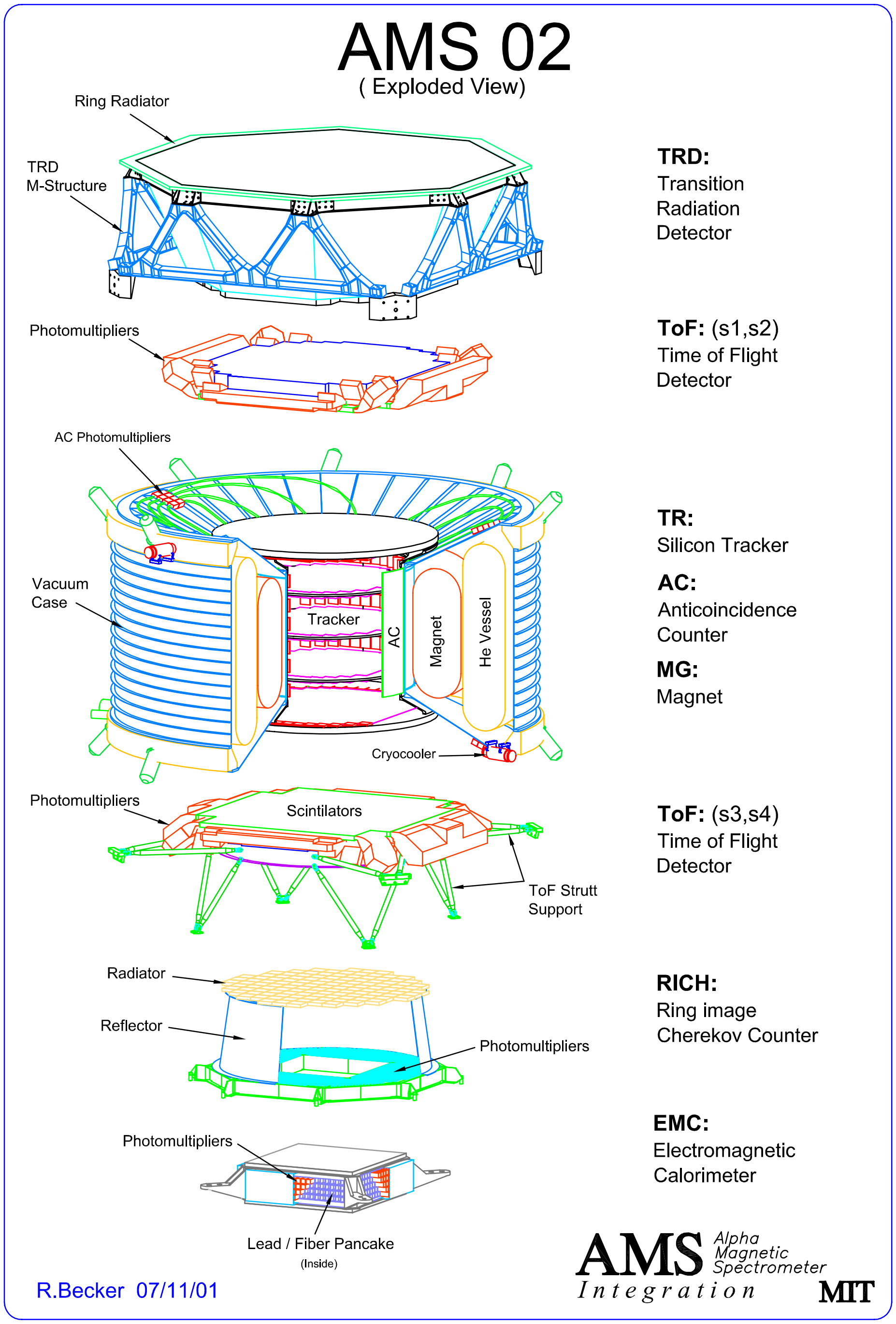

Figure 2.3: *A whole expanded view of the AMS spectrometer* [131].

The different subdetectors are more thoroughly described in the following and detailed in reference [126].

2.3.1 Transition Radiation Detector

The Transition Radiation Detector (TRD) [132] is placed at the top of the AMS spectrometer. Transition radiation (TR) is an electromagnetic radiation in the X-ray energy region ($\sim 1-50\,\mathrm{keV}$) that is emitted when charged particles cross the boundary between two media with different dielectric constants: ϵ_1, ϵ_2. The TR energy is proportional to the relativistic γ-factor (Lorentz factor). Since the emission of transition radiation has a threshold of $\gamma \approx 500$, light particles such as positrons have a much higher probability of emitting TR than heavy particles such as protons. This allows for a proton suppression in the momentum range of $10-300\,\mathrm{GeV}$ with a rejection factor of 10^2-10^3.

The emission probability at a single interface is very small ($\sim10^{-2}$) but this can be enhanced by a multilayer structure which implies multiple transitions.

The AMS-02 TRD consists of 328 modules made of a fleece radiator 20 mm thick and straw tube proportional wire chambers filled with a Xe/CO_2 (80%:20%) gas mixture at 1 bar absolute from a recirculating gas system designed to operate for more than 3 years in space. Each module, shown in Figure 2.6, contains 16 straws of lengths between 0.8 and 2 m and with a diameter of 6 mm and 72 μm of wall thickness. The fleece radiator and the corresponding proportional wire straw tubes where the TR is detected (see Figure 2.4) are arranged in 20 layers. The upper and lower four layers are oriented parallel to the AMS-02 magnetic field while the middle 12 layers run perpendicular to provide 3D tracking. They are supported in a conically shaped octagon structure, as shown in Figure 2.5, built of aluminium honeycomb material with carbon fiber skins and bulkheads.

The challenge consists in building such a detector in a space qualified solution with strict limits on gas tightness, weight, power consumption and outgassing whilst assuring structural safety and gas homogeneity in a harsh environment.

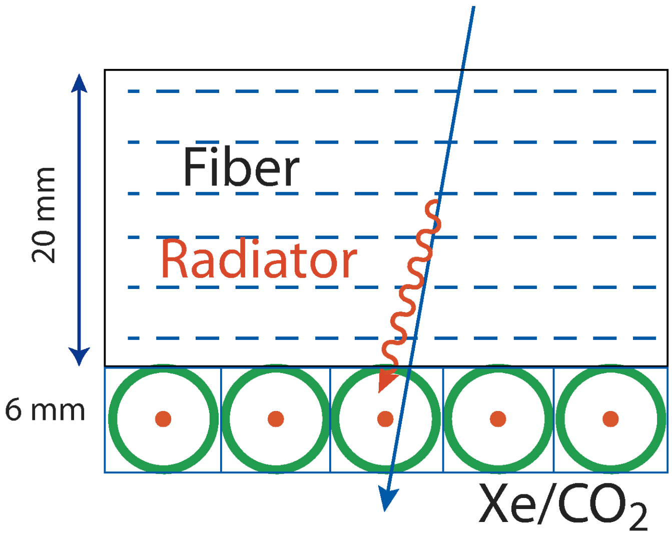

Figure 2.4: *Transition radiation principle applied to the AMS-02 Transition Radiation Detector.*

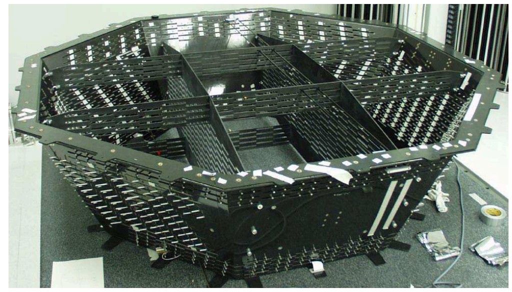

Figure 2.5: *The TRD octagon support structure.*

Figure 2.6: *AMS-02 TRD module with 16 straw tubes.*

2.3.2 Time-Of-Flight

The Time-Of-Flight (TOF) system [133] is expected to provide the fast trigger (FT) within 200 ns for charged particles with a negligible inefficiency; select, at the trigger level, particles within the AMS acceptance; distinguish between upward and downward particles at the 10^{-9} level; measure the particle velocity β with $\sigma_\beta = 3\%$ for protons; estimate the value of the particle absolute charge up to Z $\simeq$ 20 which complements the measurements made in other subdetectors.

The TOF system consists of four planes of 8, 8, 10, 8 plastic scintillator counters each. The planes are roughly circular with 12 cm wide scintillator paddles, one pair of planes above the magnet called the upper TOF and one pair below, the lower TOF. Both planes are shown in Figure 2.7. Each plane has a sensitive area of 1.2 m^2 and within one plane the paddles are overlapped by 0.5 cm to avoid geometrical inefficiencies. In order to have efficient background selection and to help the offline analysis, the paddles in the two adjacent planes are perpendicularly placed.

Scintillators are 1 cm thick and the light is collected by two or three Hamamatsu R5946 photomultiplier tubes (PMT) in each side. This guarantees a redundant system. The TOF operation at regions with very intense magnetic fields forces the use of shielded fine mesh phototubes and the optimization of the geometry of the light guides, with some of them twisted and bent. This minimizes the angle between the magnetic field and the PMT axis. Figure 2.8 shows a TOF scintillator paddle with twisted and bent light guides.

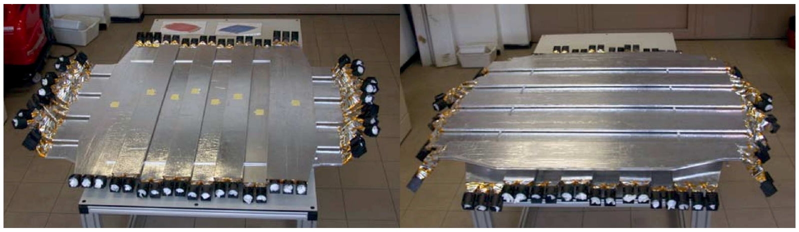

Figure 2.7: *Top view of the design and flight paddles during an assembly test of the upper* (left) *and lower* (right) *TOF.*

Figure 2.8: *Assembled TOF paddle.*

The measurement in the TOF of the crossing time between scintillator planes allows to extract the velocity through $\beta = \Delta L/\Delta t$. The time of flight resolution for two scintillators, tested in a test beam at CERN in October 2003 with indium beam fragments of 158 GeV/c/nucleon, is shown in Figure 2.9 as function of the particle charge. One of the tested scintillators had bent and twisted light guides (C2) like the one presented in Figure 2.8, while the other one had bent light guides (C3). A time resolution of 180 ps was measured for this conservative configuration. However, as the measurement in AMS-02 will be done with four independent measurements, the time resolution which can be inferred is of the order of 130 ps for a MIP[1]. In this time-of-flight measurement system $\Delta\beta$ is intrinsically related with the TOF time resolution, Δt:

$$\frac{\Delta\beta}{\beta} = \frac{\Delta t}{t} = \frac{\Delta t}{L}\beta c \tag{2.1}$$

where L is the distance between the TOF planes. For a flight distance of $\sim$1 m and a time precision $\Delta t = 130$ ps, the relative resolution for TOF velocity measurement is $\Delta\beta/\beta \simeq 3\%$ for particles with $\beta \sim 1$.

[1]Minimum Ionizing Particle

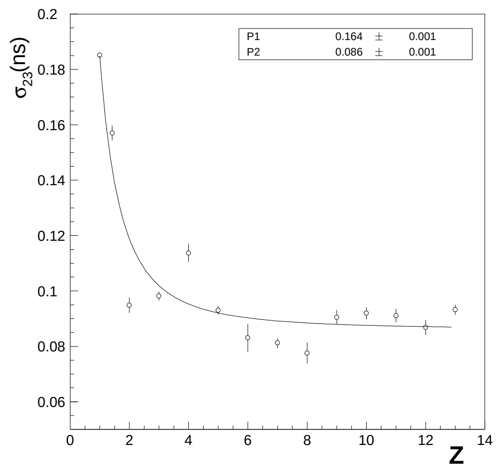

Figure 2.9: *Time of flight resolution for a set of two scintillators and different charged nuclei. Results were obtained with nuclei fragments of an indium beam of 158 GeV/c/nucleon taken at CERN in October 2003.*

2.3.3 Superconducting Magnet

A key feature of the AMS-02 detector, responsible for a major part of its analyzing power, is a strong superconducting magnet of 0.86 T in the center which corresponds to slightly more than six times the value of the AMS-01 permanent magnet. The bending power $B\,L^2$ is $0.862\,\mathrm{T\,m}^2$. The design was mainly influenced by the constraints on the maximum weight allowed, while providing the largest possible geometrical acceptance and bending power.

The superconducting magnet system for AMS-02 [134] consists of a pair of large Helmholtz ('dipole') coils together with two series of six smaller racetrack coils circumferentially distributed between them, as shown in Figure 2.10. The dipole coils are used to generate the majority of the transverse magnetic field. The racetrack coils are included to increase the magnitude of the overall dipole field; to reduce the magnitude of the stray field outside the magnet (maximum stray field is 4 mT at a radius of 2.3 m) and to reduce the magnetic dipole moment ($\vec{\mu} \sim 0$) of the magnet system to avoid an undesirable torque on the ISS resulting from the interaction with Earth's magnetic field.

All superconducting coils are situated inside a vacuum tank and operated at a temperature of 1.8 K with superfluid helium. The magnet coils and the toroidal helium storage vessel with a volume of about 2500 ℓ are screened from heat radiation by a series of cold helium gas thermal shields. Figure 2.11 shows a layout of the AMS-02 magnet system including helium vessel and vacuum tank. The free bore of the magnet system has a diameter of 1.1 m. The outer diameter of the vacuum tank is 2.7 m and its height is 1550 mm. The magnetic field points in $-x$ direction.

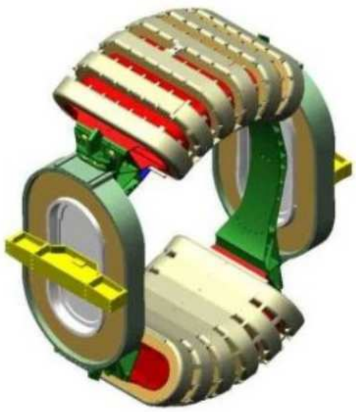

Figure 2.10: *AMS-02 coil configuration.*

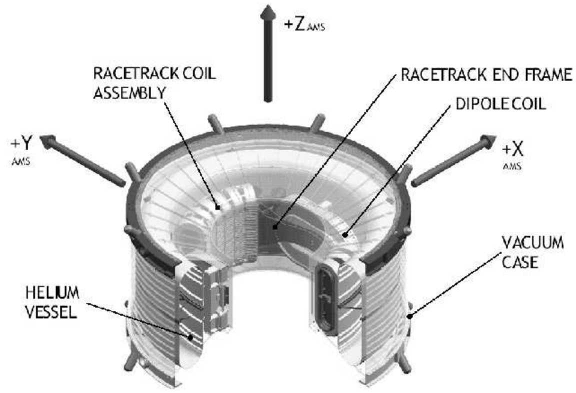

Figure 2.11: *Layout of the superconducting magnet.*

The magnet will be launched with no field, it will be charged only after installation on the ISS. Because of parasitic heat loads, the helium will gradually boil away throughout the lifetime of the experiment. After the project time of 3 to 5 years, the helium will be used up and the magnet will warm up and will no longer be operable.

2.3.4 Tracker

The central part of the AMS detector is occupied by the silicon tracker detector (STD). The tracking system [135] is composed of 8 layers of double-sided silicon microstrip sensors with 2264 units, $51.36 \times 72.05 \times 0.30\,\text{mm}^3$ each with a total area of $\sim$6.7 m^2 arranged in 5 planes. There will be a total of $\sim$2500 silicon sensors arranged on 192 ladders. A ladder is made of a variable number of silicon sensors (from 7 to 15). The strips are daisy-chained to increase the detection surface while using a limited number of readout channels. The three inner tracker planes have silicon ladders on both sides and the two outer planes only on one side. Figure 2.12 shows one of the inner planes completely equipped.

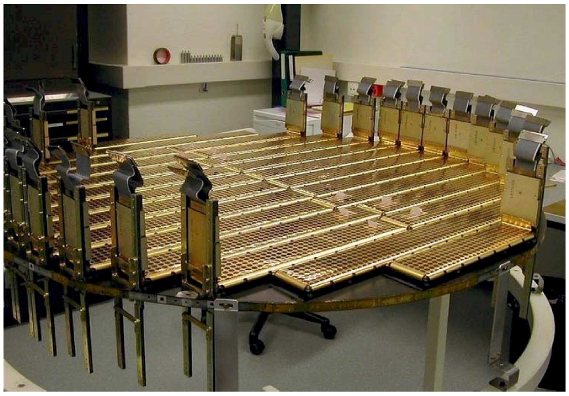

Figure 2.12: *Tracker inner plane equipped with ladders.*

.

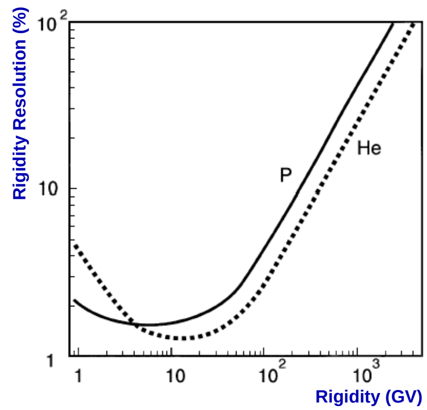

Figure 2.13: *Rigidity resolution for protons and helium nuclei as function of the particle's rigidity.*

The position of the charged particles crossing the tracker layers is measured with a precision of $\sim$10 μm along the bending plane (YOZ) and $\sim$30 μm on the transverse direction. Particles rigidity ($R = pc/|Z|e$) is measured with an accuracy better than 2% up to 20 GV and the maximal detectable rigidity is around 3 TV. The rigidity resolution for protons and helium nuclei is shown in Figure 2.13.

The absolute value of the electric charge is also measured from energy deposition (dE/dx samplings) up to $Z \sim 26$. Such extended measurement is possible due to the low noise and wide dynamic range of the silicon readout electronics.

2.3.5 Ring Imaging Čerenkov detector

The Ring Imaging Čerenkov Detector (RICH) will be located right after the last TOF plane and before the electromagnetic calorimeter. It is a proximity focusing device with a dual radiator configuration on the top made of aerogel and sodium fluoride (NaF). The expansion height is 46.9 cm. Its detection matrix is composed of 680 photomultipliers and light guides and a high reflectivity conical mirror surrounds the whole set. The RICH was designed to measure the velocity of singly charged particles with a resolution $\Delta\beta/\beta$ of 0.1%, to extend the charge separation up to iron, to contribute to e/p separation and for albedo rejection.

A more detailed description of this subdetector is given in the next chapter.

2.3.6 Electromagnetic Calorimeter

The Electromagnetic Calorimeter (ECAL) [136] is located at the very bottom of the AMS detector just below the RICH and is a fine grained lead-scintillating fiber sampling calorimeter that provides an accurate 3-dimensional imaging of the longitudinal and lateral shower development. It provides high ($\geq 10^6$) electron/hadron discrimination in combination with other AMS subdetectors and good energy resolution, expected to be $\Delta E/E \simeq 10.2\%/\sqrt{E(\mathrm{GeV})} \oplus 2.3\%$. This result was evaluated from beam test data analysis depicted in Figure 2.14 (right). The ECAL provides a standalone photon trigger signal and also provides AMS with non converted γ's detection capability with an angular resolution of $\sim 1^o$.

The AMS-02 ECAL consists of a lead-scintillating fiber sandwich with an active area of $648 \times 648\,\mathrm{mm}^2$ and a thickness of 166.5 mm. The calorimeter is composed of 9 superlayers, each 18.5 mm thick and made of 11 grooved, 1 mm thick lead foils interleaved with layers of 1 mm diameter scintillating fibers and glued together with epoxy.

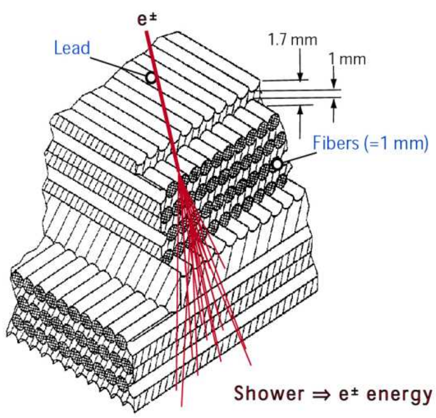

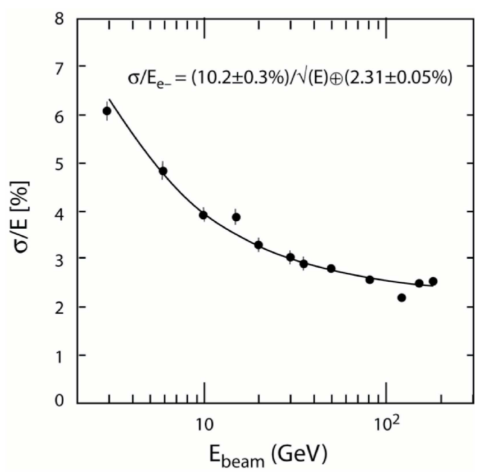

Figure 2.14: *Scheme showing AMS02 ECAL lead-scintillating fiber structure* (left). *ECAL energy resolution as funtion of the electron beam energy. These results are from the beam test at CERN, in July 2002, using electrons with an energy from 3 to 180 GeV* (right).

In each superlayer, fibers run in one direction only. The detector capability of reconstructing the shower in a 3-D image is achieved by piling up the superlayers with fibers alternatively parallel to the x-axis (4 layers) and y-axis (5 layers). Left-hand scheme of Figure 2.14 illustrates the lead-scintillating fiber calorimeter of AMS-02.

The calorimeter has a total weight of 496 kg and a thickness corresponding to $\sim 17X_0$ radiation lengths.

At one end of the fibers a multi-pixel (2×2) photomultiplier (Hamamatsu R7600-00-M4) is placed. Each anode covers an active area of 9×9 mm^2, corresponding to 35 fibers, defined as a cell with a granularity ∼0.5 Molière radius. In total the detector is divided into 1296 cells (324 PMTs) which allows 18 samplings of the electromagnetic shower.

2.3.7 Anticoincidence Counters

The AMS-02 anticoincidence counters (ACC) [126] are made of scintillators BICRON BC414, 8 mm thick that surround the silicon tracker and are fitted tightly inside the inner bore of the superconducting magnet as seen in Figure 2.15 (left). There are 16 scintillator paddles with dovetailed edges for hermetic purposes. The ACC detects particles that enter the tracker laterally, beyond the AMS acceptance. Those particles may confuse the charge determination if they leave hits in the tracker close to the tracks of interest. The ACC scintillation counters design allows a high efficient rejection of undesirable particles.

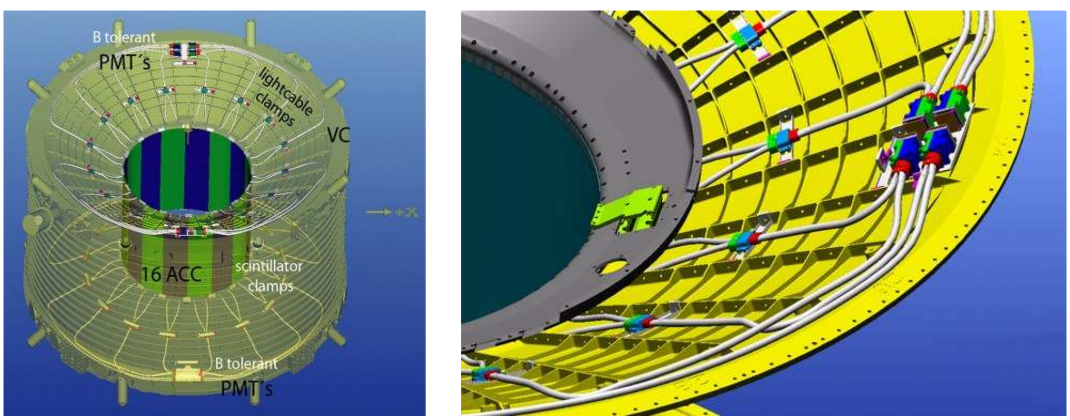

Figure 2.15: *ACC System inside the inner bore of the AMS-02 magnet* (left). *ACC light transport system, from the fibers embedded in the panels, through the couplings to the PMTs located on the outer rim of the vacuum case* (right).

The mesh photomultipliers that register the light signals from the ACC panels are Hamamatsu R5946 and have to work in a moderate (∼ kG) magnetic field at locations on the top of and on the bottom of the magnet vacuum case, approximately 40 cm from the racetrack coils. To deal with this and to minimize the effect, the PMTs are oriented with their axis parallel to the stray field. Wavelength shifter fibers Kuraray Y-11(200)M, 1 mm wide, are used to collect light from the scintillation panels and are embedded in grooves milled into the scintillation panels. Groups of 37 fibers are collected in two output ports at both ends of the counters. They have two photomultipliers in each end, mounted on the rim of the vacuum case. Right-hand panel of Figure 2.15 depicts the ACC light transport system.

2.3.8 Star Tracker

AMS-02 will have a star tracker on board. Gamma rays are not affected by the solar, galactic and intergalactic magnetic fields, so they point to their source. To relate these sources with phenomena observed in other bands of the electromagnetic spectrum like X-ray region, ultra-violet, visible, infrared and radio, it is necessary to have an accurate measurement of the direction to which the detector is pointing when the event occurs. Because the space station is a large and flexible structure it is necessary to make this measurement with a device attached directly to AMS-02. The star tracker called AMICA [137] (for Astro Mapper for Instrument Check of Attitude) will perform this measurement. In AMS the highest angular precision ($\sim$arcmin) is given in the measurement of converted gamma rays by the silicon tracker. So to avoid any systematic shifts the device is attached to the silicon tracker structure. A star-mapper is conceptually an imaging, optical instrument able to autonomously recognize a stellar field through the matching of the observed point sources with an on-board astrometric/photometric catalogue and to calculate its own orientation with respect to an inertial frame. The AMICA on AMS is responsible for providing real-time information that is going to be used off-line for compensating the large uncertainties in the ISS flight attitude and the structural elasticity degrees of freedom. This device provides a precise ($<$20 arcsec) real-time (at rates up to 20 Hz) 3D transformation of the AMS mechanical x-y-z frame to sky coordinates.

As shown in Figure 2.16, it consists of a pair of small optical telescopes (AMICA Star Tracker Cameras or ASTCs) mounted on either side of the upper silicon tracker.

Each telescope consists of an optics system, a low frame-transfer charge coupled device (CCD), a support and a baffle to limit reflected daylight. The AMICA optical system consists in a special, fast lens f/1.25 with 600 mm aperture and 75 mm focal length, filtered to pass 475 to 850 nm for noise reduction and to prevent saturation, as well as protect from IR and UV. The CCD covers a field of $6.3^0 \times 6.3^0$ with an image scale of 0.36 μm/arcsec.

Figure 2.16: *Star Tracker mounting on the AMS-02.*

The two cameras are identified as 'starboard' (ISS right wing) and 'import' (ISS left wing) according to the ISS technical conventions. They have to be oriented to maximize their view toward space, avoiding both the rotating solar planels of the ISS as much as possible (the starboard can not avoid a $\sim$10% average time obscuration) and attached radiators and the central part of the ISS. In addition, having two cameras pointing in opposite directions ensures that at least one will always have a clear view of space without solar interference.

2.3.9 GPS

In AMS-02 it is necessary not only a directional correlation provided by the star tracker but also a precise temporal correlation (of the order of few microseconds) between AMS-02 measurements and UTC[2] time for direct comparison with the

[2]Coordinated Universal Time

measurements from other missions. Time information is obtained from the ISS, but due to the limitations of the LRDL[3] the reference time accuracy would be a few tenths of seconds, which is insufficient. In AMS, short time periods, up to few seconds, can be accurately measured with a precision of the order of sub-microseconds by the trigger system. Nevertheless, they are subject to long term drift and lack of an absolute reference. To overcome this AMS-02 will be equipped with a global positioning system (GPS) with two patch type antennae mounted on an upper USS[4] member pointing in different directions to ensure that the signals from a sufficient number of GPS satellites can always be caught.

[3] Low Rate Data Link

[4] The Unique Support Structure (USS) is the primary structural element of the AMS-02 payload. Its purpose is to structurally support the cryomagnet cold mass and the whole detector during launch, landing and on-board loading and integrates them with shuttle and ISS.

Chapter 3

The RICH Detector of the AMS Experiment

Let there be light.
in Genesis 1:3

Čerenkov detectors have been widely used in high energy physics and astrophysics for particle identification (PID) purposes. Several examples of their application in astrophysics experiments like in balloon experiments are BESS [9], CAPRICE [8], ISOMAX [7]. In particular, AMS-02 will be equipped with a proximity focusing RICH detector. Their use allows to measure the velocity and charge magnitude of charged particles in a very accurate way, leading to particle identification (PID). They rely on the properties of the emitted radiation by a particle crossing a dielectric medium (radiator) with a velocity greater than the light speed in the same medium.

Different Čerenkov detectors can be classified in the following groups: differential counters, threshold counters and Ring Imaging CHerenkov counters (RICH) [138, 139, 140, 141].

3.1 Čerenkov Radiation

The Čerenkov radiation effect was identified and characterized, in 1934, by Vavilov and Čerenkov while they were trying to understand the origin of the weak luminescence that salt solutions emit when struck by gamma rays. Čerenkov published a paper in which he proved that the light emission was caused by Compton electrons moving quickly through the liquid and showed the relationship between the emission angle and the refractive index of the medium [142]. In 1937 Čerenkov radiation was explained in the frame of classical electrodynamics by I. M. Frank and I. E. Tamm [143]. The quantum formulation of the theory of the Čerenkov effect was elaborated by Ginsburg a few years later [21]. In 1958, Čerenkov, Frank and Tamm were jointly awarded with the Nobel Prize in Physics for the discovery and interpretation of Čerenkov radiation.

The use of this radiation for particle physics experiments had to wait for the end of World War II and the development of the vacuum photomultiplier which allowed time coincidence measurements as well as single photoelectron sensitivity.

Phenomenological description

A charged particle crossing a dielectric medium, with a refractive index n, polarizes the atoms along its track so that they become electric dipoles. Owing to the transient nature of this phenomenon, polarized atoms relax back to equilibrium by emitting a short electromagnetic pulse. If the speed of the particle, $v = \beta\ c$, is lower than the speed of light in the medium, $c_n = c/n$, the polarization is symmetric around the trajectory points of the particle and the interference between the wavefronts does not occur (Figure 3.1 (left) (a) [144, 145]). On the other hand, if the speed is greater than the speed of light in the medium, the wavefronts generated in each point of the particle's path create a constructive interference, a net dipole field appears even at large distances from the particle and coherent radiation is emitted with an angular aperture θ_c with respect to the direction of motion, with the photons uniformly distributed in the surface of a cone with an aperture 2 θ_c. This is the Čerenkov effect, and θ_c is the Čerenkov angle. Figure 3.1 (left) (b) illustrates the polarization for the case $v > c/n$ [144, 145].

The necessary condition, $v > c/n$, implies the inequality 3.1.

$$\beta > 1/n \tag{3.1}$$

and can be understood from the Huygens's construction of Figure 3.1 (right) which shows the formation of "Huygens' spherical wavelets", generated along the particle trajectory. The same construction also implies the cosine of the opening angle of

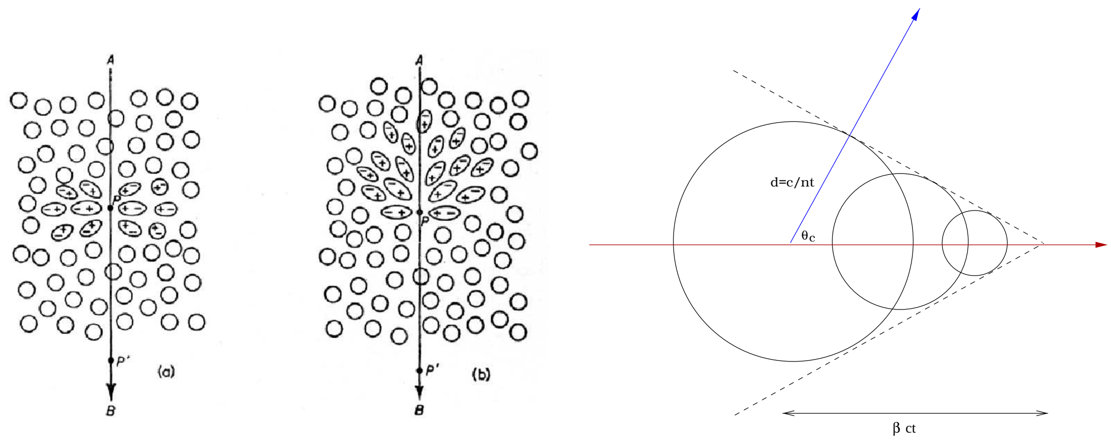

Figure 3.1: *Illustration of the Čerenkov effect* [144, 145] (left). *Huygens's construction for the Čerenkov radiation emitted by a particle traveling with a speed v greater than c/n, the speed of light in the medium. The resulting wavefront is indicated by the dashed line and moves in the direction of the arrow* (right).

the Čerenkov cone, named *Mach cone*, $\cos\theta_c$ should obey expression 3.2.

$$\cos\theta_c = \frac{ct/n}{\beta ct} = \frac{1}{\beta n} \tag{3.2}$$

Consequently, the determination of θ_c is a direct measurement of the velocity of the particle. The lowest value of β that obeys equation 3.1 is called the *threshold* velocity and is determined by the refractive index n of medium.

According to equation 3.2, the emission angle depends on particle speed (β) and on the refractive index (n). For different refractive indices there are different *threshold* velocities or threshold momenta and different maximum emission angles, as can be seen in Figure 3.2.

The resulting radiation covers a band of frequencies corresponding to the various Fourier components of the electromagnetic pulses emitted by the medium dipoles. It propagates normal to the Mach cone surface and it is linearly polarized along the direction perpendicular to the Čerenkov cone surface, where the electric field $\vec{E}$ oscillates. Figure 3.3 illustrates the Čerenkov light polarization vectors [146].

The energy carried off by Čerenkov radiation (E) per unit of length (dx) and range of frequency ($d\omega$) for a particle of charge Ze was calculated by Frank and

Tamm and takes the form [146]:

$$\frac{d^2E}{dxd\omega} = \frac{Z^2\alpha\hbar}{c}\left(1 - \frac{1}{\beta^2 n^2(\omega)}\right)\omega = \frac{Z^2\alpha\hbar}{c}\omega\sin^2\theta_c, \tag{3.3}$$

where $\alpha = \frac{e^2}{4\pi\epsilon_0\hbar c} = 1/137.04$ is the fine structure constant. Because of the chromatic dispersion of the optical medium, n is a function of the radiation frequency ω. The radiated energy grows linearly with the frequency and with the square of the electric charge.

From the previous expression it can be deduced that the energy loss due to the Čerenkov effect is much smaller than the ionization energy loss. In the case of an electron that moves with $\beta \simeq 1$ across 1 cm of water ($\bar{n} = 1.334$), in the spectral range $\lambda = 400-700$ nm, the electron loses about 5×10^{-4} MeV by the Čerenkov effect, whereas its energy loss by ionization is 2 MeV [146].

Since the energy carried by each photon is:

$$E_\gamma = \hbar\omega \tag{3.4}$$

and being N_γ^{rad}, the total number of radiated photons, the total radiated energy, E

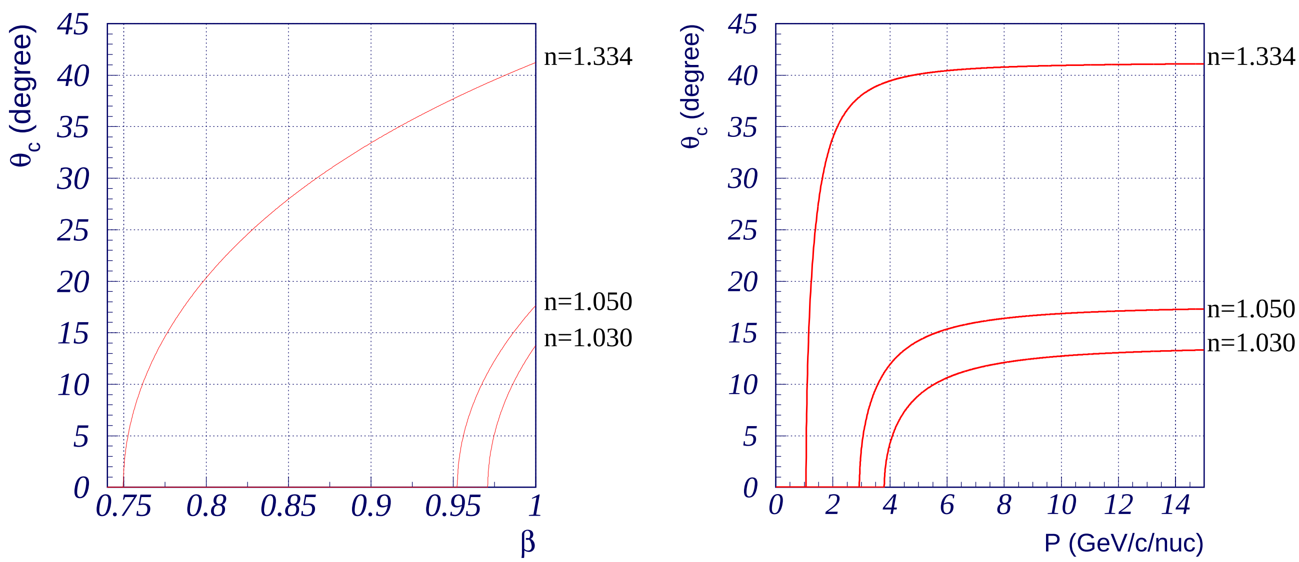

Figure 3.2: *Dependence of the emission angle (θ_c) with the particle velocity (β) and variation for materials: aerogel and NaF* (left). *Dependence of the emission angle (θ_c) with the particle's momentum per nucleon (P) for two materials: aerogel and NaF* (right).

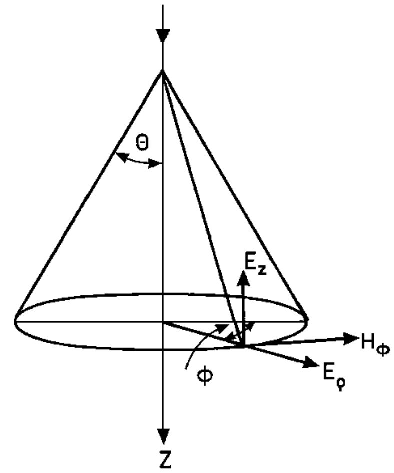

Figure 3.3: *Čerenkov light polarization vectors. The electric vector $\vec{E}$ lies in the plane defined by the particle direction and the photon direction* [146].

is

$$E = N_{\gamma}^{rad} E_{\gamma} \Rightarrow dE = E_{\gamma} dN_{\gamma}^{rad}, \tag{3.5}$$

allowing the number of radiated photons per unit of length and range of frequency to be expressed as:

$$\frac{d^2 N_{\gamma}^{rad}}{dx d\omega} = \frac{Z^2 \alpha}{c} \left(1 - \frac{1}{\beta^2 n^2(\omega)}\right). \tag{3.6}$$

On the other hand, the number of radiated photons per unit length and energy is given by

$$\frac{d^2 N_{\gamma}^{rad}}{dx dE_{\gamma}} = \frac{2\pi\alpha}{hc} Z^2 \left(1 - \frac{1}{\beta^2 n^2}\right), \tag{3.7}$$

which results from substituting $d\omega$ by $dE_{\gamma}/\hbar$ in equation 3.3 and using 3.5. The n dependence with the energy E_{γ} is not explicitely written. It is notorious that the light yield increases with radiator thickness (L), the squared particle charge (Z^2), the particle velocity (β) and the refractive index of the medium (n). The constant term in expression 3.7 is ∼370 $\mathrm{cm^{-1}eV^{-1}}$, which allows to write:

$$\frac{d^2 N_{\gamma}^{rad}}{dx dE_{\gamma}} \simeq 370\ Z^2 \left(1 - \frac{1}{\beta^2 n^2}\right) \left[\mathrm{cm^{-1}eV^{-1}}\right]. \tag{3.8}$$

The number of photons emitted per unit path and per unit energy interval is constant for a given charge Z and this number is a fundamental quantity for the detector design.

The total number of photons emitted in a radiator of thickness L can be obtained by integrating equation 3.8. Taking into account the overall efficiency (ϵ) for detecting the emitted photons which includes the effects of their propagation up to the arrival into the photodetectors (collection efficiency) and the detection efficiency (quantum efficiency) of the devices, the number of photoelectrons per unit of length (cm) is

$$N_{p.e.} \simeq 370\ Z^2 L < \sin^2\theta > \int \epsilon(E)\, dE = 370\ Z^2 L < \sin^2\theta >< \epsilon > \Delta E. \tag{3.9}$$

On the other hand, the total number of radiated photons per unit of length in terms of the wavelength range is obtained using the following integration:

$$\frac{dN_\gamma^{rad}}{dx} = 2\pi\alpha Z^2 \int_{\lambda_1}^{\lambda_2} \left(1 - \frac{1}{\beta^2 n^2(\lambda)}\right) \frac{d\lambda}{\lambda^2}\ . \tag{3.10}$$

The number of Čerenkov photons emitted per unit of wavelength interval $d\lambda$ is proportional to $d\lambda/\lambda^2$, consequently most of the photons are emitted in the UV region. Moreover if the variation of $n(\lambda)$ (for a discussion of this variation, see subsection 3.3.1) is smooth in the same range,

$$\left\langle 1 - \frac{1}{\beta^2 n^2(\lambda)} \right\rangle = \left\langle 1 - \cos^2\theta_c \right\rangle = \left\langle \sin^2\theta_c \right\rangle . \tag{3.11}$$

The number of radiated photons per unit of length comes

$$\frac{dN_\gamma^{rad}}{dx} = 2\pi\alpha Z^2 \left\langle \sin^2\theta_c \right\rangle \left(\frac{1}{\lambda_1} - \frac{1}{\lambda_2}\right) . \tag{3.12}$$

3.2 Physics aims with RICH

The **R**ing **I**maging **Č**erenkov detector (RICH) was designed to perform highly accurate velocity measurements with a relative resolution $\Delta\beta/\beta \sim 0.1\%$ for $\beta \simeq 1$ and $Z = 1$ particles and to extend the electric charge separation at least up to the iron element ($Z = 26$). The RICH will also contribute to the $e^-/\bar{p}$ and e^+/p discrimination through an efficient mass separation The lower energy region will be covered with the TOF starting at 1.5 GeV. The RICH will also contribute to the rejection of albedo particles which are not expected to generate a response from the counter.

The mass of a particle is related to its momentum, p, and velocity, β, through the expression $m = \frac{p}{\beta}\sqrt{1-\beta^2}$ and its determination is based on the measurement

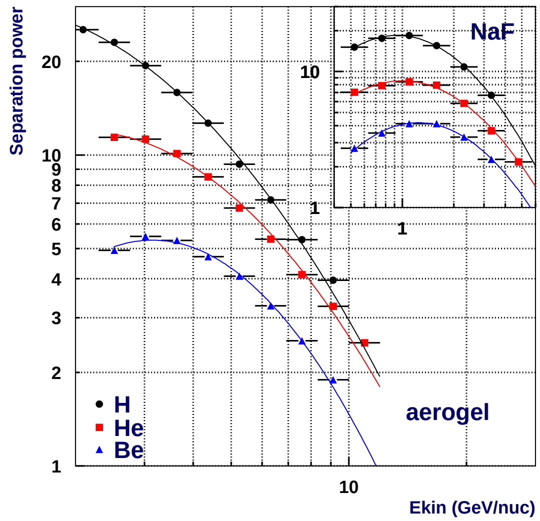

Figure 3.4: *RICH separation power for H, He, Be isotopes* (left).

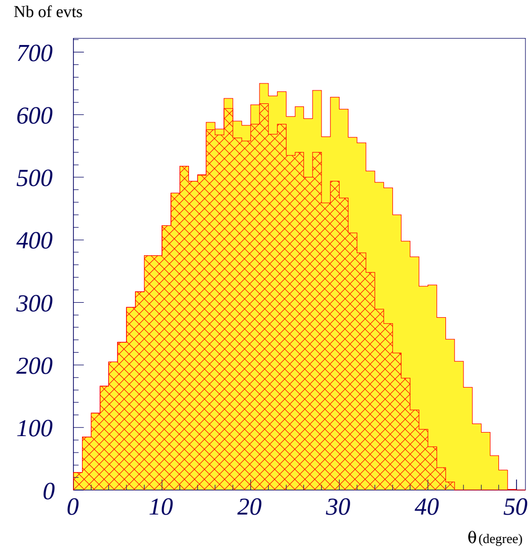

Figure 3.5: *The RICH acceptance is around 80% of the AMS acceptance. RICH accepted polar angles are represented in the shaded region and AMS accepted polar angles are in the continuous region.*

of both quantities. In AMS-02 the momentum is extracted from the information provided by the Silicon Tracker (see subsection 2.3.4) with a relative accuracy better than 2% for the energy region interesting for isotope mass separation. The associated mass uncertainty depends on both the momentum and velocity accuracy $\Delta m/m = (\Delta p/p) \oplus \gamma^2 (\Delta\beta/\beta)$, where $\gamma = E/m$ is the Lorentz factor. From the previous equation it is clear that the error on the velocity will dominate as the momentum increases. The expected results concerning mass separation with the AMS/RICH for hydrogen (D/p), helium (^{3}He/^{4}He) and beryllium (^{10}Be/^{9}Be) were shown in Figure 1.8.

The separation power, defined as the number of mass sigma, σ_m, between the two mass peaks, $\frac{\Delta m}{\sigma_m}$ is shown in Figure 3.4. Looking at the separation power for different elements, at different energies, for both radiators and imposing a separation between the mass peaks of at least $2 - 3\sigma_m$, it is visible that RICH is able to discriminate isotopes, such as helium (^{3}He/^{4}He) and beryllium nuclei (^{10}Be/^{9}Be), up to a kinetic energy per nucleon of $\sim$10 GeV and $\sim$8 GeV, respectively.

If AMS-02 was not equipped with the RICH detector mass separation could still be done using the TOF's velocity measurement. However, due to the poor velocity resolution obtained ($\sim$3%) it would separate helium isotopes only up to low energies ($\sim$1 GeV/nucleon) and would be hard to separate beryllium isotopes.

The RICH geometrical acceptance is of $\sim$0.4 m^2 sr, which is around 80% of the AMS acceptance. Figure 3.5 compares the polar angle distribution for a simulated set of events passing through AMS and the RICH detector.

3.3 RICH setup

The AMS/RICH is a proximity focusing device with a dual radiator configuration on the top made of a low refractive index radiator, aerogel $n = 1.050$, and a central square of sodium fluoride (NaF); a high reflectivity mirror surrounding the whole set and a detection matrix with light guides and photomultiplier tubes (PMTs). The RICH has a truncated conical shape with an expansion height of 46.9 cm, a top radius of 60 cm and a bottom radius of 67 cm. The total height of the detector is 60.5 cm. The detection plane has a $64 \times 64\,\mathrm{cm}^2$ central square hole to minimize matter in front of the electromagnetic calorimeter. In Figure 3.6 a perspective and a schematic view of the RICH detector with the corresponding dimensions is represented.

When a charged particle crosses the dielectric material of the radiator with a velocity higher than the light speed in the medium, a cone of Čerenkov photons is emitted. This light cone intersects the detection basis, drawing a ring, as the one represented in Figure 3.7. Complex photon patterns can occur at the detector plane due to mirror reflected photons. The event displayed is generated by a simulated beryllium nucleus passing in the sodium fluoride radiator.

It is called a proximity focusing detector because due to the radiator thickness there are series of concentric Čerenkov rings emitted, each corresponding to a different emission point located along the particle's path. In the simple case of the vertical incidence of the particle illustrated in Figure 3.8, the focusing effect is almost attained since the expansion height, H, is much larger than the radiator thickness, H_{rad}. Consequently, the ring width, $W = H_{rad} \tan\theta_c$, is negligible compared with the ring radius, R. For $\beta \simeq 1$, $W \sim 0.8$ cm for an $n = 1.050$ aerogel

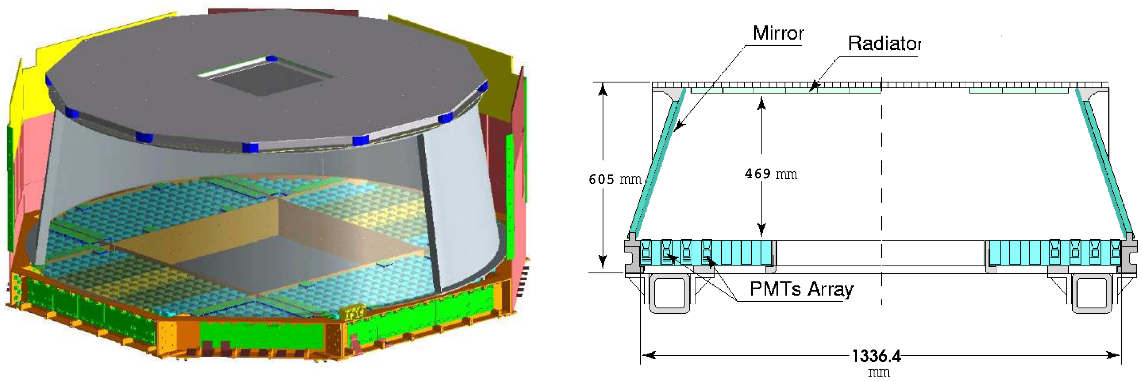

Figure 3.6: *Perspective and side-view of the RICH detector* [147].

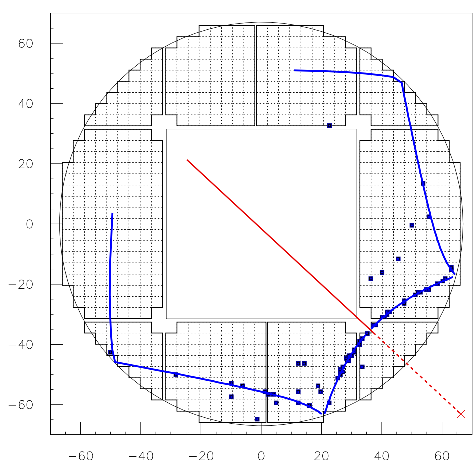

Figure 3.7: *Beryllium event with $\beta \simeq 1$ generated in the NaF radiator and detected in the PMT matrix. This pattern includes reflected and non-reflected branches. The outer circular line corresponds to the lower boundary of the conical mirror and the small squares are the photomultipliers. More details of the matrix are shown in Figure 3.25.*

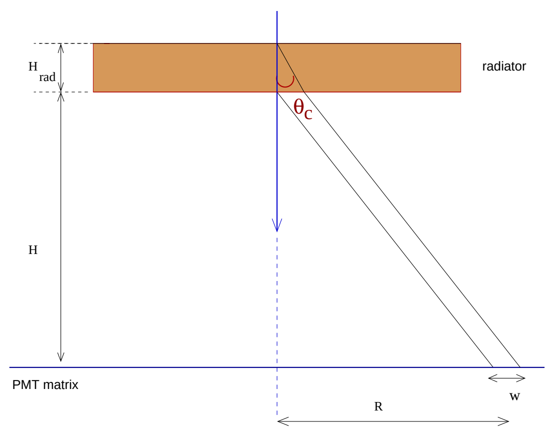

Figure 3.8: *Effect of the radiator thickness in the case of vertical incidence. Instead of a well defined ring, there are concentric rings according to the radiation emission point.*

radiator, 2.5 cm thick.

For different inclinations, W will also be a function of the particle polar angle θ and of the azimuthal angle of the photon φ.

The RICH design was drastically constrained by volume, weight (194.8 kg), power consumption (110 W), long term reliability of components, the magnetic field in the photodetector region, which will reach close to 300 G in the photodetector volume, and the amount of matter traversed since below the matrix there will be an Electromagnetic Calorimeter. The proximity focusing principle, using solid radiators and photomultiplier detectors, has been considered as the most suitable technique to meet all the requirements [148] above.

Within AMS-02, as illustrated in Figure 2.3, the RICH is located on the lower part of the spectrometer, between the lower Time-Of-Flight and the Electromagnetic Calorimeter. The RICH is being built by INFN-Bologna, Centro de Investigaciones Energéticas, Medioambientales y Tecnológicas (CIEMAT), Instituto de Astrofisica de Canarias, Laboratório de Instrumentação e Física Experimental de Partículas (LIP), University of Maryland, Florida A&M, Universidad Nacional Autónoma de México (UNAM) and Laboratoire de Physique Subatomique et de Cosmologie de Grenoble (LPSC). Its assembly has already started at CIEMAT in Spain and is foreseen to be finished in January 2008. The final integration of the RICH in AMS will take place at CERN in 2008.

3.3.1 Radiator

The radiator is a key component of any RICH detector. It determines the kinetic energy range of measurements and the velocity and charge resolution due to its optical properties.

The choice of the material for the radiator was strongly constrained by the fact that it must operate in outer space. In these conditions, a solid material is preferred to any gaseous or liquid kind of radiator by its higher robustness and simpler construction. In the domain of solid radiators the choice is not broad. Among classical materials the lower refractive index is proportioned by the sodium fluoride crystal (NaF) with $n \simeq 1.334$ which has already been used with satisfactory results in the RICH detector of the cosmic ray balloon experiment CAPRICE [149, 150]. Another possibility is offered by silica aerogel (AGL[1]) already used in the ATC of the AMS-01 flight.

The AMS-02 RICH radiator has a dual composition made of 92 square aerogel tiles with a side length of 11.4 cm, 2.5 cm thick with a refractive index 1.050 and 16 sodium fluoride tiles with the same side length and a thickness of 5 mm in the centre covering an area of $34\times34\,\mathrm{cm}^2$. The radiator tiles are supported by a 1 mm thick layer of Hesaglas [151] methacrylate ($n = 1.46$) free of UV absorbing additives. There are gaps between the aerogel tiles of 1 mm filled with black PORON walls for structure rigidity purposes. Figure 3.9 shows a scheme of the RICH radiator while the right-hand picture shows the radiator container with some assembled tiles.

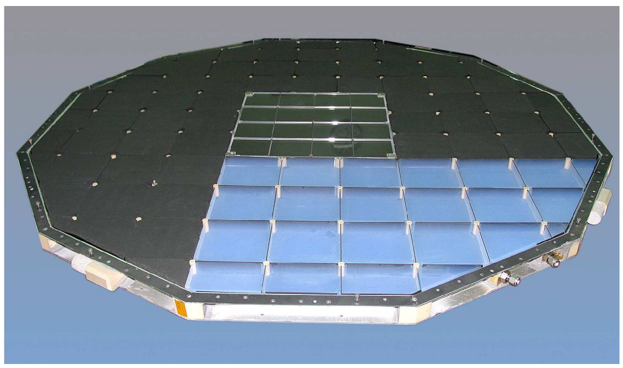

Figure 3.9: *Radiator container with part of the tiles assembled.*

The implementation of a double radiator setup constituted by sodium fluoride, with a refractive index of 1.334, in the center and aerogel tiles surrounding the sodium fluoride provides a larger acceptance and extends to lower values the particle momentum range covered overlapping with the TOF's range [58]. This will impose further constraints on the propagation models of cosmic rays, based on the measurement of the ratios D/p, ^{3}He/^{4}He and ^{10}Be/^{9}Be.

The kinetic energy per nucleon threshold is a function of the refractive index and is given by $T_{th} = \left(n/\sqrt{n^2-1} - 1\right) m$, where m is the nucleon mass. For aerogel 1.050 and sodium fluoride the thresholds are respectively, 0.5 GeV/nucleon and 2.1 GeV/nucleon. These thresholds are illustrated in both plots of Figure 3.10 as well as the Čerenkov angle (left) and the radiator light yield (right) for both radiators.

[1]This is only a short name, not to be confused with a chemical formula.

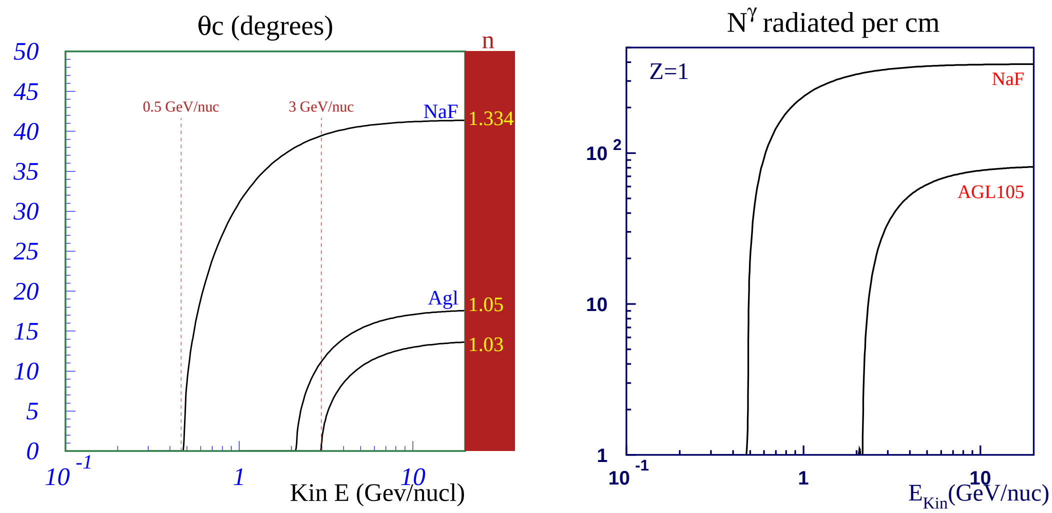

Figure 3.10: *Variation of the Čerenkov angle with the kinetic energy for different radiator materials: aerogel 1.030, 1.050 and sodium fluoride* (left).
Evolution of the number of photons that are emitted when a singly charged particle crosses aerogel 1.030 and sodium fluoride with the kinetic energy (right).

As previously mentioned, this design has the additional advantage of partially overcoming the central ECAL dead area, which is a real problem for the innermost particle impact points in a radiator only composed of aerogel.

A set of events crossing the RICH detector were simulated within the AMS acceptance, for the case of an aerogel radiator with a refractive index of 1.050, a thickness of 2.5 cm, and for an expansion volume height of 46.2 cm. The average ring acceptance, understood as the fraction of visible photons, was calculated for each event and is represented as function of the X and Y coordinates of the particle impact point in the radiator, in Figure 3.11. Events passing close to the radiator centre have low photon ring acceptances since most of radiated photons fall within the non-active detection region.

Particles reaching the radiator within 15 cm of its centre have ring acceptances lower than 22%. Moving on from the radiator centre, the ring acceptance increases. Close to the radiator borders the photon ring acceptance decreases again due to the photons escaping through the radiator edges.

Replacing the central aerogel tiles with a radiator having a higher refractive index like sodium fluoride would minimize this since particles crossing the NaF with $\beta \simeq 1$

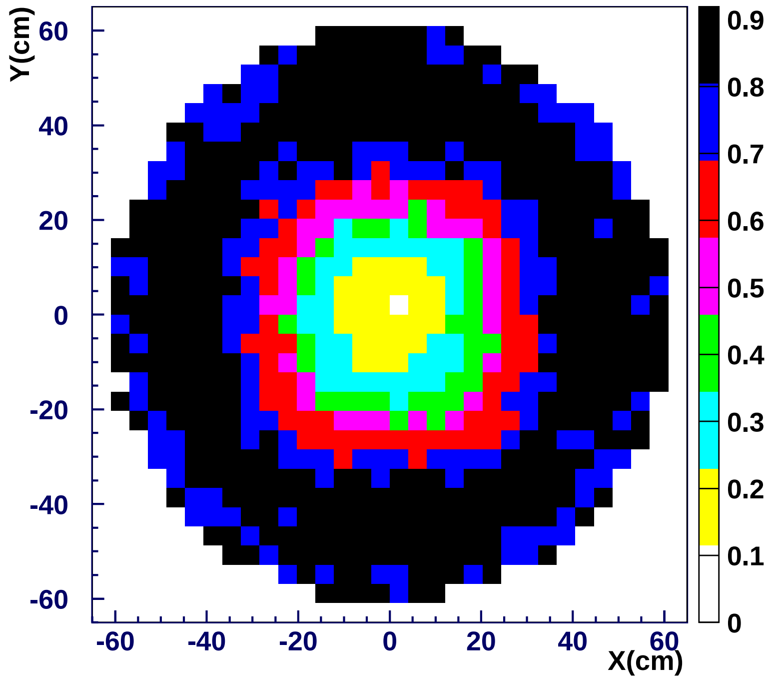

Figure 3.11: *Distribution of the average Čerenkov ring acceptance as function of the the coordinates of the particle impact point in the 1.050 aerogel radiator, for a set of events simulated within RICH acceptance.*

will radiate photons with a Čerenkov angle $\theta_c \sim 42^o$. Given the wider Čerenkov cone in NaF, the fraction of photons falling in the inactive region is minimized and consequently the reconstruction efficiency is increased.

For a more complete study on the choice of a dual composition for the RICH radiator see thesis [58].

The NaF radiator covers an acceptance of 11% of the total number of particles crossing the RICH radiator.

The presence of a sodium fluoride radiator in a particle's path contributes with 4.6% of radiation length, while aerogel contributes with 2.3%. From the point of view of the weight of the detector, critical in objects to be sent to the outer space, the sodium fluoride will contribute with 1.5 kg. The total weight of aerogel, NaF and radiator container is 16.4 kg.

For aerogel 1.050 the radiation light yield is $N_\gamma = 83/\mathrm{cm}$ for a unitary charge with

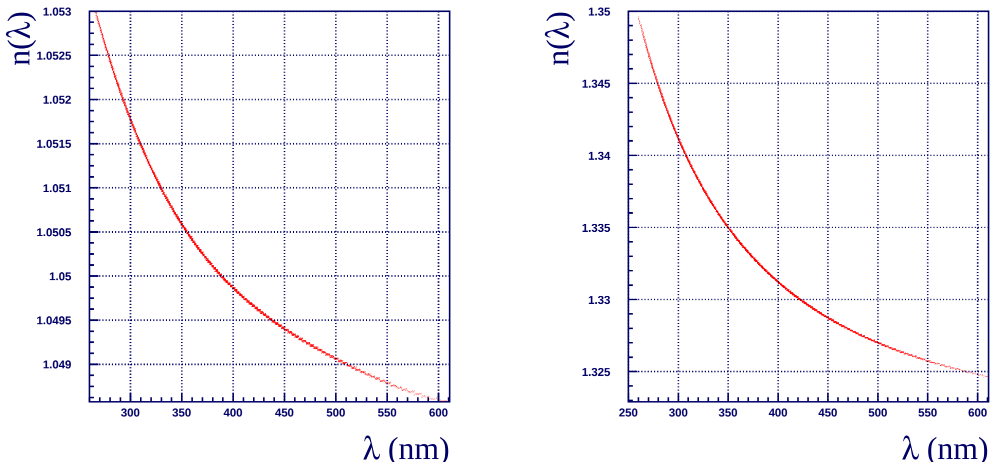

Figure 3.12: *Chromatic dispersion, used in simulation, in the aerogel* $n = 1.050$ *radiator* (left) *and in the NaF radiator* (right).

$\beta \simeq 1$ while for NaF is $N_\gamma = 389/\text{cm}$. These values are obtained from integration of equation 3.7 along the range of the Čerenkov emission energy ($\Delta E \simeq 2.4\,\text{eV}$). The right-hand plot of Figure 3.10 shows the evolution of the number of radiated photons in NaF and aerogel with the kinetic energy per nucleon of the particle.

Any optical medium is characterized by a chromatic dispersion law, which means that the refractive index depends on the wavelength λ of the photons that cross the medium ($n(\lambda)$). Consequently for θ_c comes:

$$\cos(\theta_c) = \frac{1}{\beta n(\lambda)}. \tag{3.13}$$

As a result a dispersion from the expected value of θ_c calculated using the reference value for n is observed. This is more significant for the NaF radiator than for the aerogel as can be observed in Figure 3.12. The amplitude variation of the refractive index within the detection range of the photomultipliers in the NaF is $\Delta n_{NaF} \sim 0.025$ (right), nearly six times greater than in the aerogel case (left), that is $\Delta n_{AGL} \sim 0.0044$. Figure 3.13 shows the variation of the refractive index with respect to the nominal value for aerogel n=1.050 and NaF. Therefore, the wavelength spectrum of the detected photons determines the resulting Čerenkov angle spectrum due to this radiator chromaticity. This *detected wavelength spectrum* depends not only on the intrinsic Čerenkov radiation emission spectrum of equation

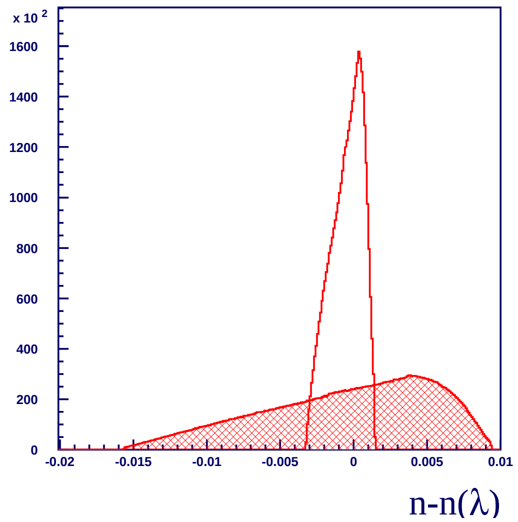

Figure 3.13: *Variation of the refractive index with respect to the nominal value both in aerogel $n = 1.050$ (plain distribution) and sodium fluoride (shaded distribution) due to the chromatic effect.*

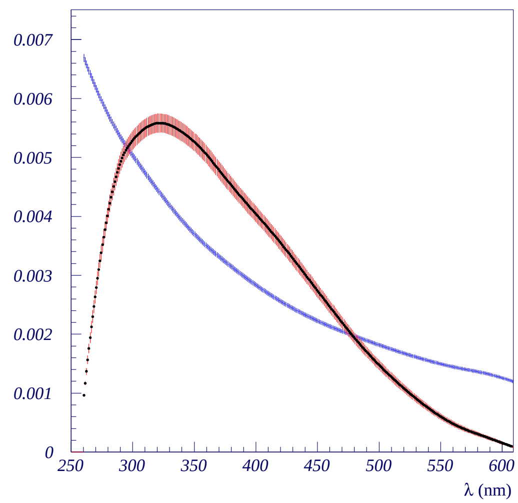

Figure 3.14: *Wavelength spectrum of the Čerenkov photons (at emission and detection). The production spectrum of Čerenkov photons is the monotonous decreasing curve ($\frac{dN}{d\lambda} \propto \frac{1}{\lambda^2}$). The convolution of this spectrum with the detection PMT efficiency spectrum gives rise to the second curve. Both spectra are normalized to unit.*

(3.10) but also on the PMT photocatode sensitivity (Figure 3.24). There are still other minor effects such as the Rayleigh scattering wavelength dependence and the absorption wavelength spectrum of the plastic foil layer below the radiator tiles that can produce some modulation on this *detected wavelength spectrum*.

In this way, considering only the convolution of the emission spectrum with the PMT efficiency spectrum of Figure 3.24, we show what would be the wavelength spectrum of the detected photons in Figure 3.14. For an easier appreciation of the change of form, both spectra are normalized to unit. Note that by decreasing of the dispersion of the photons wavelength spectrum, this convolution has a nice effect which is to attenuate the chromaticity.

Nonetheless, the chromatic effect remains and has a direct implication on the Čerenkov angle resolution, since even for a fixed particle velocity there is not a single

Figure 3.15: *Aerogel transparency.*

value for the refractive index in the Čerenkov relation:

$$\theta_c(\lambda) = \arccos \frac{1}{\beta\, n(\lambda)} \; . \tag{3.14}$$

The effect of the chromaticity in the reconstructed velocity resolution will be analysed in the next chapter.

The final choice for the aerogel is a hydrophilic aerogel produced by Boreskov Institute of Catalysis Institute in Novosibirsk (CIN) with a refractive index 1.050. The reasons for this choice will be carefully discussed in Chapter 6.

Silica Aerogel

Silica aerogels (AGL) have been produced with a broad range of refraction indices, from 1.006 to 1.14, bridging the gap between gas and solid (liquid) Čerenkov radiators. In fact traditional gas and liquid radiators have a refractive index either smaller than 1.0018 (C_5F_{12}) or larger than 1.27 (liquid C_6F_{14}) [152]. The use of silica aerogel as a radiator in Čerenkov threshold counters was suggested by M. Cantin in 1974 [153]. Since then it has been used in several Čerenkov detectors and recently in HERMES [154] at DESY, LHCb [155] at CERN and in AMS-01 [156].

Aerogel is a man-made material that could have a density as low as three times that of air. It consists of grains of amorphous silica (SiO_2) with sizes ranging from 1 to 10 nm linked together in a three-dimensional structure filled by trapped air. This structure determines an internal surface close to 1000 m^2/g that plays a key role in the chemical and physical properties. Aerogel's refractive index n can be related to its density ρ according to the known equation

$$n = 1 + k(\lambda)\rho \tag{3.15}$$

with k being a non-dimensional, wavelength dependent quantity of the order of 0.2 [157] at $\lambda = 400\,\text{nm}$. The knowledge of this coefficient is necessary for a fast and simple refractive index control during production. Density values ranging from $0.003\,\text{g/cm}^3$ to $0.55\,\text{g/cm}^3$ are available corresponding to refractive indices of $n = 1.0006$ and $n = 1.11$ respectively. The transparent look of aerogel is shown in Figure 3.15. The aerogel production in Novosibirsk [158] has started in 1986 and the first samples appeared in 1988. Nowadays silica alcogel blocks are synthesized via a two-step method from tetraethoxysilane. High-temperature supercritical extraction of alcohol solvent is performed to process wet alcogel to aerogel. Then aerogel blocks are baked at 640°C to remove organic residuals and to improve aerogel transparency.

The granular structure of aerogel with a typical length scale of few nanometers determines its optical properties. Due to this structure, photons that cross the material suffer Rayleigh scattering, losing their original direction. The macroscopic scattering cross-section is proportional to the inverse of the forth power of the photon's wavelength ($\sigma_{scat} \propto \frac{1}{\lambda^4}$) and on the other hand is the inverse of the scattering length ($\sigma_{scat} = \frac{1}{L_{scat}}$). The transmittance, t, is a measure of the fraction of unscattered photons at the exit of the radiator. It is a function of the path length crossed by the photon in the medium, according to the expression below, which is a good approximation in the photon wavelength region from 300 nm to 700 nm:

$$t(x, \lambda) = A \exp(-Cx/\lambda^4) = A \exp(-x/L_{scat}), \tag{3.16}$$

where x is the distance crossed in the radiator and A is the measured transmission in the long-wavelength region. The interaction length is given by $L_{scat} = \frac{\lambda^4}{C}$ where the coefficient C, called the clarity coefficient, is a measure of the material transmittance. The greater the clarity coefficient the lower the transmittance. The NaF has a negligible clarity coefficient and the chosen aerogel has a value of $0.0052\,\mu\text{m}^4\text{cm}^{-1}$ [159].

The bluish haze that surrounds aerogel samples is an effect of the Rayleigh scattering since short wavelengths are the most severely affected by the continuous scattering mechanism. Therefore, an important concern associated with the design and construction of a RICH detector with an aerogel radiator is if the Čerenkov photons that transverse the aerogel without any scattering are in sufficient number to allow the measurement of their emission angle with the expected accuracy. The fraction

R_γ of photons with wavelength λ that come out undeflected from the radiator after being produced is given by

$$R_\gamma = A\lambda^4(1 - \exp(-CL/\lambda^4))/CL. \tag{3.17}$$

In fact, from expression 3.12 the total number of photons produced along the aerogel length L is expressed by

$$\frac{dN_\gamma^{rad}}{dx} = K \Leftrightarrow N_\gamma^{rad} = K\int_0^L dx = KL; \tag{3.18}$$

while the total number of photons produced along the aerogel and crossing out the tile without suffering Rayleigh scattering is given by

$$dN_\gamma^{no\ scat} = K\bar{p}_\gamma dx \tag{3.19}$$

where $\bar{p}_\gamma$ is the probability of a photon being produced at a depth x and do not interact in the radiator which can be written as $\bar{p}_\gamma = Ae^{-(L-x)/L_{scat}}$. Considering the interaction length $L_{scat} = \lambda^4/C$, the following result may be obtained

$$dN_\gamma^{no\ scat} = KAe^{-(L-x)/L_{scat}}dx. \tag{3.20}$$

Evaluating the integral along all the crossed distance L the previous expression can be expressed as

$$N_\gamma^{no\ scat} = KAe^{-l/L_{scat}}\int_0^L e^{x/L_{scat}}dx = N_\gamma^{no\ scat} = KA\lambda^4(1 - \exp(-CL/\lambda^4))/C. \tag{3.21}$$

Finally R_γ is obtained as

$$R_\gamma = \frac{N_\gamma^{no\ scat}}{N_\gamma^{rad}} = A\lambda^4(1 - \exp(-CL/\lambda^4))/CL. \tag{3.22}$$

Photons can also be absorbed in the radiator material. In aerogel the absorption is negligible compared with Rayleigh scattering. In fact, the absorption rate is two orders of magnitude below the scattering rate so it can be neglected in a first approach [160]. In NaF, absorption would be the only significant interaction that photons can suffer but negligible since the radiator thickness is very small compared to the absorption length ($L_{abs} \sim 100\,\mathrm{cm}$).

Another photon dispersion effect present in silica aerogel is the forward scattering (FS) effect (Mie effect). In contrast to the nearly isotropic Rayleigh scattering, the anisotropy in the dielectric constant of the medium causes a light scattering which is strongly forward peaked, as suggested by its name. FS is responsible for the sometimes fuzzy or deformed images of objects viewed through aerogel. This surface effect was first studied in reference [161] and studied in detail in reference [162]. According to these references, forward scattering comes mostly from the boundaries of the aerogel tile crossed by light and affects a large fraction of the Čerenkov photons in the whole wavelength range. For each photon refracted out of the radiator a probability P_{FS} of scattering on a surface cluster was assigned. In this case, the photon suffers forward scattering with an angular distribution according to $P(\theta) = (\sin\theta/\delta\theta^2)\exp(-\sin^2\theta/2\delta\theta^2)$.

Aerogel optical measurements

For a good resolution on the velocity measurements to be attained several aspects concerning the aerogel tiles have to be controlled since they will operate in space for a long term. Several measurements of the optical properties of the aerogel (clarity and refractive index) have been done at LPSC, Grenoble and at CIEMAT, Madrid. The aerogel ageing, as well as an intensive study on the effect of thermal variations and mechanical vibrations in the mentioned properties was carried both at CIEMAT and UNAM.

An experimental setup to measure the aerogel transmittance was mounted in CIEMAT. It is composed of a support wheel housing 4 aerogel samples placed in vacuum, a LED, a spectrophotometer CARY-Win-UV sensitive to photons' wavelengths in the range $200-800\,\text{nm}$ and a PC. The apparatus is illustrated in Figure 3.16.

Left-hand plot of Figure 3.17 shows the adjusted function of the form presented in 3.16 to the data points of the transmittance variation with the photon wavelength for a sample of aerogel $n = 1.030$ from Novosibirsk. The results for the maximum transmittance (A) and clarity (C) coming out from the fit to the data points for the three aerogel samples from Novosibirsk and Matsushita manufacturers are shown in Table 3.1. The sample that presents the best clarity value is the Matsushita aerogel.

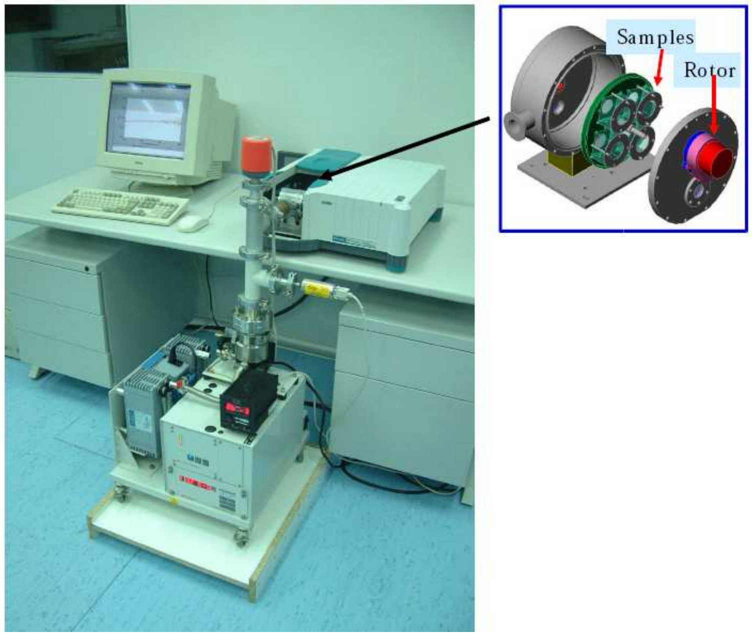

Figure 3.16: *Transmittance measurement setup.*

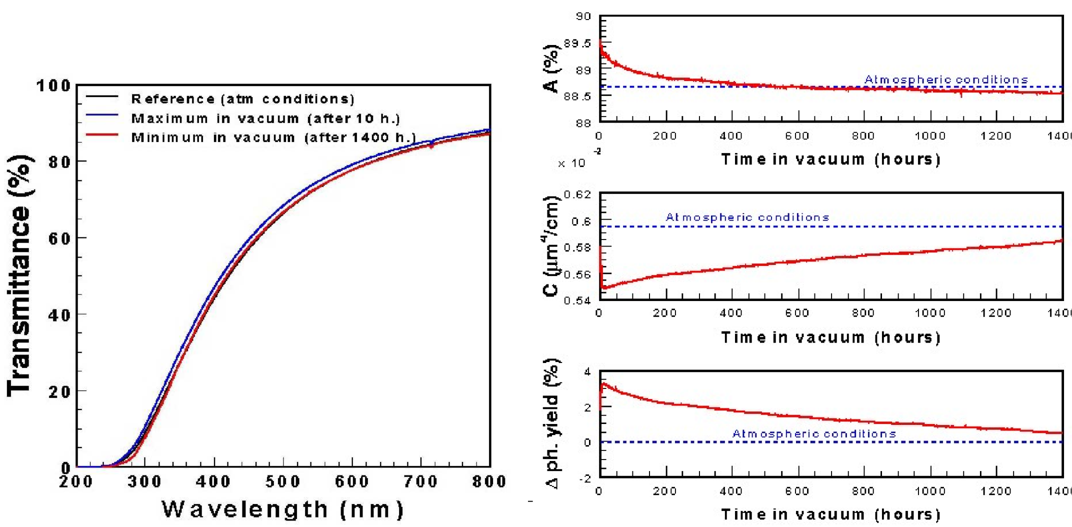

Figure 3.17: *Spectrum of the transmitted light through the aerogel sample from Novosibirsk* $n = 1.030$ (left). *Aerogel ageing curves* (right).

Manufacturer	n	$A \pm \sigma_A$ (%)	$C \pm \sigma_C$ (μm^{4}cm^{-1})
Novosibirsk	1.030	94.77±0.27	0.00509±0.00003
Matsushita	1.030	96.79±0.98	0.00379±0.00012
Novosibirsk	1.050	97.02±0.38	0.00524±0.00005

Table 3.1: *Maximum transmittance and clarity measured in laboratory for the three aerogel simples from Novosibirsk and Matsushita manufacturer* [163].

The variation of maximum transmittance and clarity with time, which is generically called the *aerogel ageing* was also measured.

The results show a degradation on clarity of $0.05 \times 10^{-2}\,\mu$m^{4}cm^{-1}year^{-1} which corresponds to 10%/year. This leads to a decrease on the number of radiated photons lower than 3%.

The aerogel refractive index was also measured and this procedure will be described in Chapter 9.

3.3.2 Mirror

A high-reflectivity mirror surrounding the whole RICH expansion height was included to increase the device acceptance. Around 33% of the photons produced in the aerogel point outside the detection matrix. The inclusion of a high reflectivity mirror recovers a great majority of these photons.

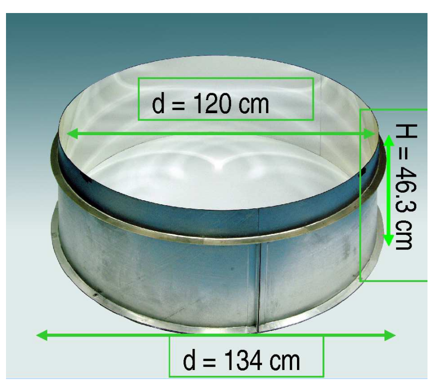

Figure 3.18: *RICH conical mirror.*

The RICH mirror has a truncated conical structure with an expansion height of

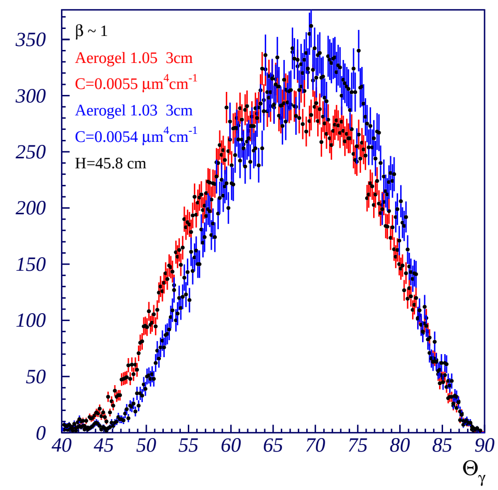

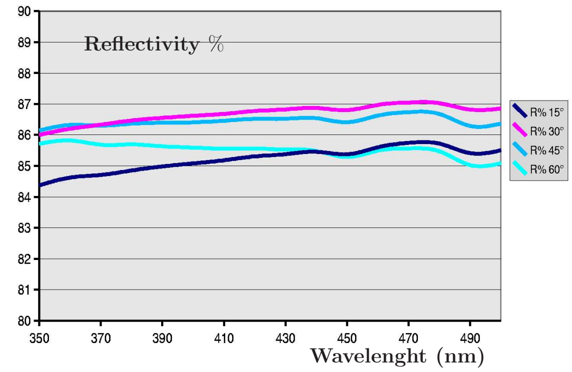

Figure 3.19: *Photons' incident angle at the mirror in the flight setup, events within AMS acceptance* (left). *Mirror reflectivity measurement in the laboratory as function of the photon wavelength for different incident angles: 15°, 30°, 45°, 60°* (right).

46.3 cm, a top radius of 60 cm and a bottom radius of 67 cm. It weights around 3.5 kg and is illustrated in Figure 3.18. It consists of a carbon fiber reinforced composite substrate with a multilayer coating made of aluminium (100 nm) and silicon dioxide, SiO_2, (300 nm) vacuum deposited on the inner surface.

The reflector is produced in 120° composite segments, which are framed with composite ribs at the entire perimeter of the mirror. It is made using a replica technique using a mandrel (a die) on which the carbon fiber plies are positioned before being cured. The mandrel and plies are oven cured under vacuum. The polishing process consists of covering the mirror surface with a thin layer of resin (a few tenths of a millimeter), epoxy, to eliminate as much as possible the roughness of the carbon fiber (≤15 nm). After a second cure process, the mechanical part of the lateral surface is ready. Next, the flanges and the ribs are glued to the lateral surface using the mandrel as a reference. The three sectors are produced and assembled. The final step is the coating by the electron gun method, the most experienced method, to guarantee deposition uniformity. This ensures a reflectivity higher than 85% for 420 nm wavelength photons.

Figure 3.19 (left) shows the photons' incident angle with respect to the normal

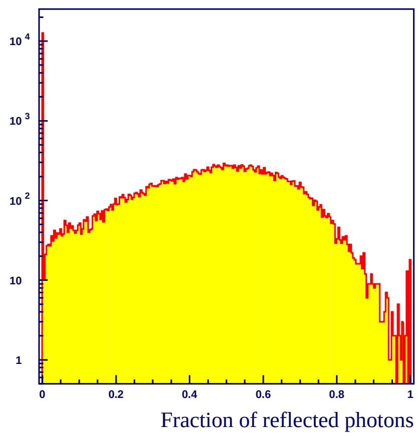

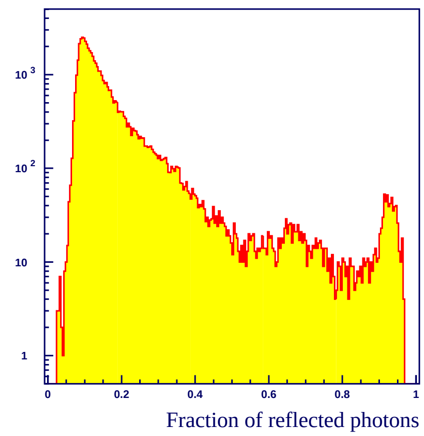

Figure 3.20: *Fraction of reflected photons at the detection matrix (at the top light guides level) generated by a sample of particles generated in the AMS acceptance, with $\beta \simeq 1$ in aerogel 1.050* (left) *and sodium fluoride* (right) *together with an expansion volume height of 46.2 cm. (Mirror reflectivity=0.85).*

to the mirror surface in the flight setup, for events with $\beta \simeq 1$, simulated within AMS acceptance impacting in two types of aerogel radiator: CIN1.050 $C = 0.0055\,\mu\text{m}^4\text{cm}^{-1}$ and CIN1.030 $C = 0.0054\,\mu\text{m}^4\text{cm}^{-1}$. The maximum incidence is around 65° for the flight configuration. Right-hand plot of the same Figure presents the mirror reflectivity measurement in the laboratory as function of the photon wavelength for different incident angles: 15°, 30°, 45°, 60°. The measurements confirm the expectations, a reflectivity higher than 85% for most of the wavelengths for photons with an incident angle of 60° is attained.

Figure 3.20 presents the fraction of the photon generated by a particle with $\beta \simeq 1$ that reaches the PMT readout matrix after suffered reflection. In the sodium fluoride case, all the events have reflected photons due to the larger emission angle ($\theta_c \sim 41°$). In aerogel around 70% of events have reflected photons.

3.3.3 Light guides and detection cells

In order to reduce dead areas between adjacent photomultipliers and consequently to increase the photon collection efficiency, an array of light guides was added, coupled to each photomultiplier. A light guide unit is a pyramidal polyhedron composed

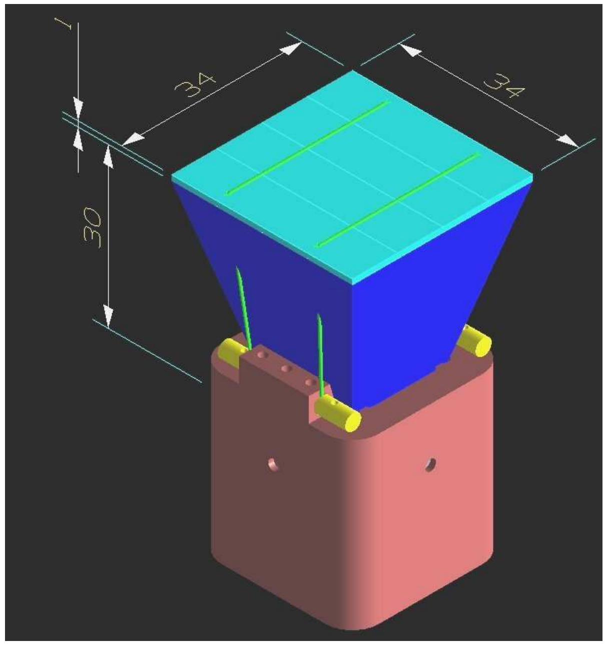

Figure 3.21: *PMT housing plus light guide* [131].

of 16 independent, plastic tubes glued on a plastic plate. The tubes are made of an acrylic plastic free of UV absorbing additive (DIAKON LG 703) [126] with a refractive index of 1.49 close to the one of the PMT window (n = 1.5). These characteristics were chosen to obtain a transmittance as high as possible over the wavelength range of the PMT detection (from ∼300 to 650 nm), a low density to minimize the weight of the whole structure and a thermal expansion coefficient small enough to withstand temperature gradients without significant deformation.

A schematic insertion of the light guide with a PMT is shown in Figure 3.21 and a picture of the entire detection cell is presented in Figure 3.22. The cell fits inside a shielding tube to protect the PMT from the stray magnetic field (300 G) that is not shown in the last picture. Despite the purpose of reducing the dead areas between adjacent PMTs there are gaps of 3 mm even at the top of the light guides because of the presence of the shielding and to mechanical assembly reasons.

The 16 pieces that compound the light guide, with three different shapes, are held together by a thin layer (1 mm) on the top made of Hesaglas acrylic [151]. Inside the light guide, photons are conducted by internal reflections. The light guide unit is optically coupled to the active area of phototube cathode through a 1 mm flexible

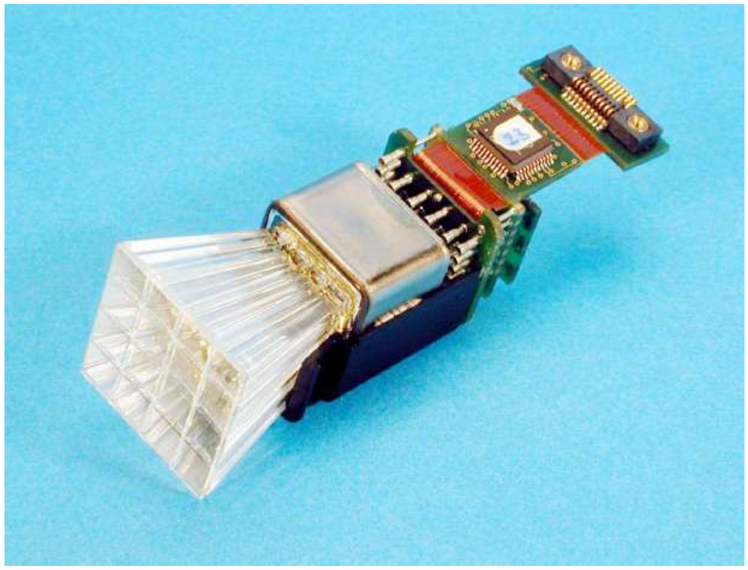

Figure 3.22: *Detection cell including PMT, front-end electronics, light guide matrix and (half) housing shell* [148].

optical pad. With a total height of 31 mm, a total volume of 13 cm^3 and a collecting surface of $34\times34\,mm^2$, it presents a readout pixel size of 8.5 mm. The optimum dimensions have been determined to maximize the photon collection efficiency.

The light guide is mechanically attached through nylon wires to the photomultiplier polycarbonate housing. The housing has been designed to ensure the alignment of the photomultiplier pixels and the light guide within the shielding cells.

3.3.4 Photomultipliers

The detection matrix is composed of 680 photomultiplier tubes (PMTs) that withstand moderate magnetic fields. The Hamamatsu R7600-00-M16 [164] was the chosen photomultiplier for the AMS-02 RICH due to the reduced size, fast response under low operational voltage (800 V), large anode uniformity and low sensitivity to external magnetic fields [126]. Also required are a good tolerance to night/day temperature variations in space, a good resistance to vibration and feasible operation in vacuum. On the other side, RICH operating principles require a PMT with a high quantum efficiency, a precise spatial resolution for velocity resolution purposes, a good single photoelectron resolution and a linear response in a wide range of charges for a charge identification at least until the iron.

The photomultiplier selected is the 4×4 multianode R7600-00-M16 from Hamamatsu, with a sensitive zone of $4{\times}4\,\mathrm{mm}^2$ and a pitch of 4.5 mm. The photocathode is a bialkali with a borosilicate window. It provides a single photoelectron response. The chromatic range of counter will be limited at short wavelengths by the cutoff of the borosilicate window, the spectral response is from 300 to 650 nm, with the maximum at $\lambda = 420\,\mathrm{nm}$, according to the curve shown in 3.24. Considering the wavelength spectrum of the radiated Čerenkov photons, taking into account the chromatic dispersion, $n(\lambda)$, which is more relevant for the NaF case, the average quantum efficiency comes

$$< \epsilon_{\mathrm{Q.E.}} >= \frac{\int_{\lambda_{min}}^{\lambda_{max}} \epsilon_{\mathrm{Q.E.}} \frac{1}{\lambda^2} \left(1 - \frac{1}{\beta^2 n(\lambda)^2}\right) d\lambda}{\int_{\lambda_{min}}^{\lambda_{max}} \frac{1}{\lambda^2} \left(1 - \frac{1}{\beta^2 n(\lambda)^2}\right) d\lambda} \tag{3.23}$$

which gives for $\beta \simeq 1$ particles in aerogel a mean quantum efficiency $< \epsilon_{\mathrm{Q.E.}} >= 0.1443$ and for the sodium fluoride $< \epsilon_{\mathrm{Q.E.}} >= 0.1444$. These values were computed from a simulation that took into account the chromatic effect and the Hamamatsu curve shown in 3.24. Figure 3.14 already introduced the wavelength spectrum of the detected photons.

When photons strike the photocathode window and the excited electrons in the valence band get enough energy to overcome the vacuum level barrier, they are emitted into the vacuum as photoelectrons. The charge amplification is obtained due to a chain of 12 dynodes which results in a gain of the order of 10^6 for an applied voltage of 800 V. The single photoelectron resolution is ∼0.7 and a large dynamical range is ensured for charge separation with the RICH.

The RICH photomultipliers will operate with a high stray magnetic field (∼300 G) so they have to be surrounded by a shielding case made of soft iron and a diamagnetic material (VACOFLUX 50). Therefore each unit of the photon detection system as shown in Figure 3.23 consists of a photomultiplier coupled to a light guide, high voltage (HV) divider plus front-end (FE) electronics, all housed and potted in a plastic shell and then enclosed in a magnetic shielding with a thickness varying from 0.8 to 1.2 mm according to the matrix position (see right-hand scheme of Figure 3.25).

The matrix is composed of different modules: square (with 143 cells) and triangular (with 27 cells) with gaps between them. As aforementioned there is a non-active area at the centre to insert the electromagnetic calorimeter (ECAL), which is a square with a side length of 63 cm. The detail of the matrix is represented in left-hand scheme of Figure 3.25.

Complete detection cells as depicted in Figure 3.23 were tested in a vibration table to ensure that they can support the acceleration during landing and take-off. The tested devices broke between 19 and 27 g_{rms}, which is more than 3 times the required qualification values.

3.3.5 Front-End Electronics

Figure 3.22 shows three printed circuit boards on the base of each PMT which form a 80 MΩ HV resistor divider which provides the bias for each dynode of the phototube, optimizing the power consumption and maintaining a very high linearity. A special ASIC (Application Specific Integrated Circuit) was developed and mounted on a forth board connected by a flexible kapton cable. It contains 16 channels of a charge preamplifier which feeds an RC-CR shaper and a sample & hold circuit, which fixes the maximum of the shaped signal. In order to increase the resolution for small signals, an amplifier with a gain ×1 or ×5 was added. A track-and-hold system allows the 16 channels of the PMT to be multiplexed, encoded in sequence, and

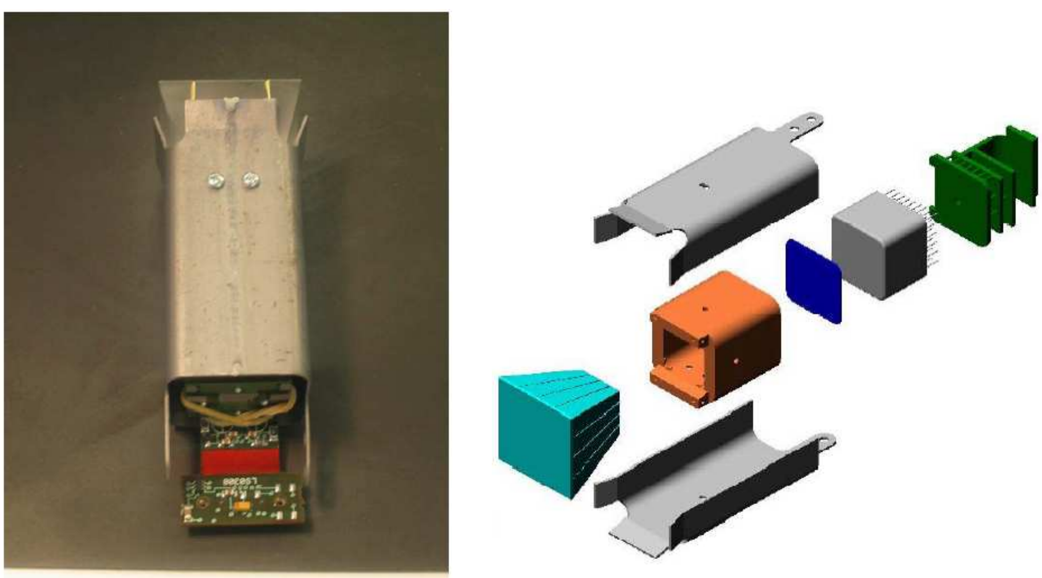

Figure 3.23: *The photon detection system* (left) *and an exploded view of the main components* (right).

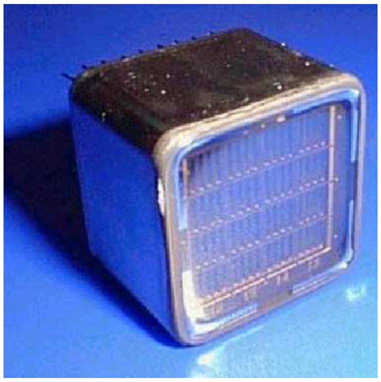

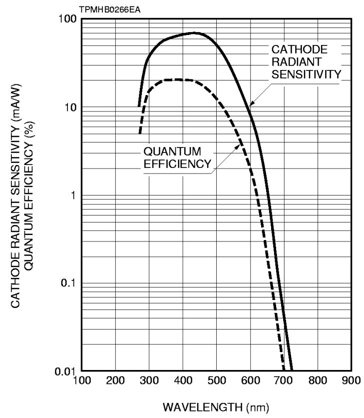

Figure 3.24: *The R7600-00-M16 Hamamatsu PMT* (left). *PMT quantum efficiency variation with the detected wavelength* (right) [164].

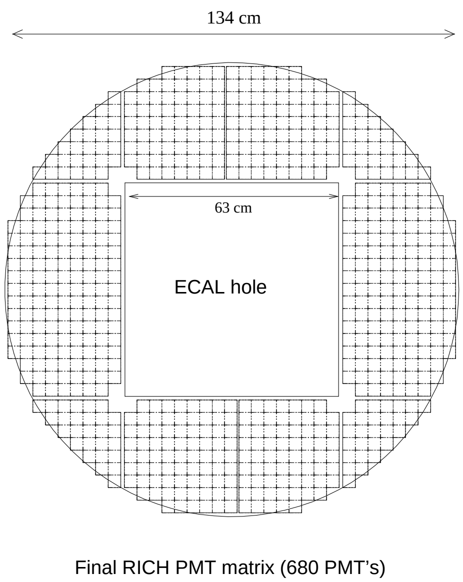

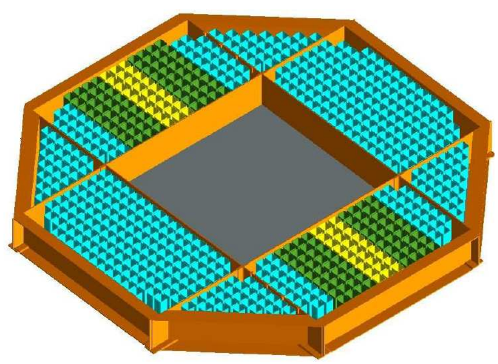

Figure 3.25: *Top view of the RICH PMT matrix (680 PMTs): detail of the matrix with the active parts and the inactive ones: ECAL hole, module gaps* (left). *Distribution of the shielding thickness depending on the magnetic field intensity: Yellow cells Thickness = 1.2 mm; Olive cells Thickness = 1.0 mm; Cyan cells Thickness = 0.8 mm*

read by the ADC (Analog to Digital Converter) [165].

3.4 RICH Standalone Simulation with GEANT 3.21

The RICH detector was fully simulated through the GEANT3.21 package, available in [166] and supported by CERN. This code has been updated several times whenever there was a design modification or a new parameter definition for the selected materials of the detector. The main idea was to develop a simulation package as close to reality as possible.

Different geometry configurations established for the flight setup, as well as for the different configurations with a RICH prototype that will be referred in Chapter 5 were implemented and the physical processes, namely Čerenkov radiation, photon scattering and absorption, were simulated. For example, all the optical properties of the aerogel like refractive index and clarity measured in laboratory were defined in the simulation.

The generated events, when not specifically described for a dedicated study, are isotropically distributed on the solid angle (before applying AMS acceptance) and uniformly distributed on the primary impact plane. A generated particle with $\beta > 1/n$ is propagated along the radiator material and generates Čerenkov photons along its track. Each photon is followed step by step until it is detected in the photomultiplier matrix. The photomultipliers' response is also simulated with a statistical function that will be introduced in Chapter 9. At the detection level a simulated event is characterized by its hit coordinates (X_i,Y_i) and by the signal of each hit (S_i).

The importance of this standalone simulation package was notorious for the optimization of several parameters of the detector like the dual radiator optimization [58]: the dimensions and the thickness of each radiator; the expansion height determination; the size of the light guide among others.

The RICH simulation was intensively used on this thesis to test the velocity and charge reconstruction algorithms that will be presented in the next chapter, to perform an evaluation of the charge systematic errors, to preview the effect of some geometry modifications and to study the detector physical prospects after some parameter variation. Two examples of the two last mentioned points are presented next. The radiator inner walls effects on the photon ring acceptance is an example of the first, while the effect of the refractive index random spread on isotope separation illustrates how this simulation can be used to foresee the detector capability with a change in the refractive index.

3.5 Design Studies

Effect of the Radiator Inner Walls on Ring Acceptance

As was described before there are opaque gaps between the aerogel tiles of 1 mm filled with black PORON foam for structure rigidity purposes. This does decrease the Čerenkov ring acceptance which is defined as the fraction of visible photons in the detection matrix. The ring acceptance takes into account the radiator outer and inner walls, the photons lost due to total reflection, the mirror reflectivity and the matrix non-active area. A deeper explanation of this concept will be introduced in the next chapter at the moment of the charge reconstruction method description, document [58] presents the subject carefully.

The idea of this study is to quantify the reduction in the number of photons due to existence of radiator walls. An *a priori*, geometrical crude and conservative calculation can be done. This is in the sense that the worst case will be taken.

Scheme 3.26 represents a side view of a radiator tile with a length L and a thickness t, as well as the contiguous tile with a wall in the middle of them. First, a particle is considered as impacting on the top of the radiator in a point D cm far from the tile edge with an inclination θ and it is assumed that all photons are radiated from the top. The idea is to calculate the percentage of events with a reduction of any amount in their photon ring acceptance due to the loss in the walls where the photons would be absorbed. With this purpose the next step is the calculation of the *active surface* defined as the tile area in which all the impacting particles would generate fully contained photons in the same tile. Assuming D_{100} as

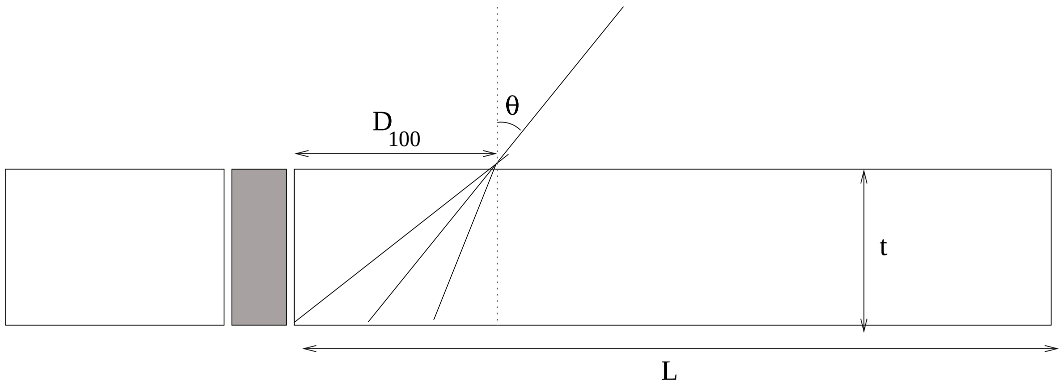

Figure 3.26: *Scheme of two contiguous aerogel tiles with a block of black PORON foam between them. Not drawn to scale.*

the impact point distance from the tile edge where this condition is fulfilled comes

$$D_{100} = t \tan\theta + t/\cos\theta \tan\theta_c \cos\theta = t(\tan\theta + \tan\theta_c). \tag{3.24}$$

Assuming $t = 3\,\mathrm{cm}$, $<\theta> \simeq 20^{\mathrm{o}}$ (mean value of distribution 3.5) and $\theta_c \sim 13.86^{\mathrm{o}}$ $(n = 1.03)$ follows

$$D_{100} = 0.61\,t\,[\mathrm{cm}] = 1.83\,\mathrm{cm} \tag{3.25}$$

and finally for the *active surface*, S_a and for the *total surface*, S_t,

$$S_a = (L - 2D_{100})^2 \tag{3.26}$$

$$S_t = L^2 \tag{3.27}$$

which straightforward gives the *inactive surface*, S_i

$$S_i = 4D_{100}(L - D_{100}) \tag{3.28}$$

In fact,

$$\frac{S_i}{S_t} = \frac{4D_{100}(L - D_{100})}{L^2} = 54\% \tag{3.29}$$

however this is the worst case in the sense that only particles with an azimuthal angle ϕ that makes them point outside the tile are being considered. In fact, for the same impact region considered as inactive there are particles impacting with opposite values of ϕ that would generate fully contained rings. We can roughly multiply this value for 1/4 which allows to conclude that around 13.5% of the events are somehow affected, losing part of their photons. However, in order to have a more feasible answer to the aforementioned effect a complete simulation of the radiator PORON gaps was done and compared with the case with no PORON.

- Simulated radiator: Matsushita aerogel
  - Tile radiator pitch = 11.4 cm
  - Refractive index = 1.03
  - Clarity = $0.0058\,\mu\mathrm{m}^4\mathrm{cm}^{-1}$
- Expansion height: 46.3 cm
- Polyester foil: 1 mm thick
- Mirror reflectivity: 85%

Particles were generated within all the AMS acceptance and selected in order to be within the RICH acceptance.

Figure 3.27 presents two event displays of the same event impacting in the same aerogel radiator point $(-20, 51.7)$ cm represented by a dot. Both displays are a top view of the detection matrix where the particle track is also represented. On top of it, the symbols $\bullet$ and $\times$ indicate the positions at the radiator top level and at the detection matrix level, respectively. The second display also presents the double radiator configuration and each radiator tile location is discriminated. In the case represented on the left-hand the radiator tiles were simulated in a contiguous geometry while on the right the gaps between them were introduced. The first case shows, for the same track and same impact position, an event with a fully contained ring with a direct branch and a reflected branch while in the second a clear loss of photon ring acceptance is observed in the reflected branch due to the absorption of Čerenkov photons in the black PORON foam.

A set of 1×10^6 events crossing only the aerogel radiator were simulated within the AMS acceptance and in the conditions established above. The average ring acceptance was calculated for each event and is represented as function of the X and Y coordinates of the particle impact point in the radiator. Once more the gaps were simulated in one case and not in the other. Figure 3.28 depicts the result for both

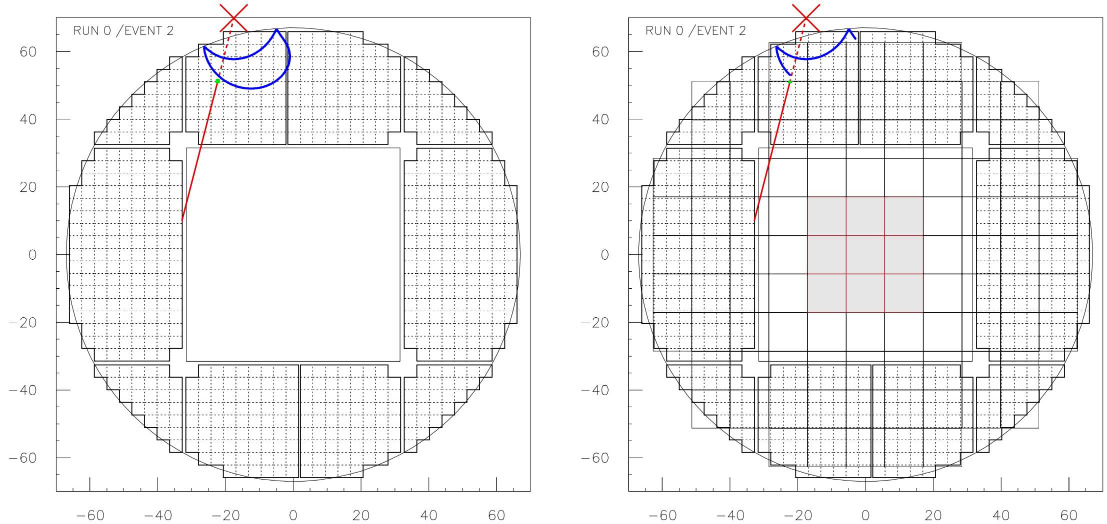

Figure 3.27: *Two displays of the same simulated event in a Matsushita aerogel radiator n=.1030, C= 0.0058 μm^{4}cm^{-1} with no black PORON walls between the tiles* (left) *and in a radiator with inner opaque walls* (right).

cases, respectively, on the left-hand and on the right-hand plots. On the left-hand the result is similar to the one presented in Figure 3.11 for the final aerogel radiator $n = 1.050$. Events passing close to the NaF radiator (closer to the center), have the lower photon ring acceptances since part of the radiated photons still fall within the non-active region. On the right-hand mapping, there is a visible additive effect which is the reduction of the photon ring acceptances correlated with a specific grid distribution that coincides with the gaps between the aerogel tiles. Particles impacting close to the gaps with incidences that differ from the vertical clearly generate events with reduced photon ring acceptance.

The next step is to quantify the photon ring acceptance reduction. Bringing this idea in mind a direct test is to look at the ratio of the calculated acceptance for the events generated in a geometry with gaps and the calculated photon ring acceptance for the case with no gaps for the same event. Both quantities are calculated in an event-by-event basis. Figure 3.29 shows this computation with all the distribution normalized to the total number of events. It is visible that 11% of the events have their acceptance reduced by any amount due to the presence of the radiator

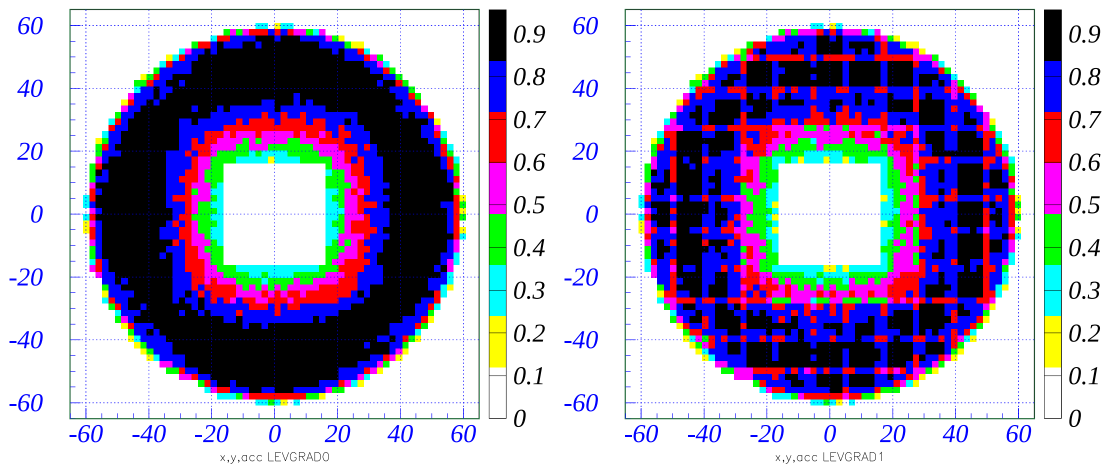

Figure 3.28: *Čerenkov ring acceptance distributions according to the impact coordinates for aerogel 1.030 both in the case with no black PORON gaps between the tiles* (left) *and considering them* (right). *The events were generated within all the AMS acceptance and the radiator is the same described in text*

gaps. This value is obtained by counting the population below the peak of 1, which represents the amount of events that stay unaffected (89%). It is directly read from the plot that 2% of events with null acceptance are introduced in the case of the geometry with gaps while it is computed an average acceptance reduction around 8%. This value is much more optimistic and realistic than the conservative geometric calculation.

The relevance of the mirror presence for aerogel events comes out from the analysis of the mirror acceptance distribution illustrated in Figure 3.30 (left). In the simulated aerogel together with the described geometry around 60% of the events have reflected photons and 4% of the events have fully reflected patterns which can be read from the peak at zero (40%) and from the peak at one for the mirror acceptance, respectively.

In a similar way, to study the influence of the black PORON gaps in the mirror acceptance the same type of plot, representing the ratio between the calculated mirror acceptance for the events generated in a geometry with gaps and the calculated mirror acceptance for the case with no gaps for the same event, was done and is presented in Figure 3.30. Once more both quantities are calculated in an event-by-event

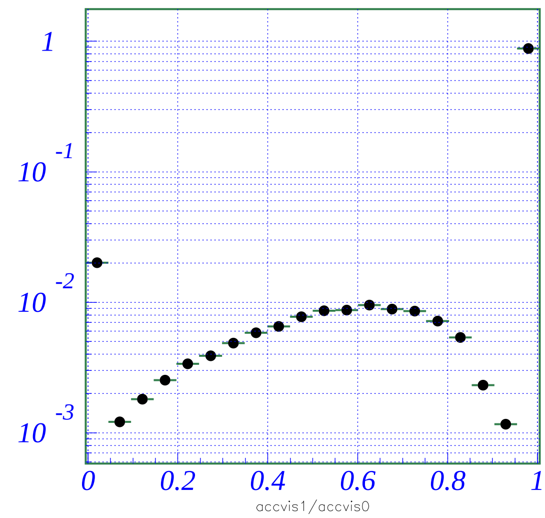

Figure 3.29: *Ratio between the visible acceptance calculated for events generated in a geometry with black PORON gaps and the visible acceptance calculated for events generated in a geometry without gaps.*

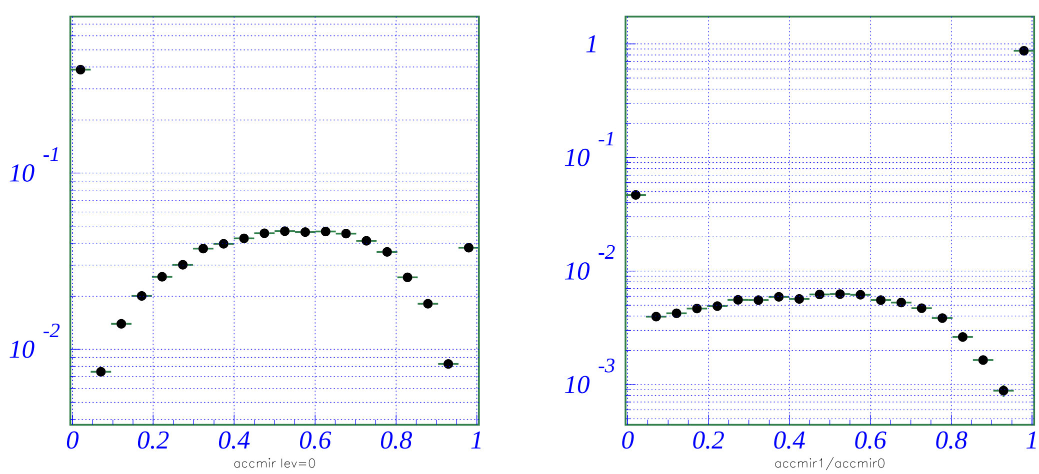

Figure 3.30: *Distribution of the mirror acceptance computed from reflected patterns generated in an aerogel radiator* $n = 1.03$ (left). *Ratio between the mirror acceptance calculated for the events generated in a geometry with PORON black walls and the visible acceptance calculated for the events generated in a geometry without PORON* (right).

basis. Figure 3.30 (left) shows this computation with all the distribution normalized to the total number of events. It is visible that 13% of the events have their acceptance reduced by any amount due to the presence of the radiator gaps. This value is similarly obtained by counting the population below the peak of 1, which represents the amount of events that stay unaffected (87%). It is directly read from the plot that 5% of events with null acceptance appear in the case of the geometry with gaps while an average acceptance reduction around 11% is computed. This reduction value is slightly higher than the reduction amount for the whole pattern but it is also not very significant.

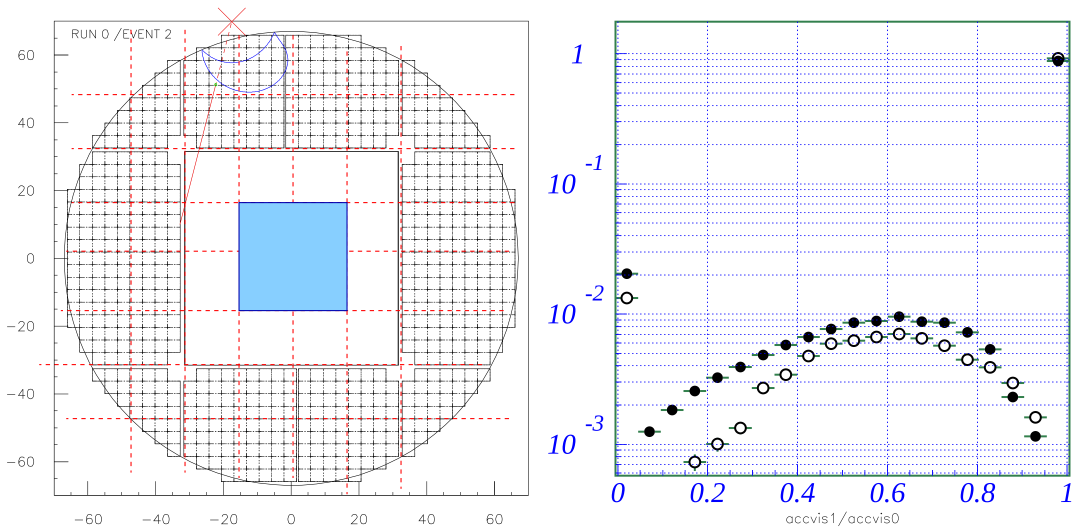

Figure 3.31: *Event display with a larger radiator tile configuration. Ratio between the visible acceptance calculated for the events generated in a geometry with PORON black walls and the visible acceptance calculated for the events generated in a geometry without PORON. The two distributions correspond to the case of a tile width of 11.4 cm (full dots) and a tile width of 17 cm (open dots).*

The final step of the study intended to observe what would happen if a larger radiator tile configuration was introduced. The studied dimension was half of the NaF square width which is around 17 cm. Figure 3.31 (left) illustrates the new radiator tile division with a dashed line. The event is the same depicted in Figure 3.27 where its previous geometry is discriminated. A smaller reduction in the photon ring acceptance is expected but it is necessary to quantify it. The same plot, representing the ratio between the calculated photon ring acceptance for events generated in a geometry with gaps and the calculated photon ring acceptance for the case with no gaps for the same event, was done. Figure 3.31 shows it in the distribution with open dots, while the distribution describing the previous geometry with smaller tiles is superimposed with full dots.

It is observed that events with reduced acceptance constitute now 8% of the total number of events instead of 11%. Now only 1.3% of the events have null acceptance while before they summed up to 2%. The average acceptance reduction in the case of a larger tile pitch is around 6%, quite close to the previous 8%.

Conclusion

The presence of opaque gaps between the aerogel tiles of 1 mm filled with black PORON foam does have an effect on the photon ring acceptance, specially for events generated by particles impacting close to the tile borders. Considering a tile pitch of 11.4 cm the simulation in the defined conditions foresees that 11% of the events lose some part of the photons compared to the case with no gaps between the tiles. An average acceptance reduction ∼8% is expected, which is not very significant since the radiator under construction has a high light yield for $Z = 1$ particles (11 photoelectrons). On the other hand, since 60% of the events falling in the RICH have reflected photons it was relevant to quantify the same reduction for these reflected photons. 13% of the events presented a reduced mirror acceptance while the average acceptance reduction amounts to 11%, which is still not very significant. The simulation predicts that an enlargement of the aerogel tile pitch to 17 cm which is half of the sodium fluoride square side length leads to 8% of the events with part of its acceptance reduced while the mean acceptance reduction is around 6%. This value does not show a great improvement and the tile enlargement does not appear to be an advantage since as was stated above 8% of acceptance reduction is not significant. Therefore, for rigidity purposes it is worth having blocks of PORON foam between the aerogel tiles which will not significantly reduce the photon ring acceptance.

Chapter 4

Velocity and Charge Reconstruction Algorithms

The human mind has first to construct forms, independently, before we can find them in things.

Albert Einstein

4.1 Introduction

This chapter introduces the two reconstruction methods for velocity and electric charge measurements developed at LIP for cosmic charged particles impacting in the RICH detector. The velocity reconstruction method was first developed by J. Borges [167] and later on optimized and tuned, while the electric charge reconstruction method was first established by A. Keating [168] and then improved in the present study. Article [169] presents an overview of both reconstruction methods.

The event reconstruction consists of the Čerenkov angle determination which directly leads to the velocity (β) measurement. The complete reconstruction algorithm will be described in detail, as well as its optimization procedure. All the uncertainties that affect the Čerenkov angle determination will be thoroughly explained in the begining of the present chapter.

The electric charge reconstruction method will be also minutely described as well as the systematic uncertainties that affect the determination of this quantity. Simulation results will be shown for both velocity and charge algorithms. Finally the conclusions will be presented.

4.2 Čerenkov angle uncertainties

The accuracy of the velocity measurement made with the RICH depends on the accuracy of the Čerenkov angle reconstruction. Aerogel and NaF show intrinsically different sensitivities to the Čerenkov angle as is explicit in the following relation derived from the Čerenkov angle relation 3.2:

$$\frac{\Delta\beta}{\beta} = \tan\theta_c \Delta\theta_c. \tag{4.1}$$

The uncertainty in θ_c ($\Delta\theta_c$) arises from different factors:

- pixel size of PMT readout matrix (ΔR_P);
- radiator thickness ($H_{rad} \Rightarrow \Delta R_T$);
- radiator chromaticity ($n(\lambda) \Rightarrow \Delta R_n$).

Consequently the uncertainty in θ_c is given by:

$$\Delta\theta_c = \underbrace{\Delta\theta_c^{pixel} \oplus \Delta\theta_c^{thick}}_{\Delta\theta_c^{geom}} \oplus \Delta\theta_c^{chrom}; \tag{4.2}$$

where $\Delta\theta_c^{geom}$ accounts for the uncertainty sources of geometrical nature (pixel size and radiator thickness) and $\Delta\theta_c^{chrom}$ accounts for the intrinsic chromaticity.

In first approximation the geometrical Čerenkov angle uncertainty estimation can be obtained from particles with $\beta \simeq 1$ impinging perpendicularly on the detector and neglecting refraction at the radiator transition. The detected photon ring width can be related to the photon arm (d) and to the transverse ring width ($\Delta R_\perp = \Delta R \cos\theta_c$) through:

$$\tan(\Delta\theta_c) \sim \frac{\Delta R_\perp}{d} \sim \frac{\Delta R \cos\theta_c}{H/\cos\theta_c} = \cos^2\theta_c \frac{\Delta R}{H}. \tag{4.3}$$

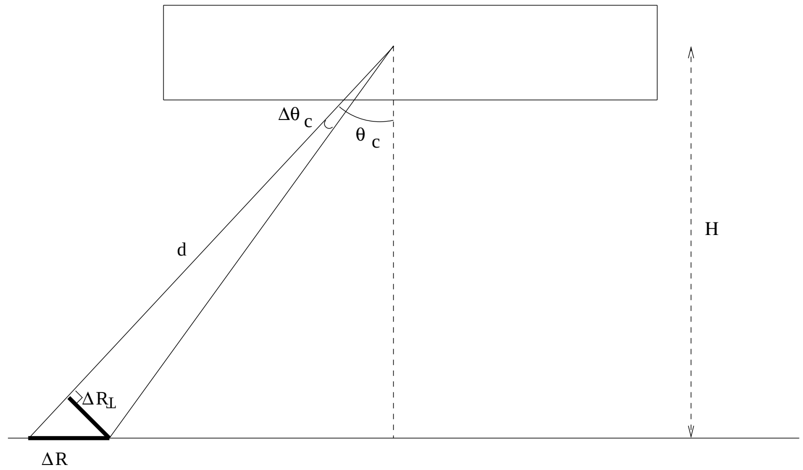

Figure 4.1: *Uncertainty of the reconstructed θ_c due to the photon ring width uncertainty.*

Given the small uncertainty in θ_c ($\Delta\theta_c \ll 1$), the error on the Čerenkov angle is obtained,

$$\Delta\theta_c \sim \cos^2\theta_c \frac{\Delta R}{H}. \tag{4.4}$$

where $\Delta R = \Delta R_P \oplus \Delta R_T$ with ΔR_P and ΔR_T being the increase of the ring width due to the pixel size effect and due to the radiator thickness, respectively.

As the Čerenkov reconstructed angle is an average on the individual reconstructions based on each detected photon of the Čerenkov pattern, the final error will be lower than the single hit contribution. In fact the error in mean angle in every event scales down with the number of photoelectrons, N, detected on the reconstructed pattern.

$$\theta_c = \frac{\sum_i \theta_{ci}}{N} \Rightarrow \Delta\theta_c = \frac{\Delta\theta_c \text{ single hit}}{\sqrt{N}} \tag{4.5}$$

From now on the refraction at the exit of the radiator will be taken into account. Therefore the ring radius can be written as:

$$\begin{aligned} R &= T\tan\theta_c + H\tan\theta_r \\ &\simeq H\tan\theta_r \qquad\qquad (T/H \ll 1) \end{aligned} \tag{4.6}$$

with θ_r representing the angle of the refracted photon at the radiator's exit. Hence, performing the derivative of the last expression and using the Snell's law the uncertainty on the Čerenkov angle can be expressed as:

$$\Delta\theta_c \approx \frac{\Delta R}{H}\frac{(1 - n^2\sin^2\theta_c)^{3/2}}{n\cos\theta_c}. \tag{4.7}$$

Radiator thickness

Since the Čerenkov detector of AMS is a proximity focusing RICH, the radiator thickness introduces a spreading of the photons on the Čerenkov ring. From Figure 3.8, for a vertical incidence, $\Delta R_T = W = T \tan\theta_c$. For aerogel 1.05 with $C = 0.0052\,\mu\mathrm{m}^4\mathrm{cm}^{-1}$ an effective thickness T_{eff} should be assumed due to the scattered photons. Assuming a uniform distribution for the photon emission along the radiator,

$$\Delta R_T = \frac{\Delta R_T}{\sqrt{12}} = \frac{\ell}{\sqrt{12}} tan\theta_c. \tag{4.8}$$

For the $n = 1.050$ aerogel radiator, $T_{eff} = 1.7\,\mathrm{cm}$ thick, $\Delta R_T \sim 1.8\,\mathrm{mm}$ while for the sodium fluoride radiator, 0.5 cm thick, $\Delta R_T \sim 1.3\,\mathrm{mm}$.

Pixel size

The pixel granularity corresponds to the cell detection areas of the light guides ($3.4\,\mathrm{cm}/4 = 8.5\,\mathrm{mm}$) and brings an error to the measurement of the hit coordinates used in the reconstruction of the ring. Consequently, the Čerenkov angle measurement is also affected. The pixel contribution for the uncertainty ΔR arises from the independent uncertainties present on each coordinate of the detected point, $(\Delta X\,, \Delta Y)$, as follows:

$$\Delta R_P = \frac{X \Delta X}{R_P} \oplus \frac{Y \Delta Y}{R_P}\,.$$

Since pixels are squared, $\Delta X = \Delta Y$ leading thus to:

$$\begin{aligned} \Delta R_P &= \Delta X = \Delta Y \\ &= \frac{\delta x}{\sqrt{12}} = \frac{0.85\,\mathrm{cm}}{\sqrt{12}} \approx 2.5\,\mathrm{mm}\,. \end{aligned} \tag{4.9}$$

Chromaticity

The chromatic effect was already introduced in subsection 3.3.1, where it was shown that it is more relevant for the sodium fluoride radiator than for the aerogel, as shown in Figure 4.2. For aerogel 1.050 $\frac{\Delta n}{n} = 0.10\%$ while for sodium fluoride $\frac{\Delta n}{n} = 0.43\%$. According to expression 4.10, for a particle with $\beta \simeq 1$ crossing the NaF radiator the dominant factor producing a larger chromatic effect in the emitted photons is

$\frac{\Delta n}{n}$, since θ_c would be higher than in aerogel for the same β. Neglecting the photon's refraction comes:

$$\begin{aligned} \Delta\theta_c &= \frac{1}{\tan\theta_c}\frac{\Delta n}{n} \\ &= \frac{1}{\sqrt{(n\beta)^2-1}}\frac{\Delta n}{n}. \end{aligned} \tag{4.10}$$

The next step will be introducing the refraction effect. On the other hand the cosine of the reconstructed Čerenkov angle can be expressed as $\cos\theta_c^{rec} = \frac{1}{\beta\bar{n}}$ with $\bar{n}$ being the average refractive index calculated within the detection range of the photomultiplier. Combining this information allows to write 4.6 as:

$$R = H\frac{\bar{n}\sin\theta_c^{rec}}{\sqrt{\bar{n}^2\sin^2\theta_c^{rec}}} \tag{4.11}$$

hence manipulating the expression and observing the geometry of Figure 4.1 leads to the following expression for the sine of the reconstructed angle

$$\sin\theta_c^{rec} = \frac{R}{\bar{n}}\sqrt{\frac{1}{R^2+H^2}} = \frac{1}{\bar{n}}\frac{R}{d}. \tag{4.12}$$

consequently the cosine is written as:

$$\cos\theta_c^{rec} = \frac{1}{\bar{n}}\sqrt{\bar{n}^2 - \frac{R^2}{d}}. \tag{4.13}$$

On the other hand from the emitted Čerenkov angle a similar expression can be written as:

$$\frac{1}{\beta n(\lambda)} = \frac{1}{n(\lambda)}\sqrt{n^2(\lambda) - \left(\frac{R}{d}\right)^2} \tag{4.14}$$

and after some manipulation the following geometrical expression can be obtained

$$\left(\frac{R}{d}\right)^2 = n^2 - \frac{1}{\beta^2} \tag{4.15}$$

and therefore

$$\cos\theta_c^{rec} = \frac{1}{\bar{n}}\sqrt{\bar{n}^2 - n^2 + \frac{1}{\beta^2}}. \tag{4.16}$$

which can be derived in order of the real refractive index leading to the chromatic uncertainty in θ_c given by:

$$\Delta\theta_c^{rec} = \frac{\beta^2 n}{\tan\theta_c^{rec}}\Delta n. \tag{4.17}$$

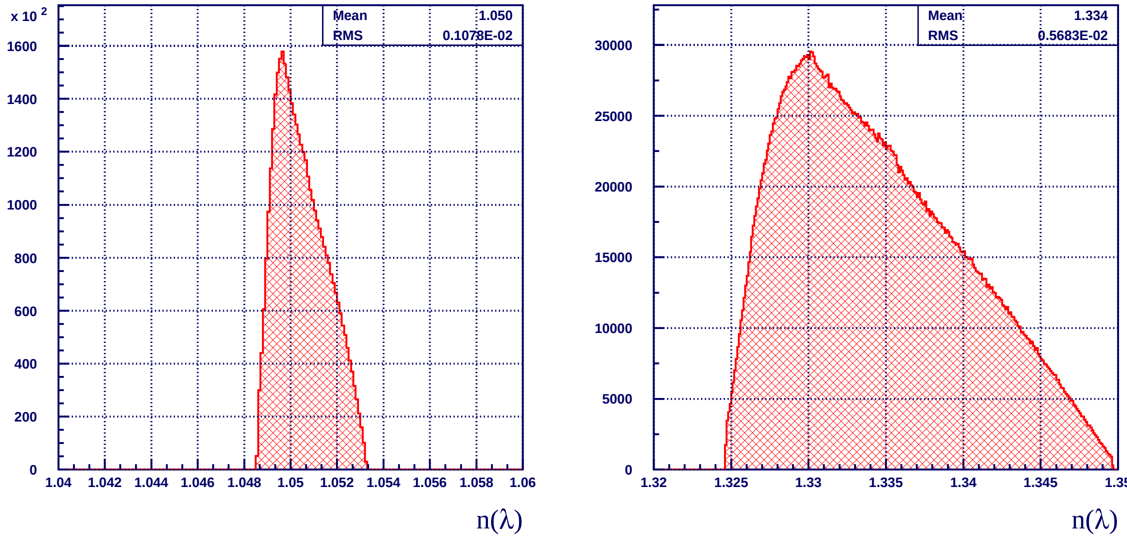

Figure 4.2: *Refractive index variation due to the chromatic effect for an aerogel radiator* $n = 1.050$ (left) *and for sodium fluoride* (right).

A Čerenkov angle uncertainty of $\sim$3.2 mrad is expected for aerogel 1.050 while for sodium fluoride a spread of $\sim$4.8 mrad is foreseen. This is in agreement with the observed uncertainty for the reconstructed θ_c ($\Delta\theta_c$) in aerogel and NaF illustrated in Figure 4.3. This distribution was obtained performing a simulation of the chromatic effect in both radiators. In this simulation Čerenkov photons were generated with a wavelength distribution law in $1/\lambda^2$ and for each of them the refractive index $n(\lambda)$ is calculated. The quantum efficiency cut is a priori applied and for each detected photon the Čerenkov emission angle is calculated.

Conclusions

To summarize the effect of all the geometrical uncertainties (radiator thickness + pixel size) and the chromatic uncertainty on the error of the reconstructed Čerenkov angle allows to write

$$\Delta\theta_c = \frac{1}{\sqrt{N}} \left[\left(\frac{(\Delta R_T \oplus \Delta R_P)}{H} \frac{(1 - n^2 \sin^2\theta_c)^{3/2}}{n \cos\theta_c} \right) \oplus \left(\frac{\beta^2 n}{\tan\theta_c^{rec}} \Delta n \right) \right] . \qquad (4.18)$$

with N being the number of photoelectrons.

The contribution of each uncertainty to the final single-hit resolution for the Čerenkov angle and velocity is summarized in Table 4.1.

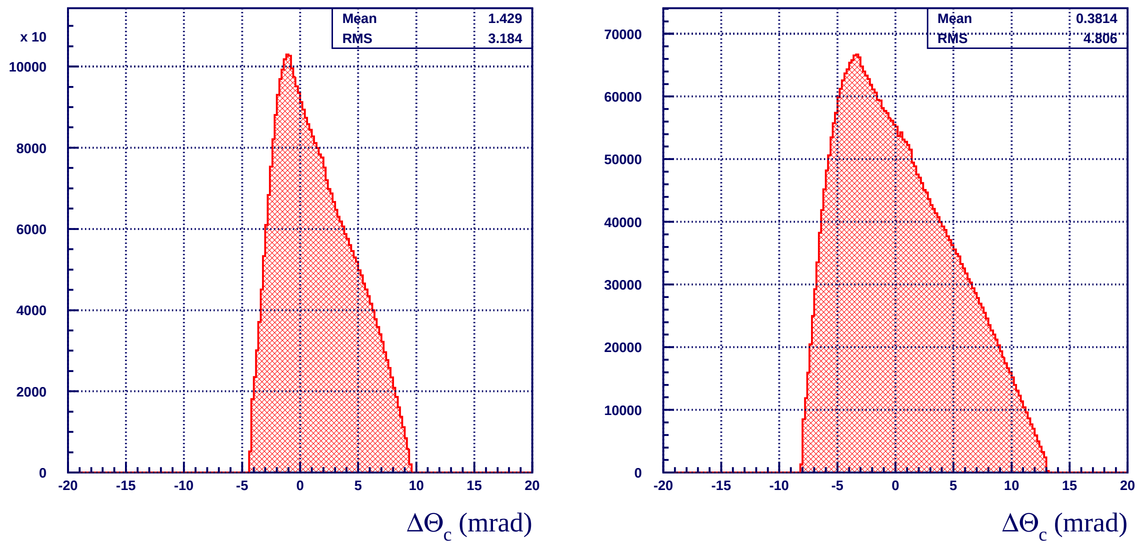

Figure 4.3: *Uncertainty of the reconstructed θ_c due to the chromaticity effect for an aerogel radiator n=1.050* (left) *and for sodium fluoride* (right). *Reconstruction for particles with $\beta \simeq 1$.*

	$\Delta\theta_c^{geom}$ (mrad)		$\Delta\theta_c^{chrom}$	$\Delta\theta_c$	$\Delta\beta/\beta$
	$\Delta\theta_c^{thick}$	$\Delta\theta_c^{pixel}$	(mrad)	(mrad)	($\beta \simeq 1$)
AGL	3.3	4.6	3.2	6.5	2.1×10^{-3}
NaF	0.3	0.6	4.8	4.8	4.2×10^{-3}

Table 4.1: *Single-hit estimated uncertainties for Čerenkov angle (θ_c) and velocity (β).*

4.3 Velocity Reconstruction Algorithm

4.3.1 Pattern fitting

The aperture angle of the emitted photons with respect to the radiating particle is known as the Čerenkov angle, θ_c, and since there is a relation 3.2, here remembered, between the charged particle velocity (β) and this aperture, β is straightforward derived from the Čerenkov angle reconstruction.

$$\cos\theta_c = \frac{1}{n\beta} \tag{4.19}$$

A charged particle with $\beta > c_{medium}$ that impacts on the top of the RICH dielectric medium of the radiator emits photons uniformly along its track. The photons are either refracted or fully reflected at the radiator's boundary, depending on their incident angle (θ_i). Those which pass the radiator can have reflections on the conical mirror and then reach the photomultiplier plane where they can be detected. Therefore, a hit pattern is produced with a geometrical ring acceptance depending on the radiator particle's impact point (I), particle's direction (θ, ϕ) and photon's aperture angle (θ_c). This is schematically represented on the following Figure 4.4.

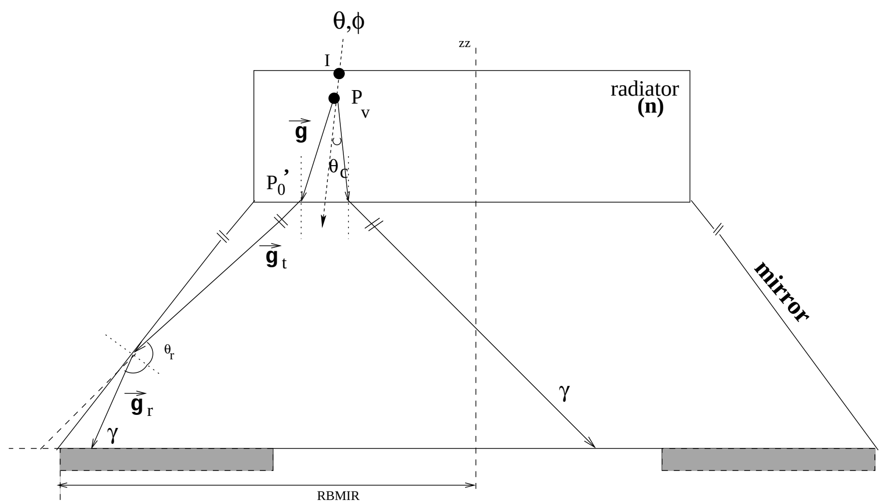

Figure 4.4: *Scheme with the photon's path length through the RICH detector. One of the photons is reflected and the other, at right, reaches directly the photomultiplier plane of the detector.*

This pattern can be regarded as a parametric function given by

$$\overrightarrow{R}_{pat}(\varphi\ ;\theta_c) \equiv \{X_{pat}(\varphi;\theta_c), Y_{pat}(\varphi;\theta_c)\}, \quad 0 < \varphi < 2\pi$$

where $\{X_{pat}, Y_{pat}\}$ are the coordinates for the points of the curve parameterized by φ. The variable θ_c is the only free parameter for the fit since the Čerenkov angle reconstruction procedure relies on the highly accurate information of the particle direction (θ, ϕ) provided by the tracker. This will correspond to the axis of the cone described by the photons' trajectories.

The procedure developed to reconstruct these patterns can be summarized as a parametric ray tracing of the trajectories of the Čerenkov photons in a simplified framework where all of them are emitted at a single point inside the radiator.

The kinematic configuration of the mother particle is described by 6 parameters: the spherical angular coordinates $\{\theta, \phi\}$ together with a point $P_v = \{x_v, y_v, z_v\}$

specify the trajectory. The velocity is given by θ_c. In our framework, all the photons will be emitted at P_v; see Figure 4.5.

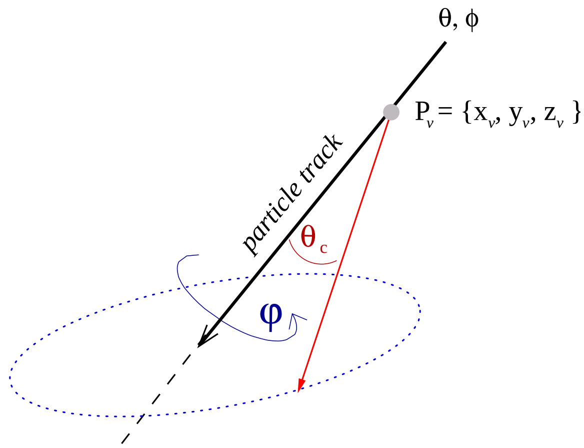

Figure 4.5: *Illustration of the photon tracing. Assigning values to the particle trajectory parameters* $\{x_v, y_v, z_v, \theta, \phi\}$*, each photon is parameterized by* θ_c *and the azimuthal angle* φ [167].

Knowing the particle trajectory parameters, and for a given value of θ_c, each photon trajectory is parameterized by a single azimuthal parameter φ ($0 < \varphi < 2\pi$). The meaning of this azimuthal angle φ is well illustrated in Figure 4.5. The photons' trajectories are traced through the detector, up to their impact points in the detection matrix. It is the intersection of these trajectories with the detection matrix that constitutes the Čerenkov fitting pattern.

Complex photon patterns can occur at the detection plane due to mirror reflected photons, as can be seen on the right-hand display of Figure 4.6. The event displayed is generated by simulated beryllium nuclei in the sodium fluoride radiator. Each touched pixel is called a hit. The θ_c reconstruction developed at LIP is based on a fit to the Čerenkov photon pattern. As depicted by the schematic draw of Figure 4.6, the idea is to find the pattern that better fits the collection of detected photons in the PMT readout matrix.

To summarize, the tracing can be seen as a procedure that takes φ as the input and gives the corresponding detection point in the matrix $\{x_d, y_d\}$ as the output. For more details on these calculations constituting the support of this tracing procedure see thesis [58]. With this tool the distances between the data points (hits) and a predicted pattern can easily be computed.

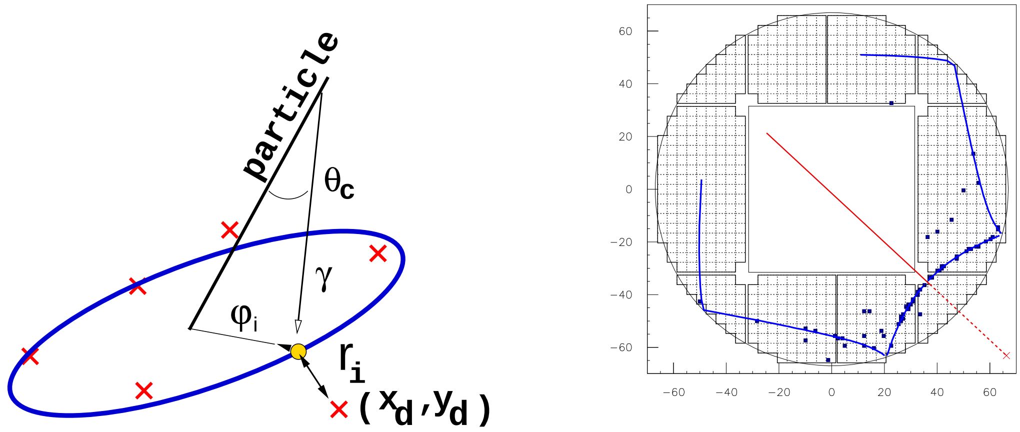

Figure 4.6: *Schematic view of an incoming particle generating hits in the PMT readout matrix that provide the input to the pattern fit* (left). *Beryllium event display generated in a sodium fluoride radiator* (right).

4.3.2 Maximum likelihood method

As was previously mentioned, the Čerenkov angle reconstruction procedure relies on the highly accurate information of the particle direction (θ, ϕ) provided by the tracker. The emitted Čerenkov photons can suffer interactions inside the aerogel radiator (Rayleigh scattering and absorption) and forward scattering at the exit of the aerogel, while in the sodium fluoride radiator photons can only suffer absorption. Outside the radiator photons can be either absorbed or reflected on the mirror and can fall in an active or non-active area of the detection matrix. Consequently, the reconstruction of the Čerenkov angle has to deal with two types of photons; those which are only slightly deviated from the expected photon pattern due to the pixel granularity, radiator thickness and chromaticity effects and those which spread all over the detector, as the photomultipliers noise. The former type corresponds to the signal that produces the Čerenkov ring. The distance of these photons to the expected pattern is almost gaussian distributed reflecting essentially the uncertainty related with pixel size, radiator thickness and chromaticity. A more careful observation of the residuals distribution computed relatively to the expected θ_c pattern for a 2.5 cm thick, 1.050 refractive index aerogel radiator with $C = 0.00512\,\mu\text{m}^4\text{cm}^{-1}$ is introduced in Figure 4.7. A structure well described by a double gaussian function is

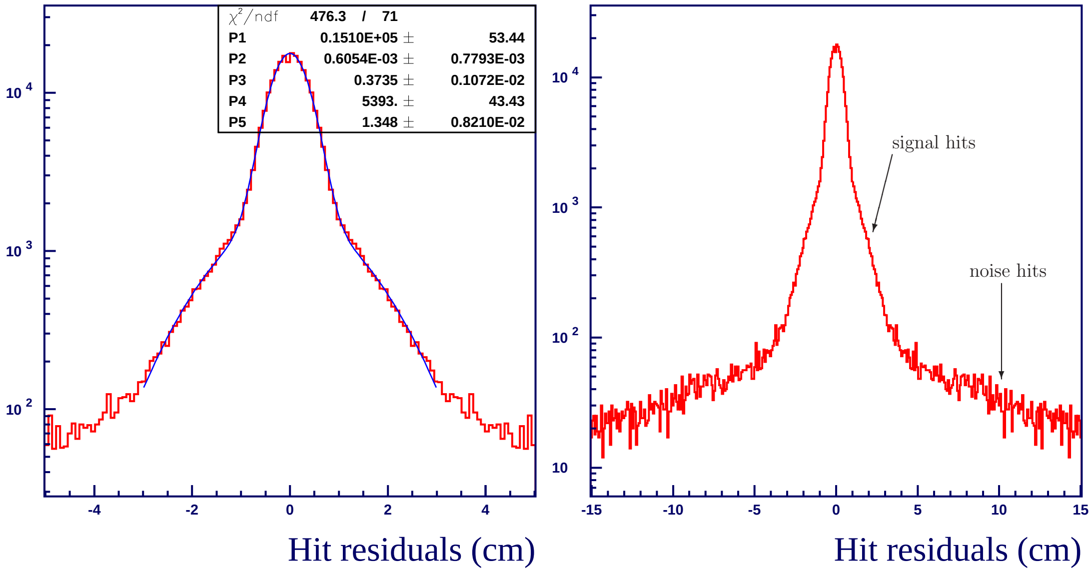

Figure 4.7: *Hits residuals relatively to the expected pattern for 50000 simulated helium events in all AMS acceptance for an aerogel 1.050 radiator setup, 2.5 cm thick with* $C = 0.00512\,\mu\mathrm{m}^4\mathrm{cm}^{-1}$*, and an expansion height of 46.2 cm. The right-hand plot shows the same distribution in an extended scale.*

visible. The function used to fit the distribution is given by the sum of two gaussian functions centered at the same mean value μ ($\mu = 0$), where N_i, σ_i are respectively the number of hits in each population and the gaussian width:

$$\begin{aligned} F(x) &= G_1(\mu, \sigma_1, N_1) + G_2(\mu, \sigma_2, N_2) \qquad (4.20) \\ &= \frac{N_1}{\sqrt{2\pi}\sigma_1} \exp\left[-\frac{1}{2}\left(\frac{x-\mu}{\sigma_1}\right)^2\right] + \frac{N_2}{\sqrt{2\pi}\sigma_2} \exp\left[-\frac{1}{2}\left(\frac{x-\mu}{\sigma_2}\right)^2\right]. \end{aligned}$$

The presence of a second gaussian is necessary to take into account the forward scattering effect introduced in Chapter 3 and the pixel effect. The former implies that part of the photons are scattered away from the reconstructed ring but forward peaked generating an enlargement of the residuals distribution. The latter implies that discrete hit coordinates will appear with a distance among them which is a multiple of the pixel size (8.5 mm) or a multiple of the pixel diagonal ($\sqrt{2} \times 8.5$ cm). Therefore the double gaussian description is applied both to aerogel and sodium fluoride events.

It is convenient to weight the hits, excluding the particle hits, according to their distances to each hypothetical θ_c pattern during the fit. A natural approach to this task is to use a maximum likelihood function [170] in which a probability is assigned to each hit included in the fit. For a random variable x distributed according to a probability density function (p.d.f.) $f(x;\theta)$ with a known form but unknown parameter θ, the probability that n random independent measurements of x, $(x_1, x_2, ..., x_n)$, are in the intervals $[x_1, x_1 + dx]$, $[x_2, x_2 + dx]$ ... $[x_n, x_n + dx]$ is given by

$$P(x_i \in [x_i, x_i + dx_i]) = \prod_{i=1}^{N} f(x_i\ ;\theta) dx_i. \tag{4.21}$$

If the p.d.f. $f(x)$ and the parameter θ describe those data then a high probability for the data that were actually measured is expected. Since dx_i do not depend on the parameters, the same reasoning applies to the following function $\mathcal{L}(\theta)$ called the likelihood function

$$\mathcal{L}(\theta) = \prod_{i=1}^{N} f(x_i\ ;\theta). \tag{4.22}$$

The present case study can be written as

$$\mathcal{L}(\theta_c) = \prod_{i=1}^{N} \mathcal{P}[r_i(\theta_c)] \tag{4.23}$$

where the parameter to estimate is θ_c and the random variable is replaced by the hit residual, r_i, to the currently considered θ_c pattern. $\mathcal{P}$ is the probability density function followed by the residuals r_i, in fact

$$r_i(\varphi_i, \theta_c) = \sqrt{\left(X_{exp}(\varphi_i, \theta_c) - x_i\right)^2 + \left(Y_{exp}(\varphi_i, \theta_c) - y_i\right)^2} \tag{4.24}$$

where φ_i is the hit azimuthal position in the photon pattern which is necessary to evaluate for each residual. $\mathcal{P}\{r_i(\theta_c)\}dr$ describes the probability of a hit placed at a distance r_i from the expected pattern given by a certain θ_c being at $r < r_i < r + dr$.

The probability density function for a detected hit being either signal or noise should be of the type

$$\mathcal{P}_{total}(r) = \mathcal{P}_{signal}(r) + \mathcal{P}_{noise}(r). \tag{4.25}$$

As was mentioned before the signal is well described by a double gaussian function. Therefore, the signal p.d.f. term can be expressed by

$$\mathcal{P}_{signal}(r) = C_{signal}\left(\frac{\alpha_1}{\sqrt{2\pi}\sigma_1}\exp\left[-\frac{1}{2}\left(\frac{r}{\sigma_1}\right)^2\right] + \frac{\alpha_2}{\sqrt{2\pi}\sigma_2}\exp\left[-\frac{1}{2}\left(\frac{r}{\sigma_2}\right)^2\right]\right) \tag{4.26}$$

where the meaning of each parameter of the gaussian was already established and $\alpha_i = \frac{N_i}{N_1+N_2}$ with $i = 1, 2$.

In first and good approximation the tail of the residuals distribution (background hits) can be assumed as flat and therefore described by a constant p.d.f. function

$$\mathcal{P}_{noise}(r) = C_{noise}. \tag{4.27}$$

The values of the constants C_{signal} and C_{noise} will be fixed from the normalization of the overall p.d.f. ($\mathcal{P}_{total}$). So for an event with N hits, S hits belonging to *signal* and B hits to *background*,

$$N = S + B \Leftrightarrow 1 = \frac{S}{N} + \frac{B}{N}, \tag{4.28}$$

which implies the normalization condition:

$$\int_0^D \mathcal{P}_{signal}(r)dr = \frac{S}{N} \quad \text{and} \quad \int_0^D \mathcal{P}_{noise}dr = \frac{B}{N} = b, \tag{4.29}$$

where D represents the maximum distance of a hit to the pattern and is identified with the active matrix dimensions. After integration the following values are obtained:

$$\begin{aligned} C_{signal} &= \frac{S}{N} \\ C_{noise} &= b\frac{1}{D}. \end{aligned} \tag{4.30}$$

The final combined probability function can be written, taking into account that $\frac{S}{N} = 1 - b$, as

$$\mathcal{P}(r) = (1-b)\left(\frac{\alpha_1}{\sqrt{2\pi}\sigma_1}\exp\left[-\frac{1}{2}\left(\frac{r}{\sigma_1}\right)^2\right] + \frac{\alpha_2}{\sqrt{2\pi}\sigma_2}\exp\left[-\frac{1}{2}\left(\frac{r}{\sigma_2}\right)^2\right]\right) + \frac{b}{D}. \tag{4.31}$$

with the independent parameters σ_1, σ_2, $\alpha_i = \frac{N_i}{N_1+N_2}$ with i=1,2 and D to be evaluated from the residuals distribution, and b, the background fraction. From the fit presented in Figure 4.7 the gaussian widths are evaluated to be $\sigma_1 = 0.374 \pm 0.001$ cm and $\sigma_2 = 1.348 \pm 0.008$ cm and normalization factors N_1 and N_2 describe the relative population of the two gaussians, so from the same figure $\alpha_1 = 0.76$ and $\alpha_2 = 0.34$. The D parameter is taken as 134 cm which is the diameter of the matrix, corresponding to the spatial domain on which each residual falls into. To evaluate the background fraction b it is necessary to define a cut distance d_{cut} that separates the population of hits that are signal and the population that belongs to the background. This implies a fine tuning of the parameter b that will be explained in the next subsection.

The defined probability should also take into account the signal strength n_i which is proportional to the number of emitted photons without suffering from the saturation of the hits occupancy.

The final likelihood function can be written as

$$\mathcal{L}(\theta_c) = \prod_{i=1}^{N} \mathcal{P}^{n_i}[r_i(\theta_c)]. \tag{4.32}$$

The weight will be considered as the signal strength for $n_i > 1$, otherwise it will be assumed to be 1 in order to avoid the single photoelectron dispersion ($\sigma_{pe} \sim 0.76$). Figure 4.8 shows the single photoelectron distribution extracted from test beam data in 2003.

For numerical reasons the minimized function is $-log\mathcal{L}(\theta_c)$ which is equivalent to the maximization of $\mathcal{L}(\theta_c)$. This does not change the minimum position, but merely enlarges the function curvature close to the minimum.

Particle signal in the light guide

When a particle crosses the light guide material which has a high refractive index ($n = 1.49$), it produces a large number of Čerenkov photons. In fact, about six times more photons per unit length are produced than in the aerogel 1.050. As a consequence clusters of several hits come up in a small area confined into the same photomultiplier. It is desirable to reject these hits from the fit to the Čerenkov pattern. The reconstructed event display of Figure 4.9 shows the effect described. If particle clusters were not removed from the set of points to fit the reconstructed pattern would be the inner one instead of the (clearly visible) expected one.

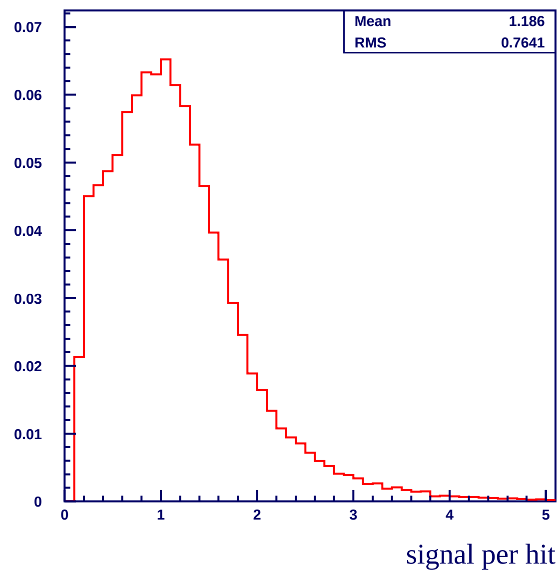

Figure 4.8: *Single photoelectron signal extracted from test beam data.*

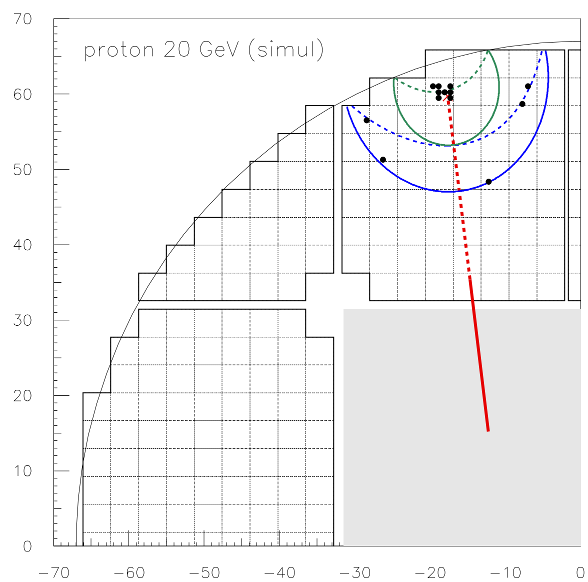

Figure 4.9: *Effect of particle hits on the pattern fit* [167]*. Without removing particle hits the reconstructed pattern would be the inner one. The larger ring is the simulated Čerenkov pattern.*

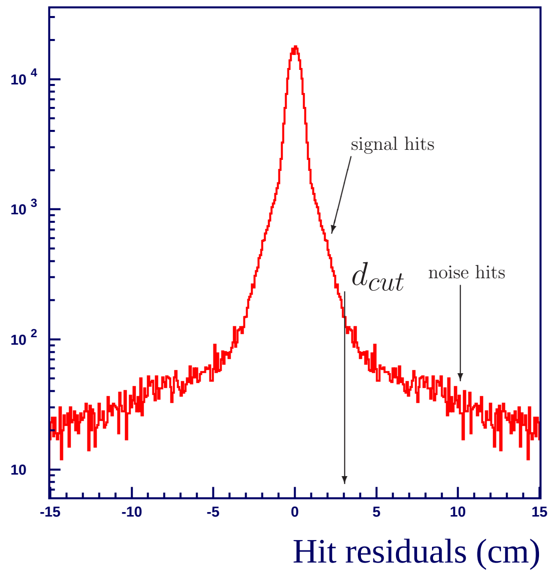

Figure 4.10: *Hit residuals relatively to the expected pattern for 50000 simulated helium events in all the RICH acceptance for an aerogel 1.050 radiator setup, 2.5 cm thick with* $C = 0.0052\,\mu\mathrm{m}^4\mathrm{cm}^{-1}$*, and an expansion height of 46.2 cm: cut distance for separation between signal and background hits.*

In this velocity reconstruction method, hits closer than 5 cm from the particle impact point at the readout matrix are rejected. The impact point results from the extrapolation of the AMS track to the readout matrix.

4.3.3 Optimization studies

Background level tuning

As was previously mentioned, evaluating the background fraction b is equivalent to defining a cut distance d_{cut} that separates the population of hits that are signal and the population that belongs to the background. In simple terms the cut distance will be the distance up to which hits will be considered as signal hits and will be associated to the Čerenkov ring. Beyond the cut distance only background hits are considered to be present in the residuals distribution. Figure 4.10 illustrates the cut distance for separation between signal and background hits.

In practice the problem implies solving the following equation for different cut distances which gives different background levels (b).

$$(1-b)(G_1(d_{cut})+G_2(d_{cut}))=\frac{b}{D} \tag{4.33}$$

Samples of 10000 helium events with $\beta \simeq 1$ were simulated within all the AMS acceptance, impacting uniformly in the aerogel region of the RICH radiator. The relative velocity resolution σ_β/β is estimated from the distribution ($\beta^{sim}-\beta^{rec}$) where $\beta^{sim} \simeq 1$, for each established pair (b, d_{cut}). The evolution of $\frac{\sigma_\beta}{\beta}$ with d_{cut} is presented in the left-hand plot of Figure 4.11. The velocity resolution improves with the cut distance, according to expectations, up to a value around 1 cm. This was foreseen because signal hits belonging to the Čerenkov pattern are being added to the reconstruction. For distances beyond 1 cm a flat region is observed where the relative velocity resolution for helium nuclei in aerogel 1.050, 2.5 cm thick in the flight setup is around $(0.636 \pm 0.006) \times 10^{-3}$. The existence of this region proves that by associating more hits to the ring the velocity resolution is not degraded which is a consequence of the fact that the probability density function is weighting well the signal and the background hits. For distances from the ring greater than 4 cm results suggest that the resolution starts to degrade. However in the flat region the velocity resolution is insensitive to the cut distance. Therefore it was decided to set the cut distance at d_{cut}=2.0 cm, which leads to a background level b=0.776 and to a resolution of $(0.635 \pm 0.006) \times 10^{-3}$ for the helium nuclei in the same setup.

The right-hand plot of Figure 4.11 shows the relative velocity resolution for helium nuclei in the aerogel 1.050 radiator versus the cut distance using a likelihood with a double gaussian description for the signal probability together with the same study using a single gaussian in the signal function in the p.d.f. $\mathcal{P}(r) = (1-b)G_1(r_i) - \frac{b}{D}$. This model leads to a lower d_{cut} which is 0.60 cm corresponding to a background level $b = 0.950$ and finally to a optimized velocity resolution of $(0.638 \pm 0.006) \times 10^{-3}$ which is compatible to the optimized value using the double gaussian model. However from Figure 4.7 it can be seen that the hits with a distance of 0.60 cm are clearly in the central gaussian region, which indicates that they are good candidates for signal hits. Such a low value for the cut distance that optimizes the velocity resolution suggests that the whole signal region is not being well described by the p.d.f. that uses only one gaussian for the signal probability.

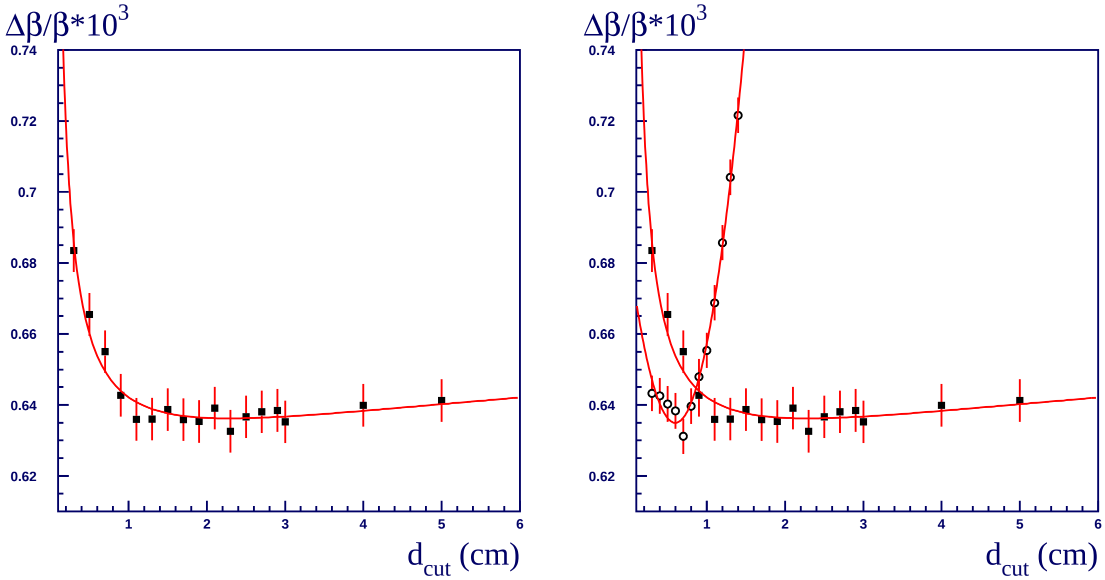

Figure 4.11: *Relative velocity resolution for helium nuclei in aerogel 1.050, 2.5 cm thick in the flight setup versus cut distance between signal and noise hits spatial distribution. On the left the probability density function in the likelihood uses a double gaussian description for the signal probability while on the right the same result is plotted (full squares) together with the result using a single gaussian (open dots).*

The model with a double gaussian for the signal description will be adopted instead of the single gaussian model. The reconstruction efficiency for protons using the first model is 1% increased with respect to the efficiency using the description with only one gaussian. In addition b parameter is less sensitive to radiator properties using a double gaussian description. The optimized velocity resolution for the two models is comparable.

Photon emission point

The emission point in the radiator assumed for photon tracing in the pattern fit procedure is a parameter that is a source of systematic error for velocity reconstruction. The lower this point is chosen the larger will be the reconstructed Čerenkov angle. This feature is illustrated in the scheme of Figure 4.12.

It was mentioned several times before that the Čerenkov photons are emitted along the entire particle track in the dielectric material of the radiator. However, in

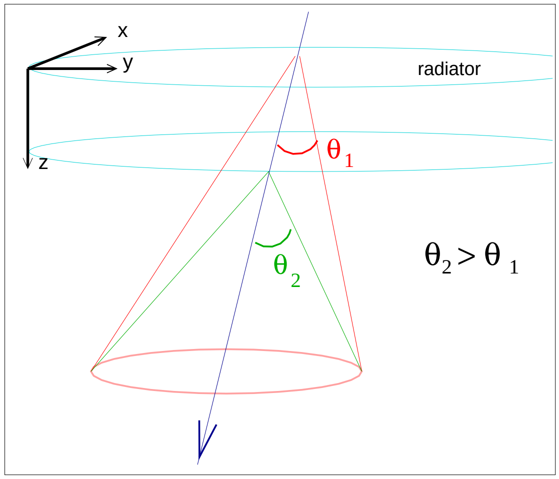

Figure 4.12: *Illustration of the emission point effect on θ_c reconstruction. Moving the emission point from the top to the bottom of the radiator necessarily leads to different reconstructed angles: θ_1 and θ_2. The scheme is not drawn to scale.*

aerogel they can interact through different effects: Rayleigh scattering and absorption. The cross section for Rayleigh scattering is $\sigma_{scat} \propto \frac{1}{\lambda^4}$ while for the absorption it is $\sigma_{abs} \propto \frac{1}{\lambda^2}$ [160], so only the first effect will be considered for the calculation of the mean photon emission vertex. Considering p as the interaction probability per unit of length, which is given by $p = \frac{C}{\lambda^4}$ where C is the radiator clarity, the photon mean free path can be expressed as

$$< x >= \frac{\int x \ p^{\overline{int}} dx}{\int p^{\overline{int}} dx}. \tag{4.34}$$

According to equation 3.20 and using the variables defined in Figure 4.13 $p^{\overline{int}}$, the photon non-interaction probability for a crossed distance $x = f(\theta, \phi, \theta_c, \varphi)$, is given by ke^{-px}. Hence,

$$< x >= \frac{\int_0^\ell x \ k \ e^{-px} dx}{\int_0^\ell k \ e^{-px} dx}, \tag{4.35}$$

which simplified is expressed by

$$< x >= \ell \left(-\frac{1}{p\ell} - \frac{1}{e^{-p\ell} - 1} \right). \tag{4.36}$$

Assuming as a first and crude approximation the photon path defined by $\ell = \frac{h}{cos\theta}$ with $< \theta >\sim 20^0$ which is in fact the distance crossed by the particle and $< \lambda >\sim$ 358 nm, $C = 0.0052 \, \mu\text{m}^4\text{cm}^{-1}$ and $H_{rad} = 2.5\,\text{cm}$ comes $< x > \sim \ 1.53$ which is

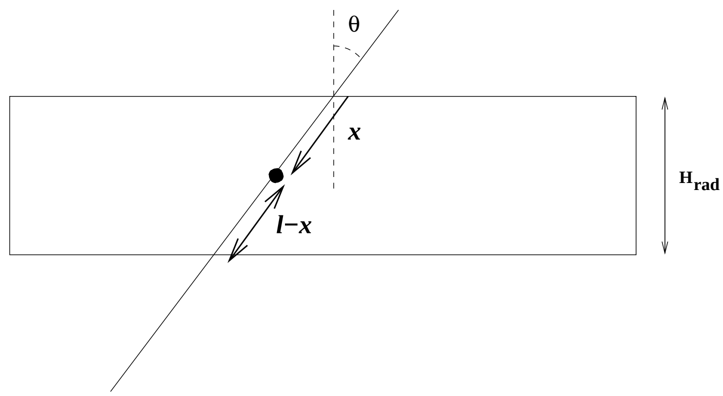

Figure 4.13: *Illustration of the mean photon emission vertex in the radiator with a thickness H_{rad}. The total distance crossed by the photon is l, while x is the distance crossed until an interaction.*

61% of the radiator height. In reality the distance crossed by the photon is also a function of the particle direction (θ,ϕ), the Čerenkov angle (θ_c), the photon emission point (z) and the photon azimuthal angle φ, that is $d_\gamma(\theta, \phi, \theta_c, z, \varphi)$. Obviously the foreseen emission point is not in the middle point of the radiator height. Since the Rayleigh scattering probability increases with the radiator crossed length it is expectable that the photons emitted near the radiator top are most scattered and thus lost from the ring. So a z origin coordinate closer to the bottom is expected with a shift depending on the clarity coefficient. The greater the clarity, the higher the expected shift.

The emission point was fine tuned using the RICH simulation. It is constrained to be along the particle track so that the z emission coordinate is the only remaining degree of freedom. For the study the fraction of radiator height that is the z coordinate divided by the radiator thickness ($\frac{z}{H_{rad}}$) was considered.

The velocity reconstruction was applied using samples with 20000 helium events generated within the RICH acceptance with $\beta \simeq 1$ by simply varying the emission coordinate z. The expected effect is a direct shift of the reconstructed β peak from the unity. This effect can be appreciated in Figure 4.14 which shows distributions of $(\beta^{sim} - \beta^{rec})$ for photon emission vertex at 44% and 70% of the radiator thickness at right and at left, respectively.

Figure 4.15 presents the evolution of the systematic error of the mean recon-

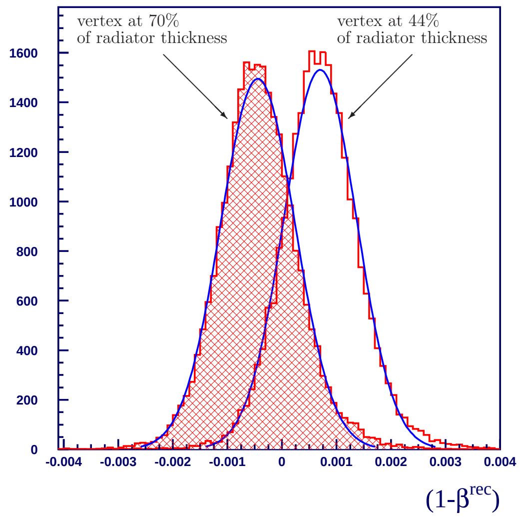

Figure 4.14: *$\beta^{sim} - \beta^{rec}$ distributions for vertex at 44% and 70% of the radiator thickness. An aerogel 2.5 cm thick with a clarity coefficient $C = 0.0052\,\mu\mathrm{m}^4\mathrm{cm}^{-1}$ was simulated.*

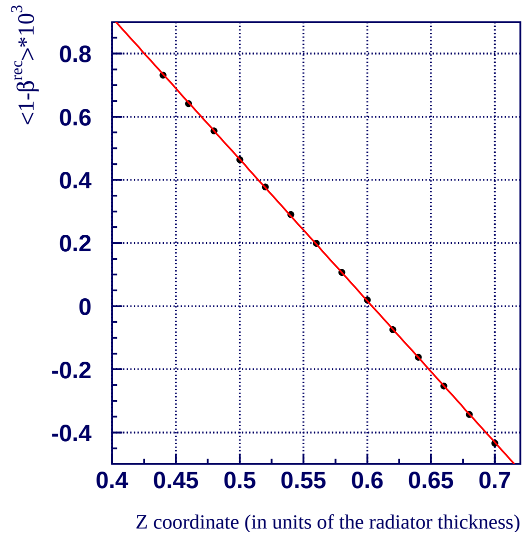

Figure 4.15: *Simulation study showing the fine tuning of the z coordinate of the emission point assumed for the pattern tracing. An aerogel 2.5 cm thick with a clarity $C = 0.0052\,\mu\mathrm{m}^4\mathrm{cm}^{-1}$ was simulated.*

structed velocity value with the percentage of radiator height. This shows a linear variation with the optimal emission vertex at 60.4% of the radiator height. The value obtained with the simulation performed is in agreement with the value obtained from the calculation presented above.

Background level tuning for sodium fluoride

The same optimization study applied to aerogel was also done for the sodium fluoride radiator. The residuals distribution can be observed in Figure 4.16 (left). A double gaussian function can be fitted to the distribution and it is clear that the population of the second gaussian is relevant.

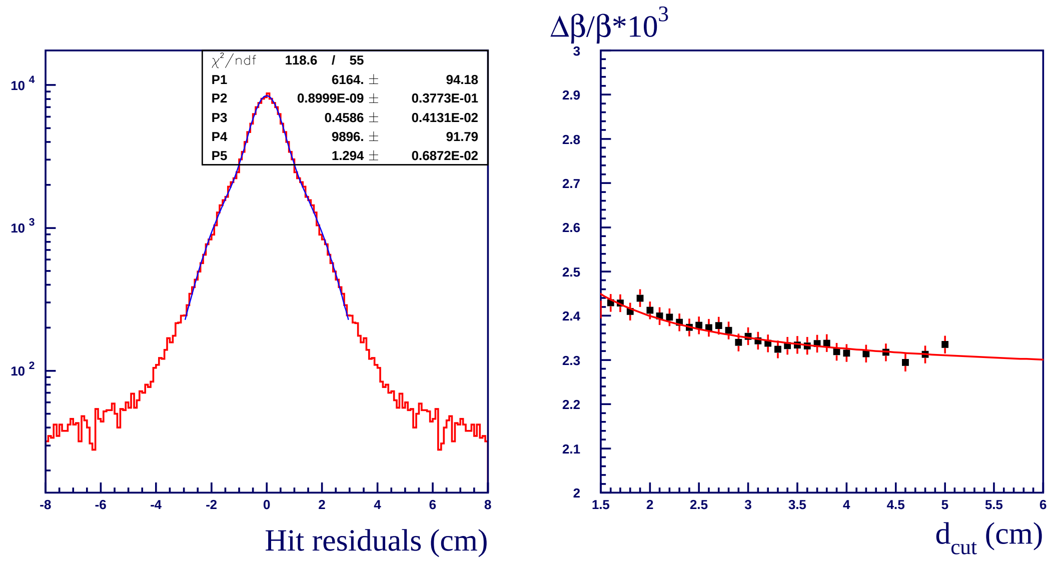

Figure 4.16: *Hit residuals with respect to the expected pattern for 50000 simulated helium events in all AMS acceptance for a sodium fluoride radiator setup, 0.5 cm thick, and an expansion height of 46.2 cm* (left). *Relative velocity resolution for helium nuclei in sodium fluoride, 0.5 cm thick in the flight setup versus cut distance between signal and noise hits in the spatial distribution* (right).

For the optimization procedure, evaluating the background fraction b implies the definition of a cut distance d_{cut} that separates the population of hits that are signal and the population that belongs to the background. In practical terms the problem once more consists in solving equation 4.33 for different cut distances leading to different background levels. Samples of 50000 helium events with $\beta \simeq 1$ were simulated within all the NaF acceptance. The relative velocity resolution σ_β/β is again estimated from the distribution $(\beta^{sim} - \beta^{rec})$ where $\beta^{sim} \simeq 1$, for each established pair $(b,\, d_{cut})$. The evolution of $\frac{\sigma_\beta}{\beta}$ with d_{cut} is presented in the right-hand plot of Figure 4.16. The velocity resolution improves slightly as the cut distance increases and reaches a stable region after $d_{cut} = 3\,\mathrm{cm}$ where the relative velocity resolution for helium nuclei in NaF, for the flight setup is around $(2.33 \pm 0.02) \times 10^{-3}$. Since the velocity resolution stabilizes for $d_{cut} = 3\,\mathrm{cm}$, this will be increased to 4 cm for reconstruction efficiency improvement, which corresponds to a background level of $b = 0.186$.

4.3.4 Simulation results: velocity studies

The results presented in this subsection have been collected in the framework of the RICH standalone simulation mentioned in Chapter 3. The most fundamental parameters used from now on are presented in Table 4.2.

aerogel radiator	n	1.05
	H_{rad}	2.5 cm
	C	$0.0052\,\mu\mathrm{m}^4\mathrm{cm}^{-1}$
NaF radiator	n	1.334
	H_{rad}	0.5 cm
foil	n	1.56
	H_{foil}	1.0 mm
expansion height		46.2 cm
light guide	n	1.49
	size	34 mm
	pitch	37 mm
mirror reflectivity		85%

Table 4.2: *Simulated parameters.*

Figure 4.17 shows reconstructed Čerenkov patterns using the velocity reconstruction algorithm described in this section. The patterns at left are generated in aerogel while the patterns at right are generated in the sodium fluoride radiator. The particle direction is traced with a straight line segment and the particle impact point at the top of the radiator corresponds to the point where the solid line turns into a dashed line. The impact point at the detection plane is represented by a crossed point. Čerenkov rings generated by different charged particles are shown and it is clearly visible that the velocity reconstruction algorithm is even able to recognize complex patterns like the ones generated in sodium fluoride. These patterns may contain reflected branches generated by photons that are reflected only once and by multi-reflected photons. The given examples introduce patterns with segments coming from double reflections.

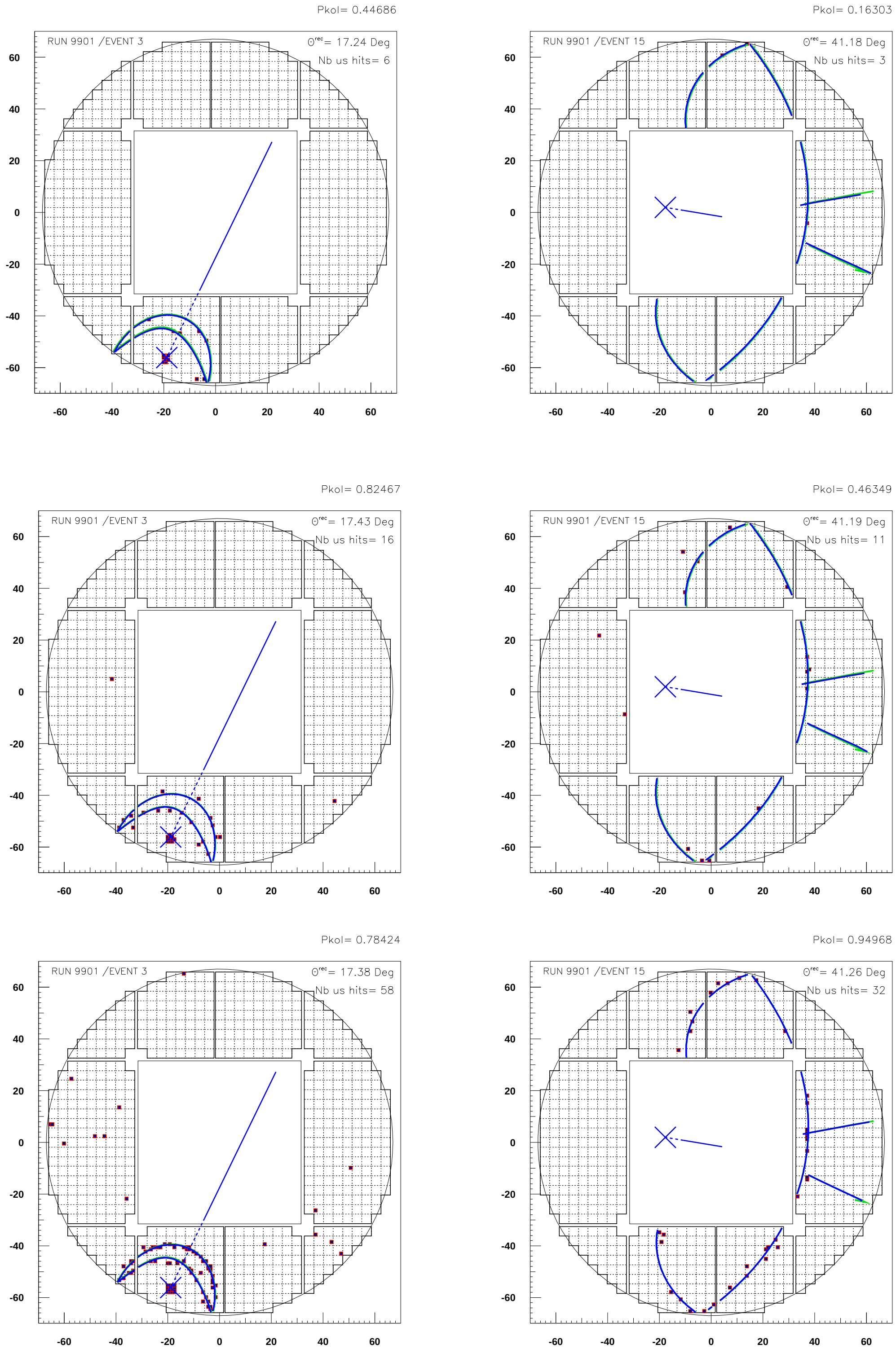

Figure 4.17: *Reconstruction of simulated protons* (top), *helium* (middle) *and beryllium* (bottom) *nuclei in aerogel 1.050, 2.5 cm thick radiator* (left) *and sodium fluoride* (right). *The reconstructed pattern includes both reflected and non-reflected branches.*

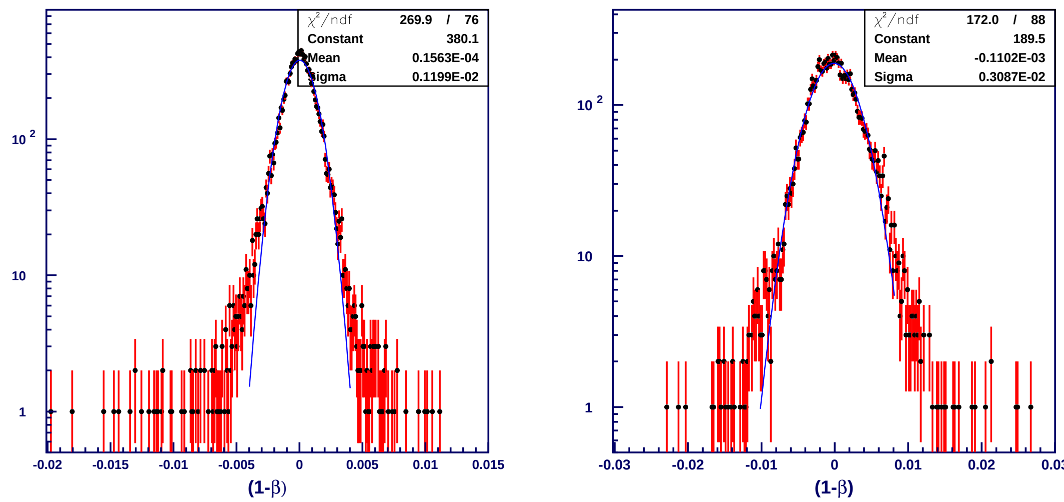

Figure 4.18: *Distribution of* $(\beta^{rec} - \beta^{sim})$ *for protons* ($\beta \simeq 1$) *impacting in the aerogel* (left) *and in the sodium fluoride radiator* (right).

Figure 4.18 (left) introduces the reconstructed velocity distribution from simulated proton data in aerogel. It is a sample with 50000 events generated within the aerogel radiator acceptance with $\beta \simeq 1$. A gaussian fit is applied to the distribution and the resolution foreseen for singly charged particles is estimated to be $\sigma_\beta = (1.20 \pm 0.01) \times 10^{-3}$. This value fulfills the requirement of measuring proton velocity with a resolution of one per thousand. The reconstructed velocity distribution for protons in sodium fluoride is presented in the right-hand plot of Figure 4.18. In the present case a resolution of $\sigma_\beta = (3.09 \pm 0.03) \times 10^{-3}$ is attained for singly charged particles. Some tail events are visible in both reconstruction. They arise from reconstructions with a low number of hits and could be eliminated imposing a number of reconstructed hits in the Čerenkov pattern higher than four. Unless it is explicitly mentioned all the accepted reconstructions have at least three hits associated to the reconstructed ring.

The obtained resolution for singly charged particles is in full agreement with the predicted uncertainty presented in Table 4.1 for aerogel. However the NaF resolution extracted from simulation is better than the calculated one due to the bias introduced in the distribution of the number of hits used in the reconstructed ring. This result will be confirmed in Figure 4.19 (left) showing a good agreement with the resolution extracted from σ_β evolution with Z.

Figure 4.19 shows the evolution of β resolution with the charge obtained with aerogel and NaF radiators in the flight setup. It is expected that velocity resolution varies according to a law $\propto 1/Z$, as expected from the charge dependence of the photon yield in the Čerenkov emission up to a saturation limit set by the granularity of the detection matrix. Therefore the law

$$\sigma_\beta(Z) = \sqrt{\left(\frac{A}{Z}\right)^2 + B^2} \tag{4.37}$$

should rule the evolution. Here, A is the β resolution for a singly charged particle while B is the asymptotic term with the meaning of the resolution for a very high charge. For aerogel $A = (1.263 \pm 0.005) \times 10^{-3}$ and $B = (0.202 \pm 0.001) \times 10^{-3}$ while for sodium fluoride $A = (4.44 \pm 0.01) \times 10^{-3}$ and $B = (0.531 \pm 0.001) \times 10^{-3}$. The evaluated resolution for singly charged particles in sodium fluoride is better than the expected result from the fit to the other charges, as confirmed from the misaligned point for $Z = 1$. This is due to the bias introduced in the event sample due to the three hits cut.

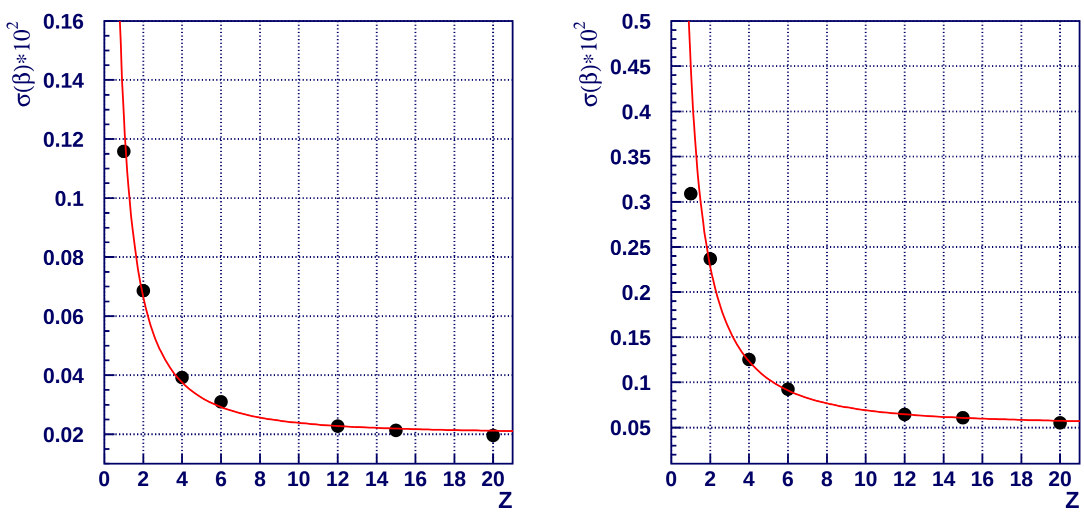

Figure 4.19: *Expected evolution of the β resolution with the charge obtained with aerogel* (left) *and sodium fluoride* (right) *radiators in the flight setup.*

The velocity resolution for each radiator can be extracted from the gaussian fit to both distributions in Figure 4.18 as stated above, however the values obtained should not be directly compared to characterize each radiator reconstruction capability because of the different statistics on the number of hits. The distributions on the number of hits associated to the reconstructed proton patterns in aerogel and sodium fluoride are presented in Figure 4.20. A mean number of 7.8 hits is used in aerogel while 3.9 hits are used in a proton event reconstruction performed with sodium fluoride.

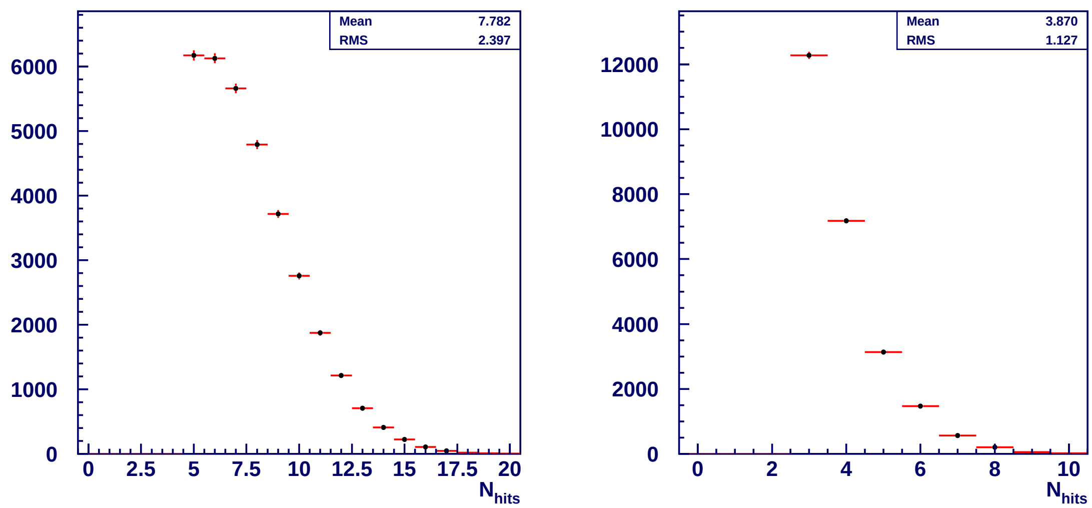

Figure 4.20: *Number of hits on the reconstructed pattern for proton events in aerogel* (left) *and in sodium fluoride* (right).

Figure 4.21 shows the distribution of the number of photoelectrons for proton events with $\beta \simeq 1$ impacting in the aerogel (left) and NaF (right) radiators. The fitted functions allow to disentangle the photon ring acceptance effect a concept that will be introduced in subsection 4.4.3. From the fit to the aerogel distribution is extracted a mean number of 8.87 photoelectrons for 100% contained proton rings, while for the NaF radiator a mean number of 4.32 photoelectrons is expected in the same conditions. The method used to derive these numbers is given in detail in appendix A.

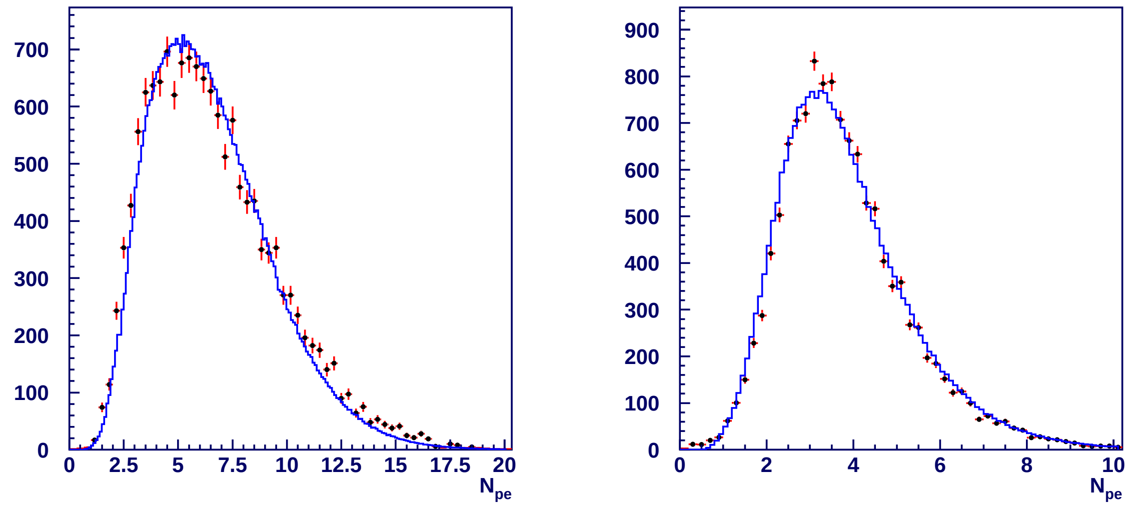

Figure 4.21: *Number of photoelectrons for $\beta \simeq 1$ proton events in the aerogel* (left) *and NaF* (right) *radiators.*

The single-hit resolution is the proper estimator to compare the intrinsic resolutions for the reconstructed velocity in each radiator. This estimator is built multiplying the factor $\sqrt{N_{hits}}$ by the $(\beta^{rec} - \beta^{sim})$ for every event. Figure 4.22 shows the single-hit velocity resolution for aerogel for simulated particles with $\beta \simeq 1$.

Figure 4.22 (right) shows the evolution the single-hit velocity relative resolutions for aerogel and sodium fluoride with the simulated momentum per nucleon.

All the accepted reconstructions have at least three hits associated to the reconstructed pattern. In fact, reconstructions with two associated hits could be considered since the Čerenkov angle reconstruction has only one free parameter (θ_c). However, due to the background contribution, reconstructions with only two hits suffer from contamination and are rejected.

4.4 Charge Reconstruction Algorithm

4.4.1 Method description

The Čerenkov photons produced in the radiator are uniformly emitted along the particle path, L, inside the dielectric medium and their number per unit of energy depends on the particle's charge, Z, velocity, β, and on the refractive index, n,

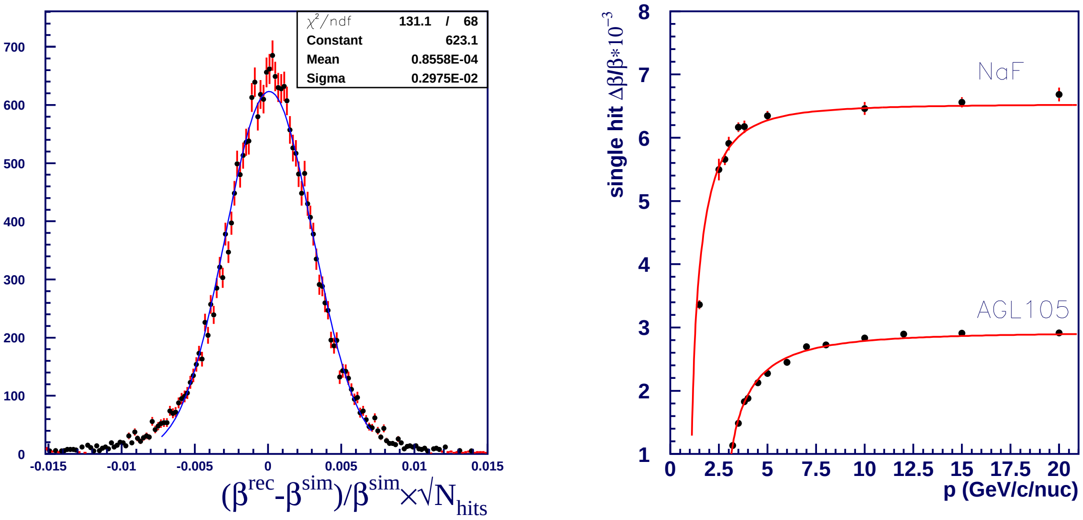

Figure 4.22: *Single-hit relative β resolutions for aerogel for $\beta \simeq 1$ particles* (left) *and single-hit relative β resolutions for aerogel and sodium fluoride versus the simulated momentum per nucleon* (right).

according to the expression:

$$\frac{dN_\gamma}{dE} \propto Z^2 L \left(1 - \frac{1}{\beta^2 n^2}\right) = Z^2 L \sin^2\theta_c \tag{4.38}$$

Therefore, to reconstruct the charge the following procedure is required:

- Čerenkov angle reconstruction (θ_c).
- Particle path estimation, ΔL, which relies on the information of the particle direction provided by the tracker.
- Photoelectron counting associated to the Čerenkov ring.
- Photon detection efficiency evaluation.

  The number of radiated photons (N_γ) which will be detected (N_{pe}) depend on:

  – the interactions with the radiator: absorption and Rayleigh scattering in the aerogel case (ε_{rad});

  – the photon ring acceptance: part of the photons are lost through the radiator's lateral and inner walls, due to total reflection in the radiator-air transition, because of mirror absorption and because some photons fall into a non-active area (ε_{geo});

– the light guide losses (ε_{lg});

– the photomultiplier quantum efficiency (ε_{pmt}).

Hence,

$$N_{pe} \propto N_{\gamma}^{rad} \varepsilon_{rad}\, \varepsilon_{geo}\, \varepsilon_{lg}\, \varepsilon_{pmt} \tag{4.39}$$

After all the detection efficiency factors are calculated the charge of the incident particle is simply given by

$$Z^2 = \frac{N_{pe}}{N_{pe}(Z=1)} \propto \frac{N_{pe}}{\varepsilon_{TOT}} \frac{1}{\Delta L} \frac{1}{\sin^2 \theta_c}. \tag{4.40}$$

Each point will be explained in detail in the following subsections.

4.4.2 Counting of the number of photoelectrons

The number of photoelectrons related to the Čerenkov ring has to be counted within a fiducial area in order to exclude the uncorrelated background noise. Therefore, photons which are scattered in the radiator are excluded. The signal is integrated until the same cut distance used in the velocity reconstruction algorithm. For aerogel 1.050 this value is $d_{cut} = 2\,\text{cm}$. The right-hand plot of Figure 4.23 shows the integrated number of hits as function of the distance to the ring. It is visible that at 20 mm the integrated signal is already stable.

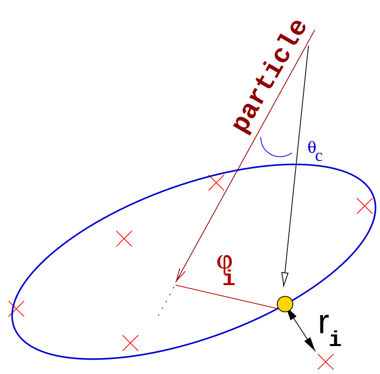

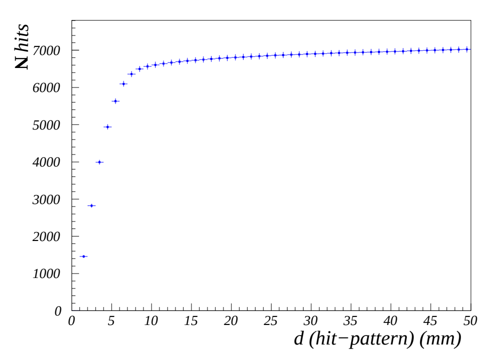

Figure 4.23: *Distribution of the integrated number of hits as function of the hit distance* (right) *to the reconstructed Čerenkov pattern generated in the aerogel radiator 1.050* (left).

4.4.3 Photon ring acceptance

The ring acceptance measures the fraction of radiated photons that reach the photomultiplier matrix. It is computed considering the different photon loss factors:

- escaping through the radiator's lateral and inner walls;
- totally reflection at the following interfaces: radiator-air, radiator-foil and foil-air;
- losses in the conical mirror (assumed to have a reflectivity of ∼85%);
- fall in a non-active area of the detection plane (gaps in the PMTs, matrix modules junctions, hole of the electromagnetic calorimeter, dead PMT or pixel).

Figure 4.24 shows a representation of the Čerenkov photon pattern generated by an incident particle whose impact point in the radiator is (x,y) and direction is (θ,ϕ).

The photon pattern represented with a solid line corresponds to the photons reaching directly the photomultipliers. Those photons which are reflected in the mirror produce a pattern represented by a dashed line. Finally, the photons which fall in non-active areas are represented by a dotted line.

For a certain event, the photon ring acceptance is obtained by adding the different fractions of *visible* photons; namely, the fraction of photons hitting the PMT matrix directly (ε_{geo}^{Dir}) and the fraction of incident photons in the mirror (ε_{geo}^{Mir}) weighted by the mirror reflectivity (ρ). Therefore the photon ring acceptance can be written as:

$$\varepsilon_{geo} = \varepsilon_{geo}^{Dir} + \rho\, \varepsilon_{geo}^{Mir} \tag{4.41}$$

Conversely, the ring *invisible* acceptance gives account of the fraction of photons lost in the calorimeter hole (ε_{geo}^{Hol}) and in the radiator interfaces.

Since Čerenkov photons are emitted azimuthally uniform in particle's reference frame the values of ε_{geo}^{Dir}, ε_{geo}^{Hol} and ε_{geo}^{Mir} are easily obtained by taking into account the differences between the azimuthal angles (φ) corresponding to the extreme intersection points of the Čerenkov cone with the non-active regions of the detector, φ^h, and with the mirror, φ^m.

$$\varepsilon_{geo}^{Dir} = \frac{|\varphi_1^m - \varphi_1^h| + |\varphi_2^m - \varphi_2^h|}{2\pi} ; \varepsilon_{geo}^{Mir} = \frac{|\varphi_2^m - \varphi_1^m|}{2\pi} ; \varepsilon_{geo}^{Hol} = \frac{|\varphi_2^h - \varphi_1^h|}{2\pi} . \tag{4.42}$$

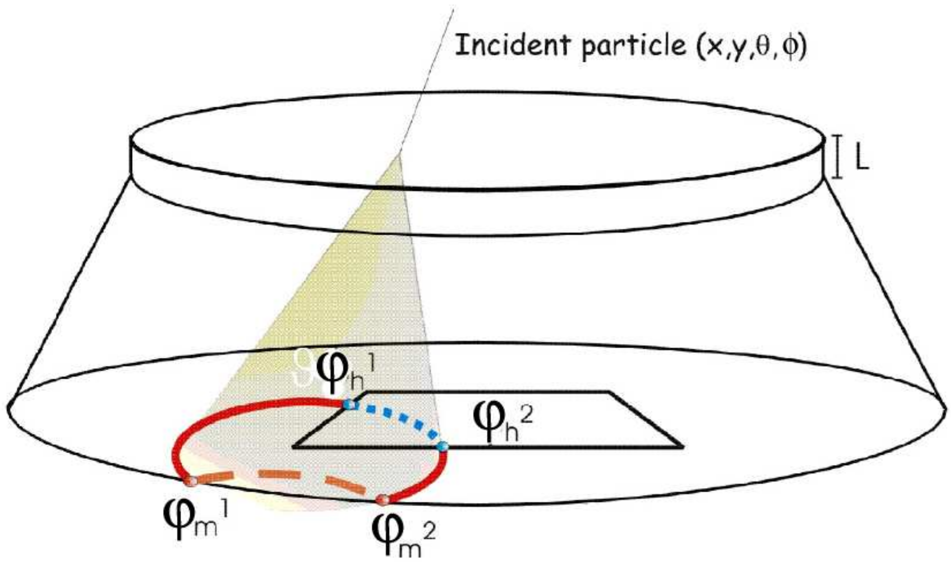

Figure 4.24: *3-dimensional view of photon pattern tracing in RICH detector, where* φ_h^i *are azimuthal angles that are the limits of visibility of the Čerenkov pattern by intersection with the inactive detection region of the matrix and* φ_m^i *are the extreme intersection points of the Čerenkov pattern with the conical mirror.*

For more details on this calculation see thesis [58].

The previous calculations where applied to several events and two of them are showed below in Figure 4.25. The aerogel event has a ring acceptance ε_{geo}=81.6% while the sodium fluoride event has a ring acceptance ε_{geo}=33.1%. In the latter case, a large fraction of photons are totally reflected in the sodium fluoride-air interface and another part fall in the ECAL hole.

Figure 4.27 shows the distributions of the photon ring acceptances for events with $\beta = 0.999$ falling in the 1.050 aerogel radiator (left) and in the sodium fluoride square (right). Basically in both cases there are no fully contained rings in the matrix. In the aerogel distribution a peak between ~80% and ~95% appears that corresponds to events almost fully contained and to totally reflected events that are also almost fully contained because the reflectivity is set at 85%. The percentage of invisible events in aerogel is 1.5% while in the sodium fluoride there are no events falling totally in a non-active detector region. For sodium fluoride, a large fraction of events falls in the range from 10% to 35% and the maximum detected acceptance

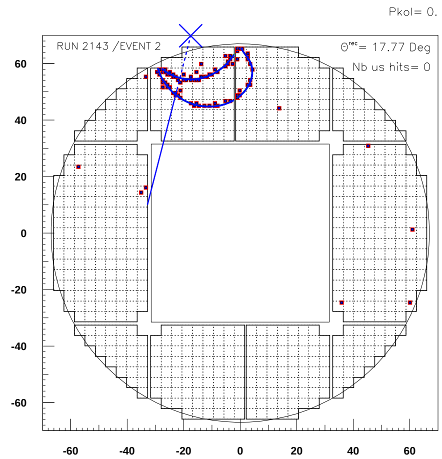

Impact point=(-22.6;50.0;0.0)		ε_{geo}^{Dir}=29.7%
$\theta = 22.8^{\circ}$	$\phi = 75.6^{\circ}$	ε_{geo}^{Mir}=61.1%
$\beta = 0.999$	$\theta_c = 17.75^{\circ}$	ε_{geo}^{Inv}=9.3%

Figure 4.25: *Beryllium event detected in the PMT matrix, generated in aerogel radiator,* $n = 1.050$, *2.5 cm, with an expansion volume height of 46.2 cm.*

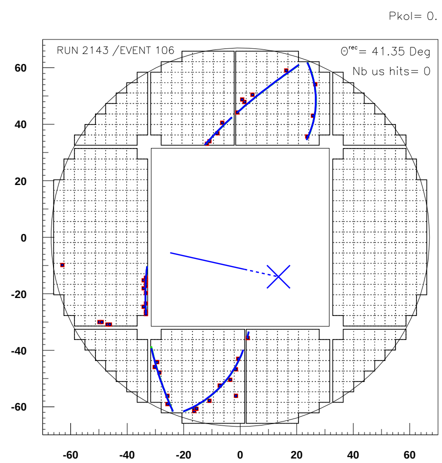

Impact point=(1.3;-11.3;0.0)		ε_{geo}^{Dir}=20.8%
$\theta = 15.01^{\circ}$	$\phi = 347.5^{\circ}$	ε_{geo}^{Mir}=14.5%
$\beta = 0.999$	$\theta_c = 41.38^{\circ}$	ε_{geo}^{Inv}=64.7%

Figure 4.26: *Beryllium event detected in the PMT matrix, generated in sodium fluoride radiator,* $n = 1.334$, *with an expansion volume height of 46.2 cm.*

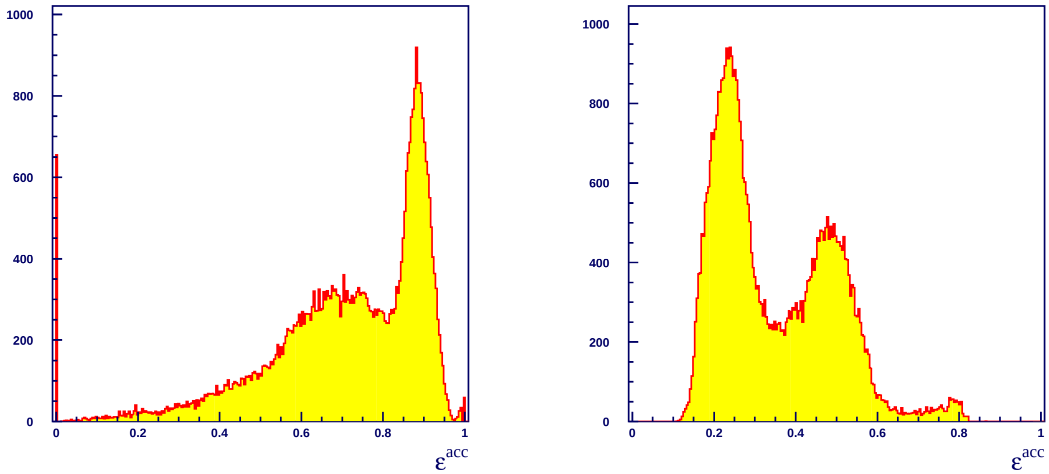

Figure 4.27: *Distribution of the photon ring acceptance given by* $\varepsilon_{geo}^{Dir} + \rho\, \varepsilon_{geo}^{Mir}$*, with* ρ*=0.85: for an aerogel radiator,* n = 1.050 (left)*; for a sodium fluoride radiator,* n = 1.334 (right)*; both setups with an expansion volume height of 46.2 cm. Particles generated in all the AMS acceptance, with* $\beta = 0.999$.

value is slightly above 80%. The distribution presents two distinct populations of events peaked at 25% and at slightly less than 50%. The last one corresponds to events with the direct branch not affected by the presence of the matrix hole, leading to higher values of the photon ring acceptance, while the first population corresponds to events that despite having large rings see a significant part of the direct photons fall in the dead square with a side length of 64 cm.

The extreme variation of ε_{geo} from event to event is clear in both aerogel and sodium fluoride.

4.4.4 Detection efficiencies evaluation

Radiator efficiency

The main interactions suffered by the Čerenkov photons inside the aerogel radiator are Rayleigh scattering and absorption while for the sodium fluoride radiator the only significant interaction that photons can suffer is absorption but negligible since the radiator thickness is very small compared to the absorption length. The absorption rate is two orders of magnitude below the scattering rate in the aerogel so it can be neglected in a first approach [160]. The radiator efficiency depends on the distance, $d_\gamma(\theta, \phi, \theta_c, z, \varphi)$, crossed by the photons inside the radiator, which is function of the particle direction (θ,ϕ), of the Čerenkov angle (θ_c), of the photon emission point (z) and of the photon azimuthal angle φ. The photon crossed distance can be simply written as $d_\gamma(z, \varphi)$ for each photon generated by the same particle. It is calculated by integrating the probability of a photon not to interact in the radiator, $p_\gamma^{\overline{int}} = e^{-d_\gamma(z,\varphi)/L_{int}}$, along the radiator thickness and along the photon azimuthal angle (φ). For Rayleigh scattering, the interaction length depends on the wavelength of the photons, according to expression:

$$L_{int} = \lambda^4/C \tag{4.43}$$

where C is the aerogel clarity.

Therefore, the fraction of photons surviving to the radiator interaction (*radiator efficiency*) can be evaluated through the following expression:

$$\varepsilon_{rad} = \frac{1}{\Delta\varphi H_{rad}} \int_0^{H_{rad}} dz \int_{\varphi^i_{min}}^{\varphi^i_{max}} e^{-\frac{d(z,\varphi)}{L_{int}}} d\varphi \tag{4.44}$$

where H_{rad} is the radiator thickness. Figure 4.28 presents the evaluated radiator efficiency, ε_{rad}, for an aerogel radiator (1.050), 2.5 cm thick, with a clarity coefficient $C = 0.0052\,\mu\text{m}^4\text{cm}^{-1}$. The radiator efficiency in aerogel is around 65%. Equation 4.43 shows a dependence on the photon's wavelength that is an unknown variable for each photon. An average wavelength could be used but this quantity would depend on the radiator's clarity. The best solution would be parametrizing the interaction length as function of the clarity. In this algorithm the function L_{int} is given by

$$L_{\text{int}}(C) = \frac{0.0327}{C^{0.867}}\,(\text{cm}), \tag{4.45}$$

where C is expressed in $\mu\text{m}^4\text{cm}^{-1}$. The derivation of this parameterization will be explained in the next paragraph.

For a matter of simplicity the integration on the variable λ was not considered in expression 4.44. If it was explicitly written it would be:

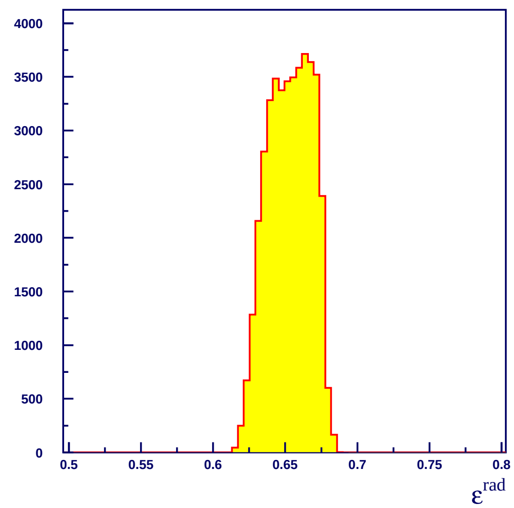

Figure 4.28: *Radiator efficiency, ε_{rad}, for an aerogel radiator (1.050), 2.5 cm thick, with a clarity coefficient $C = 0.0052\,\mu\text{m}^4\text{cm}^{-1}$.*

$$\epsilon_{\text{rad}} = \frac{1}{\Delta z \Delta\varphi \int_{\Delta\lambda} f(\lambda) d\lambda} \int_{\Delta z} \int_{\Delta\varphi} \int_{\Delta\lambda} e^{-\frac{d(z,\varphi)}{\lambda^4/C}} f(\lambda)\, d\lambda d\varphi dz. \tag{4.46}$$

The function $f(\lambda)$ is the detected wavelength spectrum for the Čerenkov photons, which corresponds to the convolution of the emission spectrum with the PMT efficiency spectrum.

The derivation of the parameterization (4.45) used to go from the model of equation (4.46) to equation (4.44) consisted in searching which value for L_{int} should be used in equation (4.44) to obtain the same result of equation (4.46).

More simply, the parameterization is obtained by equalling expression (4.46) to (4.44) and solving numerically the resulting equation on the variable L_{int}. Explicitly:

$$p_\gamma^{\overline{int}} - \frac{1}{\Delta z \Delta\varphi} \int_{\Delta z} \int_{\Delta\varphi} e^{-\frac{d(\varphi,z)}{L_{\text{int}}}} d\varphi dz = 0 \qquad \text{for } L_{\text{int}}, \tag{4.47}$$

where $p_\gamma^{\overline{int}}$ represents the computation of the triple integral of equation (4.46). Here $p_\gamma^{\overline{int}}$ stands for the 'probability of not interacting'.

Repeating this procedure for a set of different clarity values, a curve of points, which can be parameterized, is obtained. The result is displayed in Figure 4.29.

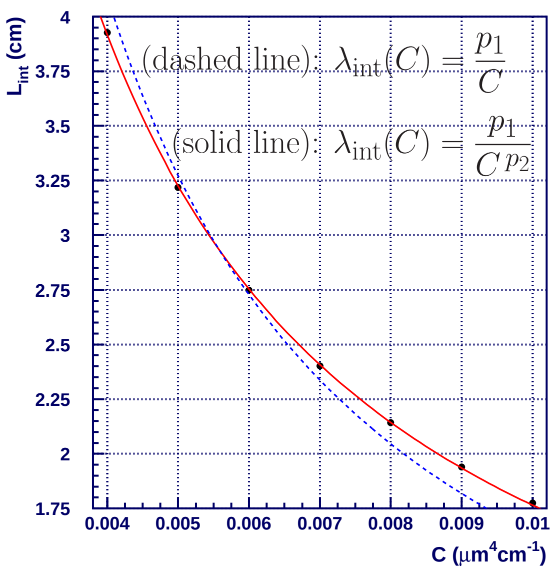

Figure 4.29: *Interaction length versus clarity with two different fitted models: one free parameter (dashed line) and two free parameters (solid line).*

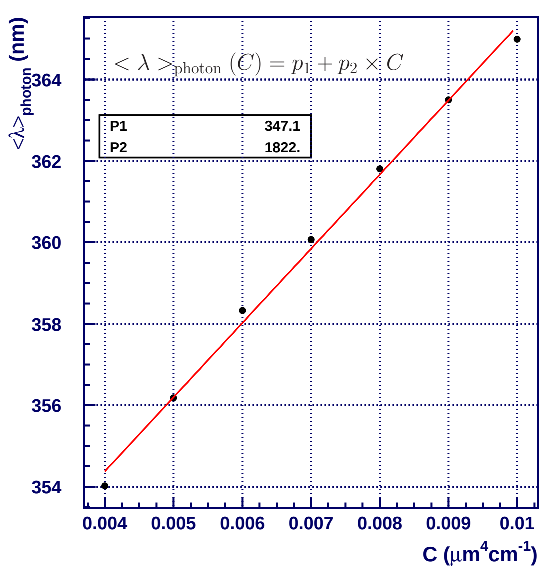

Figure 4.30: *Effective average photon wavelength versus clarity with linear fit.*

Upon the points, two different fits are presented. The dashed line corresponds to the model $L_{\rm int}(C) = \frac{p_1}{C}$, where p_1 is the only free parameter. This fit model is clearly inadequate. The solid line corresponds to the model $L_{\rm int}(C) = \frac{p_1}{C^{p_2}}$, where both p_1 and p_2 are free parameters. This model corresponds to the parameterization of equation (4.45). The values obtained for the two-parameter fit are: $p_1 \simeq 0.0326$ (in $\mu{\rm m}^{4\times0.867}{\rm cm}^{0.133}$), $p_2 \simeq 0.867$ (dimensionless). The odd units of p_1 result from using a non-integer value for the exponent p_2. In fact, for each clarity coefficient of a certain radiator material, the average photon wavelength $<\lambda>$ needed to reproduce the interaction length $\lambda_{\rm int}$ is not constant as can be appreciated in Figure 4.30. The effective average photon wavelength introduced in the radiator efficiency calculation is $<\lambda>_{\rm photon} = [p_1\, C^{(1-p_2)}]^{0.25}$ with $p_1 \simeq 0.0326$ (in $\mu{\rm m}^{4\times0.867}{\rm cm}^{0.133}$), $p_2 \simeq 0.867$

(dimensionless), as presented above.

Light guide efficiency

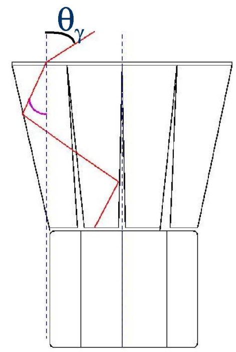

Figure 4.31: *Light guide scheme with the definition of the photon incident angle (θ_γ).*

Photons can be reflected when reaching the light guides' surface or be transmitted between adjacent light guide divisions. The light guide efficiency factor ϵ_{lg} depends on the incidence angle of the photons on its top (θ_γ). This photon angle is schematically represented in Figure 4.31. The distribution of the photon's incident angle on the top of the light guide is shown in the left-hand plot of Figure 4.32 for photons radiated in aerogel 1.030, aerogel 1.050 and sodium fluoride. For photons generated in aerogel the incidence angle in the top of the light guide is up to less than 50° while for sodium fluoride is up to 70°. The light guide efficiency as function of the incident angle at the top of the light guide cell is presented in the right-hand distribution of Figure 4.32 which was extracted from the RICH simulation.

This efficiency is calculated event by event taking into account the probability of a given photon getting into the photomultiplier cathode since it entered the light guide, and integrating it along the reconstructed photon pattern:

$$\varepsilon_{lg} = \frac{1}{\Delta\varphi} \int_{\Delta\varphi} \epsilon_{lg}[\theta_\gamma(\theta, \theta_c, \varphi)] d\varphi. \qquad (4.48)$$

Distributions of the light guide efficiencies for events within AMS acceptance in aerogel 1.050 (left) and in sodium fluoride (right) are shown in Figure 4.33.

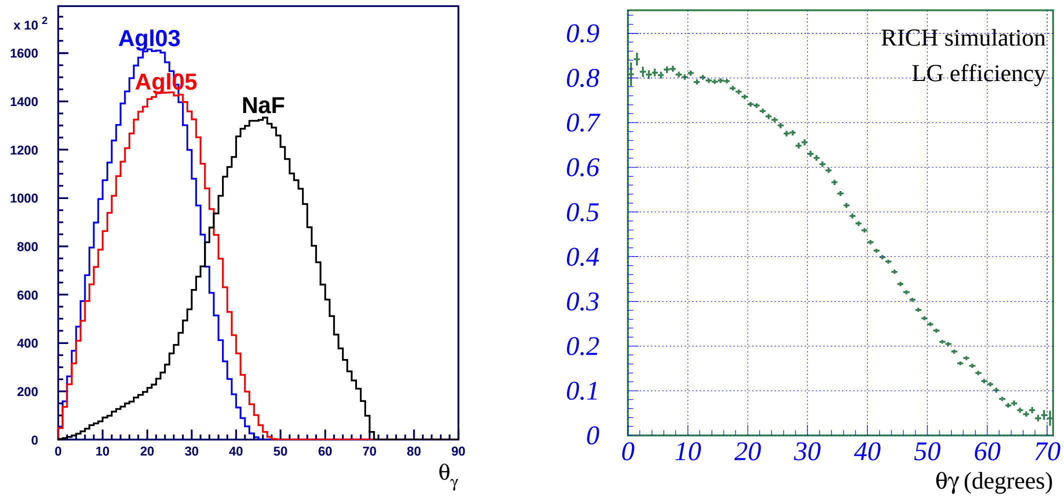

Figure 4.32: *Incidence angles at the top of light guide for aerogel and sodium fluoride* (left). *Light guide efficiency as function of the incident angle at the top of the light guide* (right).

The light guide efficiency is lower for photons radiated in the sodium fluoride ($25\% < \epsilon_{lg} < 47\%$) than for photons radiated in aerogel 1.050 ($43\% < \epsilon_{lg} < 82\%$) due to the higher incident photon angles.

In this algorithm the light guide efficiency is calculated only as function of θ_γ. In fact this is also function of the photon azimuthal angle, φ, $\epsilon_{lg}[\theta_\gamma(\theta, \varphi)]$ and of the light guide prism, from now on called light guide pipe, on which it impacts. The 16 pipes have three different geometries: central, lateral and corner pipes. This fact means different inclinations of the pipe walls with respect to the guide top surface and to the photon incident direction and consequently different detection efficiencies. However, an average over all the photon azimuthal angles and for the three pipe types is done for the light guide efficiency calculation.

Photomultiplier efficiency

The PMT quantum efficiency is defined as the ratio between the number of photons reaching the PMT photocathode and the number of photoelectrons produced. It will be assumed as a constant value ($\sim$14%) for each event since the photon wavelength spectrum is not affected by the reducing factors. It results from the convolution of the photons' radiated energy spectrum with the quantum efficiency curve of the

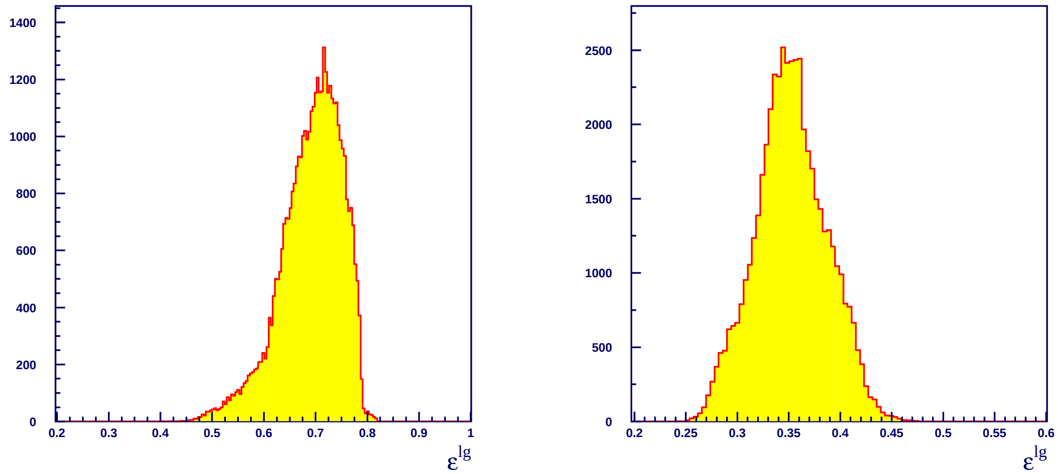

Figure 4.33: *Distribution of the light guide efficiencies for events within the AMS acceptance in aerogel 1.050* (left) *and in sodium fluoride* (right).

photomultiplier as expressed in equation 3.23. However, this factor will be applied as a multiplicative correction factor evaluated from simulation as will be explained in the next paragraphs.

Total efficiency

The overall event efficiency can be written as:

$$\varepsilon_{tot} = \frac{1}{2\pi H_{rad}} \int_0^{H_{rad}} dz \sum_i^{n_{paths}} \rho_i \int_{\varphi^i_{min}}^{\varphi^i_{max}} d\varphi \left[e^{-\frac{d(z,\varphi)}{L_{int}}} \varepsilon_{lg}(\theta_\gamma) < \varepsilon_{pmt} > \right] \tag{4.49}$$

where H_{rad} is the radiator thickness, θ_γ is the polar angle of the radiated photon, n_{paths} is the number of visible branches constituting the reconstructed pattern (i.e. reflected and direct branches), and ρ_i is the reflectivity for the i^{th} path.

Figure 4.34 (left) presents the overall efficiency ε_{tot}, without taking into account the PMT efficiency, for a sample of events crossing the aerogel radiator, while Figure 4.34 (right) presents the same distribution for events generated in the sodium fluoride radiator. In aerogel 1.050 this total efficiency is lower than 50% while in NaF it is between 4% and 30% with a peak structure reflecting the same effect present in the photon ring acceptance distribution (right-hand panel of Figure 4.27). The previous

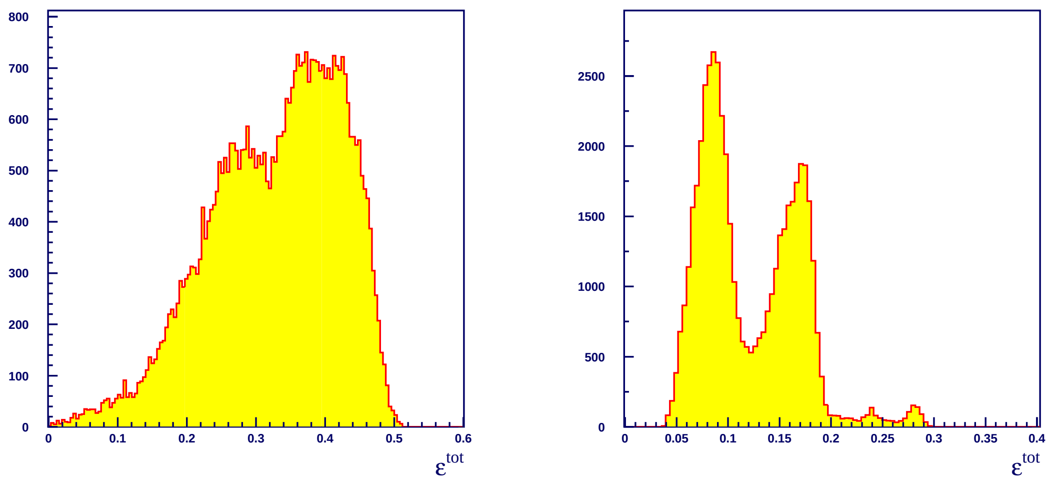

Figure 4.34: *Distribution of light guide efficiencies for events within the AMS acceptance in aerogel 1.050* (left) *and in sodium fluoride* (right).

overall factor was an analytical calculation, however a sampling was done to evaluate the fraction of photons lost in the gaps between the aerogel tiles and in the dead spaces between light guides. This non-analytical strategy was followed for sake of simplicity in the calculations and consequent computing time saving.

In addition, a multiplicative correction factor can be evaluated from simulation by comparing the calculated overall detection efficiency with the detection efficiency computed from simulation as the ratio between the number of photoelectrons and the number of radiated photons ($N_\gamma^{det}/N_\gamma^{rad}$). In fact not only the effect of PMT quantum efficiency but also the effect due to the presence of a plastic foil after the radiator with a certain absorption ($<\varepsilon_{other}>$), which are small contributions, can be extracted from the slope of the line adjusted to the population of points in Figure 4.35. The spread of the scattered point distribution with respect to the straight line with a slope different than one reflects the overall factors.

In this framework,

$$\varepsilon_{tot}(reconstruction) \cdot <\varepsilon_{pmt}> \cdot <\varepsilon_{other}> = \varepsilon_{tot}(simulation), \qquad (4.50)$$

which allows us to write

$$<\varepsilon_{pmt}> \cdot <\varepsilon_{other}> = \frac{\varepsilon_{tot}(simulation)}{\varepsilon_{tot}(reconstruction)} = \frac{1}{slope}. \qquad (4.51)$$

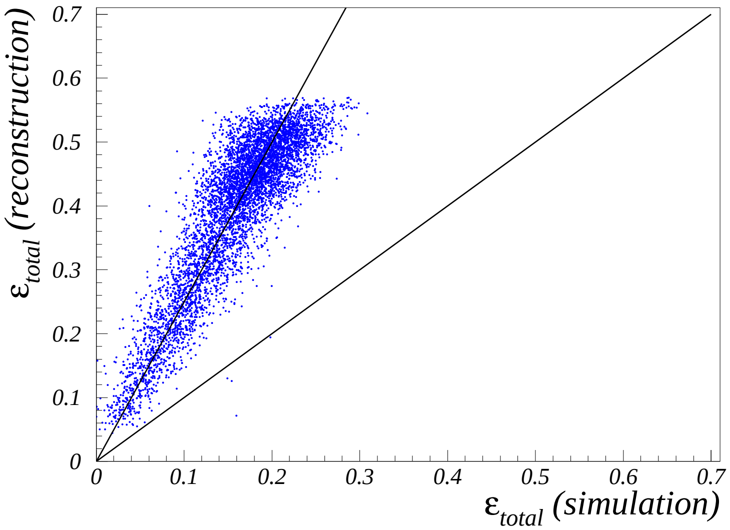

Figure 4.35: *Comparison between the evaluated efficiency and the value obtained from simulation for aerogel 1.050.*

The mean quantum efficiency value affected by the aforementioned small corrections is

$$< \varepsilon_{pmt} > \cdot < \varepsilon_{other} > \sim 14\%. \tag{4.52}$$

4.5 Charge Reconstruction Uncertainties

The number of radiated photons by an electric charge Z, crossing a dielectric medium with $\beta > c_{medium}$ is given by:

$$N_\gamma \propto \Delta L Z^2 \sin^2 \theta_c, \tag{4.53}$$

where ΔL is the radiator length crossed by the charged particle. The same quantity can be written in terms of the number of photons emitted by a proton ($N_{\gamma 0}$) with the same velocity and with the same crossed radiator length,

$$N_\gamma = N_{\gamma 0} Z^2. \tag{4.54}$$

The same relation is valid for the number of photoelectrons, N_{pe}, from here on called N and N_0, the number of photoelectrons detected in a $Z = 1$ ring. Hence, the charge

Z can be expressed as

$$Z^2 = \frac{N}{N_0} \tag{4.55}$$

an this error can be written as

$$\Delta Z = \frac{1}{2}\frac{1}{N_0 Z}\Delta N. \tag{4.56}$$

Replacing $Z = \sqrt{\frac{N}{N_0}}$, comes:

$$\Delta Z = \frac{1}{2\sqrt{N_0}}\frac{\Delta N}{\sqrt{N}}. \tag{4.57}$$

The error on the measured number of photoelectrons, ΔN, has different components:

$$(\Delta N)^2 = (\Delta N^{stat})^2 + (\Delta N^{PMT})^2 + (\delta N^{syst})^2, \tag{4.58}$$

where ΔN^{stat} is the statistical uncertainty, $\Delta N^{stat} = \sqrt{N}$; $\Delta N^{PMT} = \sqrt{N}\sigma_{pe}$ is the error associated to the PMT signal amplification, where σ_{pe} is the single photoelectron channel width; finally δN^{syst} is the systematic error whose origin will be discussed after all the algebraic manipulation.

Replacing ΔN in expression 4.57 and after some manipulation finally comes:

$$\Delta Z = \frac{1}{2}\sqrt{\underbrace{\frac{1+\sigma_{pe}^2}{N_0}}_{\text{statistical error}} + Z^2 \underbrace{\left(\frac{\delta N}{N}\right)^2}_{\text{systematic error}}}. \tag{4.59}$$

This expression describes the two distinct types of uncertainties that affect the measurement of Z: the statistical and the systematic. The statistical term is independent of the electric charge and depends essentially on the Čerenkov signal detected for singly charged particles (N_0) and on the resolution of the single photoelectron σ_{pe}. The systematic term increases with Z and dominates for higher charges. It appears due to non-uniformities at the radiator level coming from spatial variations in the refractive index, tile thickness or clarity; or due to non-uniformities in photon detection efficiency, which can take the form of a global photomultiplier gain variation due to temperature effects, a magnetic field perturbation or an intrinsic variation that arises from the different gains and quantum efficiencies; non-uniformities in the light guide properties (material, geometry, etc.) or on the optical coupling between light guides and photomultipliers.

The uncertainty coming from non-uniformities in the detection cells is scaled down on an event by the factor $\sqrt{N_{channels}}$. Therefore non-uniformities at the level of the photomultiplier are less important since a multianode PMT is used.

The RICH goal of a good charge separation in a wide range of nuclei implies the choice of photomultiplier tubes with a good single photoelectron resolution, a radiator with a high light yield to directly reduce the statistical error and a strict control of the systematic errors which limit the identification of nuclei for higher charges. The last feature implies a good mapping and monitoring of potential non-uniformities present on the detector. Concerning the non-uniformities at the radiator level, the charge dependence with the refractive index, radiator thickness and clarity will be deduced next. The control of the systematic uncertainties at the detection level will be studied in Chapter 9.

4.5.1 Refractive index tolerance

To cover a wide range of charge separation in the RICH detector as can be observed in Chapter 6 a maximum systematic uncertainty of the order of 1% can be tolerated. The total number of photons emitted in a radiator of thickness L can be obtained by integrating equation 3.8 which leads to $N_\gamma \propto \sin^2\theta_c = 1 - \frac{1}{\beta^2 n^2}$ that implies

$$\frac{\Delta N_0}{N_0} \equiv \frac{\Delta(1-\frac{1}{\beta^2 n^2})}{1-\frac{1}{n^2}} \equiv \frac{\Delta(n-1)}{n-1} (\text{for } \beta \simeq 1 \text{ and for } n{=}1.050). \tag{4.60}$$

Hence,

$$\frac{\Delta(n-1)}{n-1} \sim \left(\frac{\Delta N_0}{N_0}\right)_{\text{syst}} \equiv 10^{-2} \Rightarrow \frac{\Delta n}{n} = \frac{\Delta(n-1)}{n-1} \times \frac{n-1}{n} \sim 10^{-4} \tag{4.61}$$

From the point of view of the velocity reconstruction the acceptable variation for the refractive index can be estimated based on the limit of the beryllium isotope mass separation which is the highest element that AMS expects to be able to separate in a wide range of kinetic energy which is from $0.5 \lesssim E \lesssim 8\,\text{GeV/nucleon}$ (see section 1.3). According to what was discussed before, neglecting photons refraction at the radiator/air transition, the relative resolution of β is given by

$$\frac{\Delta\beta}{\beta} = \frac{1}{\sqrt{N}} \sqrt{(\tan\theta_c)^2 \Delta\theta_c^{\,2} + \left(\frac{\Delta n}{n}\right)^2} \tag{4.62}$$

where $\frac{\Delta n}{n}$ is the variation in the refractive index due to the chromatic effect and N is the total number of photoelectrons in the event. Since in aerogel $n = 1.050$ $\frac{\Delta n}{n} \sim 1.1 \times 10^{-3}$, $\Delta\theta_c \sim 4\,\mathrm{mrad}$ and $\tan\theta_c \sim 0.32$ and for beryllium nuclei $N^{Be} \sim N^H \cdot (Z=4)^2 \sim 110$ comes $\frac{\Delta\beta}{\beta} \sim 1.1 \times 10^{-4}$.

The inhomogeneities of the refractive index that are being discussed appear as a systematic contribution that will add up quadratically to the velocity uncertainty.

$$\left(\frac{\Delta\beta}{\beta}\right)_{TOT} = \left(\frac{\Delta\beta}{\beta}\right) \oplus \left(\frac{\Delta n}{n}\right)_{syst} \tag{4.63}$$

The first parcel is $\sim 1.1 \times 10^{-4}$ which automatically constrains $\left(\frac{\Delta n}{n}\right)_{syst}$ to be not greater than 10^{-4} if the purpose is not to affect the present kinetic energy limit for beryllium isotope separation.

The reconstructed mass has an uncertainty which is related to the velocity and momentum uncertainties through the following relation:

$$\frac{\sigma}{M} = \gamma^2 \frac{\Delta\beta}{\beta} \oplus \frac{\Delta p}{p}; \tag{4.64}$$

So the higher is the measured β value the greater is the degradation in the mass resolution because $\frac{\Delta\beta}{\beta}$ is highly amplified by the γ^2 factor. It is expectable that a degradation in $\frac{\Delta\beta}{\beta}$ could be significant in the context of isotope separation.

In brief the constraints for the refractive index variation are of the same order for charge reconstruction and for velocity reconstruction affecting beryllium mass separation.

4.5.2 Radiator thickness tolerance

Variations on the radiator thickness will have implications on the Z quality measurement.

The number of radiated photons emerging out from the radiator without suffering Rayleigh scattering depends on the radiator thickness and on the clarity. This natural reasoning arises from the fact that the integrated signal for the charge computation is calculated by adding the signal of the hits correlated with the Čerenkov ring which are those produced by unscattered photons.

The total number of radiated photons along the aerogel height H_{rad} and crossing out the tile without suffering Rayleigh scattering is given by

$$N_{\gamma}^{\overline{int}} = \int_{0}^{H_{rad}} \frac{dN}{dz}\, p_{\overline{int}}\, dz, \tag{4.65}$$

where $\frac{dN}{dz} = K$, $p_{\overline{int}}$ is the probability of a photon not interacting after crossing a distance z, $p_{\overline{int}} = e^{-pz}$ with $p = \frac{1}{L_{int}} = C/\lambda^4$ where C is the clarity coefficient. After integration the following expression is obtained

$$N_{\gamma}^{\overline{int}} = K\ L_{int}(1 - e^{-pz}). \tag{4.66}$$

The systematic error due to a radiator thickness variation will be

$$\frac{\Delta N}{N} = \frac{\Delta N_{\gamma}^{\overline{int}}(z)}{N_{\gamma}^{\overline{int}}} = \frac{p\Delta z}{e^{pz} - 1}, \tag{4.67}$$

which leads to

$$\Delta z = L_{int}(e^{pz} - 1)\frac{\Delta N_{\gamma}^{\overline{int}}(z)}{N_{\gamma}^{\overline{int}}}. \tag{4.68}$$

Considering a charge systematic uncertainty of the order of 1%, whose origin will be explained later in section 6.5, the same consideration is applied to $\frac{\Delta N_{\gamma}^{\overline{int}}(z)}{N_{\gamma}^{\overline{int}}}$ that together with $L_{int} = 3.12\,\mathrm{cm}$ implies that the allowed variation in the radiator thickness is $\Delta H_{rad} = \Delta z \sim 0.4\,\mathrm{mm}$.

For the previous deduction two simplifications were used. First, the photon path length was identified with the particle crossed distance; second this distance was calculated as the distance crossed by a vertical particle in the radiator, $l = H_{rad}$. However, as $< \theta > \sim 20^0$ the assumed photon path length is only 6% different from the mean particle length. In reality the distance crossed by the photon is a function of the particle direction (θ,ϕ), of the Čerenkov angle (θ_c), of the photon emission point (z_γ) and of the photon azimuthal angle φ, $d_\gamma(\theta, \phi, \theta_c, z_\gamma, \varphi)$.

4.5.3 Clarity tolerance

Studying the reconstructed charge variation with the aerogel clarity C is simply studying the variation with the scattering interaction length L_{int} since a relative variation on the clarity is a direct variation of the scattering interaction length:

$$\frac{\Delta L_{int}}{L_{int}} = \frac{\Delta C}{C}. \tag{4.69}$$

The systematic error due to a clarity variation will be

$$\frac{\Delta N}{N} = \frac{\Delta N_{\gamma}^{\overline{int}}(L_{int})}{N_{\gamma}^{\overline{int}}} = \frac{\left(\frac{\partial N_{\gamma}^{\overline{int}}}{\partial L_{int}}\right)\Delta L_{int}}{N_{\gamma}^{\overline{int}}} \tag{4.70}$$

and after some manipulation it can be written as

$$\frac{\Delta N_{\gamma}^{\overline{int}}(L_{int})}{N_{\gamma}^{\overline{int}}} = \left(\frac{\Delta L_{int}}{L_{int}}\right)\left(1 - \frac{H_{rad}/L_{int}}{e^{H_{rad}/L_{int}} - 1}\right) = 0.35\left(\frac{\Delta L_{int}}{L_{int}}\right). \tag{4.71}$$

Considering $L_{int} = 3.12\,\text{cm}$ and allowing for a systematic uncertainty $\frac{\Delta N_{\gamma}^{\overline{int}}(H_{rad})}{N_{\gamma}^{\overline{int}}}$ of the order of 1% the maximum acceptable relative variation on L_{int} or on the clarity is of the order of 3%.

$$\frac{\Delta L_{int}}{L_{int}} = \frac{\Delta C}{C} \sim 3\% \tag{4.72}$$

The same simplifications for the photon crossed distance inside the radiator used in the previous subsection were assumed.

4.5.4 Simulation results: charge studies

Figure 4.36 (left) shows the reconstructed charge peaks from simulated hydrogen, helium, beryllium, carbon and oxygen nuclei in the aerogel radiator. Each sample has 20000 events and was generated in the aerogel radiator acceptance. Figure 4.36 (right) presents the evolution of the charge resolution with the same charge. The data points are fitted with the law of equation 4.57 and the parameters obtained are $\sigma_{pe} = 0.56 \pm 0.01$ and $\frac{\Delta N}{N} = (4.24 \pm 0.05)\%$. $Z = 1$ was excluded of the fit due to its better resolution than the expected from the σ_Z evolution with Z. In fact, the low number of photoelectrons associated to proton events and the required minimal number of hits generate a truncated distribution not really gaussian and consequently a simple gaussain fit does not evaluate correctly the width of this peak.

4.6 Conclusions

The velocity of the cosmic rays with the RICH detector of the AMS experiment can be measured through the reconstruction of the Čerenkov angle using a maximum

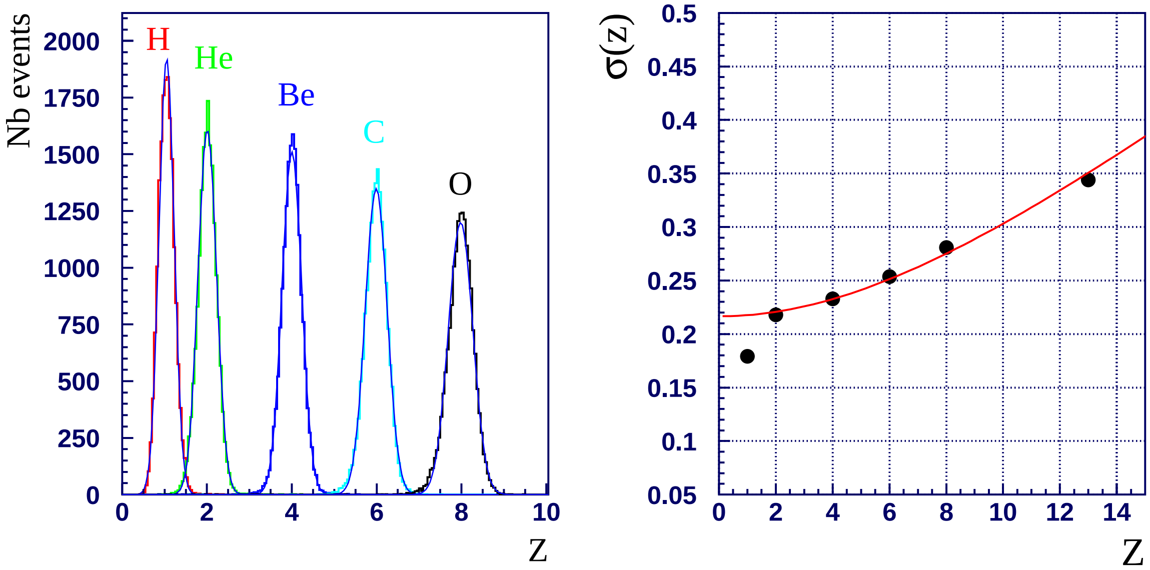

Figure 4.36: *Charge reconstruction with simulated data in the RICH detector with the aerogel 1.050 radiator* (left). *Charge resolution obtained with a gaussian fit to the charge peaks of the distribution pn the left* (right).

likelihood approach. The method consists on finding the Čerenkov angle maximising the overall probability of the detected hits to belong to its corresponding pattern. Charge reconstruction is made in an event-by-event basis. It is based both on the velocity reconstruction procedure, which provides a reconstructed photon pattern, and on a semi-analytical calculation of the overall efficiency to detect the radiated Čerenkov photons belonging to the reconstructed photon ring.

The velocity reconstruction algorithm was optimized and a resolution of $\sigma_\beta = (1.20 \pm 0.01) \times 10^{-3}$ is attained for protons with $\beta \simeq 1$ in aerogel $n = 1.050$ while in the sodium fluoride a resolution of $\sigma_\beta = (3.09 \pm 0.03) \times 10^{-3}$ is attained for the same kind of particles.

Electric charge is reconstructed with a systematic of $\frac{\Delta N}{N} = (4.24 \pm 0.05)\%$.

Chapter 5

The RICH prototype of the AMS Experiment: 2003 Beam Test

... where the web was born!
CERN webpage

5.1 Introduction

In order to validate the RICH design, a prototype with an array of 9×11 cells filled with 96 photodetector readout units similar to part of the final model was constructed. In addition, different components associated to the RICH operation were tested and evaluated: the aerogel radiator characterization regarding the physics goals of the experiment, the charge and velocity measurements and the RICH Monte Carlo validation and tuning.

Its performance has been evaluated both with cosmic rays at sea level (mainly muons) and beam ions. The former tests took place at LPSC in Grenoble between March and August of 2002, while the latter took place in 2002 and 2003 at the CERN SPS using a beam of secondary ions produced by fragmentation of a primary beam. The description of the cosmic muon tests can be found in [148, 171] and the corresponding data analysis can be found in [167]. The detailed analysis of the 2002 beam test can be found in [172, 173]. The analysis of the 2003 beam test will be herein described and was independently presented in the thesis [163].

The cosmic-ray tests proved the correct performance of the front-end electronics as well as the performance of the readout system. The same tests proved the counter capability of measuring particle velocity as well as of measuring charges equal to unity despite the fact of a natural limitation existing on the available spectrum. However, the data acquired had limitations on the statistics due to the reduced geometrical acceptance derived from the use of wire chambers to measure the particle's track. The same subdetector did not provide a precise measurement of the particle's momentum. This constrained the complete analysis of the candidate aerogel samples for the radiator.

Moreover, the idea of performing a beam test was to study the detector's response to higher charges similar to the CR flux in space. Ideally, the ion beam test should cover the sensitivity range of the RICH counter, i.e. it should provide isotopes over the mass range $A \lesssim 30$ with $4 < P/A < 10\,\mathrm{GeV/c/nucleon}$ (P/A is the momentum per nucleon) to study the β measurement capability for nuclear mass identification (isotope separation) and it should provide higher-charged nuclei up to a realistic limit for charge separation $Z \lesssim 26$. In addition, high Z ions are also interesting to test the overall response of the photodetection system in the high Z regime. With the SPS ion beam charges up to $Z \sim 30$ were available with a suitable control of the beam settings.

In the first ion beam tests (2002), three Matshushita aerogel samples (n=1.03, 1.05) and two Novosibirsk samples (n=1.03, 1.04) were tested and their light yields were evaluated. The counter performed well but from data analysis some modifications to the front-end electronics were suggested. The idea of a second beam test arose from the need to test the new electronics, to test a mirror prototype and to evaluate the performance of a sodium fluoride sample and of new aerogel batches. The presence of a tracker prototype provided a much more precise track as well as an accurate and independent charge measurement.

5.2 RICH Prototype

The RICH prototype consists of a photomultiplier readout matrix with 96 units, corresponding to about 14% of the total number of channels in the final detector (see Figure 5.1), plus a radiator.

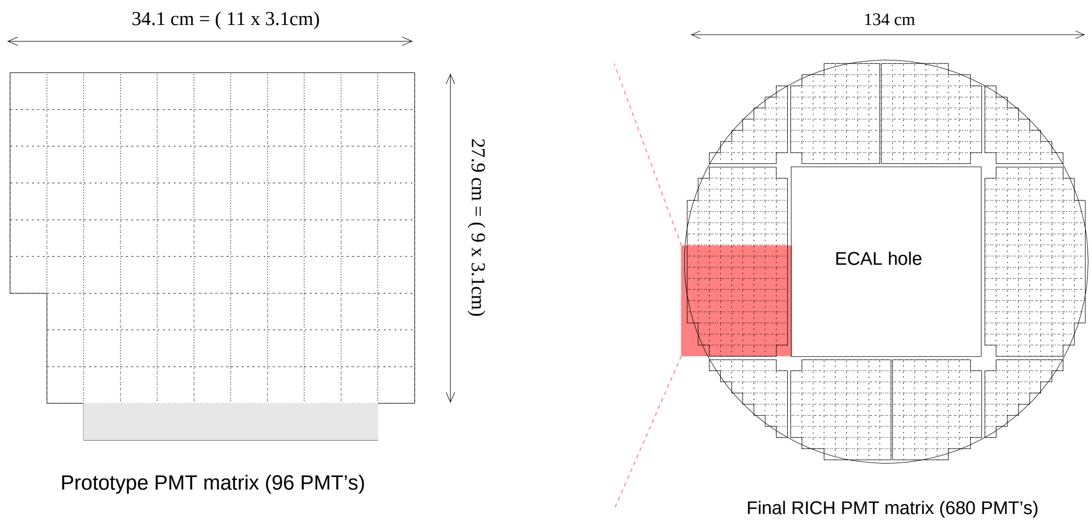

Figure 5.1: *Prototype and flight setup PMT matrices. The prototype PMT matrix consists of approximately one module of the final setup. The shadowed row of the Prototype matrix has no PMT's.*

The detection system was equipped with the final multianode photomultiplier. Since the mounting of the light guides with $31 \times 31\,\mathrm{mm}^2$ were done with no gaps, a continuous active readout area of $27.9{\times}34.1\,\mathrm{cm}^2$ was defined. This will not be the case in the flight configuration since the magnetic shielding structure was changed.

In the two beam tests, different samples of the radiator material were tested and placed in a board connected to an adjustable supporting structure allowing to use different expansion heights in order to have fully contained rings on the detection matrix like in the flight design. Different production batches from two manufacturers, Matsushita Electric Co. (MEC) [174] and Catalysis Institute of Novosibirsk (CIN) [175] with different refractive indices between 1.03 and 1.05, were analysed. A sample of sodium fluoride was also used.

Figure 5.2 shows a photographic view of the prototype setup.

The front-end electronics (see subsection 3.3.5) consists of preamplifiers that integrate the charge of the corresponding PMT anode and convert it in voltage signals. The acquisition is a process of double sampling of the analogue signal picked up at the sensors, first with gain $\times 1$ and then $\times 5$, meaning that there are data related to the 32 channels of the preamplifier ($16{\times}2$ gains). The 32 signal values are sent to the ADC (Analog to Digital Converter) that performs the digitization.

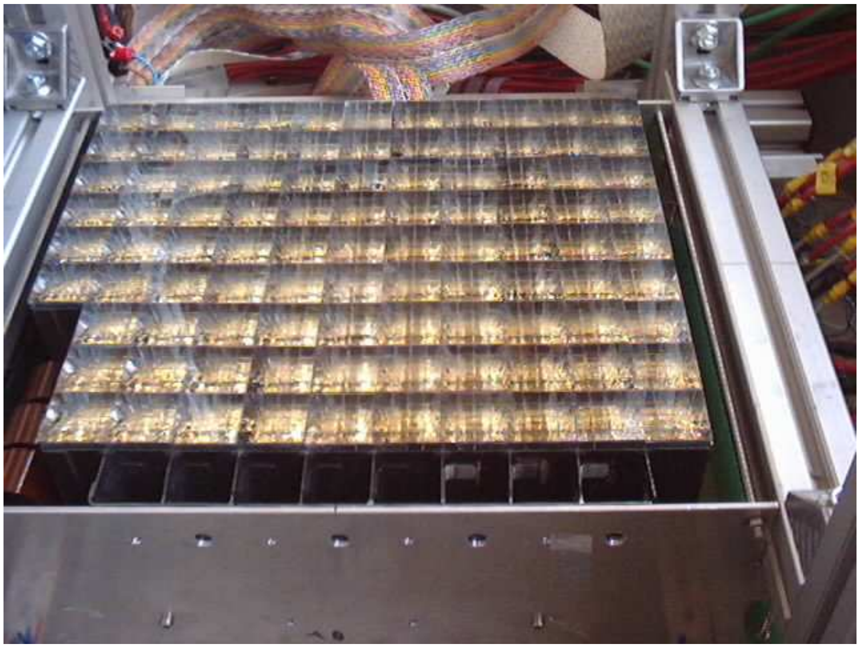

Figure 5.2: *RICH prototype.*

The front-end electronics designed at the LPSC-Grenoble is the final one to be used in the flight setup. Figure 5.3 shows the front-end chip architecture.

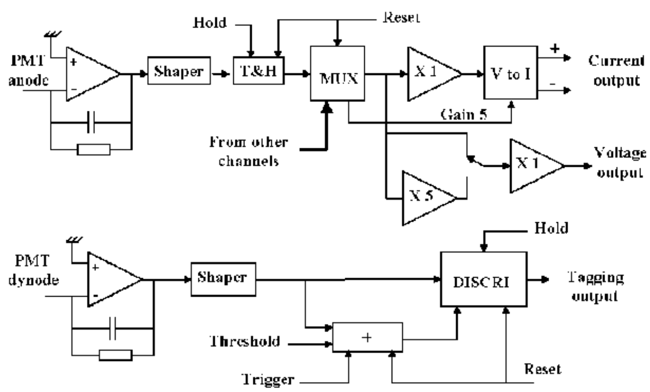

Figure 5.3: *Front-end chip architecture* [176].

The readout system consists of three CAEN boards model S9007 [177] already used in the PAMELA experiment. Each of these boards has an Altera FPGA[1] of the APEX20KE family [178] whose main task is to generate the signals to activate the read-out, process the digitized data and store the results in memory to be read from the external control. Each board is connected to 33 PMT's (528 channels).

[1]A FPGA is a programmable device that allows the integration of different logic functions.

Moreover it has an Analog Device DSP of the series ADSP2187 [179] that performs the digitized data processing and calibrates the detector.

The external control system is located 40 m away from the prototype and it is composed of a personal computer where a control program developed in LabView [180] is running; a VME module dedicated to read the registered events from the RAM memories and store the data in the hard disk of a SUN machine; and finally the power supplies of high and low voltage to feed the patch-panel, the readout boards and the *piggyback boards*[2].

The DSP operation mode can be selected from the external control room (PC) and can be switched to:

- Normal mode: By default data is taken using this mode. In this mode the DSP reduces the event data, i.e. it ignores the pixels whose signal amplitude is below a certain threshold (three σ_{ped}) and in addition proceeds to pedestal[3] subtraction. Moreover this mode performs a selection of gain: the gain $\times 5$ ADC counts are checked and if it exceeds a value lower than 3840 the gain 1 is kept, otherwise the gain 5 is retained. This results in less information to handle;

- Raw data mode: In this mode there is nor data reduction neither gain selection, every pixel is directly written in both gains in the external memory. This is the established mode for pedestal acquisition and for the electronic stability studies.

The readout and storage systems were specially designed for the RICH prototype. For a more complete description of the RICH prototype electronics see the technical note [181].

5.3 2003 Beam Test

As was mentioned in the beginning of the present chapter, the RICH prototype was subject to two beam tests, one in October 2002 and the other in October 2003 both

[2]Responsible of adapting the signals to allow the interface between the readout boards and the external controls.

[3]Electronic noise.

at CERN using the H8 line of SPS facility. In this section a complete description of the 2003 test beam will be given together with some references to the 2002 test beam. The experimental conditions were similar, yet with small but meaningful differences.

5.3.1 Experimental setup

Figure 5.4 shows a general view of the 2003 beam test setup in the experimental area H8-SPS at CERN. All the subdetectors were placed along the beam line. The prototype was placed inside a light-tight container. The setup was completed with AMS silicon tracker prototype layers placed upstream, ∼2 m far from the prototype; a TOF prototype placed downstream; two multi-wire proportional chambers (MWPC); two organic scintillator counters; and, during a certain period, a plastic Čerenkov counter. The two scintillators, placed ∼1 m apart in front of the prototype container, provided the DAQ (Data Acquisition) trigger as well as an independent charge measurement. The silicon tracker prototype provided a very precise measurement of the particle's track parameters for the event reconstruction as well as an external selection of charge. In the 2002 beam test the particle track was measured by a multiwire proportional chamber (spatial resolution of 0.21 mm) and a microstrip silicon chamber (spatial resolution of 0.99 mm). In 2003 the measurement performed by the tracker prototype was much more precise.

The 2003 setup was of a major importance because it reproduces very approximately the scenario foreseen for the AMS detector were three independent measurements of the electric charge are done by the TOF, tracker and RICH. Regarding the track reconstruction this system provides the same type of measurement: the silicon tracker prototype reconstructs the particle track based on the signals left in different planes and extrapolates it up to the RICH radiator plane. The extrapolated point is used as an input for the velocity and charge reconstruction algorithms. However, compared to the AMS conditions, the system is not complete since the superconducting magnet is missing.

+ TOF prototype

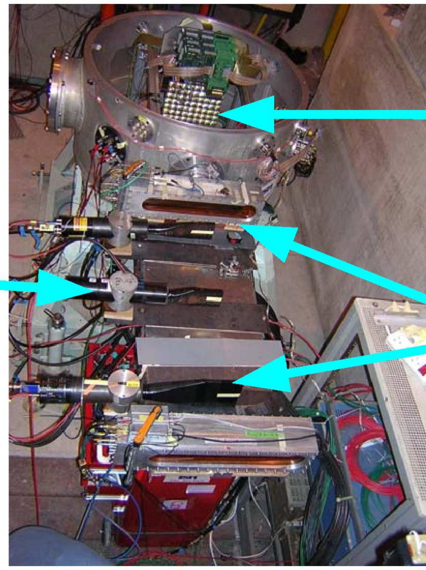

+ Tracker prototype

Figure 5.4: *Top view of the test beam 2003 experimental setup using CERN SPS facility*

Beam characteristics

The basic principle of the beam generation and transport system is of the type used at all accelerator facilities for secondary beam production. Basically a heavy ion beam is used to bombard a production target. Inside the target material, incident ions undergo nuclear fragmentation in peripheral collisions with target nuclei with a large cross section. The incident beam velocity is conserved by the fragments, with only a minor spread of few percent due to the collision kinematics.

In 2003 the secondary beam was obtained by bombardment of a lead (Pb, $Z = 82$) target with a primary beam of $\sim 10^7$, 158 GeV/c/nucleon indium (In, $Z = 49$) ions per spill from the CERN SPS, while in 2002 a beryllium (Be, $Z = 4$) production target was bombarded with 20 GeV/c/nucleon lead ions with a similar intensity.

In 2003 a monochromatic particle beam with a momentum resolution $0.15\% \leq \Delta P/P \leq 1.5\%$ was obtained. This is approximately the same momentum resolution expected for the AMS spectrometer. The optics of the line was tuned to provide a beam as parallel as possible, with a divergence smaller than 1 mrad. The beam section was $\sim$1 mm^2 for the narrow beam runs and $\sim$1 cm^2 for the spread beam runs.

The beam nuclear composition could be selected according to the desired A/Z value of the fragmentation products by setting the beam line rigidity at the appropriate value. Three main selection values were established: $A/Z = 2$ (^{4}He, ^{6}Li, ^{10}B, ^{12}C,...), $A/Z = 2.25$ to enhance the ^{9}Be peak and $A/Z = 2.35$ to enhance the indium peak. The runs with the $A/Z = 2$ setting of the beam line rigidity were narrow beam runs mentioned above while the runs with $A/Z = 2.25$ rigidity selection were spread beam runs. For more details on the beam design see references [182, 183].

Setup Configuration

Different setup configurations were established for data taking. The prototype setup could be rotated with respect to the beam line. The default configuration is established placing the prototype perpendicular to the beam line as represented in the top scheme of Figure 5.5. In the tilted configuration the detector is rotated with respect to beam line in order to allow particle incidences of 0^o, 5^o, 10^o, 15^o and 20^o (see lower left-hand scheme of Figure 5.5). The prototype setup rotates, as a single piece, around a fixed point that is placed $\sim$1.2 cm from the detection plane.

With the prototype fixed in the rotated position, data can be acquired with a mirror prototype, which is a segment with 1/12 of the total azimuthal coverage, placed close to a lateral side of the detection matrix as represented in the lower right-hand scheme of Figure 5.5. The last interesting configuration for data acquisition consists in leaving the prototype in the default configuration and taking data with the same radiator and the same expansion distance but placing the radiator in different points with respect to the incident beam direction. The runs acquired in these conditions are referred to as *scan runs* and are specially dedicated to the study of tile uniformity.

The different setup configurations enabled the evaluation of both the prototype performance and the reconstruction algorithms with data similar to the flight conditions.

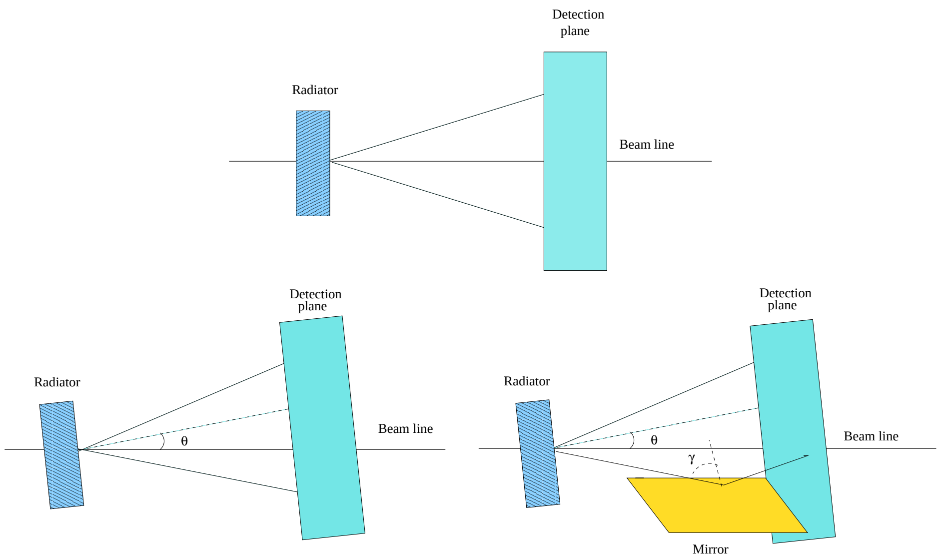

Figure 5.5: *Scheme with the different setup configurations established for prototype data acquisition. Default configuration* (top). *Tilted setup* (bottom left). *Tilted setup with mirror prototype* (bottom right).

5.3.2 Data Characterization

During the 2003 test beam, which lasted ten days (from Wednesday, 22$^{\mathrm{nd}}$ to Friday, 31$^{\mathrm{st}}$ October), around 10 million events were acquired. The prototype expansion distance was adjusted in order to have fully contained rings, varying from $\sim$7 cm for the sodium fluoride runs up to $\sim$43 cm in the aerogel case. Some examples of fully contained rings measured with the beam of ion fragments with the A/Z=2 setting for beam rigidity can be observed in Figure 5.6. The photon patterns from left to right and from top to bottom correspond to Z=2 (helium), Z=3 (lithium), Z=7 (nitrogen), Z=12 (magnesium), Z=18 (argon) and Z=27 (cobalt) ions impacting on aerogel radiator, n=1.03, 3 cm thick. The expansion distance was set at 42.3 cm.

5.3.3 Other subdetectors

The set of additional subdetectors present in the prototype beam test setup is responsible for providing an external trigger as well as giving the particle track and/or giving a complementary charge measurement.

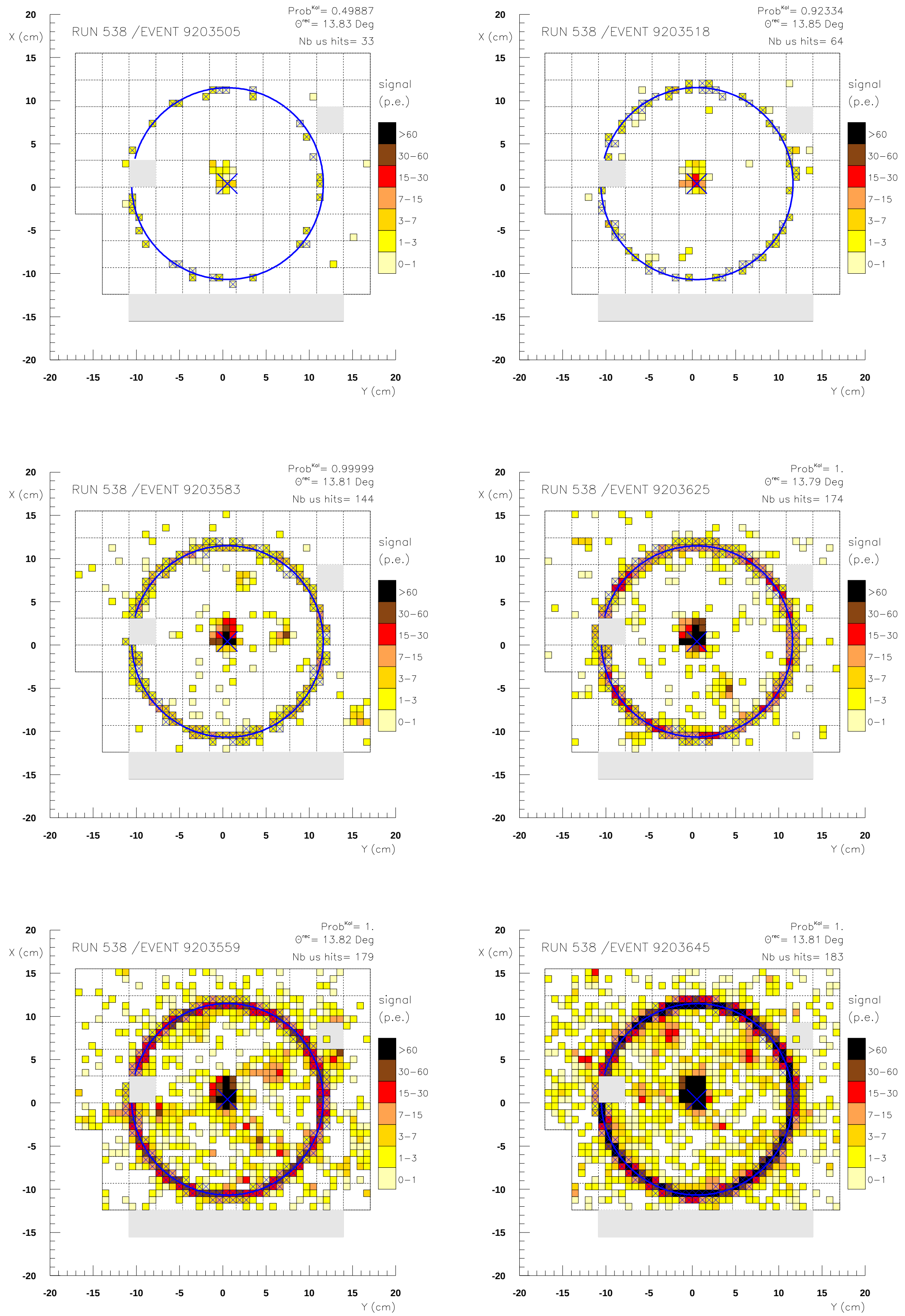

Figure 5.6: *Examples of Čerenkov rings obtained with the beam of ion fragments. The photon patterns correspond to Z=2,3,7,12,18 and 27, from left to right and from top to bottom.*

Scintillator counters

Two organic scintillators, 100×100 mm^2, of the type NE-102 coupled through light guides with RTC-2262B photomultipliers were placed in the beam path for trigger purposes and $\frac{dE}{dx}$ measurements. Figure 5.7 shows the ADC signal spectra measured

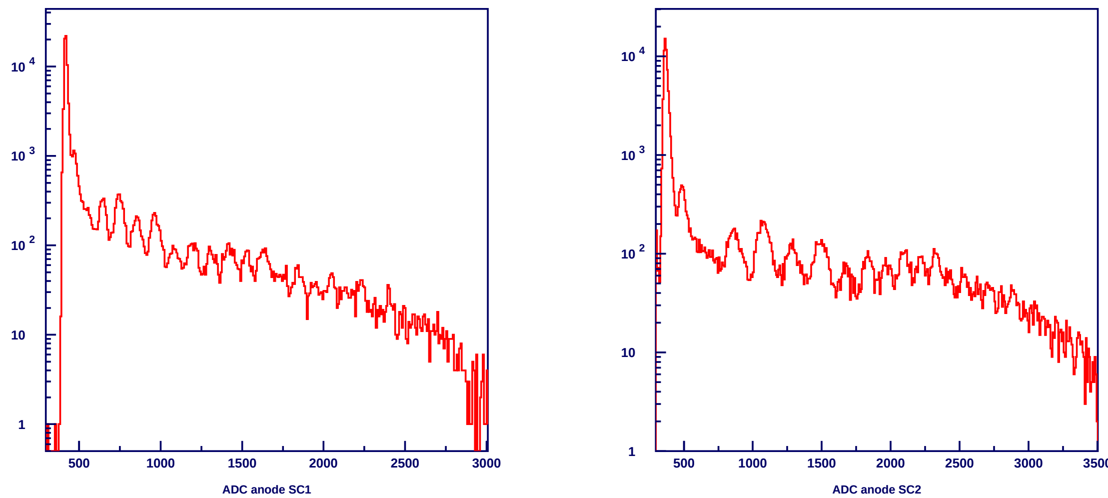

Figure 5.7: *ADC signal spectra for both organic scintillators used in 2003 test beam: SC1* (left)*, SC2* (right)*. The setting of beam rigidity was A/Z=2.*

by both scintillators. Visible and well separated charge peaks are observed in both SC1 and SC2. In a stable setup, for charged particles with the same velocity, the signal is expected to be proportional to Z^2. However, for high charges ($Z \gtrsim 6$), quenching effects occur and the response departs from the expected behaviour on Z^2. Charge separation is visible up to $Z \sim 15 - 20$ for a $A/Z = 2$ beam.

The calibration procedure is done run by run and at least one charge peak must be identified. The case of Be ($Z = 4$) is very illustrative of how this can be done. Since ^{8}Be is not a stable nuclide, the corresponding yield of this element for the $A/Z = 2$ setting, is basically absent from the beam population. This unmistakable, wider gap seen in charge spectra of Figure 5.7 identifies its neighbouring peaks as $Z = 3$ (lithium) and $Z = 5$ (boron).

The calibration for low charges is based on the peak value determination for each scintillator performing individual gaussian fits. Peak coordinates are used to calibrate up to $Z \sim 18$. After this limit, due to the low statistics, the peaks are

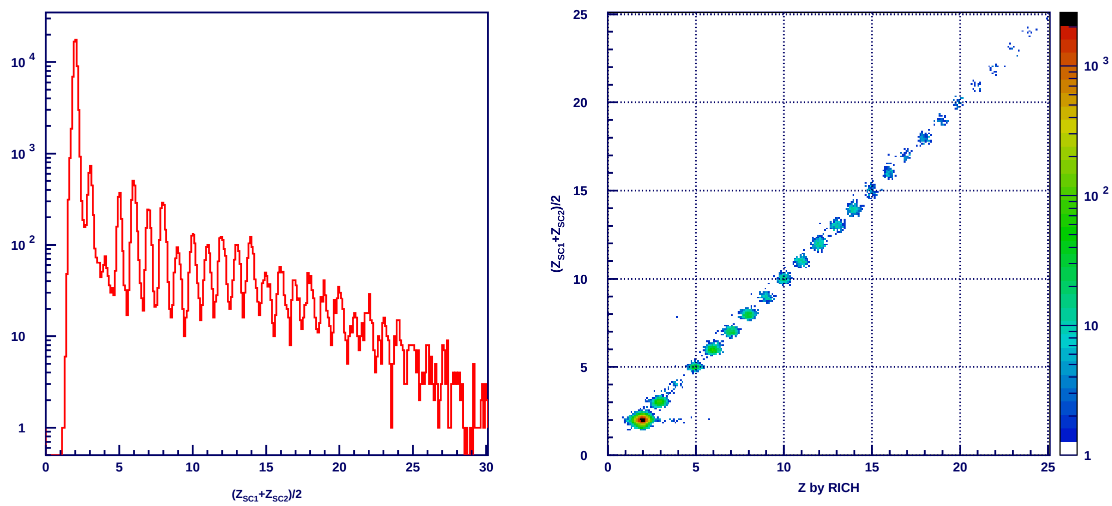

Figure 5.8: *Reconstructed charge spectrum obtained combining anode signals from both scintillators* (left). *The setting of beam rigidity was A/Z=2. Comparison of the charge measurements made by the organic scintillators and by the RICH* (right).

not clearly visible which determined that the calibration is done in a first step by linear extrapolation combining measurements from both scintillators. After that the distribution of $\Delta Z = Z_{SC1} - Z_{SC2}$ is used for cross calibration and the charge measured by one scintillator is corrected to be in agreement with the other, which means ΔZ peaking at zero. The peaks are now visible and their position can be evaluated to the correct place. The final result is the average of the two charge measurements. The charge spectrum of Figure 5.8 (left) with visible peaks up to $Z \sim 26$ is obtained after applying the compatibility cut between the two measurements $|Z_{SC1} - Z_{SC2}| < 0.5$. Finally, Figure 5.8 (right) presents the comparison of charge values measured by the scintillators and RICH. Ion separation can be seen up to $Z = 25$ and an excellent correlation is obtained. For the detailed study on scintillator calibration see reference [184].

Silicon Tracker prototype

A silicon tracker detector (STD) prototype [185] with six ladders, five of them with 12 sensors and one with nine sensors, was present during the 2003 beam test taking synchronized data with the RICH prototype. Data were stored in an ASCII file with the following information:

- Tracker run number and a common event number
- Charge measurement with information on the number of ladders used and χ^2 of the measurement both for S- and K-sides[4]
- Track data: offset, slope, χ^2 of linear fitting and number of ladders used in the fit.

The track is linearly extrapolated from the tracker coordinates to the top of the RICH prototype radiator:

$$\begin{aligned} x_{\mathrm{EXTR}} &= x_{\mathrm{STD}} + \Delta x + lD \\ y_{\mathrm{EXTR}} &= y_{\mathrm{STD}} + \Delta y + mD \end{aligned} \tag{5.1}$$

where (x_{STD},y_{STD}) is the reconstructed position in the tracker, l and m are the two slopes in each direction, Δx and Δy are the offsets between the origin of the tracker frame and RICH frame in the test beam and D is the distance between the silicon tracker and RICH prototypes. The extrapolation of the track to the RICH frame (x_{EXTR},y_{EXTR}) has to be compatible with the RICH measurement (x_{RICH},y_{RICH}) (obtained by a procedure similar to the one explained in subsection 5.10). The alignment consists of determining the values of Δx, Δy and D by minimization of the residuals between the track determined by the RICH and the STD track extrapolated to the RICH. For more details on the track reconstruction analysis see [163].

This extrapolated track is very useful, as will be proved later, since it will be used as input for the RICH velocity reconstruction and consequently for charge reconstruction as well.

On the other hand, the charge measurements provided by the tracker provided an independent way of selecting charges for velocity and charge reconstruction quality studies. The result of the combined measurements of six ladders is shown in

[4] The junction side strips, or S-side, have a readout pitch of 110 μm. The ohmic side, or K-side (its name coming from the fact of being the side where the kaptons are connected), strips have a readout pitch of 208 μm. The particle's curvature is measured by the sensors in the S-side due to its better resolution.

Figure 5.9 for both S-side (left) and K-side (right). Nuclei can be identified up to iron (Z=26) with K-side and up to argon (Z=18) with the S-side. Figure 5.10 (left)

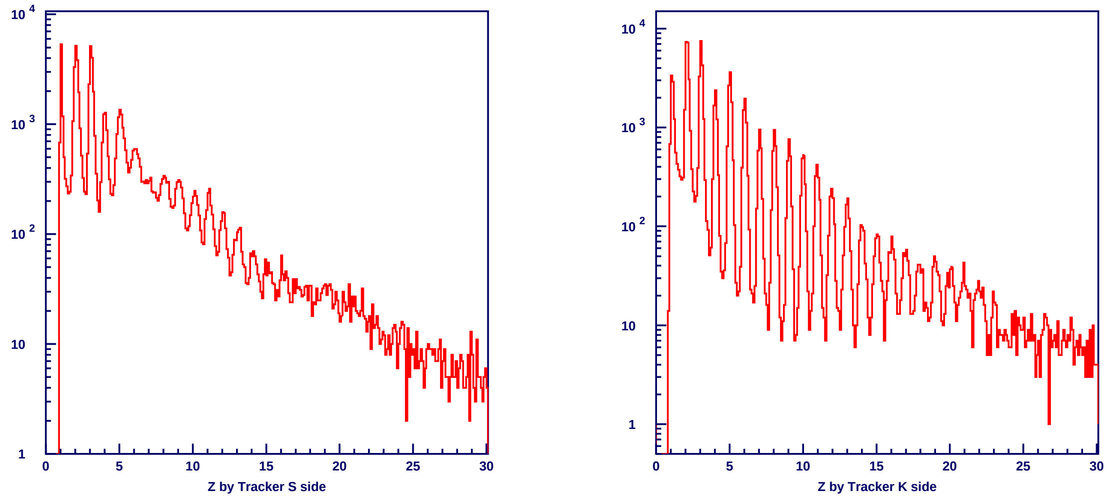

Figure 5.9: *Reconstructed charge spectra by prototype tracker S-* (left) *and K-side* (right).

presents the comparison between the charge measured by the RICH and the charge measured by the tracker K-side while the right-hand plot shows the same comparison between S-side measurement and RICH. An excellent correlation is obtained in both cases.

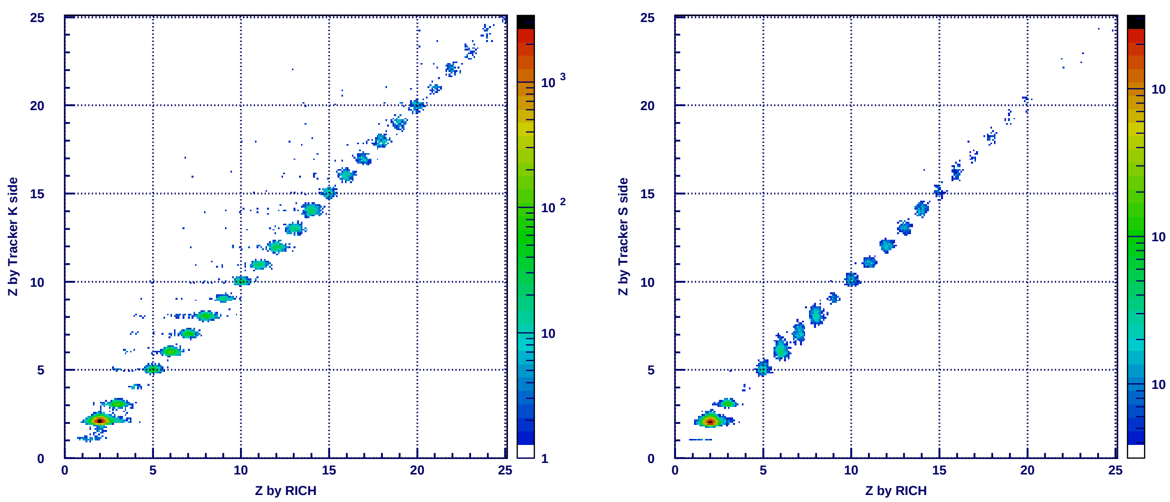

Figure 5.10: *Comparison between charge measurements made by the K-side of silicon tracker prototype and the RICH* (left) *and between the S-side and the RICH* (right).

Time-of-Flight prototype

In the 2003 beam test [186], four TOF scintillator counters with different configurations of the light guides were tested: C1, C2, C3 and C4, according to their order in the beam line. C1 and C4 had straight light guides, C3 had bent light guides and C2 had twisted and bent light guides.

TOF measures the crossing time between two scintillator planes and extracts the velocity through β=$\Delta L/\Delta t$. The time-of-flight resolution for C2 and C3 as function of particle charge is shown in Figure 5.11 (left) as function of the particle charge. As was described one of the tested scintillators had bent and twisted light guides (C2) while the other one had bent light guides (C3). A time resolution of 180 ps was estimated for this conservative configuration. However, since the crossing time in AMS02-TOF will be done with four independent measurements, the time resolution which can be inferred is of the order of 130 ps for a MIP.

As was said in Chapter 2, TOF, like the tracker, measures the charge through dE/dx samplings. Figure 5.11 (right) shows the charge measurement from the anode signal of one of the TOF counters (C2) tested in ion beam at CERN in 2003, which in principle is the most unfavourable case. Charge separation up to aluminium is visible.

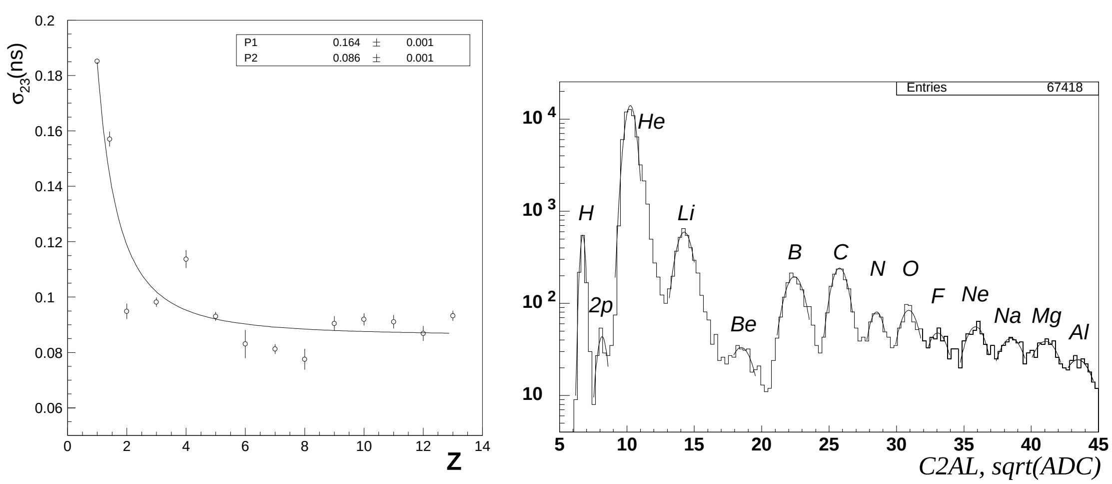

Figure 5.11: *TOF measurements with a set of two scintillators: time of flight resolution for different charged nuclei* (left) *and charge measurements* (right) [126].

5.3.4 Radiator Samples

One of the main purposes of the 2003 beam test was to select the aerogel radiator for the flight setup with the best optical properties based on a high light yield, good velocity resolution (better than 10^{-3} for $Z = 1$ particles) and large range of charge identification (up to $Z \sim 26$). Different aerogel batches from two different manufacturers: Matsushita Electric Co. (MEC) [174] and Catalysis Institute of Novosibirsk (CIN) [175] were tested. Some samples from the 2002 beam test were also submitted to test. Two samples of sodium fluoride from Crystran Ltd [187] were also studied. Table 5.1 shows the list of the tested radiators.

Short name	Manufacturer	n	size ($l \times w \times h\,\mathrm{mm}^3$)	2002	2003
CINy03.103	Novosibirsk	1.03	$100 \times 100 \times 30$		$\surd$
CINy03.104	Novosibirsk	1.04	$57 \times 57 \times 26$		$\surd$
CINy03.105	Novosibirsk	1.05	$55 \times 55 \times 25$		$\surd$
CINy02.103	Novosibirsk	1.03	$50 \times 50 \times 25$	$\surd$	$\surd$
MECy03.103	Matsushita	1.03	$115 \times 115 \times 11$ (3 tiles)		$\surd$
MECy03.1036	Matsushita	1.036	$42 \times 56 \times 11$ (3 tiles)		$\surd$
MECy02.103	Matsushita	1.03	$113 \times 113 \times 11$ (2 tiles)	$\surd$	$\surd$
MECy03.105	Matsushita	1.05	$100 \times 100 \times 11$ (2 tiles)	$\surd$	$\surd$
NaF	Crytan Ltd	1.334	$80 \times 80 \times 5$		$\surd$
NaF10mm	Crytan Ltd	1.334	$80 \times 80 \times 10$		$\surd$

Table 5.1: *Silica aerogel and sodium fluoride radiators studied in the 2003 beam test. Some of the samples were also tested in 2002. The number between brackets in the tile size entry refers to the number of tiles piled up to obtain the final radiator thickness. The dimensions presented refer to a single tile.*

5.4 Data Characterization

All the data taking, performed over a ten-day period, was real-time monitored using a visualization program developed by the CIEMAT group. The program reads a certain number of events stored in memory and displays the Čerenkov patterns. At a first glance this allows to check if the ring is fully contained, if it presents a reflected branch, in case one is expected, or if the kaptons are correctly collecting the signal. The scintillator's ADC countings were also shown. However, this is just a quick check of the data quality. Prior to data analysis, a set of actions are performed:

- calibration: photomultipliers, MWPC, scintillators, track alignment;
- checking of the detection matrix stability;
- checking of the beam characteristics.

5.5 Photomultiplier Calibration

An accurate photomultiplier calibration is a key condition for an accurate charge measurement.

As in the flight matrix, the prototype PMT's are powered by groups with the same high voltage (HV) regulators. This requires that PMT's are sorted by their gains, which were previously measured. The PMT's in each group controlled by a given HV unit have their gains contained in a narrow range in order to provide a uniform response that does not limit the established dynamic range of the detector. In the 2003 beam test the nine photomultiplier kaptons were fed with the high voltage values described in Table 5.2.

Kapton Nb	1	2	3	4	5	6	7	8	9
Voltage (V)	758	768	800	832	836	841	845	852	866

Table 5.2: *Nominal voltage values applied to each of the nine kaptons.*

The first step is the calibration of each of the 1536 channels. A calibration procedure shall provide the evaluation of two important characteristics for each channel within each photomultiplier: its electronic noise and its response to light.

For each channel it is necessary to determine the pedestal position which associated with the pedestal width σ_{ped} indicates the threshold to apply in the reduced mode. The pedestal width gives a measure of the channel's electronic noise. The pedestal width is less variable than the peak position and has an average value of

~ 5 ADC counts in gain $\times 5$. The peak value is subtracted from the raw ADC signal, and ADC corrected readings lower than three standard deviations of the respective pedestal are rejected.

It is important to know, channel by the channel, the response to a single photoelectron (p.e.) with amplification factors 1 and 5. This is known as the gain and is essential for charge reconstruction. The number of photoelectrons is given by $\frac{<\#ADC>-<Ped>}{Gain}$.

The status of the channel is also registered indicating if the channel is working correctly or not. Problematic channels are discarded from the reconstruction. The problems detected more often are an excess of noise, double or negative pedestal and extremely low gain.

Regular calibration runs were taken along the test beam period.

Calibration runs

Data used for calibration belong to one of two types:

- LED[5] run: A widely used method of determining the gains consists in measuring the collected signal in the anode at very low levels of light, where the great majority of successes detected in the PMT were generated by only one incident photon: single photoelectron method. The signal obtained is what is called the single photon answer. Data acquisition is done in raw mode, measuring the complete ADC spectrum as shown in Figure 5.12 (right). Table 5.3 summarizes the LED runs taken in raw mode, additional runs are available in reduced mode. However these runs were not used for calibration since the gains obtained were systematically higher then the gains obtained from raw modes (5%).

- Pedestal run: data acquired in the absence of light to simply measure the electronic noise. Data are also collected in raw mode and the trigger is generated by software. Table 5.4 summarizes the pedestal runs collected.

[5]Light Emitting Diode

Run	Day	Nb events	Mode	HV (V)
1001	22	7319	raw	nominal
611	30	25718	raw	nominal
635	31	10603	raw	[nominal]−50 V

Table 5.3: *LED runs.*

Run	Day	Nb events	Mode	HV (V)
1000	22	2066	raw	nominal
501	23	3032	raw	nominal
524	25	6141	raw	nominal
528	25	4240	raw	nominal
536	25	7076	raw	nominal
558	26	7024	raw	nominal
577	27	2122	raw	nominal
596	28	2308	raw	nominal
605	29	7045	raw	nominal
610	30	3116	raw	nominal
629	31	2198	raw	nominal
634	31	35419	raw	[nominal]−50 V

Table 5.4: *Pedestal runs.*

Pedestal calibration

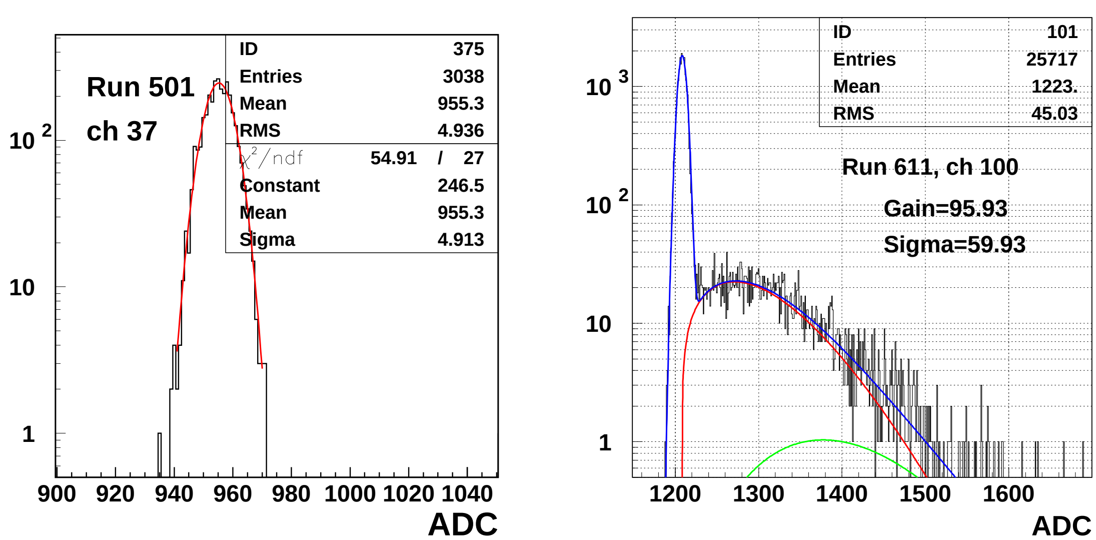

Figure 5.12: *Gaussian adjust to the pedestal of channel 37 in run 501* (left)*. Spectrum of the PMT response in the single photoelectron regime, fitted with the set of functions described in the text* (right) [163].

Both LED and pedestal runs can be used to determine the pedestal peak position and its width (σ_{ped}). Using the latter type of data, a gaussian fit is performed to the signal like it is shown in Figure 5.12 (left).

A pedestal drift was observed for all channels. It occurred mostly after human interventions in the setup and it is not observed neither inside a run nor between pedestal and LED runs. The pedestal mean value shift along the test beam period can be appreciated in Figure 5.13 (left). The mean value of the shift as well as the r.m.s. are plotted for each run. During the time bound by the vertical dashed lines, some channels of two PMTs presented negative or double pedestal. The first kapton pedestals moved to smaller values so these channels were removed from the plot.

The pedestal width is around 4.75 ADC channels in gain ×5 and is kept stable within all the data taking period as can be appreciatted in Figure 5.13 (right). The mean value and the r.m.s of the pedestal sigma distribution of all the channels are presented.

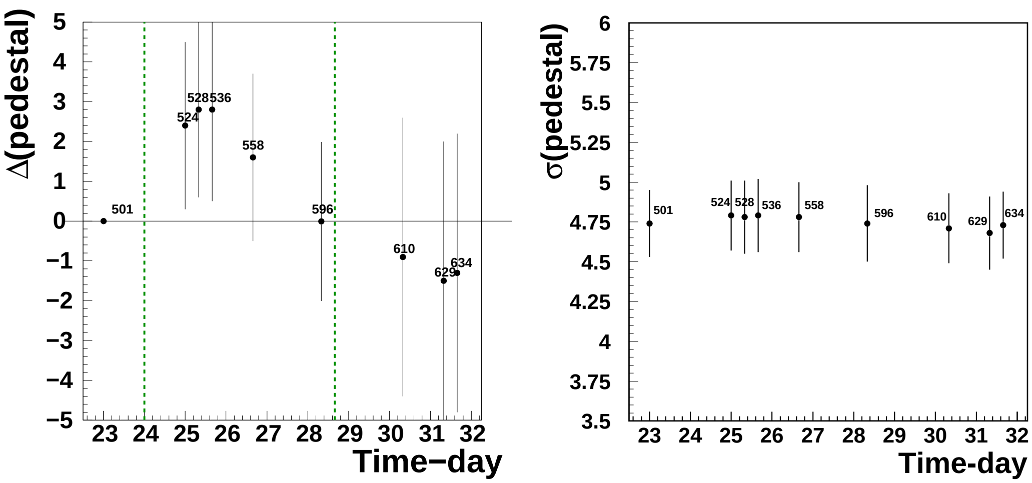

Figure 5.13: *Pedestal mean value shift during the beam test period. The mean value of the shift as well as the r.m.s. are plotted for each run* (left). *Pedestal width. The mean value and the r.m.s of the distribution of pedestal σ for all channels are presented* (right). [188]

Gain calibration

The channel-by-channel gain calibration was done using data taken with a blue LED. Run 1001 was taken at the very beggining of the beam test setup, before the in-beam data taking. Run 611 was taken one week later, while run 635 was taken with high voltage decreased by 50 V in order to accomodate a higher dynamic range required by the beam settings $A/Z = 2.35$ (nuclear fragments up to indium).

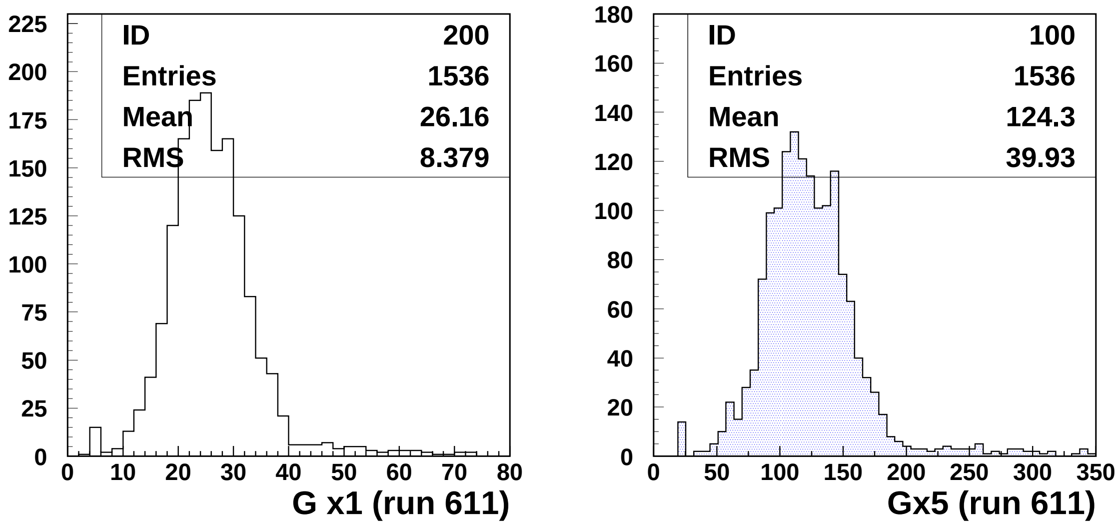

Figure 5.14: *Gain distributions with gain ×1* (left) *and ×5* (right) [188].

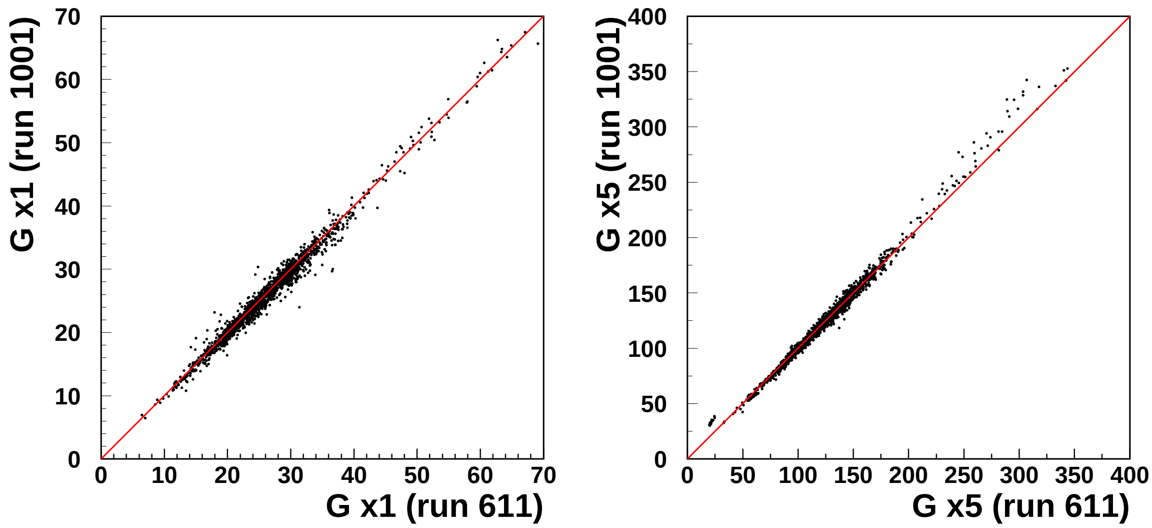

Figure 5.15: *Comparison between measured gains for all channels from run 611 and 1001 with amplification ×1* (left) *and ×5* (right) [188].

Figure 5.12 (right) shows the response of one channel in the single photoelectron regime. The fitted function corresponds to a sum of a gaussian function introduced to describe the pedestal and a set of n-photoelectron response functions whose amplitude is modulated by the Poisson distribution. More details on the fit function are given in note [189]. The overall fit shown in Figure 5.12 includes the contribution of the one and two photoelectrons response and gives the mean number of photoelectrons and the gain. The evaluated mean number of photoelectrons, $\bar{\mu}$, is 0.5, 0.22 and 0.14 for calibration runs 1001, 611 and 635, respectively. The gain of all channels measured in run 611 in gain $\times 1$ and $\times 5$ is shown in the left- and right-hand plots of Figure 5.14 respectively. The mean gain in amplification $\times 1$ is 26.16 while with amplification $\times 5$ it is 124.3 ADC channels. These results are in agreement with the gains calculated from calibration run 1001 within 2% as can be measured from the spread of the data points in Figure 5.15.

Channel status

It was not possible to calibrate less than 2% of the channels and this number varies slighly along the beam test period [163]. The channel status containing information about the quality of the gain and pedestal determination is included in a database that is read during data analysis.

5.6 Stability of the Detection Matrix

The stability of the photomultiplier gain was monitored during the beam test at different periods of time. A good observable to monitor the gain stability is the mean signal amplitude per hit in helium rings because these are the most abundant nuclei in the runs with the $A/Z = 2$ setting of the beam line rigidity. Figure 5.16 shows the distribution of the single photoelectron. The peak is at 1 p.e. but the mean value is slightly higher due to the big tail at right.

Figure 5.17 shows the signal per hit for samples of 5000 events from run 538 (left) and run 542 (right). According to this, at the run level, the observed variations are at the level of 1/1000.

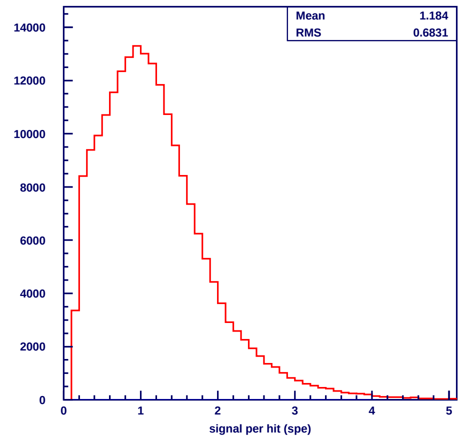

Figure 5.16: *Signal amplitude per hit for a sample of helium events.*

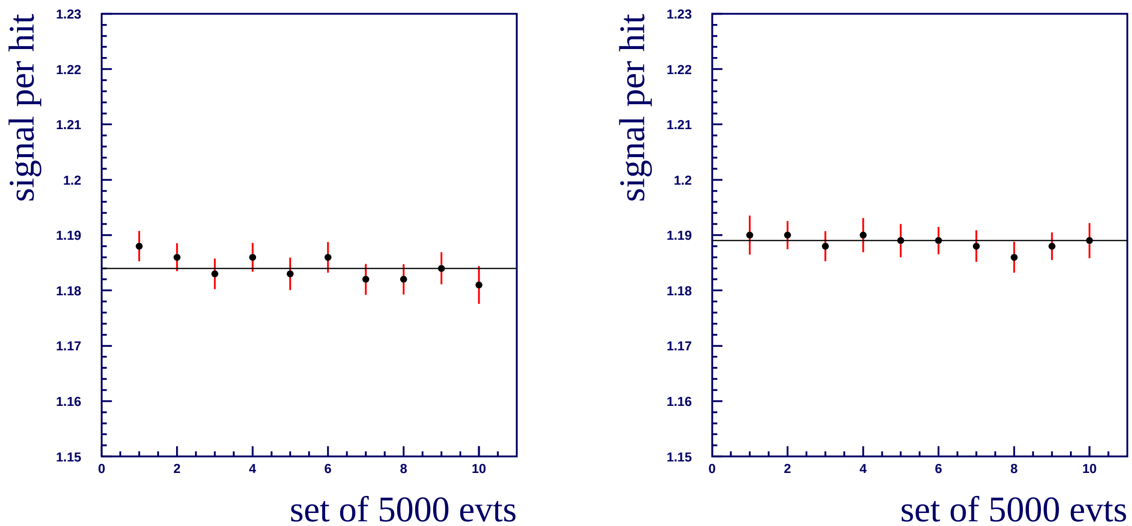

Figure 5.17: *Gain stability within two runs: run 538* (left) *and run 542* (right). *The gain stability within each run at the order of 1/1000.*

5.7 Detection of bad PMTs in data analysis

Although the calibration procedure allows to detect channels with problems and identifies them in the status files for later exclusion from the reconstruction procedure, low efficient channels can appear. Their presence is detected through the analysis of the Čerenkov signal integrated in time. Figure 5.18 shows an accumulated distribution of 34700 helium events produced in an aerogel radiator 1.03. Photomultiplier 52 (blank square) is killed because the signal analysis showed a decrease of signal in that region. The procedure to check the azimuthal distribution of the signal was simple: first, the ring was divided in four parts each covering an azimuthal region of 90°, then in six (60°), eight (45°), 12 (30°), 18 (20°) and 24 (15°) parts.

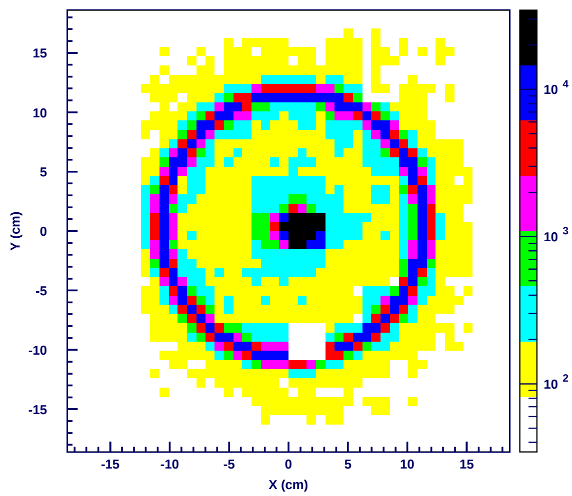

Figure 5.18: *Detection plane with a display of 34700 helium events.*

The signal was integrated within an window of 1.5 cm. The pattern division in four parts shows that the region between 270° and 360° registers a relative decrease of the signal related to the average signal of the four branches of the order of 10%, according to what is visible in the top left-hand plot of Figure 5.19. The subdivision in more parts (6, 8, 12, 18 and 24) allows to constrain the depleted region between the 255° and the 300°, as visible from the three points with a variation of 35% in the last plot of the sequence. In fact, the pattern division in 12 parts allows to approximately look at the PMT dimension which is between 25° and 30° of angular coverage. The decrease of 40% in the relative signal variation with respect to the average signal appears in the angular region occupied by photomultiplier 52 which apparently shows a lower efficiency. This photomultiplier was subsequently eliminated from reconstruction as shown in Figure 5.18.

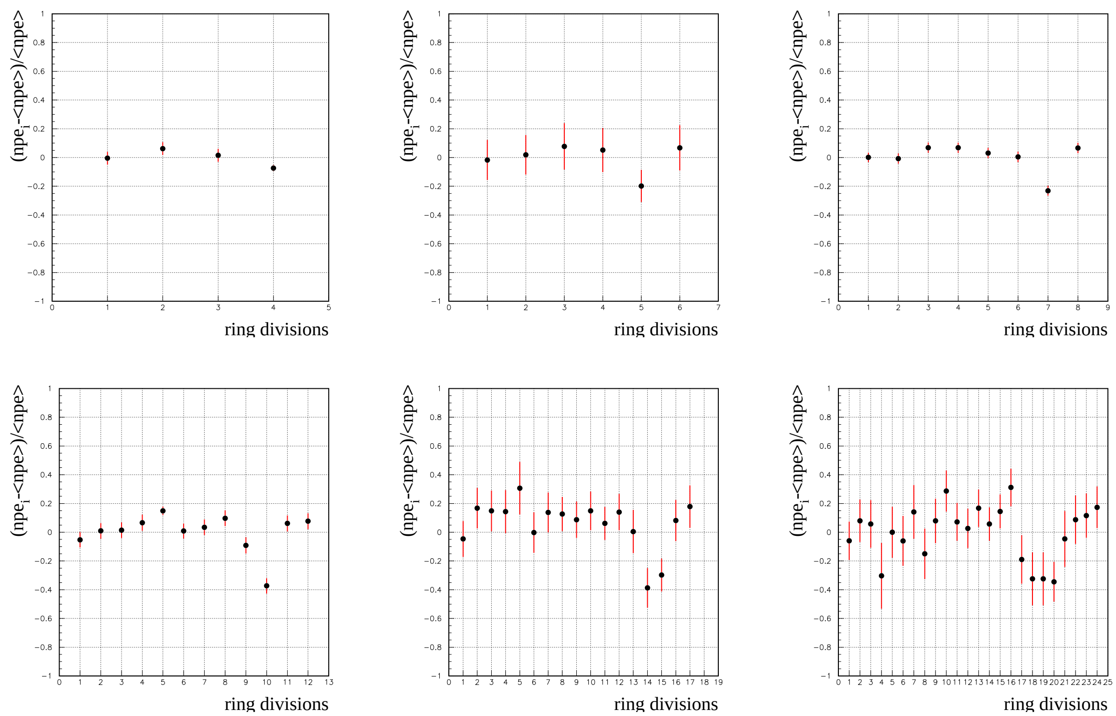

Figure 5.19: *Relative variation on the number of photoelectrons per pattern fraction of helium events. From left to right and from top to bottom: 4, 6, 8, 12, 18, 24.*

5.8 Photomultiplier Saturation Effect

The preliminary reconstructed charge analysis of the beam test data shows a shift on the charge peak position clearly visible for $Z \geq 14$. This is illustrated in Figure 5.20 in the data represented with white squares. A decrease in the reconstructed charge with respect to the expected value is noticeable and it is clear that this shift increases with charge reaching more than one charge unit for $Z = 24$. This suggests a saturation effect of the ADC. An effective correction to the non-linearity was applied. This correction consisted of using the function $corrected\ signal = A \times (signal - C)^2 + B \times (signal - C) + C$ where $A = 0.003628$, $B = 1.094335$, $C = 26.0$. The effect on the difference between the reconstructed charge value and the expected charge versus the expected charge is shown with full dots superimposed on the previous plot. The shift is now only of the order of 0.1 charge units for higher charge values. The signal values before and after the correction are registered in the plot of Figure 5.21. This correction will be applied for all the analysed runs.

Despite this single correction being applied, new measurements of the PMT linearity would be very useful.

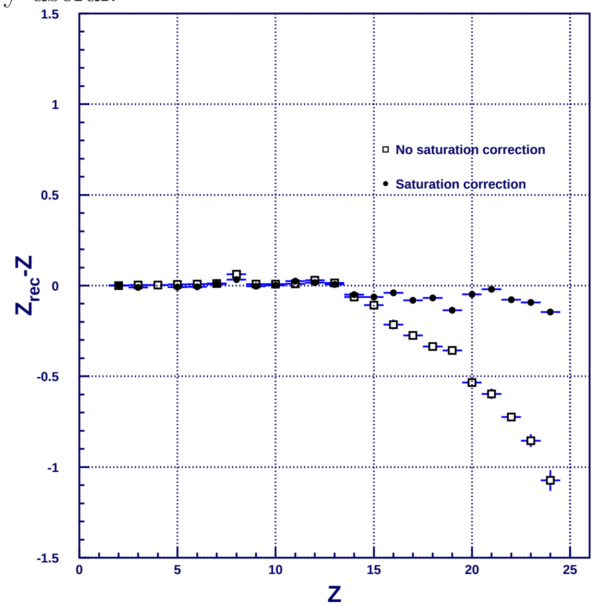

Figure 5.20: *Difference between the reconstructed charge value and the expected charge versus the expected charge. Open square points represent the data obtained without any correction in the measured signal, full dots represent the data points with a single correction, described in text, applied to the PMT channel response.*

5.9 Prototype Simulation and Reconstruction Package

The prototype simulation was included in the RICH standalone package described in section 3.4. This process had already been done to describe the 2002 beam test setup and was updated in 2003 to include the new features. The simulation code is basically common for the flight and prototype setups tested in 2002 and 2003. The choice of the setup to simulate is done by data cards. The velocity and charge reconstruction algorithms are the same apart from minor changes like the optimized velocity reconstruction parameters for the different radiators and the identification of the radiator on which the particle impacts that is specific of the flight setup. The necessary updates are basically at three levels:

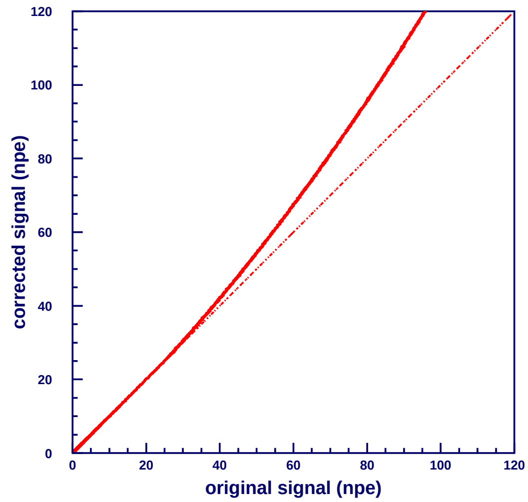

Figure 5.21: *Corrected signal given by the effective parameterization explained in the text versus original signal. The solid line represents the measurements before correction while the dashed line represents the corrected measurements.*

- First, it is necessary to read the DAQ data file generically named *cern.runnb* (e.g. cern.510). This file contains all the information about the event: run and event number, the detected hits and corresponding signal together with the information on which gain mode was used when it was acquired. Data from the auxiliary subdetectors like scintillators, Čerenkov counter, wire chambers and silicon tracker are also registered. Calibration data for the tracker are read from external ASCII files as well as the PMT calibration files with the information on gain G, σ_G, pedestal position, width and channel status.

- The simulation of the data acquisition setup is defined according to data cards that specify if the run is vertical or not and if it includes mirror or not. The geometry of the prototype was already introduced.

- Finally, a circular fit to each vertical event is used and the scintillator calibration is processed from the ADC measurements read from an ASCII file. For inclined events a velocity reconstruction with three free parameters is done to determine the velocity and the impact point at the top of the radiator (X_0, Y_0). For each event, six velocity and charge reconstructions are performed, one for each available track:

Track Type	Detector
1	wire chamber 1
2	wire chamber 2
3	RICH (from circular fit)
4	RICH (position of the pixel with the highest signal)
5	RICH (fixed point for the whole run computed from the mean value of track 3)
6	STD

Table 5.5: *Track types.*

All the read and processed data coming from the reconstruction algorithms are registered in an output file containing two CWN[6] PAW [190] ntuples numbered 1 and 2. The second one describes the run and prototype geometry and is filled just once. The first contains the variables measured and reconstructed for each event.

5.10 Event Reconstruction

Reconstruction of the particle impact point

For the vertical runs ($\theta = 0$), the particle impact point at the top of the radiator can be obtained from the Čerenkov ring. For these events the pattern is a perfect circle that can be fitted. An example of an event like this is the one presented in Figure 5.22.

The centre of the Čerenkov pattern can be obtained by using the three-point method. As the name suggests trios of points are used. The method is based on the geometrical property that the perpendicular bisector of a chord passes through

[6]Column-Wise-Ntuple. In a CWN the elements of each column are stored sequentially. The CWN storage mechanism has been designed to substantially improve access time and facilitate compression of the data, thereby permitting much larger event samples (several hundreds of Mbytes) to be interactively processed, e.g. using PAW.

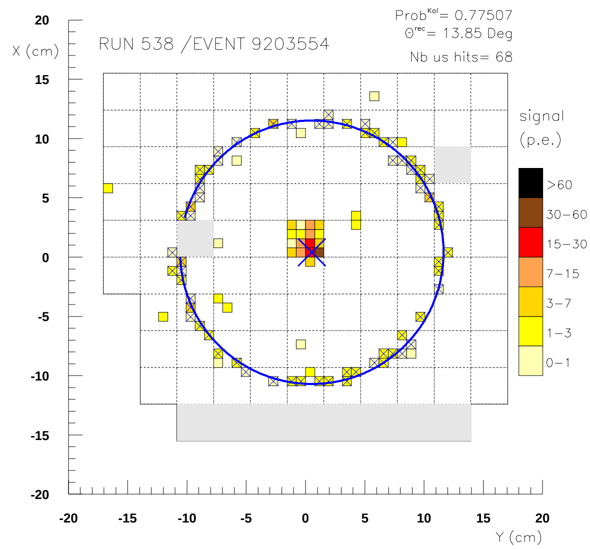

Figure 5.22: *Event from a vertical run.*

the centre of a circumference. Figure 5.23 illustrates the circumference centered at point C with coordinates (a, b). The chord $[P_1P_2]$ is perpendicular to the line segment $[M_1C]$ and in particular the half line segment $[P_1M_1]$ is also perpendicular to $[M_1C]$. The same is valid for $[P_2P_3]$ that is orthogonal to $[M_2C]$ and $[P_2M_2]$ to $[M_2C]$.

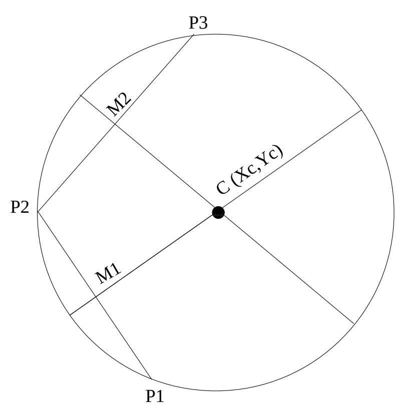

Figure 5.23: *Circumference with the centre at point C (X_c, Y_c), chords $[P_2P_3]$ and $[P_1P_2]$. M_1 and M_2 are the mean points of the chords $[P_1P_2]$ and $[P_2P_3]$, respectively.*

This is simply expressed as

$$\begin{cases} [P_1M_1] \cdot [M_1C] = 0 \\ [P_2M_2] \cdot [M_2C] = 0. \end{cases}$$

In terms of the point coordinates this is written as

$$\begin{cases} (X_{M_1} - X_1, Y_{M_1} - Y_1) \cdot (X_c - X_{M_1}, Y_c - Y_{M_1}) = 0 \\ (X_{M_2} - X_2, Y_{M_2} - Y_2) \cdot (X_c - X_{M_2}, Y_c - Y_{M_2}) = 0, \end{cases}$$

where (X_{M_1}, Y_{M_1}) and (X_{M_2}, Y_{M_2}) are the mean points of the chords $[P_1P_2]$ and $[P_2P_3]$ calculated as,

$$\begin{aligned} X_{M_1} &= \frac{X_1 + X_2}{2}, \quad Y_{M_1} = \frac{Y_1 + Y_2}{2} \\ X_{M_2} &= \frac{X_2 + X_3}{2}, \quad Y_{M_2} = \frac{Y_2 + Y_3}{2}. \end{aligned} \tag{5.2}$$

The differences in equation 5.2 can be simplified using the following notation

$$\begin{aligned} \Delta X_1 &= X_{M_1} - X_1; \quad \Delta Y_1 = Y_{M_1} - Y_1 \\ \Delta X_2 &= X_{M_2} - X_2; \quad \Delta Y_2 = Y_{M_2} - Y_2. \end{aligned} \tag{5.3}$$

Solving the system, the coordinates of the centre (X_c, Y_c) are found to be

$$Y_c = \frac{Y_{M_2} + \frac{\Delta X_2}{\Delta Y_2}\Delta X_M - \frac{\Delta X_2}{\Delta X_1}\frac{\Delta Y_1}{\Delta Y_2}Y_{M_1}}{1 - \frac{\Delta X_2}{\Delta X_1}\frac{\Delta Y_1}{\Delta Y_2}} \tag{5.4}$$

$$X_c = X_{M_1} - \frac{\Delta Y_1}{\Delta X_1}(b - Y_{M_1}). \tag{5.5}$$

These equations are solved for each established trio of hits of the event. For an event with N hits, $\frac{N!}{(N-3)!\ 3!}$ equation systems like 5.2 are built. Finally the values obtained for the centre (X_c, Y_c) are clusterized in a two-parameter space and the centre coordinates are taken to be the average coordinates of the most populated cluster.

This method was named *fitcircle* and was extremely useful in the beginning of data analysis when the tracker calibration files were not available and when the MWPC presented some problems.

Figure 5.24 shows the distribution of the reconstructed centre coordinates for helium events from beam test, with an incidence perpendicular to the matrix, calculated using the *fitcircle method*. The precision obtained is much better than the pixel

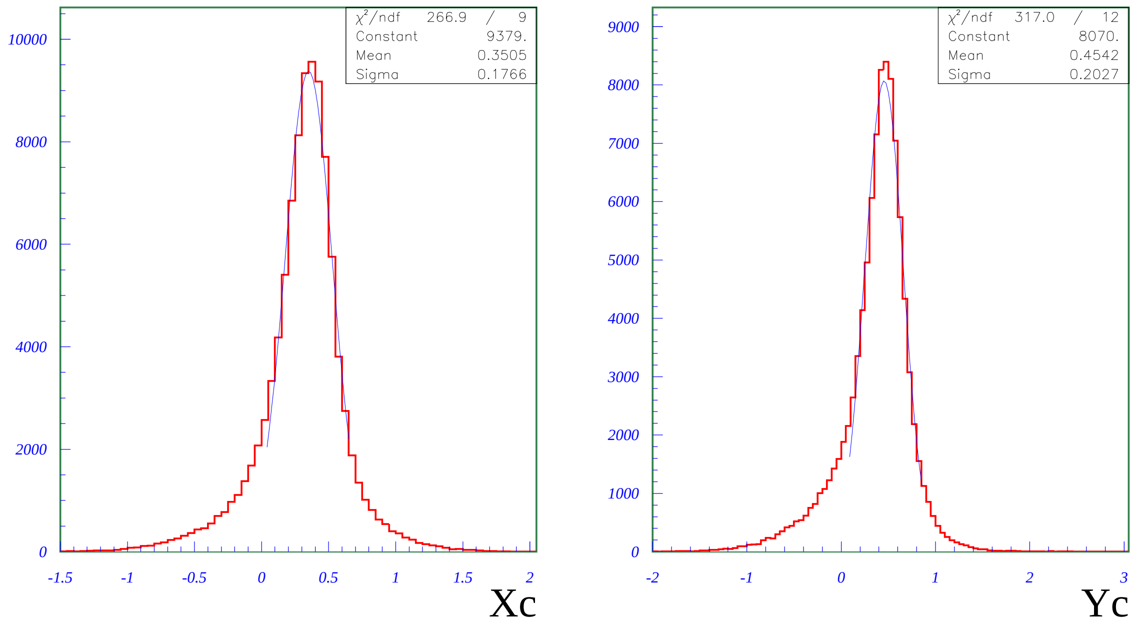

Figure 5.24: *Distributions of the reconstructed particle impact point in the detection matrix for helium events from a vertical run with a setting of beam rigidity A/Z=2.*

size: $\sigma_{X_C} \simeq 0.18$ cm and $\sigma_{Y_C} \simeq 0.20$ cm. The distributions show some tails due to the presence of background events that will be discussed in the next subsections and that were not eliminated at the present stage. The resolution of the centre determination improves using higher charges due to the higher number of hits available to the algorithm. The reconstructed mean values for the centre coordinates are basically the same, with a better resolution ($\sigma_{X_C} \simeq 0.11$ cm and $\sigma_{Y_C} \simeq 0.15$ cm). The reconstruction efficiency of this method is 94% for helium and 99% for $Z > 2$. The beam divergence measured with the tracker data is $\Delta X = 0.34$ mrad and $\Delta Y = 0.20$ mrad for runs with $A/Z = 2$, so these runs are very well focused and the developed algorithm is appropriate for vertical runs.

However the resolutions obtained above have the effect of the beam section ($\sim$1 mm^2). To eliminate the beam spread effect and to estimate the real resolution of the *fitcircle* method, the procedure was applied to a sample of helium events simulated with a fixed impact position in the radiator and the same setup conditions were fulfilled. Figure 5.25 shows the reconstructed centre coordinates for helium events with a vertical incidence. The precision of the method evaluated from

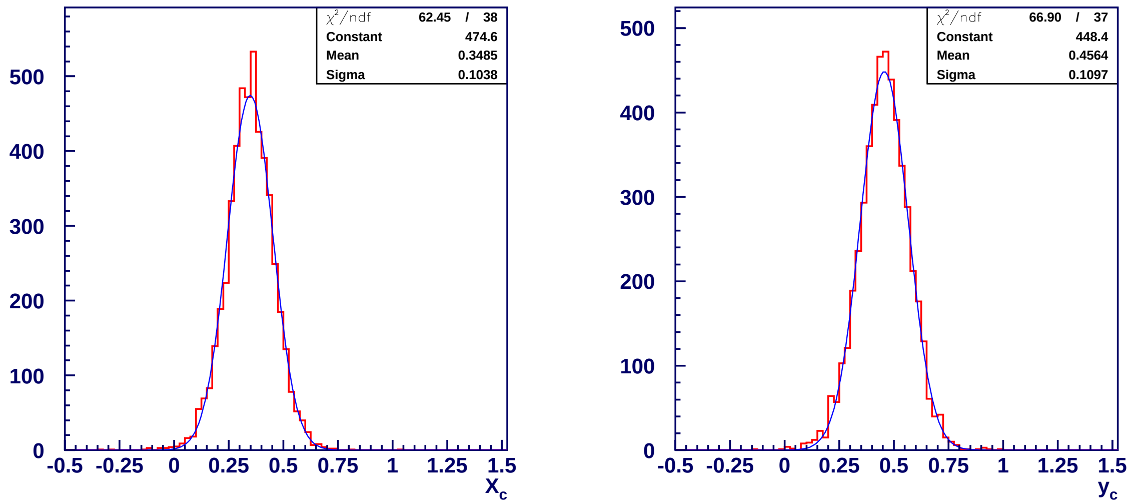

Figure 5.25: *Distributions of the reconstructed particle impact point in the detection matrix for helium events impacting vertically in the same radiator point.*

helium events is of the order of 1 mm.

The track determined by the *fitcircle* is used to perform the alignment between the RICH and the tracker prototype as mentioned in Section 5.10.

5.11 Conclusions

In order to validate the design of the AMS-02 RICH, a prototype was constructed. The performance of this prototype has been tested with cosmic muons and, in October 2002 and October 2003, in a beam of secondary ions at the CERN SPS produced by fragmentation of a primary beam in a Be and Pb target, respectively. The main purposes of the 2003 test were to validate the flight front-end electronics, characterize the aerogel and sodium fluoride radiators and evaluate the mirror reflectivity.

The present chapter introduced the RICH prototype and the 2003 beam test setup. Also give were a brief introduction on the simulation software, photomultiplier calibration, scintillator calibration and tracker alignment which measurements are essential for the data analysis that will be presented in the forthcoming chapters.

Chapter 6

Aerogel radiator studies

Life is a sum of all your choices.
by Albert Camus

6.1 Introduction

The present chapter will introduce the aerogel data analysis done with the samples available for 2003 beam test which were summarized in Table 5.1. Only vertical runs with fully contained rings will be used in the present analysis. The evaluation of the aerogel samples in order to make a final radiator choice was one of the key issues of these tests. The light yield of each sample was evaluated, as well as the velocity and charge reconstruction capabilities. Reconstruction of velocity and charge were made with two independent methods. The results presented here were obtained using LIP reconstruction methods. The data analysis was compared with Monte Carlo (MC) expectations. The radiator tile uniformity concerning the light yield (subsection 6.6.1) and the refractive index (subsection 6.6.2) was also studied. Finally, the results obtained allowed to choose the final aerogel to be used in the flight setup.

6.2 Data selection

Data selection is necessary to remove wrongly reconstructed tracks and to reject multiparticle events originated either from fragmented beam particles or due to δ-

ray emission. Fragmentation can arise from the interaction of beam nuclei with the material in their path, for example in the trigger scintillators, the Čerenkov counter, if present, or in the aluminium window of the RICH prototype. Events with a non-uniform distribution of hits in the ring are also eliminated.

The goal is obtaining a well reconstructed event sample to correctly estimate the measurement capabilities of the detector. According to this a set of event quality cuts must be defined and applied.

Track compatibility

If available, the STD track is always used in the reconstruction so it is meaningful to apply a cut on the track quality. An additional track is reconstructed from the RICH ring hits following the procedure described in Section 5.10. Figure 6.1 shows the residuals in the detector plane for both tracks. The selected tracks, are those which have at most three standard deviations from the central value determined by a gaussian fit.

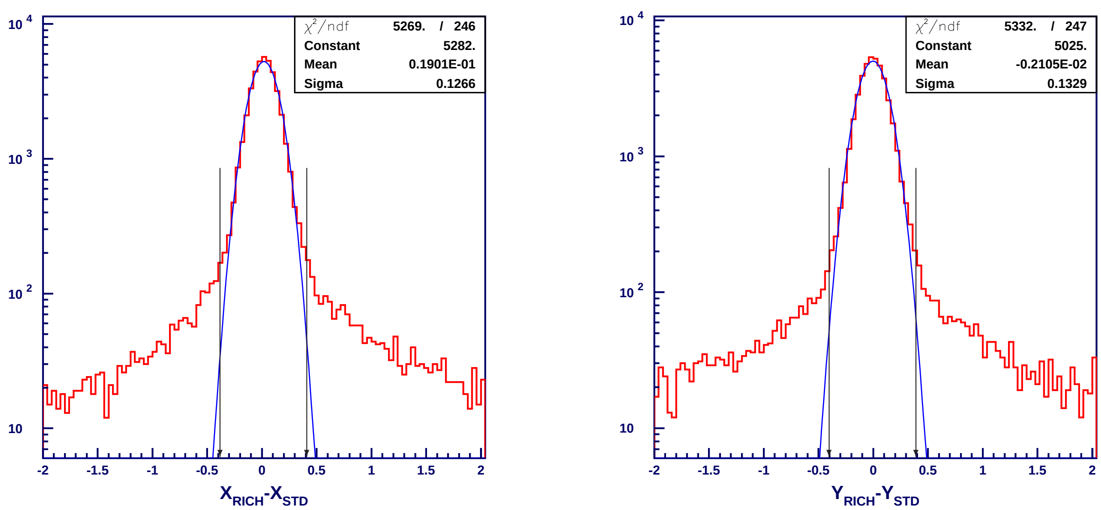

Figure 6.1: *Residuals between the x (left) and y (right) coordinates determined by RICH and by STD. The selected events have a residual within three standard deviations.*

Figure 6.1 illustrates this cut which discards events whose track reconstructed by RICH is not consistent with the STD track either due to the presence of more than one particle in the matrix originated from fragmentation or due to an abnormal presence of noisy hits.

Estimator for the number of particles crossing the RICH

It is important to eliminate events with more than one particle in the detection matrix arising from fragmentation like the event presented in Figure 6.3 (right). The estimate of the number of particles ($\mathrm{N_{part}}$) is based on the comparison of the signal per PMT with the average signal per PMT calculated using all the photomultipliers of the matrix. The expression to be calculated for each PMT is:

$$\frac{\mathrm{S_i} \times \mathrm{N_{PMT}}}{\mathrm{S_T}}. \tag{6.1}$$

where $\mathrm{S_i}$ is signal of each PMT and $\mathrm{S_T} = \sum_i \mathrm{S_i}$. The distribution of that variable is represented in Figure 6.2 (left). The cut to establish if the signal per photomultiplier corresponds to the signal left by a particle is set at 4 and is marked upon the plot. This limit separates the region of the plot with a decreasing trend from the stable part. If the previous ratio is greater or equal than 4 then one more particle is counted.

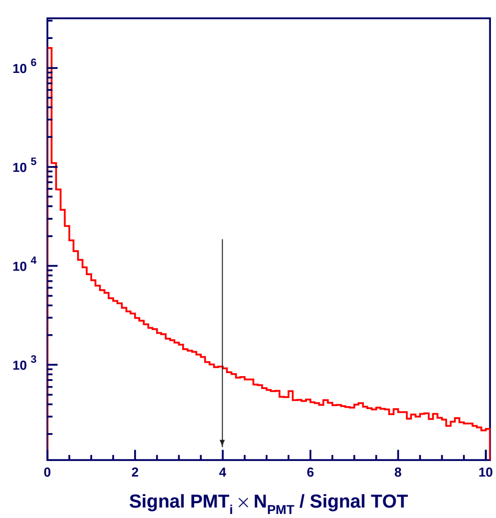

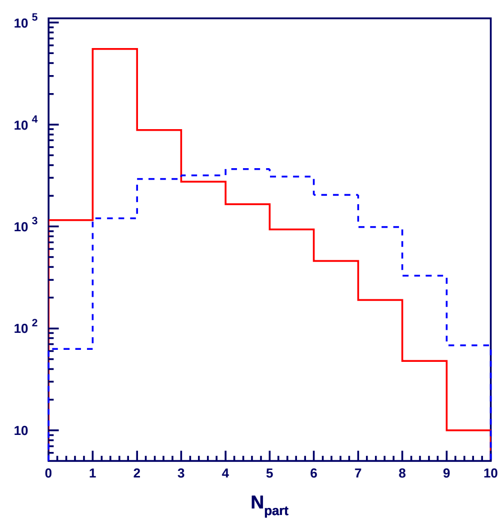

Figure 6.2: *Distribution of the signal per PMT divided by the average signal per PMT. PMTs giving a value greater or equal than four are candidates to be particle spots* (left). *Distribution of the estimated number of particles per event for events within (solid line) and out of three standard deviations in β (dashed line)* (right).

The distribution of N_{part} is introduced in Figure 6.2 (right). The distribution represented with a solid line shows the number of particles estimated to be in the matrix for events within three standard deviations of the velocity distribution. The distribution described by a dashed line corresponds to the number of particles estimated to be in the matrix for events more than 3σ away from the center of the velocity distribution.

An alternative cut to the particle number estimator to reject fragmented events and abnormally noisy events was established. Noisy events can be rejected by demanding a small noise/signal ratio. The distribution of the ratio between the signal observed out of the ring, excluding the signal of the particle hit candidates, and the signal counted in the ring is presented in Figure 6.4. The peak close to the origin represents the distribution of events with an acceptable noise/signal ratio. The cut to separate the population of events with a normal ratio from extremely noisy events is set at one. Therefore, events with an integrated signal out of the ring width greater or equal than the ring signal are excluded.

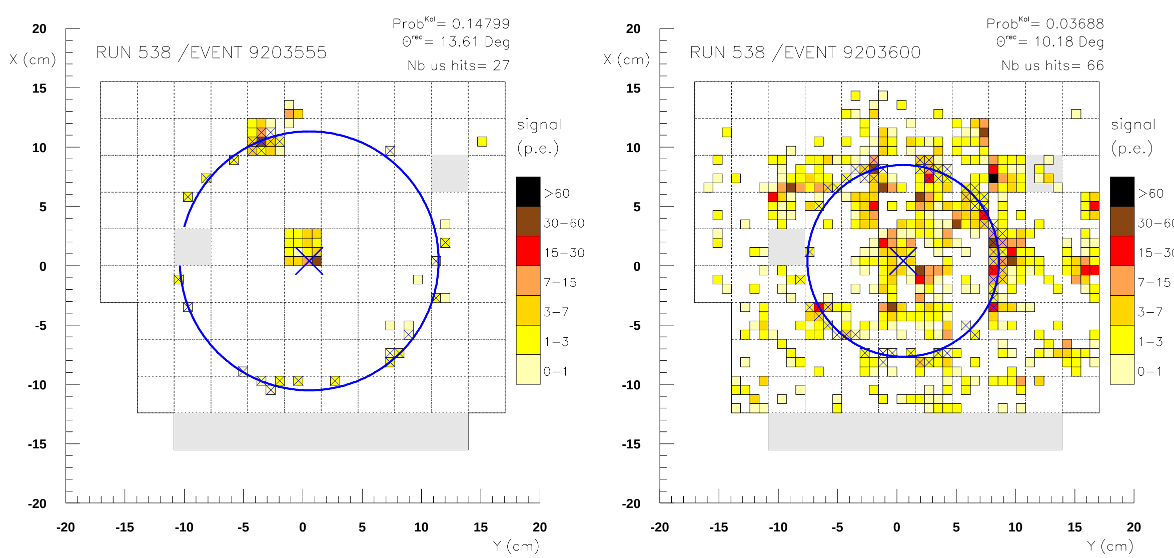

Figure 6.3: *Background events: event with clustered hits* (left) *and event with fragments* (right).

Kolmogorov probability

For events generated by vertical particles the azimuthal distribution of the hits in the detected ring should be flat since Čerenkov emission is uniform in the azimuthal angle φ (see Figure 4.5). So reconstructions like the ones shown in Figure 6.3 (left) should be rejected since they clearly correspond to odd events compared to the uniform rings depicted in Figure 5.6. Clustered hits are presented upon the Čerenkov ring.

Since the velocity reconstruction algorithm provides the hit's azimuthal angle in the particle's frame this can be used to check the uniformity of the azimuthal distribution of the hits with a Kolmogorov test.

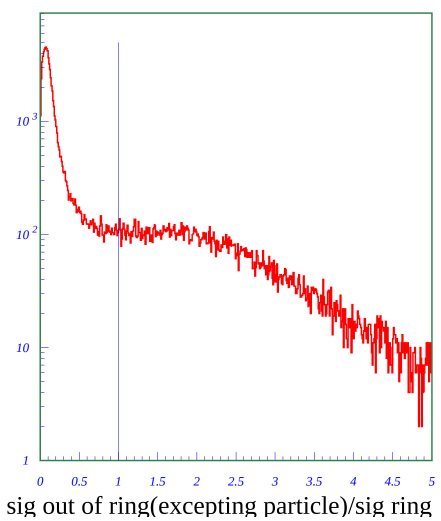

Figure 6.4: *Distribution of the ratio between the signal out of the ring, excluding the particle signal, and the ring signal. The vertical line marks the established cut value.*

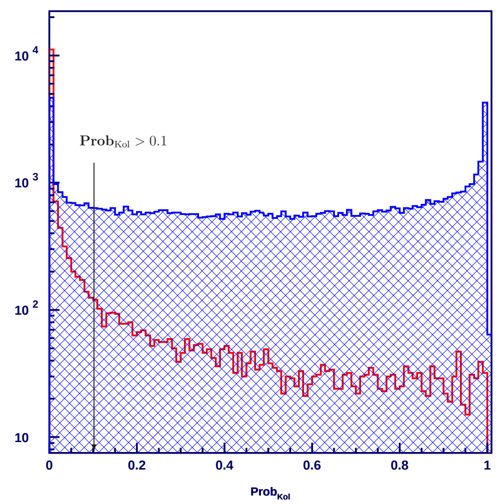

Figure 6.5: *Kolmogorov probability distribution for the events within 3σ of the velocity distribution (hatched distribution) and out of this region (plain distribution).*

Keeping in mind the purpose of eliminating the same type of events that the Kolmogorov probability is supposed to discard, an estimator called ring *flatness* was created. This is built as the average cosine of the hit azimuthal angles weighted by the hit signals, w_i, because not only the number of hits should be uniformly

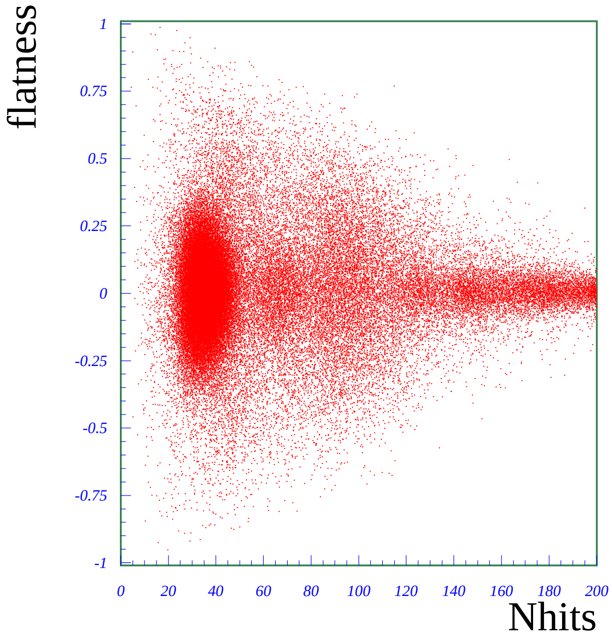

Figure 6.6: *Flatness estimator versus number of hits.*

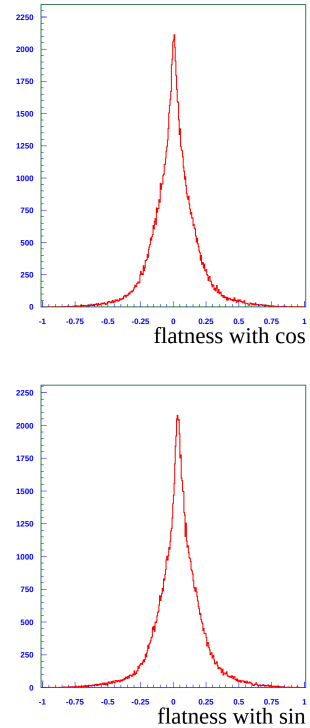

Figure 6.7: *Flatness estimator calculated with the cosine* (top) *and with the sine* (bottom) *of the hits' azimuthal angles.*

distributed but also their signals. So it is expressed as

$$Flatness = \frac{\sum_{i=1}^{nhits} w_i \cos\varphi_i}{\sum_{i=1}^{nhits} w_i}. \tag{6.2}$$

This variable scales down with the number of hits of the event and this is observed in Figure 6.6.

The same estimator with the function sine was built to eliminate events that could have one cluster in one side and another in the opposite side. This configuration would give a good value for the flatness estimated with cosine.

The reconstruction capabilities of the RICH prototype will be evaluated from a selected sample, according to the following criteria:

- compatibility between track elements from RICH and tracker;
- one particle requirement;

- azimuthal uniformity of the hits distribution.

Table 6.1 summarizes the events selection cuts.

Selection variable	cut
RICH and STD track residuals	$\|X_{RICH} - X_{STD}\| < 3\sigma$ $\|Y_{RICH} - Y_{STD}\| < 3\sigma$
N_{part}	$= 1$
$Prob_{Kol}$	> 0.1

Table 6.1: *List of selection cuts.*

The effectiveness of the cuts on the event selection was evaluated by using two data samples: a *signal sample* made of events with reconstructed velocity within two standard deviations of the expected value and *backgroud events* composed of bad reconstructed events (reconstructed velocity more than five standard deviations from the expected). The signal selection efficiency after applying all the cuts is of 65% while a very good background rejection efficiency of 97% is obtained. Table 6.2 shows the corresponding results obtained.

Selection variable	Signal efficiency	Background rejection
RICH and STD track residuals	78%	66%
N_{part}	88%	69%
$Prob_{Kol}$	89%	28%

Table 6.2: *Signal selection and background rejection efficiencies for each quality cut, applied as the last cut.*

The importance of each cut on the final selection can be estimated by applying it as a last cut to the samples. Figure 6.8 shows the reconstructed velocity distributions at different stages: prior to cuts (solid line), after N_{part} and track quality cut (filled histogram) and after Kolmogorov probability cut (hatched distribution surrounded by a dotted line). All the efficiencies presentend in Table 6.2 were estimated based on data collected with radiator CIN103 irradiated with a vertical beam. These values are quite similar for the other two aerogel radiators (MEC103 and CIN105)

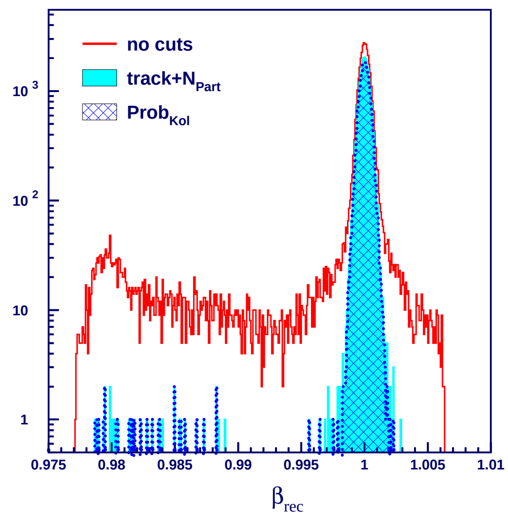

Figure 6.8: *Reconstructed velocity with helium data collected using radiator CIN103 before any event selection cut (solid line), after tracker quality cut (dashed line), after* N_{part} *cut (filled) and after Kolmogorov probability cut (hatched).*

since the selection reflects the setup and the beam conditions more than the radiator characteristics.

6.3 Velocity Reconstruction Results

The three aerogel radiators extensively studied in the 2003 beam test are shortly called CIN103, MEC103 and CIN105. Table 6.3 summarizes some effective optical parameters for each radiator together with some setup parameters. The optical parameters that characterize each aerogel were fine tunned (refractive index, clarity, forward scattering probability and the width of the forward scattering angle) looking for the agreement on different distributions. The refractive index was fine tunned forcing the average value of the reconstructed β to be compatible with the particles velocity in the beam ($\beta \simeq 1$). Then the forward scattering probability and the width of the forward scattering angle were determined through a scan on the space of these two parameters in order to find the pair that best describes the agreement between the residuals distribution in data and in MC. Finally, fixed all the other parameters the effective clarity was determined by imposing the agreement between the total signal in the Čerenkov ring in data and in MC. The complete procedure to determine the modeling parameters is thoroughly described in thesis [163].

The effective clarity value obtained for the Novosibirk radiator is close to the values measured in laboratory, already presented in Table 3.1. However, the effective value determined for the Matsushita radiator disagrees from the laboratory measurement most probably due to the fact that in the beam test three tiles, 1.1 cm thick each, were stacked in order to give the final radiator thickness while in the laboratory the measurement was performed using only one tile. Other laboratory measurements have shown that piling up aerogel tiles can degrade the overall transmittance, which puts the Matsushita aerogel in disadvantage since only tiles with a thickness of the order of 1 cm are produced. Since three different aerogel radiators

Radiator	n_{eff}	C_{eff} ($\mu m^4 cm^{-1}$)	P_d	δ_θ (mrad)	H_{rad} (cm)	H (cm)
CIN103	1.0300±0.0004	0.0052±0.0001	0.14±0.02	17±4	3.0	42.3
MEC103	1.0309±0.0003	0.0058±0.0001	0.14±0.02	23±5	3×1.1	42.3
CIN105	1.0529±0.0006	0.0055±0.0001	0.19±0.02	14±3	2.5	33.45

Table 6.3: *Silica aerogel radiators studied in 2003 beam test and their effective parameters: refractive index, clarity, forward scattering probability and standard deviation of the forward scattering angle. Aerogel thicknesses and the setup expansion heights are also presented.*

are under study and a different setup is being used, the parameters of the velocity reconstruction have to be optimized for each case.

In a first step, looking at the residuals distribution [Figure 6.9 (left)] for CIN105 fitted with a double gaussian function, as explained in subsection 4.3.2, allows us to conclude that the presence of a second gaussian is almost unnecessary. The population in the second gaussian is only 15% of the one in the central gaussian while the standard deviation of the second is two times larger than the first (in the flight setup the ratio between them is 3.6). As explained before the presence of a second gaussian is justified by the requirement of taking into account the forward scattering effect and the pixel size. The latter effect is smaller in the prototype (7.75 mm) and the former is less noticeable due to the smaller expansion height in the prototype setup (42.3 cm). Therefore for the sake of simplicity a model to describe the signal containing only one gaussian will be used.

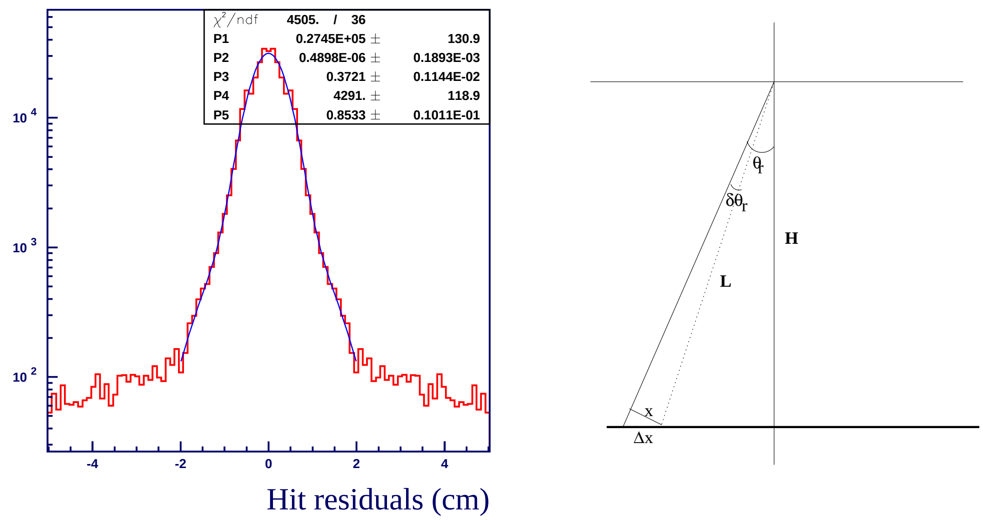

Figure 6.9: *Hit residuals with respect to the expected pattern for 50000 simulated helium events impacting vertically in an aerogel CIN105. A double gaussian function is used to fit the residuals of hits considered as signal hits* (left). *Scheme with the effect of the ring enlargement due to the forward scattering effect* (right).

The effect of the Čerenkov ring enlargement due to the forward scattering effect enhanced by a higher expansion height is illustrated in the right-hand scheme of Figure 6.9. H is the expansion height that in the flight setup is 46.2 cm while in the prototype for the runs testing CIN105 radiator was established to be 33.45 cm. The particle direction is perpendicular to the detection matrix and L is approximately the distance crossed by the photon since it leaves the radiator and impinges on the detection plane. θ_r is the photon refracted angle and $\delta\theta_r$ is the forward scattering emission angle. The ring width enlargement, Δx, depends linearly with the expansion height (H),

$$\Delta x = \frac{x}{\cos\theta_r} \sim \frac{L\tan\delta\theta_r}{\cos\theta_r} \sim \frac{H\delta\theta_r}{\cos^2\theta_r}. \tag{6.3}$$

Comparing the ring thickness generated in the flight setup with the one generated in the prototype setup comes:

$$\frac{\Delta x_{flight}}{\Delta x_{proto}} = \frac{H_{flight}}{H_{proto}} = \frac{46.2}{33.45} = 1.38. \tag{6.4}$$

The ratio between the standard deviations of the second gaussian for both cases is

$$\frac{\sigma_{flight}}{\sigma_{proto}} = \frac{1.35}{0.853} \sim 1.5 \tag{6.5}$$

which is compatible with the ratio between the foreseen ring width enlargement.

From the previous analysis it is reasonable to describe the signal population in the residual distribution by a single gaussian model. The ring residuals parametrization had to be done with simulated events in order to avoid the pixelization effect present in real data events coming from a narrow beam. The residual distributions for the three aerogel radiators fitted with the aforementioned model are introduced in Figure 6.10. All the residual distributions were obtained from simulation using events generated by particles impacting uniformly in a central radiator square of 5 cm side length. This constrained region also guarantees fully contained rings.

The likelihood function to be used is:

$$\mathcal{P}(r) = (1-b)\frac{1}{\sqrt{2\pi}\sigma}\exp\left[-\frac{1}{2}\left(\frac{r}{\sigma}\right)^2\right] + \frac{b}{D}. \tag{6.6}$$

According to what was explained before, evaluating the background ratio b implies the definition of a cut distance d_{cut} that separates the population of hits that are signal and the population that belongs to the background. In practical terms the problem reduces to solving the following equation for different cut distances which give different background levels:

$$(1-b)\ G(d_{cut}) = \frac{b}{D}. \tag{6.7}$$

Samples of 20000 vertical helium nuclei with $\beta \simeq 1$, generating fully contained events, were simulated in the CIN103 and MEC103 radiators and 10000 in the CIN105 radiator. The relative velocity resolution σ_β/β is estimated from the distribution $(\beta^{sim} - \beta^{rec})$, for each established pair $(b,\, d_{cut})$. The evolution of $\frac{\sigma_\beta}{\beta}$ with d_{cut} for each radiator is presented in Figure 6.11.

The optimized d_{cut} parameter, corresponding to the best velocity resolution, is summarized in Table 6.4 together with σ and b.

The z coordinate of the emission vertex was also tuned. The optimization procedure applied was the same described in Chapter 4. Figure 6.12 presents the evolution of the systematic error of the mean reconstructed velocity value with the fraction of radiator height for the z coordinate of the photon emission vertex for

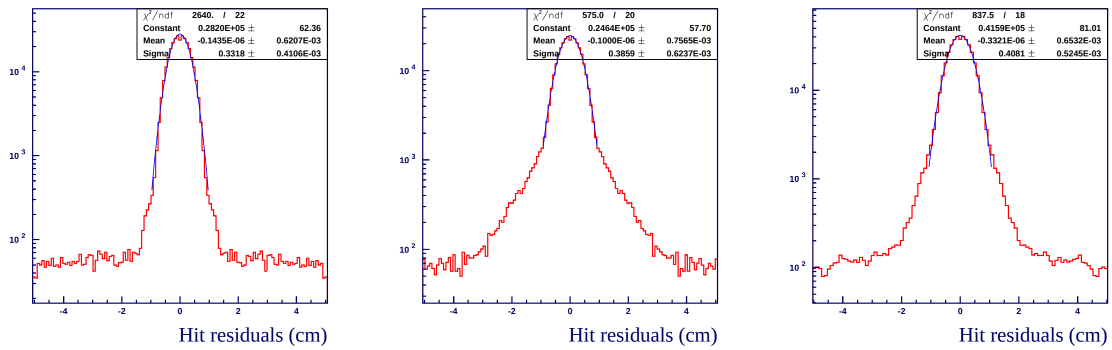

Figure 6.10: *Hit residuals with respect to the expected pattern for 50000 simulated helium events impacting vertically on aerogel CIN103* (left), *MEC103* (middle) *and CIN103* (right).

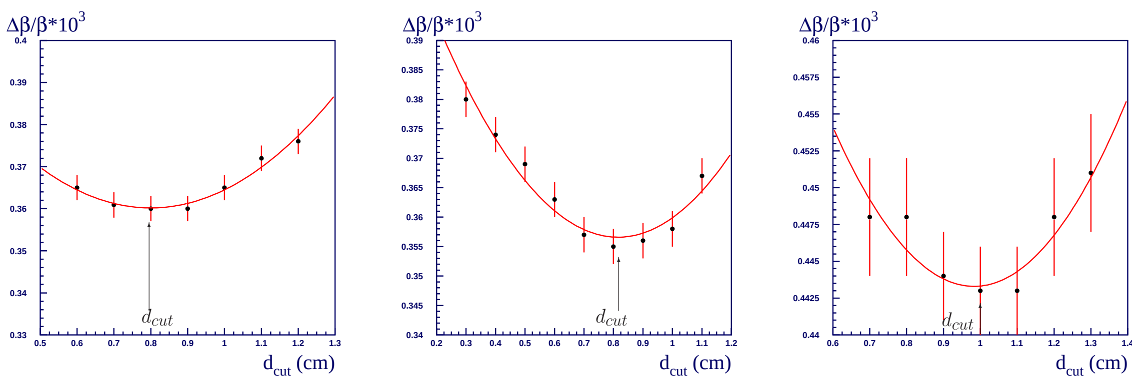

Figure 6.11: *Relative velocity resolution for helium nuclei impacting in CIN103* (left), *MEC103* (middle), *CIN105* (right) *in the prototype setup versus cut distance between signal and noise hits spatial distribution.*

the three aerogel radiators studied. All samples show a linear variation with the optimal emission vertex at 0.552, 0.564 and 0.570 of the radiator height for CIN103, MEC103 and CIN105, respectively.

radiator	σ	b	d_{cut}
CIN103	0.33	0.31	0.80
MEC103	0.39	0.46	0.82
CIN105	0.41	0.30	0.98

Table 6.4: *Optimized parameters for velocity reconstruction with the different aerogel radiators of the RICH prototype.*

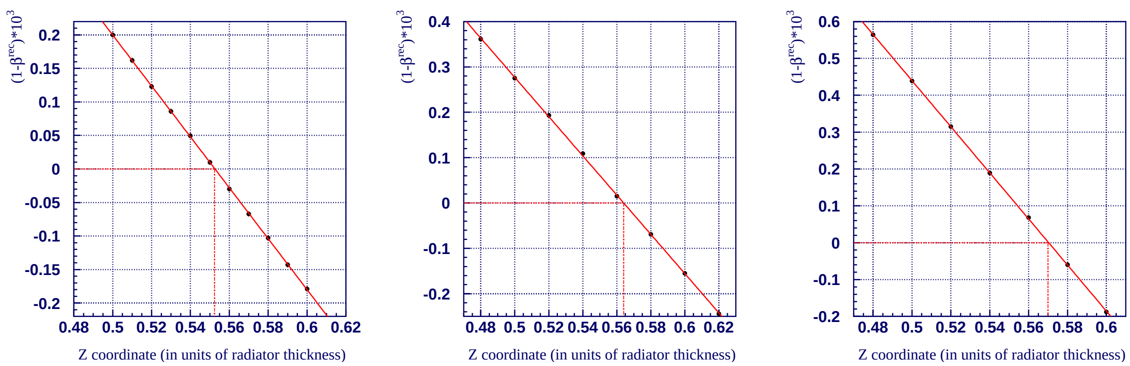

Figure 6.12: *Fine tuning of the z coordinate of the emission point assumed for pattern tracing. This simulation was done for CIN103* (left)*; MEC103* (middle) *and CIN105* (right).

The optimized reconstruction parameters, σ, b, d_{cut} and the z coordinate of the emission point were used in the data velocity reconstruction. The resolution of the β measurement was estimated using a gaussian fit to the reconstructed β spectrum like the one shown in Figure 6.13 for helium nuclei. The sample was selected according to charge measurements from both the silicon tracker prototype and the scintillators. In the present case, data were collected with the aerogel radiator CIN103, 3.0 cm thick with an expansion height of 42.3 cm. The events shown correspond to particles inciding vertically and generating fully contained rings. The track prediction used was the STD measurement. The value of β reconstructed from a simulated helium sample is also shown in the superimposed shaded histogram proving the good agreement between data and Monte Carlo.

The results on velocity resolution for $\beta \simeq 1$, helium nuclei impacting on each of the aerogel samples tested in 2003 are summarized in Table 6.5.

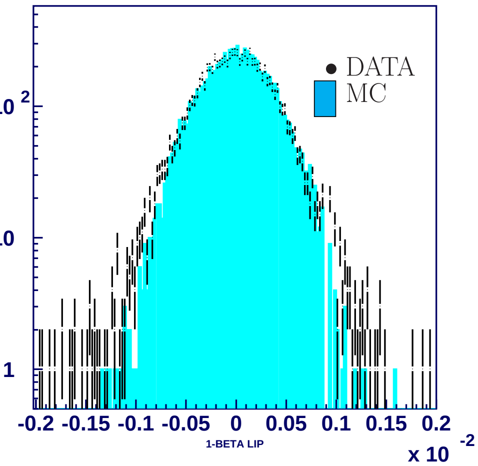

Figure 6.13: *Comparison of the* $(\beta - 1) \times 10^3$ *distribution for helium data (black dots) and simulated data (shaded).*

The velocity resolution given by equation 4.1 can be related to the setup expansion height as $\frac{\Delta\beta}{\beta} = \cos\theta_c \sin\theta_c \frac{\Delta R}{H}$ since $\tan\theta_c = \frac{R}{H}$ according to the right-hand scheme. Therefore the expansion height is inversely proportional to the velocity resolution which allows to extrapolate the results introduced in Table 6.5 for a common expansion height (33.5 cm) from the values measured at the adjusted heights.

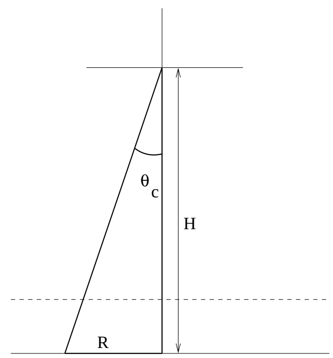

All radiators tested fulfill the RICH requirement for β measurement. In fact, CIN103 presents a slightly better value due to the smaller Čerenkov angle and the good transparency. The CIN105 radiator also presents a very precise resolution although it has a higher refractive index.

β resolution for Z=2, H=33.5 cm			
radiator	CIN103	MEC103	CIN105
$\sigma(\beta) \times 10^3$	0.421±0.003	0.434±0.002	0.459±0.004

Table 6.5: *Velocity resolution for a helium particle with* $\beta \simeq 1$ *obtained for all the aerogel samples tested in 2003 and extrapolated for a common expansion height of 33.5 cm. Data were from a beam with* $A/Z = 2$.

Finally, Figure 6.14 shows the reconstructed velocity distributions for helium events impacting in CIN103 using two different algorithms: the LIP algorithm presented in this thesis and the CIEMAT algorithm. The last algorithm is based on a single hit reconstruction [173] which means that a velocity value is reconstructed for every detected hit. The resolutions achieved with both methods are compatible and a bias in the mean reconstructed value of the order of 10^{-4} is observed. This is an expectable shift, intrinsic to the different geometrical approaches for β evaluation since one is based on an average of hit distances to the Čerenkov pattern (LIP) and the other is extracted from an average of single-hit estimated velocities, β_{hit} (CIEMAT).

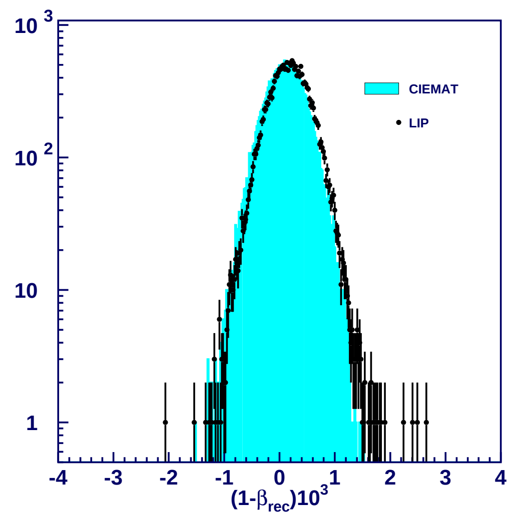

Figure 6.14: *Comparison of the* $(1-\beta)\times 10^3$ *distribution for helium data reconstructed with CIEMAT (shaded) and LIP (dotted) algorithms.*

6.3.1 Evolution of velocity resolution with charge

The charge dependence of the relative velocity resolution for the same radiator is shown in the right-hand plot of Figure 6.15. The different charges were selected using external and independent measurements performed by the silicon tracker prototype and by the two scintillators. The observed resolution varies according to a law in $1/Z$, as is expected from the charge dependence of the photon yield in the Čerenkov emission, up to a saturation limit set by the pixel size of the detection unit cell. The function used to perform the fit is the following, already introduced in Chapter 4:

$$\sigma(\beta) = \sqrt{\left(\frac{A}{Z}\right)^2 + B^2} \tag{6.8}$$

where A means the β resolution for a singly charged particle while B means the resolution for a very high charge generating a large number of hits. The fitted values are presented in Table 6.6. Simulated data points for $Z = 2$, 6, 16 are marked upon the same plot with full squares. A full agreement between data and Monte Carlo is observed for all simulated charges. Data used are from $A/Z = 2$ beams since they present a larger number of high-charged particles.

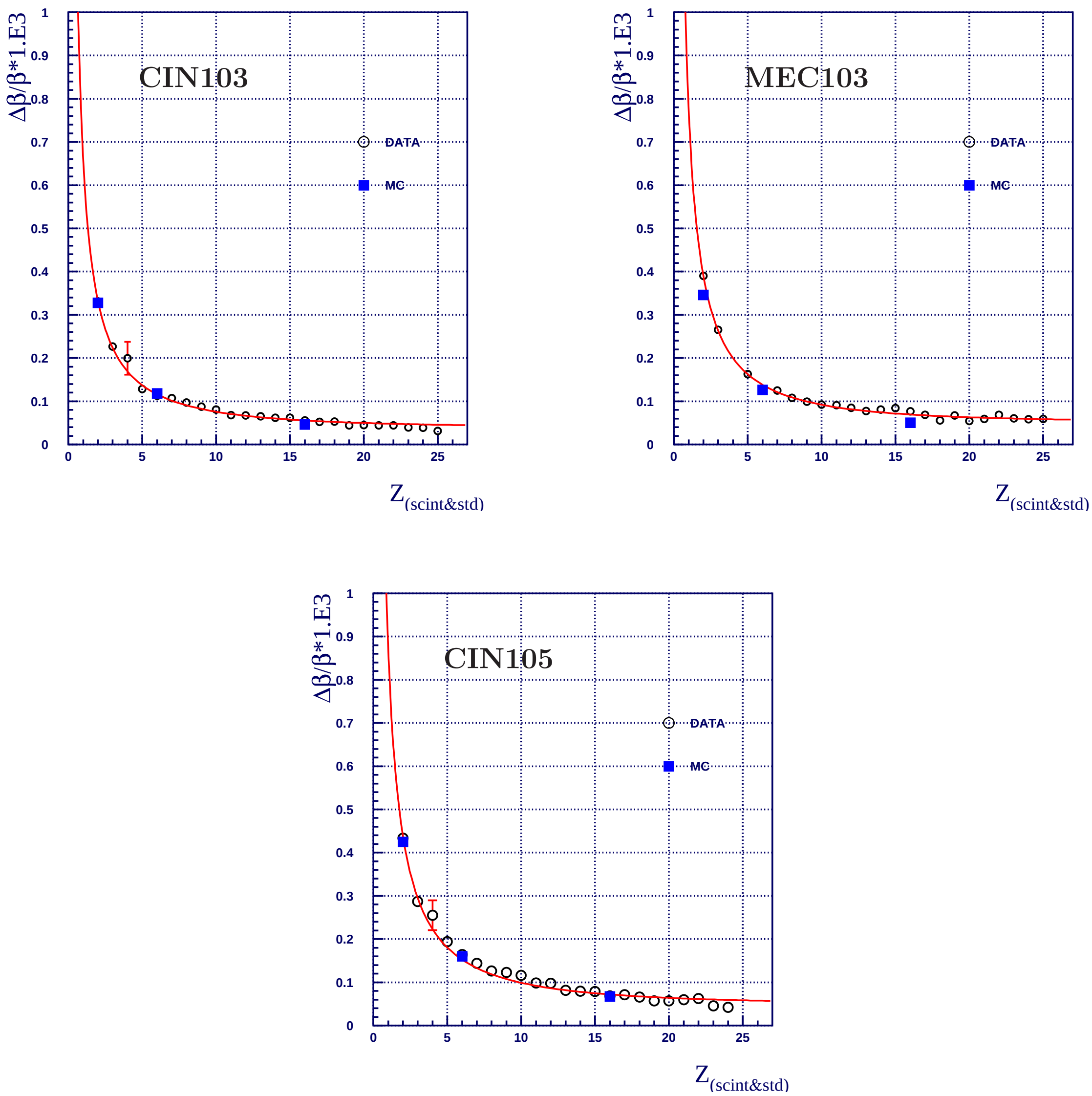

Figure 6.15: *Velocity resolution for different aerogel batches: dependence with the particle charge for data (open points) and simulation (full squares).*

The evaluated resolution for singly charged particles, given by parameter A, is

radiator	H (cm)	$A \times 10^3$	$B \times 10^3$
CIN103	42.3	0.659±0.003	0.037±0.001
MEC103	42.3	0.774±0.001	0.050±0.001
CIN105	33.3	0.872±0.003	0.047±0.001

Table 6.6: *Fitted parameters A and B from the function (6.8) applied to the velocity resolution versus Z distributions presented in Figure 6.15.*

in any case better than the predicted flight resolution for the same particles (0.1%). This is expected because the test beam is the most favourable scenario dealing with fully contained Čerenkov rings which means the maximum possible number of hits available to the reconstruction.

6.4 Light Yield Evaluation

The light yield of the aerogel radiator has implication on the velocity and charge resolutions. Therefore, the aerogel characterization is an important issue for the final choice of the radiator. The aerogel light yield depends on the tile thickness and on its optical properties (refractive index and clarity). As runs with $A/Z = 2$ have a large helium sample, the light yield is evaluated for helium nuclei and extrapolated for protons ($Z = 1$). Several factors have to be taken into account for the description of the ring signal distribution. The general case is exposed in Appendix A and the factors to be taken into account for the helium signal estimation in the beam test conditions are here exposed:

- statistical fluctuation of the number of photoelectrons:
  the large signal collected (n) for helium nuclei obey a gaussian law of mean signal μ,

$$G_1(n;\mu) = \frac{1}{\sqrt{2\pi}\sqrt{\mu}} e^{-\frac{1}{2\mu}(n-\mu)^2};$$

- photomultiplier signal amplification:
  the uncertainty associated to the charge amplification in every dynode causes a natural spread on the photoelectron response, a n photoelectrons signal will be measured (x) according to,

$$G_2(n;\mu) = \frac{1}{\sqrt{2\pi}}\frac{1}{\sqrt{n}\ \sigma_{p.e.}} e^{\left[-\frac{1}{2n}\left(\frac{x-n}{\sigma_{p.e.}}\right)^2\right]};$$

- particle velocity profile:

  all the beam particles have $\beta \equiv 1$;

- ring acceptance profile:

  only fully contained rings are used.

Therefore, the number of photoelectrons distribution will be filled according to the following function where n is the number of photoelectrons

$$f(x;\mu,\sigma_{p.e.},N_0) \propto \sum_{n=3}^{\infty} G_1(n)G_2(x,n) \qquad (6.9)$$

and the parameters to be determined are the global normalization factor N_0, the single photoelectron width $\sigma_{p.e.}$ and the average number of photoelectrons, μ.

Table 6.7 summarizes the light yield for $Z = 1$ extracted from the average number of photoelectrons for $Z = 2$ in each radiator. A good agreement is observed between the data signal and the simulated signal for CIN103 (bottom right plot of Figure 6.16).

radiator	CIN103	MEC103	CIN105
$< N_{p.e.} >$	9.99±0.04	10.66±0.04	14.27±0.05

Table 6.7: *Expected light yield for $Z = 1$, $\beta \simeq 1$ particles in CIN103, MEC103 and CIN105 radiators.*

The light yield has been evaluated from the analysis of helium samples collected in 2003 and from the analysis of proton data samples gathered in 2002 with different beam momenta between 5 and 13 GeV/c [191].

Figure 6.17 (left) shows the light yield evolution of the different aerogel samples tested in 2002 with the proton beam momentum. A fit to each set of data was applied and the light yield for a proton with $\beta \simeq 1$, generating fully contained rings in a radiator with a common thickness of 3 cm was extrapolated. The right-hand plot of the same figure shows the light yield normalized to 3 cm thickness for the different aerogel samples tested in 2002 and 2003. Two interesting features are

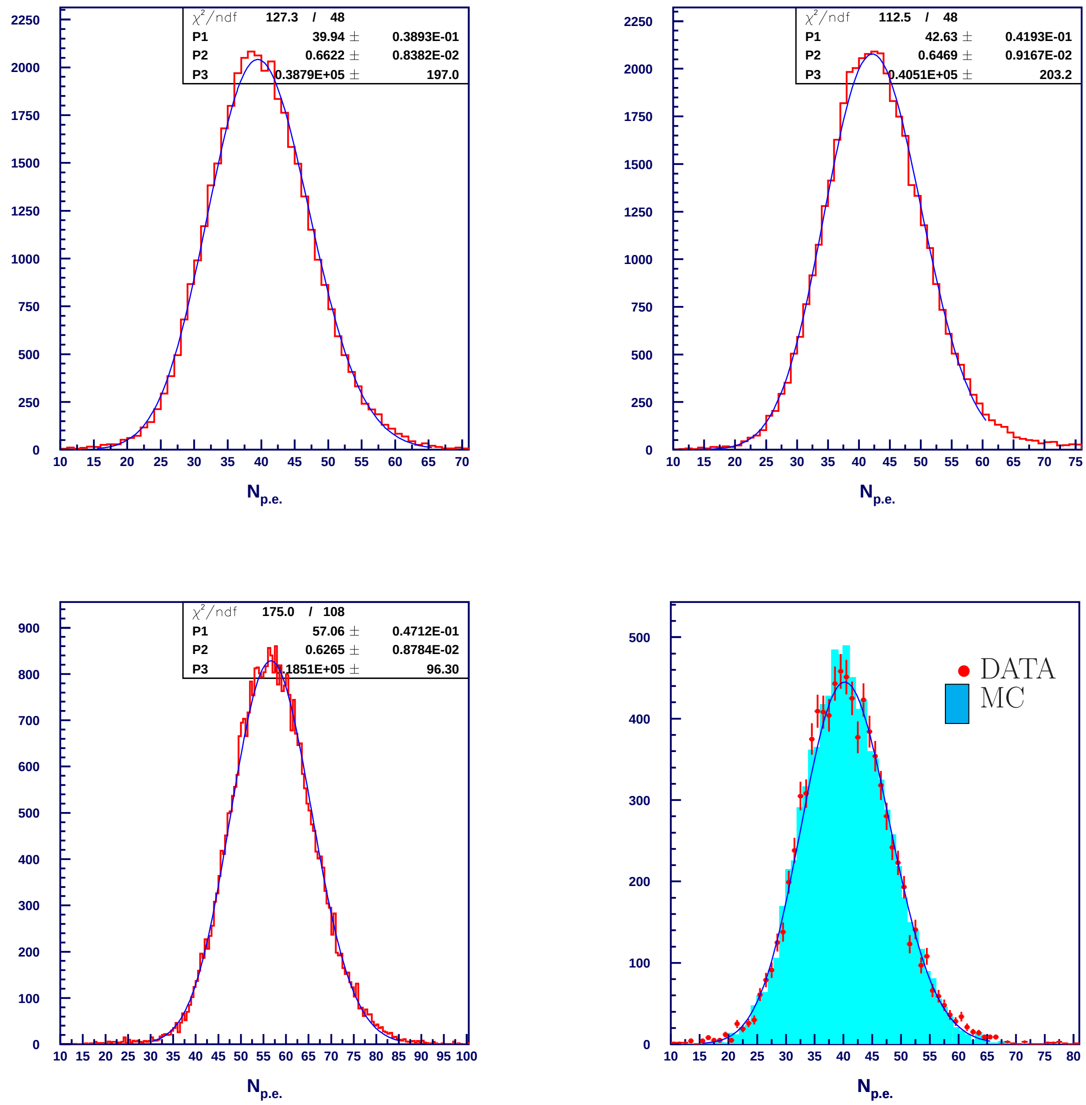

Figure 6.16: *Number of photoelectrons evaluation for Z=2 particles impinging in CIN103* (top left), *MEC103* (top right), *CIN105* (bottom left). *The results are fitted by the function 6.9. Comparison of data and MC signal for events generated in CIN103* (bottom right).

noticeable. On one hand, the same sample of CINy02.103[1] was used in both years and its light yield analysis shows the same value which proves the setup stability and the aerogel's good performance after a one-year period; on the other hand, it is clear that the highest signal comes from a CIN sample produced in 2003 with refractive index 1.050 reflecting the very good clarity ($\sim$0.0055 μm^4/cm) of the aerogel batch.

[1]The designations were the same used in Table 5.1

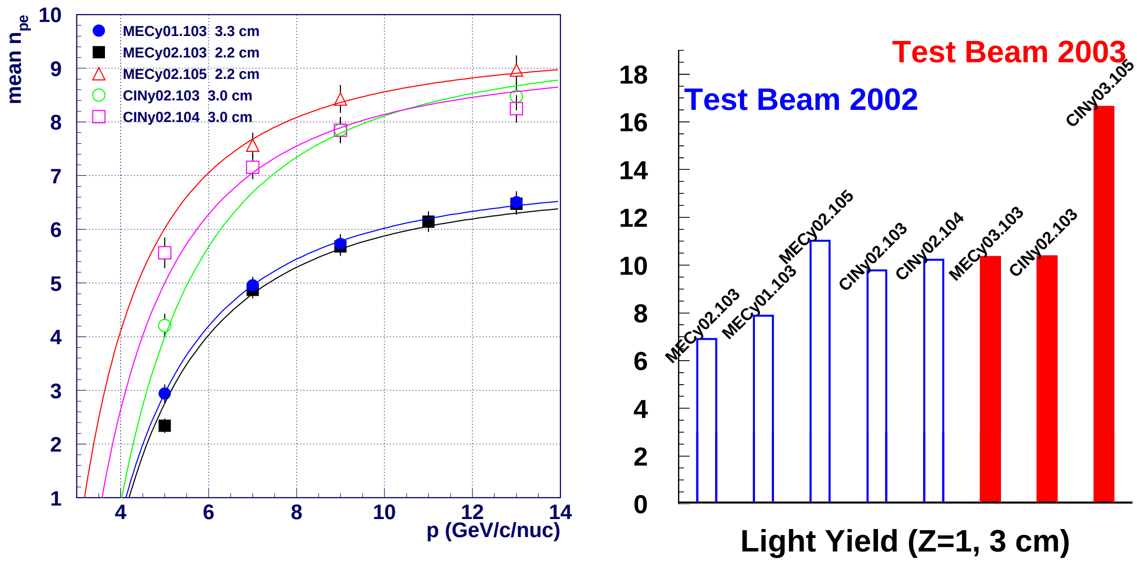

Figure 6.17: *Light yield as function of proton beam momentum for the different aerogel samples tested in 2002* (left). *Light yield comparison based on beam test data from 2002 and 2003. All values were extrapolated to fully cointained rings generated by a particle with $\beta \simeq 1$ and in an aerogel radiator with a thickness of 3 cm* (right) [191].

6.5 Charge Reconstruction Results

The spectra of reconstructed charges in the different aerogel radiator samples are shown in the panels of Figure 6.18. The reconstruction method used was the one described in section 4.4. Each spectrum displays a structure of well separated individual charge peaks over the whole range up to iron ($Z = 26$). The first three spectra refer to the charge measured with CIN103, MEC 103 and CIN105, respectively with a beam selection of $A/Z = 2$ while the lower right-hand plot refers to a beam selection of $A/Z = 2.25$ measured with the same CIN105 radiator.

The charge resolution for each element, shown in Figure 6.19, was evaluated through individual gaussian fits to the reconstructed charge peaks selected by the independent measurements performed by the scintillators and the silicon tracker prototype. The charge resolution up to $Z \sim 22$ is shown. A charge resolution for proton events slightly better than 0.17 charge units is attained with CIN105 and as expected the best charge resolution is provided by this radiator due to its higher photon yield.

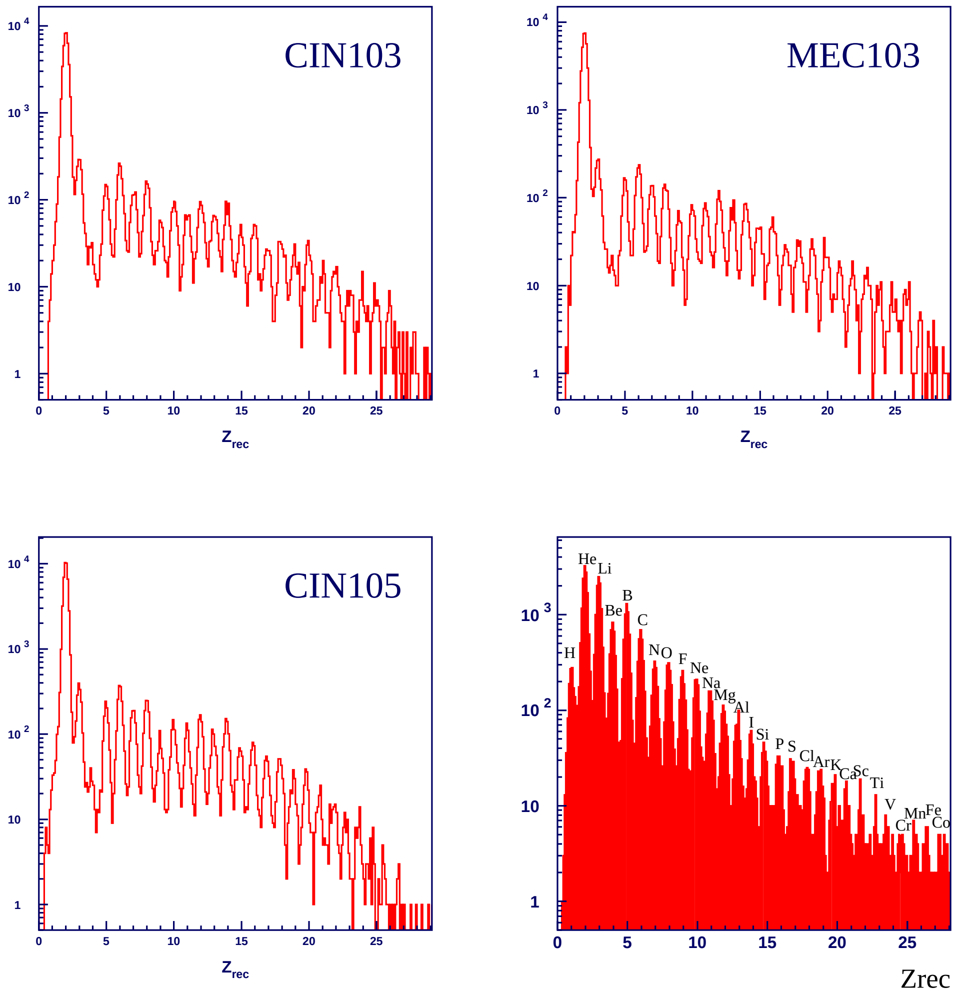

Figure 6.18: *Charge peaks distribution measured with the RICH prototype using: CIN103, 3 cm thick* (top left)*; MEC103, 3.3 cm thick* (top right)*; CIN105 2.5 cm thick* (bottom left) *with a beam selaction* $A/Z = 2$ *and a beam selection* $A/Z = 9/4$ (bottom right). *Individual peaks are identified up to Z*~ 26.

The charge resolution as function of the charge Z of the particle follows a curve that corresponds to the error propagation on Z which can be expressed as:

$$\Delta(Z) = \frac{1}{2}\sqrt{\frac{1+\sigma_{pe}^2}{N_0} + Z^2\left(\frac{\delta N}{N}\right)^2}. \qquad (6.10)$$

This expression, already presented in (4.59), describes the two distinct types of uncertainties that affect the measurement of Z: statistical and systematic. The statistical term is independent of nuclear charge and depends essentially on the

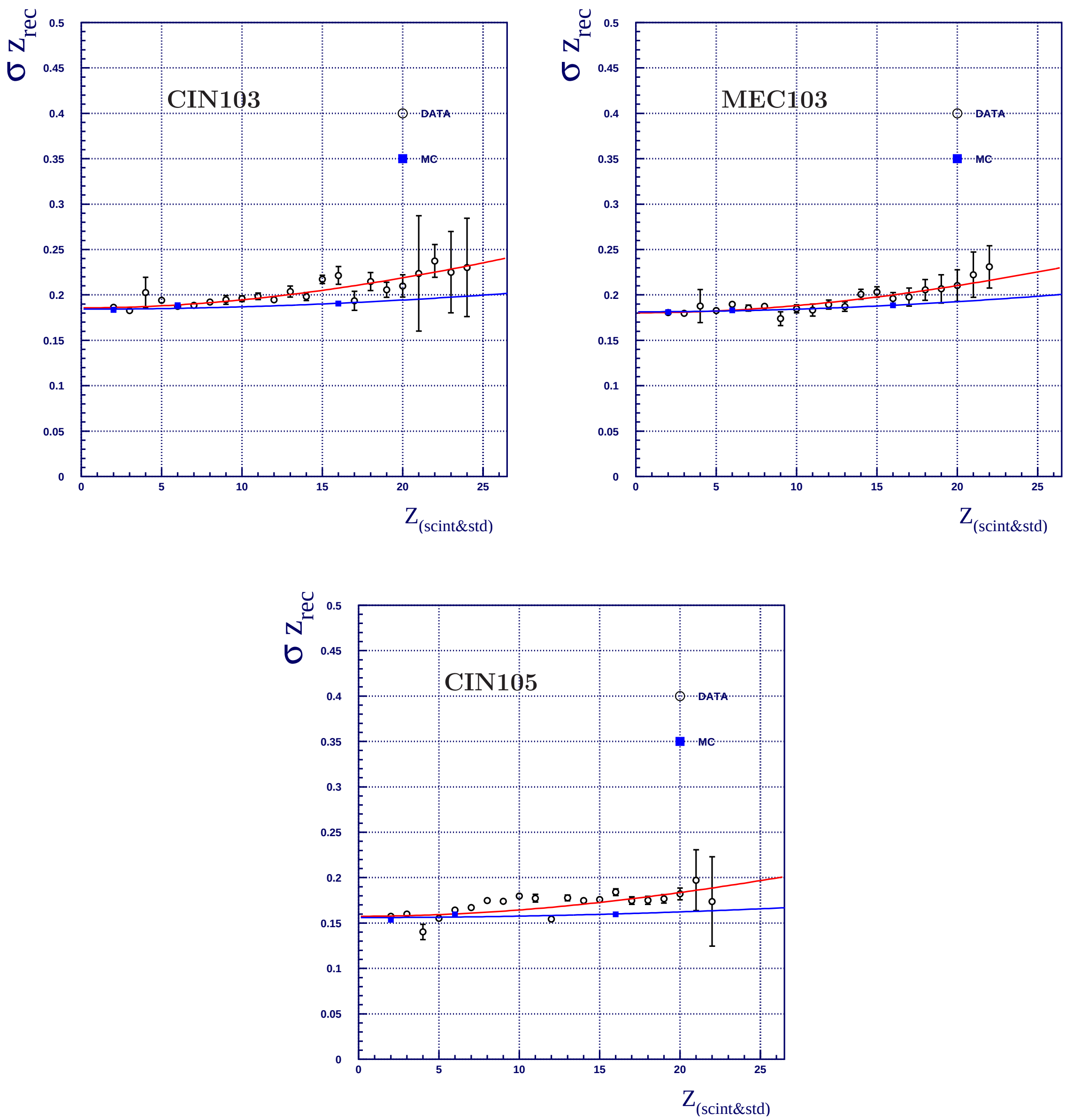

Figure 6.19: *Charge resolution for different aerogel batches. The results are fitted by the function (6.10). The dark blue squares are MC data points generated for Z=2, 6 and 16.*

amount of Čerenkov signal detected for singly charged particles ($N_0 \sim 14.27$) and on the resolution of the single photoelectron peak (σ_{pe}). The systematic uncertainty scales with Z, dominates for higher charges and is around 1%. It appears due to non-uniformities at the radiator level coming from variations in the refractive index, tile thickness or clarity or due to non-uniformities at the photon detection efficiency like PMT temperature effects or light readout non-uniformities (light guide and quantum efficiency). Monte Carlo data show a negligible systematic uncertainty (below 0.65%) as expected because the radiator is simulated as a uniform block and since all events present the same topology (vertical, fully contained rings) the touched photomultipliers always corresponds to the same sample with the same simulated response.

Table 6.8 summarizes the fitted parameters in data points and in Monte Carlo.

radiator	N_0	data type	σ_{pe} (%)	$\frac{\delta N}{N}$ (%)
CIN103	9.99±0.04	data	62.5±0.3	1.16±0.05
		MC	60.7±0.4	0.62±0.07
MEC103	10.66±0.04	data	63.7±0.3	1.05±0.07
		MC	65.0±0.4	0.64±0.08
CIN105	14.27±0.05	data	67.5±0.3	0.94±0.03
		MC	61.9±0.4	0.45±0.07

Table 6.8: *Aerogel response: signal for $Z = 1$, single photoelectron width and systematic uncertainty.*

6.6 Aerogel Tile Uniformity Studies

The thickness and the optical properties of the aerogel tiles need to be monitored as any variation on these properties will endow uncertainties on charge and velocity measurements. Prototype data collected with particles inciding in different positions of the tile can be used to evaluate its uniformity. At the tile scale a set of runs with narrow beams ($\sim 0.3\times 0.5\,\mathrm{cm}^2$) inciding in a matrix of nine points separated by $2.5-3.5\,\mathrm{cm}$ were used. In addition, wide beam runs with a section $\sim 0.7\times 1.2\,\mathrm{cm}^2$, corresponding to a beam selection of $A/Z = 2.25$ can also be used. All the setup parameters were kept stable and the different impact positions on the tile were achieved through displacements of the aerogel plane. This is for the former runs called *scan runs*, for the latter, the different impact positions resulted from the natural spread of the beam. Therefore, the measurement of both the ring signal and the velocity will be used to control the tile uniformity. The former will be sensitive to the clarity, thickness and refractive index and the latter will reflect any changes in the refractive index.

The data collected for the three radiators are summarized in Table 6.9.

radiator	Scan runs focused beam ($A/Z = 2$)		Spread runs wide beam ($A/Z = 2.25$)	
	Nb of points	H (cm)	Nb of points	H (cm)
CIN103	9	42.3	1	33.45
MEC103	9	42.3	1	33.45
CIN105	4	35.3	1	33.45

Table 6.9: *Collected data for aerogel uniformity studies.*

6.6.1 Photon yield uniformity studies

The purpose of the photon yield uniformity study is to quantify any variation of the parameters at different points of the aerogel tile that can influence the charge measurement. The strategy used to quantify these variations was to look at the mean number of photoelectrons. Helium nuclei from data samples $A/Z = 2$ were used in this study. These samples were selected according to the STD and scintillator measurements.

Figure 6.20 (left) shows the spatial distribution of scanned points in the CIN103 aerogel tile. Each point is separated from the neighbouring point by 2.5 cm. In the right-hand distribution the mean number of photoelectrons produced by helium nuclei impacting in each tile position is presented. Only eight points are available since position 5 generates Čerenkov photons close to the tile border with significant losses. The standard deviation associated to the mean number of photoelectrons

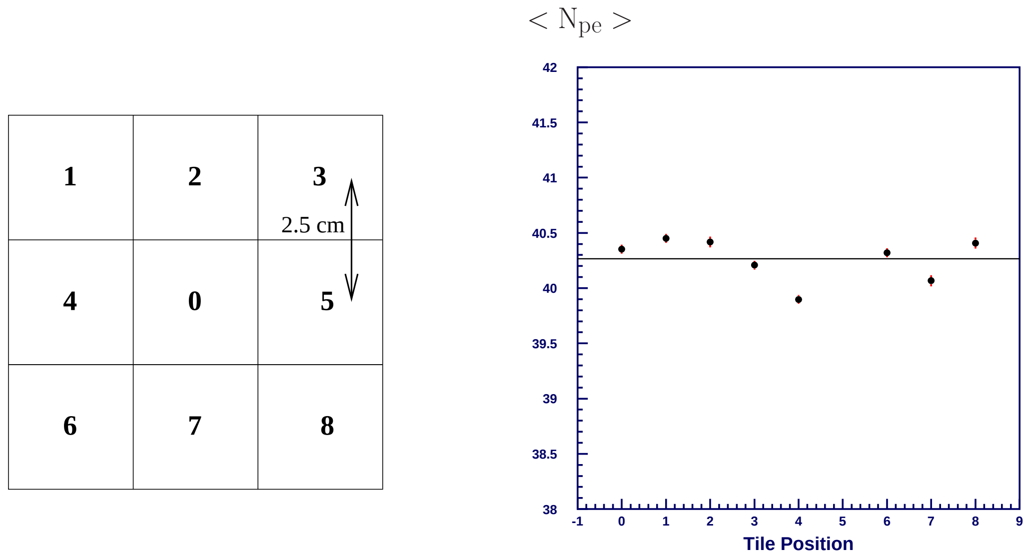

Figure 6.20: *CIN103 tile scan: tile scheme with the scanned points* (left) *and mean number of photoelectrons for Čerenkov rings generated from particles impacting in each scanned point* (right).

distribution quantifies the uniformity associated to the tile. For the set of eight measurements with CIN103 the tile uniformity was verified at the level of $(0.5 \pm 0.1)\%$.

Figure 6.21 presents the same measurements for the scan done with the MEC103 aerogel tile. In this case each point is separated from the neighbouring point by 3.5 cm. Here again only eight points are available since position 5 also generates Čerenkov photons close to the tile border with significant losses. The registered measurement for position 2 was excluded from the average of the other measurements because it is a very low value. The uniformity for MEC103 was estimated to be at the level of $(0.6 \pm 0.1)\%$.

According to the information presented in Table 5.1 the side length of CIN103 tile is 10 cm while the side length of MEC103 is 11.5 cm. However the CIN105 tile has the reduced size of 5 cm, which excludes the previous scan method for uniformity studies. Figure 6.22 shows an event with part of the ring width lost at the edge of the detection plane. Fortunately data from a wide beam are available, allowing to study the uniformity at a small scale (∼4 mm). The profile of the particle impact points for helium events is depicted in Figure 6.23 (left). The beam extension is ∼0.7 cm in the x direction and ∼1.2 cm in the y direction, covering

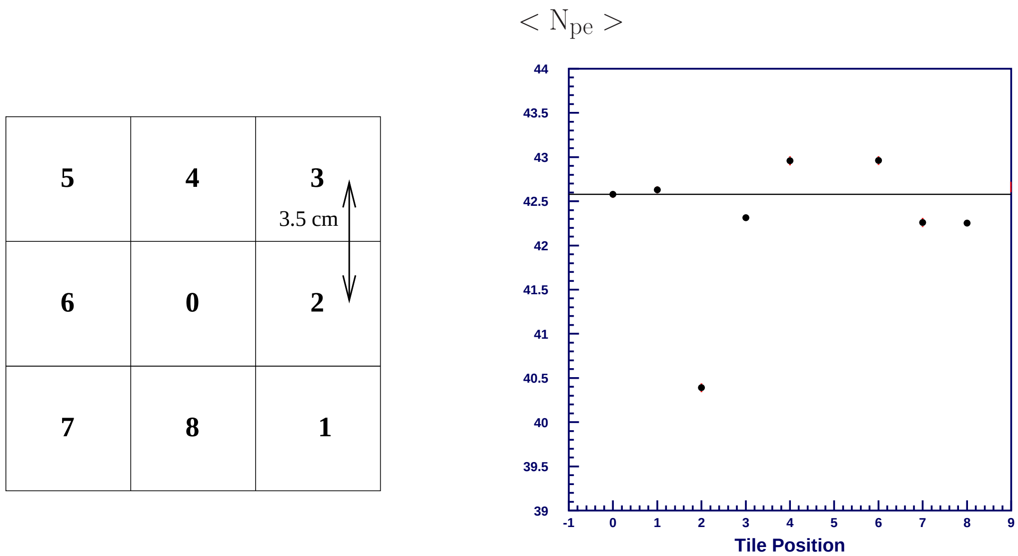

Figure 6.21: *MEC103 tile scan: tile scheme with the scanned points* (left) *and mean number of photoelectrons for Čerenkov rings generated from particles impacting in each scanned point* (right).

an area of ∼1 cm^2. The grid marked upon the figure was used to select the event samples according to the impact region and contain ∼1000 events. The grid cells have ∼4 mm of lateral dimension. A small fraction of the analyzed events had just a fraction of the Čerenkov ring, therefore an acceptance correction had to be applied to the mean number of photoelectrons. Figure 6.23 (right) shows the mean recontructed charge for the different data samples. Once more helium events were selected using scintillator and silicon tracker information, and the track used in the reconstruction was provided by the tracker. The variation on the mean charge relates to the variation on the mean number of photoelectrons as $\frac{\Delta Z}{Z} = \frac{1}{2}\frac{\Delta N_{pe}}{N_{pe}}$. A uniformity level of (0.6±0.1)% was evaluated from the mean charge variations. This can be translated in a variation of the mean number of photoelectrons of (1.2±0.1)%. The CIN103 uniformity was also evaluated using the wide beam technique. The mean reconstructed charge shown in Figure 6.24 (right) varies along the tile within (0.3±0.1)%. A uniformity on the mean number of photoelectrons of the order of (0.6±0.1)% was registered. A good agreement between the uniformity evaluated in both methods using the narrow and the wide beam is observed. The left-hand distribution shows the tracker coordinate measurements describing the beam profile used in this run.

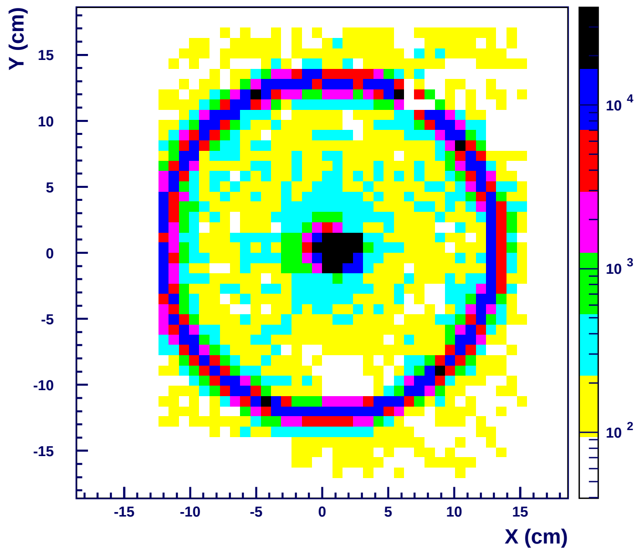

Figure 6.22: *Accumulated helium events generated by particles with the impact point at* (1.5;1.5) *cm in the CIN105 aerogel tile. Part of the ring width is lost at the left edge of the detection matrix.*

According to the study, all the radiators show a uniformity at the level of 1%.

6.6.2 Refractive index uniformity studies

Any relative variation in the refractive index directly reflects on the reconstructed velocity value according to expression 6.11.

$$\frac{\Delta\beta}{\beta} = \frac{\Delta n}{n} \tag{6.11}$$

Therefore, the tile uniformity concerning the refractive index can be evaluated looking at the variation of the mean reconstructed velocity in different points of the tile. However, this study cannot be done with the scan runs because of the uncertainty on the tile position which affects the expansion height. This systematic uncertainty is larger than the magnitude of the non-uniformies to be determined. For instance, a variation of 1 mm in the expansion height leads to a variation in the velocity measurement of the order of 10^{-3}.

The evaluation of tile uniformity will be based on data collected with a wide beam. The impact regions to be used will be the same, presented in Figure 6.23

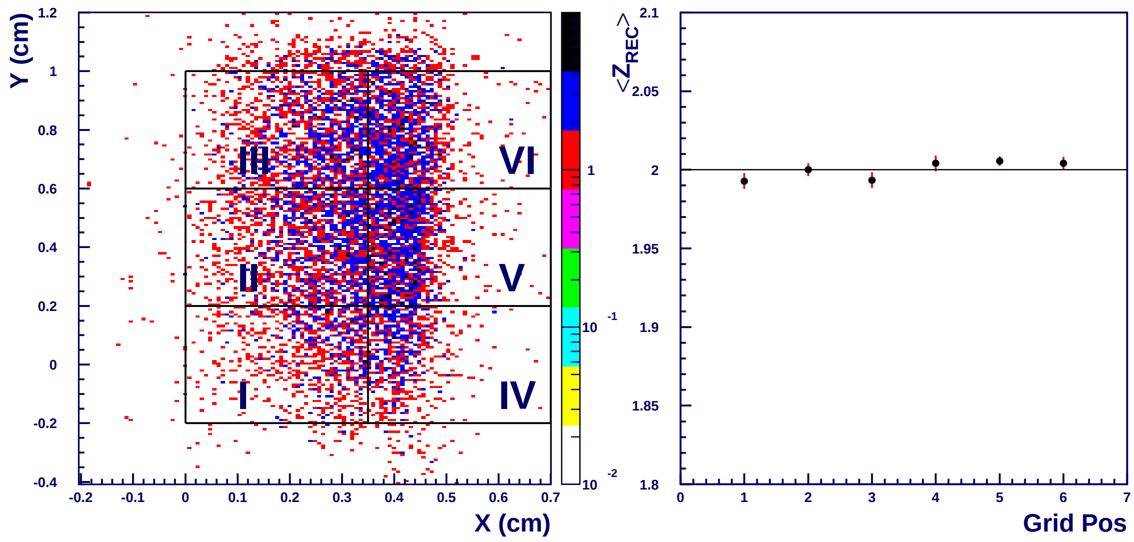

Figure 6.23: *Beam profile of a wide beam with the corresponding division in different samples for analysis* (left). *Average reconstructed charge for helium events impacting in CIN105 tile. Each point corresponds to a grid section of the wide beam* (right).

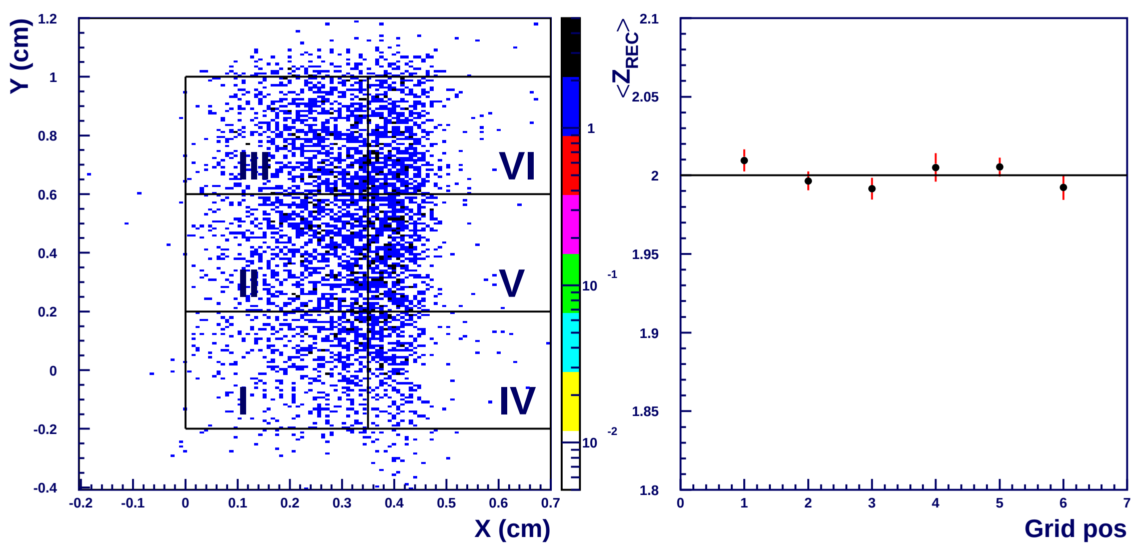

Figure 6.24: *Beam profile of a wide beam with the corresponding division in different samples for analysis* (left). *Average reconstructed charge for helium events impacting in CIN103 tile. Each point corresponds to a grid section of the wide beam* (right).

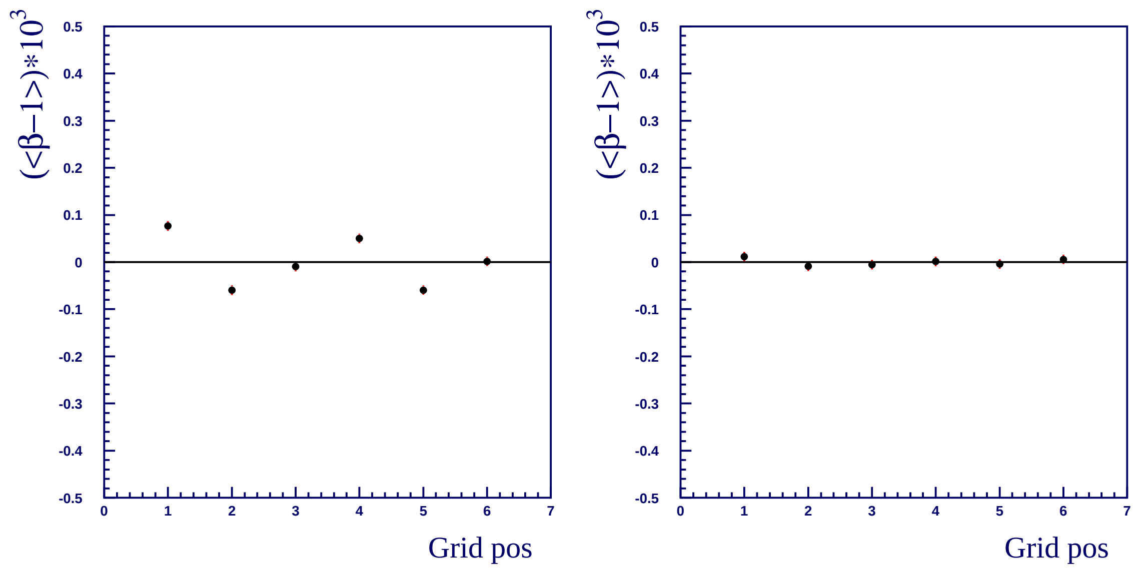

Figure 6.25: *Beam profile of a wide beam with the corresponding division in different samples for analysis* (left). *Average reconstructed charge for helium events impacting in CIN103 tile. Each point corresponds to a grid section of the wide beam* (right).

(left) and Figure 6.24 (left) for CIN105 and CIN103, respectively. The nucleus used in this study is the lithium nucleus ($Z = 3$) since in the present beam selection it is almost as abundant as the helium nucleus. This fact can be appreciated in the right bottom plot of Figure 6.18. Using this higher charge has the advantage of dealing with Čerenkov rings with more hits which leads to a more precise measurement of the average velocity value. The $Z = 3$ charge was selected using scintillators and STD information and the mean reconstructed velocity can be observed in the left- and right-hand plots of Figure 6.25 for CIN105 and CIN103, respectively. The refractive index uniformity is $\Delta n <(0.06\pm0.02)\times10^{-3}$ for CIN105 and $\Delta n <(0.007\pm0.002)\times10^{-3}$ for CIN103.

6.7 Conclusions

A complete characterization of the three aerogel radiators used in the 2003 beam test was done in the present chapter. Velocity and charge reconstruction algorithms were tested over a well selected data sample. The velocity resolution dependence with the charge and results are in full agreement with Monte Carlo simulation. All the radiators tested fulfill the RICH requirements for β measurement.

The light yield of each radiator was evaluated and is in good agreement with the Monte Carlo simulation. The measurement made clear that the highest signal comes undoubtedly from CIN105.

Charge reconstruction was studied and a clear charge separation up to $Z = 26$ was achieved. A charge resolution for helium events slightly better than $\sigma_Z \sim 0.2$ was observed together with a systematic uncertainty of the order of 1%.

The aerogel tile uniformity concerning the light yield was confirmed and the non-uniformities are smaller than 1.2% for all samples. This result was obtained both from the analysis of data obtained in different runs from a scan of the tile, except for CIN105 tile due to its reduced dimensions, and from data obtained in the same run using a wide beam. All the measured variations on the mean number of photo-electrons are consistent with the systematic uncertainty on the charge measurement (~1%).

The study of the bias in the mean value of β provides us with a direct estimation of the refractive index variation which is set to be lower than $\Delta n < 10^{-4}$. All the measured variations on the mean num

The detector design including an aerogel radiator was validated and a refractive index 1.05 aerogel was chosen for the RICH radiator, fulfilling the demand for both a large light yield and a good velocity resolution. This is particularly important for singly charged particles for which the light production would keep the reconstruction efficiency at a good level through time. In addition MEC products are available only in 1 cm thick tiles which implies the pile-up of tiles and an increase of the surface scattering. However, MEC material is hydrophobic and easier to manipulate while the CIN aerogel is hydrophilic. Nevertheless, keeping the radiator plane in dry conditions in the AMS scenario is easily achievable and does not represent a significant technical difficulty. The deterioration on a long period of the hydrophilic aerogel has been excluded by the comparison of the performance of a CIN sample in 2002 and 2003 beam test which showed no degradation in the light yield. All these facts lead the collaboration to elect CIN105 as the final aerogel radiator.

Chapter 7

Sodium Fluoride Radiator

Has anything escaped me? ... I trust that there is
nothing of consequence which I have overlooked?
Sherlock Holmes in The Hound of the Baskervilles
by Sir Arthur Conan Doyle

7.1 Introduction

As was thorougly described in the RICH setup (Chapter 3), the central part of the radiator is a squared region with $34{\times}34\,\mathrm{cm}^2$ made of sodium fluoride (NaF), with a refractive index of 1.334. This configuration provides a larger acceptance which increases the reconstruction efficiency and extends to lower values the particle momentum range covered.

During the 2003 beam test a sample of sodium fluoride with $8{\times}8\,\mathrm{cm}^2$ with a thickness of 0.474 cm, close to the 0.5 cm established for the flight setup, was tested. The purpose of the performed tests was to evaluate the response of the detector to the NaF generated events and the robusteness of velocity and charge reconstruction algorithms dealing with the NaF generated patterns. Another important point that NaF data allows to study is the light-guide detection behaviour in a region of higher photon incident angles. Due to the higher refractive index of sodium fluoride, photons are emitted with a larger Čerenkov angle which is amplified by the refraction at the NaF/air transition, and as a result they reach the light-guide surface with a greater angle to the normal than in the aerogel case.

Collected data are summarized in Table 7.1 and corresponds to different incidences. The distance between the radiator plane and the detection plane (expansion height) was adjusted to a value slightly higher than 7 cm in order to have fully contained rings in the detection plane. The beam selection was set to A/Z=2 for all the NaF study.

Run nb	$H_{\rm rad}$ (cm)	H (cm)	θ	Mirror	A/Z
557	0.474	7.2	0	no	2
561	0.474	7.2	5	no	2
562	0.474	7.2	10	no	2
564	0.474	7.2	15	no	2
565	0.474	7.2	20	no	2

Table 7.1: *Sodium fluoride data characteristics: run number (run nb), radiator thickness (H_{rad}), expansion height (H), angle between the beam line and normal to the radiator plane (θ), presence of mirror and beam selection (A/Z)*

7.2 Data With a Normal Incidence of the Beam

Figure 7.1 shows a fully contained nitrogen event ($Z = 7$) generated in the sodium fluoride radiator. The reconstructed particle impact point by the *fitcircle* method (RICH track reconstruction), explained in subsection 5.10, is marked upon the figure. This point shows a deviation with respect to the position of the pixel with maximum signal. In Figure 7.2 is visible a shift of the order of 1 cm. In fact, the beam position is very stable along the test period for A/Z=2 data and is of the order of the values for the reconstructed coordinates presented in Figure 5.24.

The result for the RICH reconstruction of the impact point is shown in Figure 7.3 for $Z = 2$ and $Z > 2$ events. The latter distribution allowed to determine an effective position of the particle impact point with a higher precision. The coordinates of the point obtained are the following (X_{eff}, Y_{eff})=(1.318;1.165) cm common to all events of the run. The deviation observed is due to the existence of cross-talk[1] between

[1]This effect consists of detecting the photon in a different PMT channel from the corresponding coupled light-guide pipe that it entered.

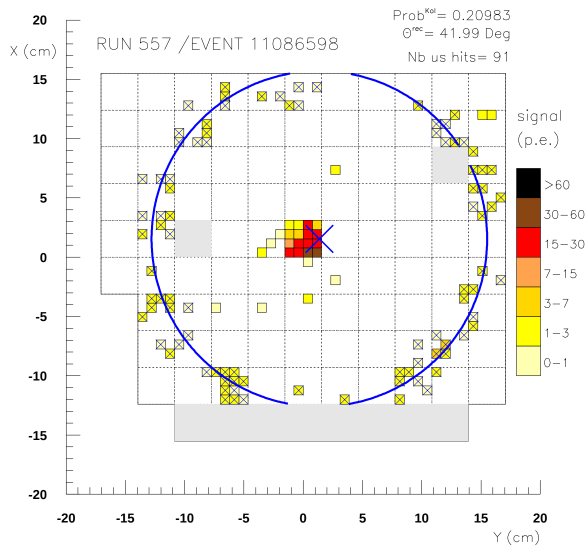

Figure 7.1: *Sodium fluoride event with Z=7. The event is a fully contained ring with the reconstructed impact point marked with a cross.*

different light-guide pipes, which enlarges the ring because of the outwards radial direction of the Čerenkov photons. In practice, this effect displaces some channels including the particle hit channels.

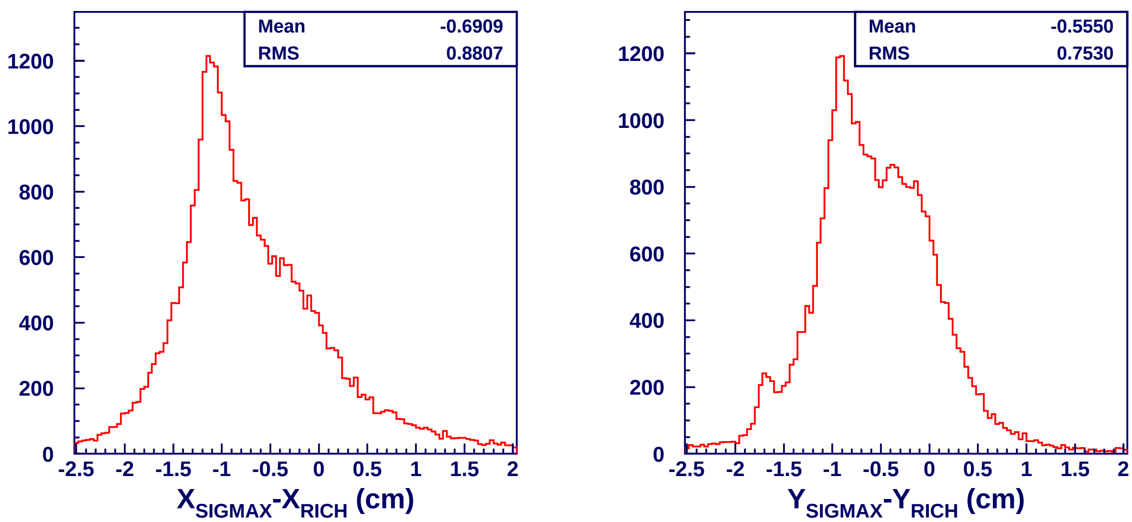

Figure 7.2: *Difference between the coordinates of the pixel with maximum signal and the reconstructed impact coordinates.*

The effective track will be used because although it does not indicate the beam

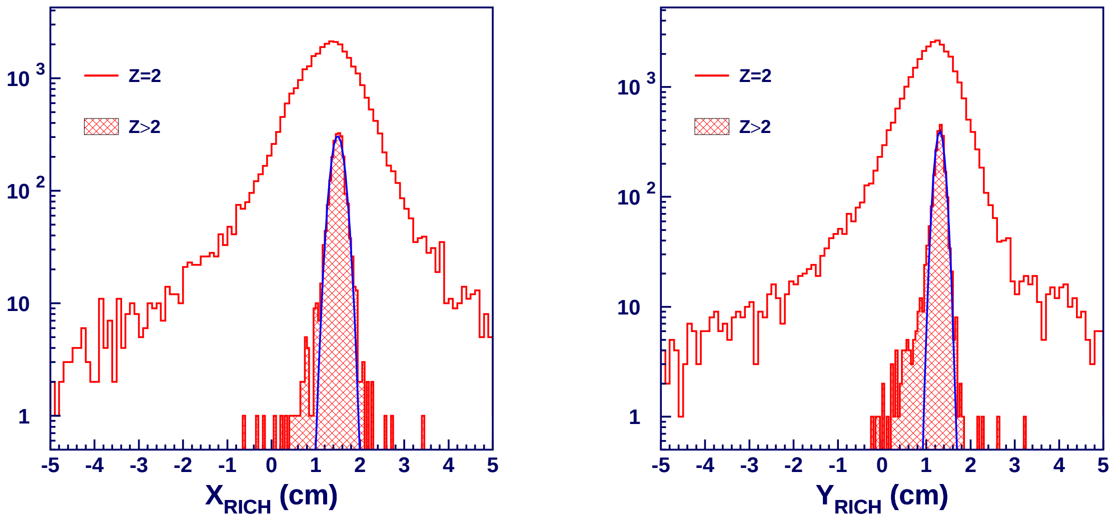

Figure 7.3: *Coordinates of the RICH reconstructed impact coordinates.*

position, it leads to a better reconstructed β resolution. Otherwise, using the nominal track the obtained β resolution is $\sim$30% worse.

7.3 Velocity Reconstruction

Before analysing the sodium fluoride data the velocity algorithm has to be tunned in a process analogous to what was done for the aerogel. The residual distribution is shown in Figure 7.4 (left). This distribution was also extracted from simulation using a uniform distribution of the particle impact point in the radiator in a central square with 5 cm. A single gaussian was fitted to the distribution and a sigma of $\sigma = 0.746 \pm 0.003$ was extracted. A likelihood function like the one described in section 6.6 was assumed and the determination of the background ratio b and of the cut distance d_{cut} followed as described before in the previous tunning procedure.

Samples of 15000 vertical helium nuclei with $\beta \simeq 1$ and fully contained rings were simulated. The relative velocity resolution σ_β/β is estimated from the distribution $(\beta^{sim} - \beta^{rec})$, for each established pair (b,d_{cut}). The evolution of σ_β/β with d_{cut} is presented in Figure 7.4 (right). The optimized cut distance is set at $d_{cut} = 2.18$ cm which corresponds to a background $b = 0.10$.

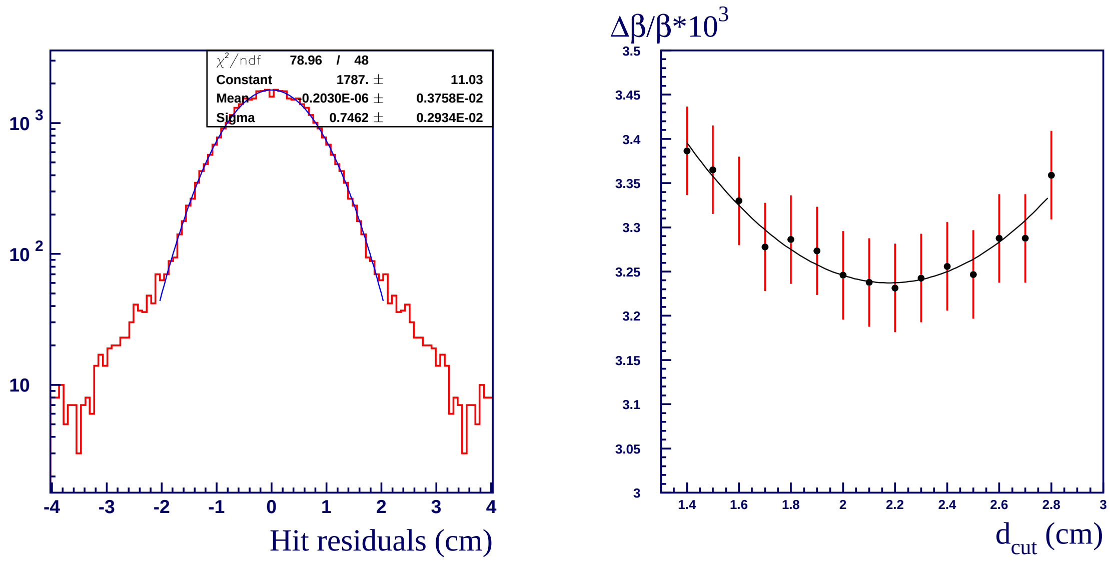

Figure 7.4: *Hit residuals relative to the expected pattern for 40000 simulated helium events in the sodium fluoride radiator of the RICH prototype* (left). *Relative velocity resolution for helium nuclei impacting in the sodium fluoride radiator in the prototype setup versus cut distance between signal and noise hits in the spatial distribution* (right).

The selected sample of events fulfilled the same criteria used for aerogel analysis (see section 6.2). The track compatibility was imposed as well as a one particle request and Kolmogorov probability > 0.1. Reconstructions with less than three associated hits were rejected. The independent charge selection was done using the scintillators and STD information.

Figure 7.5 shows the distributions of reconstructed velocity for helium nuclei using beam test data (left) and simulated data (right). The β resolution is better in data $[\sigma_\beta/\beta = (3.28\pm0.02)\times10^{-3}]$ than in MC $[\sigma_\beta/\beta = (3.47\pm0.02)\times10^{-3}]$. However the reconstructed velocity values in real data and simulation are shifted with respect to the nominal β ($\beta \simeq 1$) around two standard deviations. This is observed due to the cross-talk effect which causes an enlargement of the Čerenkov ring associated with the reduced expansion height. Assuming an enlargement δx of the ring this leads to a Čerenkov angle increase of $\delta\theta_c \simeq \delta x/H$. The same effect is present in the flight geometry. However, due to the higher expansion height (46.2 cm) compared with the reduced prototype expansion height in this run (7.2 cm) the reconstructed velocity does not suffer any visible shift.

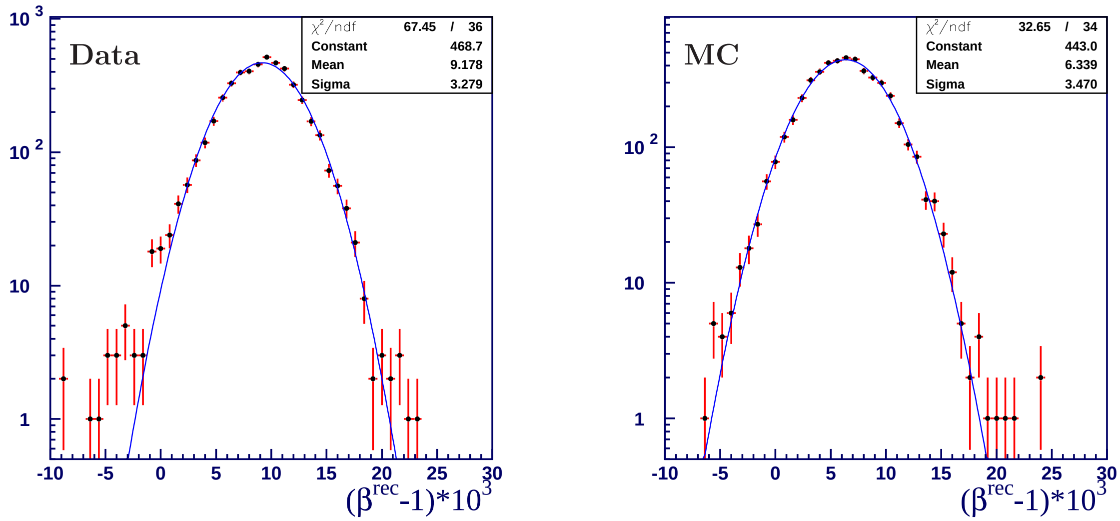

Figure 7.5: *Distribution of* $(\beta^{rec}-1)\times10^3$ *for helium events from beam test* (left) *and simulated data* (right).

Figure 7.6 (left) introduces the evolution of the relative velocity resolution with charge for sodium fluoride data. Each point is evaluated from a gaussian fit to the distribution $(\beta^{rec} - \beta^{sim})$. A fit to the data points allows to derive $\frac{\sigma_\beta}{\beta} = \sqrt{\left(\frac{6.36\pm0.04}{Z}\right)^2 + (0.77\pm0.02)^2} \times 10^{-3}$.

7.4 Charge Reconstruction

Figure 7.6 (right) shows the measured charge spectrum with the sodium fluoride radiator. Only the helium charge can be identified with a resolution $\sigma(Z=2) = 0.350\pm0.003$ charge units. This is expectable due to the reduced light yield for $Z=1$ which is of $N_0 \sim 3$ photoelectrons. This is translated in an expected statistical error for Z measurement of $\sigma(Z) = \frac{1}{2}\sqrt{\frac{1+\sigma_{pe}^2}{N_0}} \sim 0.35$, assuming $\sigma_{pe} \sim 0.7$. This confirms that sodium fluoride is not appropriate for charge reconstruction, however this was not the reason for its inclusion.

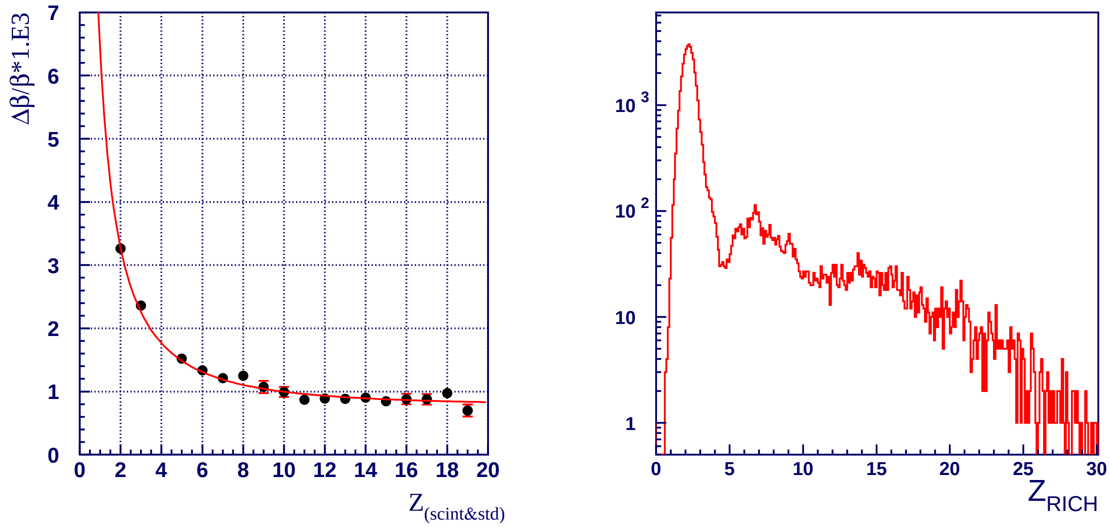

Figure 7.6: *Evolution of the relative error on reconstructed β with the particle charge for sodium fluoride* (left)*. RICH reconstructed charge with the sodium fluoride radiator* (right)*.*

7.5 Light Yield Evaluation

For the light yield evaluation a sample of helium events was analyzed. The number of photoelectrons and the number of hits were used to monitor the radiator response as the former is sensitive to any efficiency variation and the latter to the cross talk effects. Figure 7.7 shows the reconstructed signal number of photoelectrons and number of hits for both real data and simulated samples, together with the fits according to the function described in 6.4 for the number of photoelectrons. For the number of of hits a Poisson function was applied. The results are shown in Table 7.2. A disagreement between data and MC is observed. Data presents a higher signal

	$< N_{pe} >$	$< N_{hits} >$
Data	12.91 ± 0.03	11.15 ± 0.03
MC	11.26 ± 0.03	9.63 ± 0.03

Table 7.2: *Mean number of photoelectrons and hits for the reconstructed signal for a helium sample in NaF both in data and MC.*

($\sim$15%) when compared to the MC prediction.

The radiator thickness was measured to be $H_{rad} = 0.474 \pm 0.005$ cm. The thickness measurement uncertainty leads to a light yield variation of 1%, which is negli-

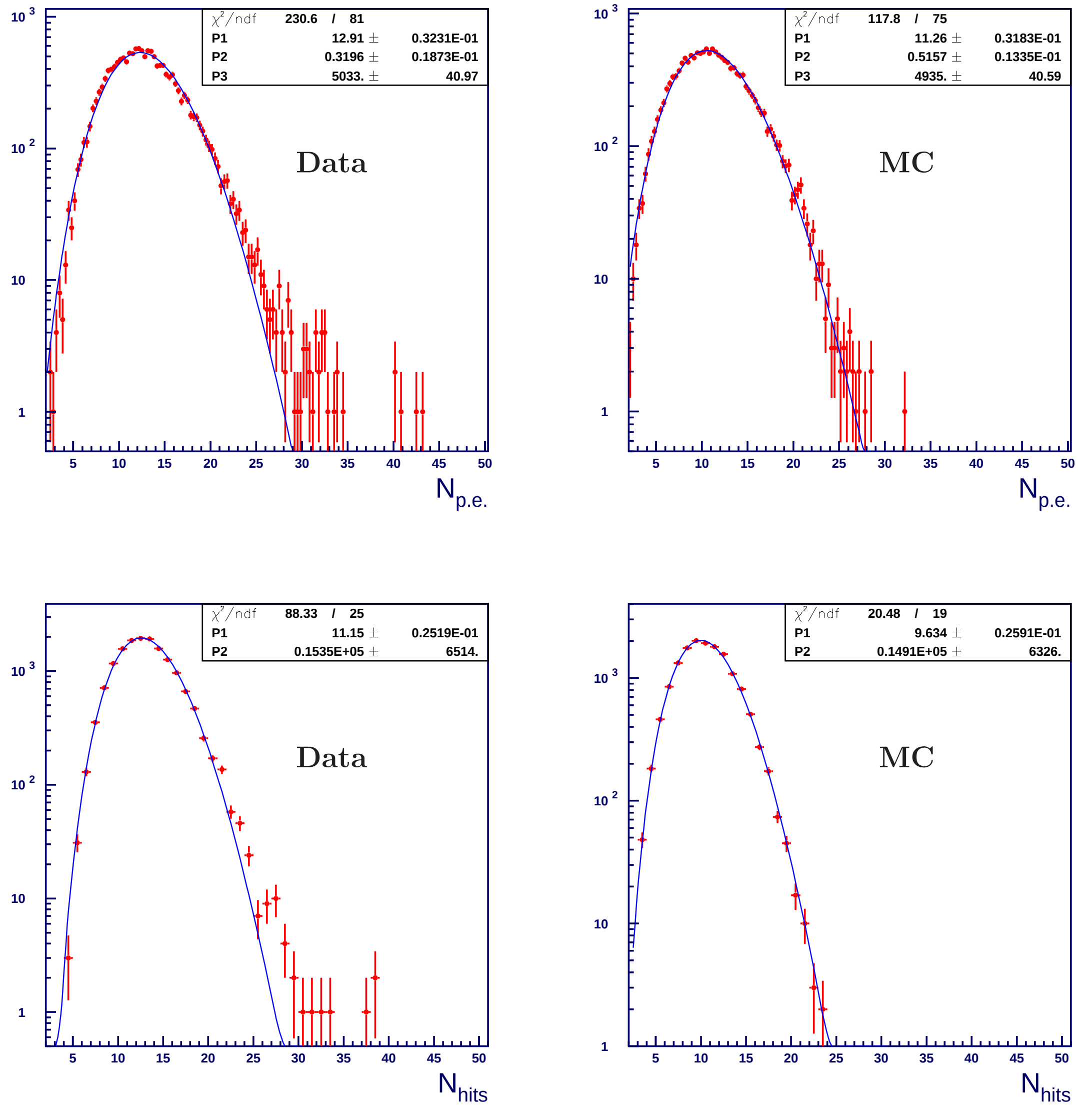

Figure 7.7: *Distributions of the number of photoelectrons* (top) *and number of hits* (bottom) *for helium events in prototype* (left) *and simulated data* (right).

gible and does not explain the observed disagreement.

A possible explanation for this disagreement is the light guide behaviour due to the large incident angle of photons at its top. The aforementioned angle, θ_γ, is represented in Figure 7.8 (left).

The results obtained for the relative variation of the light yield as function of the photon incident angles for vertical runs for each of the three radiators (CIN103, CIN105 and NaF) are shown in Figure 7.9 (left). The aerogel data for the vertical runs ($\theta_\gamma = 18.67°$) shows an agreement better than 1%.

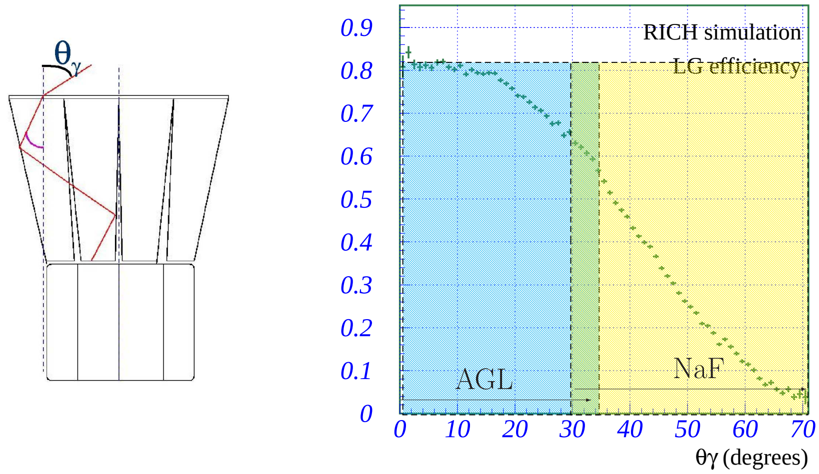

Figure 7.8: *Light-guide scheme with the definition of the photon incident angle (θ_γ). Light-guide efficiency as function of the θ_γ as derived from the RICH simulation. The angular incidences covered with beam test data are marked upon the plot for aerogel and sodium fluoride.*

The aerogel runs in the beam test allowed to test the light-guide behaviour over a photon angular region up to 35°. The NaF perpendicular configuration together with all the tested inclinations ($\theta = 5°$, 10°, 15° and 20°) allowed to study the same feature in an angular region ranging from 30 to 70°. This is visible in Figure 7.9 (right) which presents the distribution of the photon incident angles of the events depicted in Figure 7.10.

The light-guide efficiency is considerably more stable (~80%) for photon incidences up to 20° as can be observed from Figure 7.8 (right). Beyond this value it decreases very rapidly. A bad description of the light-guide behaviour in the MC simulation could be significant in the angular region corresponding to the NaF-generated photons. A detailed standalone light-guide activity was developed to have a better understanding of the light-guide detection efficiency.

7.6 Light Guide Simulation

A detailed standalone simulation of the detection cell used in the RICH prototype was developed in GEANT 3.21. The light-guide geometry was updated and some

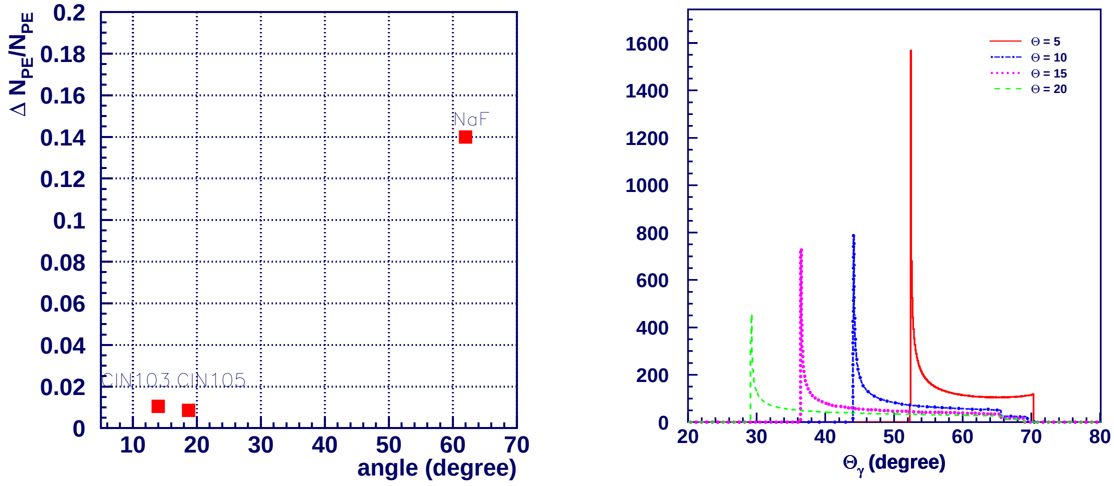

Figure 7.9: *Light yield relative variation between data and simulation as function of the photon incident angles for vertical runs for radiators CIN103, CIN105 and NaF. The aerogel data shows and agreement better than 1% while a data excess of 14% is observed in NaF* (left). *Distribution of the photon incident angles at the top of the light guide for NaF data generated by particles with inclinations $\theta = 5^o$, 10^o, 15^o and 20^o* (right).

corrections on the material properties were introduced.

Simulated geometry

As was described in Chapter 3 a polycarbonate housing surrounds the detection cell. This piece can be observed in Figure 3.22. On the previous version of the RICH simulation the housing was not introduced. Figure 7.11 shows the housing structure in dashed, surrounding the PMT, part of the front-end electronics and extending up to 10 mm from the light-guide basis. This particular geometry was introduced in the standalone light-guide simulation.

Another important change was the PMT shielding that used to be simulated as a 100% absorbing material. The shielding is represented in Figure 7.11 by a parallelepipedic shape with a height of 75 mm that basically surrounds all the detection cells. Both housing and shielding reflectivities are important to be taken into account because considering them allows to redirect photons with certain in-

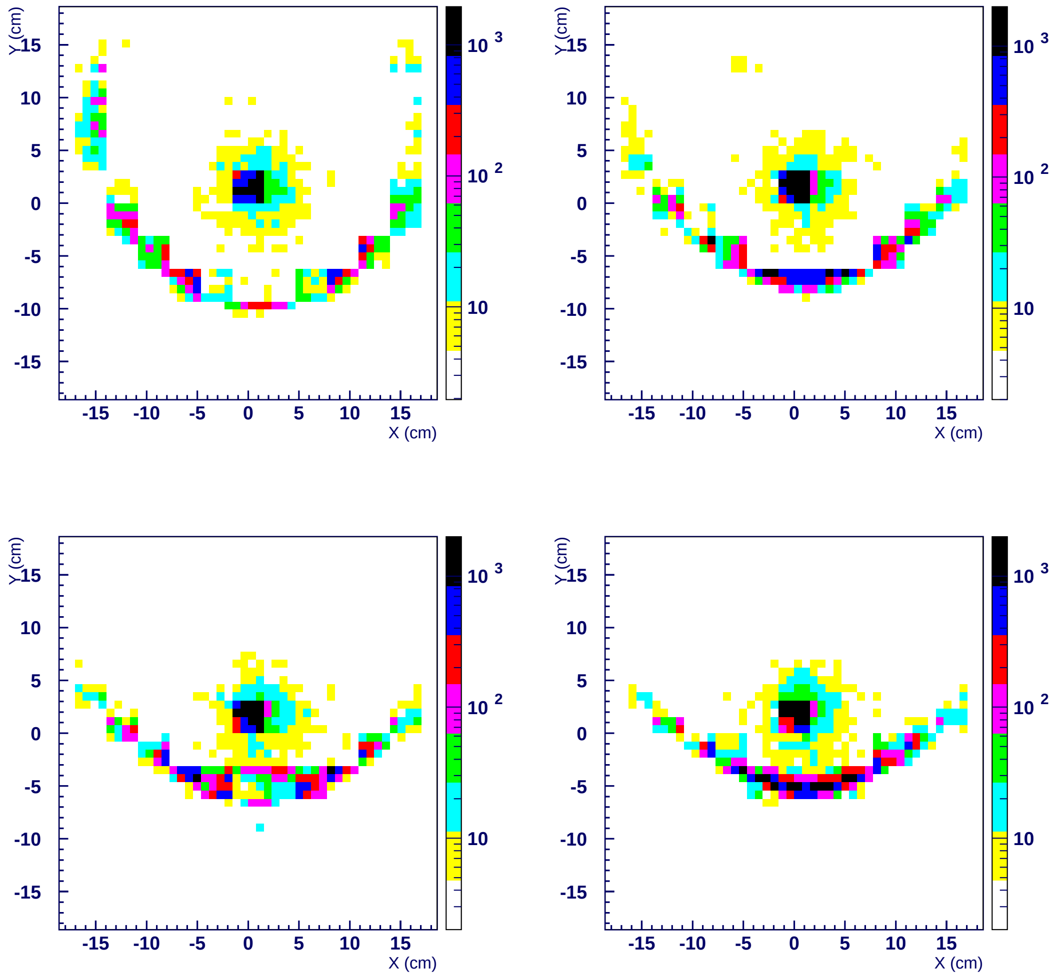

Figure 7.10: *Accumulated helium events generated by particles with $\theta = 5^o$, 10^o, 15^o and 20^o impinging in sodium fluoride.*

cidences to the light-guide piece which increases the simulated detection efficiency. The simulated geometry is presented in Figure 7.12 (left).

Reflectivity measurement

The reflectivity of the housing and shielding materials was measured at CIEMAT, Madrid with the spectrophotometer Minolta CM-2600d depicted in Figure 7.12 (right). The measurements were done with the flight pieces. In fact, the housing used in the prototype detection cells is made of the same material used for the flight, however the shielding material differs and only a piece used in the flight

Figure 7.11: *Geometry of the detection cells used in the RICH prototype. All the dimensions are expressed in mm.*

configuration was available.

The three panels represented in both Figures 7.13 and 7.14 correspond, as quoted in the figures, to the reflectivity measured with the Specular Component Included (SCI), Specular Component Excluded (SCE) and Specular Component (SCI − SCE) for different faces of the housing and for the non-welding faces of the shielding and at different points, respectively.

The spectrophotometer provides the first two measurements. SCI provides the full reflectivity while the SCE provides the non-specular component. The specular reflectivity can be extracted from a direct subtraction of the two measurements above.

A perfectly specular surface corresponds to SCI $\gg$ SCE and reflects light in a directional manner such that the angle of reflection is approximately the angle of incidence. A completely rough surface corresponds to SCI $\simeq$ SCE. This type of surface reflects light in a non-directional manner (diffusely). A perfect absorption would lead to SCI $\simeq$ SCE $\simeq 0$.

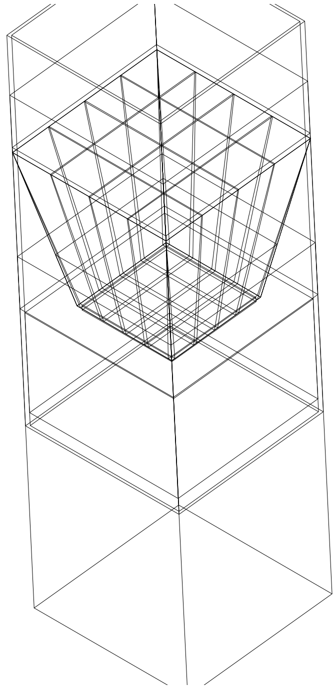

Figure 7.12: *Complete simulated detection cell: light guide, PMT, housing and shielding* (left). *Spectrophotometer Minolta CM-2600d* [192] (right).

The mean values measured for the reflectivity, for the percentage of specularly reflected photons and non-specular photons at $<\lambda>= 420\,\mathrm{nm}$ (maximum of quantum efficiency detection) are presented in Table 7.3.

	$<$refl$>$	$<$Specular component$>$	$<$Non Specular component$>$
Shielding	45%	66%	34%
Housing	5%	50%	50%

Table 7.3: *Mean values for the reflectivity measurements with Minolta CM-2600d.*

The values assumed in the simulation were:

- 5% of reflectivity with 50% of specular component for the housing specularity;
- a variable shielding reflectivity and specularity from 0 to 100%.

Simulation procedure

The Čerenkov photons were uniformly generated at the top of the light guide fulfilling the following characteristics:

Figure 7.13: *Housing reflectivity measurements with spectrophotometer Minolta CM-2600d on different faces.*

- wavelength spectrum proportional to $1/\lambda^2$ as expressed in equation 3.10 and shown in the left-hand panel of Figure 7.15;

- θ_γ uniformly generated between 0^o and 90^o (Figure 7.15, middle);

- ϕ_γ uniformly generated between 0^o and 360^o (Figure 7.15, right);

- a random polarization to the photo

Figure 7.14: *Shielding reflectivity measurements with spectrophotometer Minolta CM-2600d on non-welding faces at different points.*

The latter property was obtained considering $\vec{k}$ as the vector associated to the photon's path in the RICH frame.

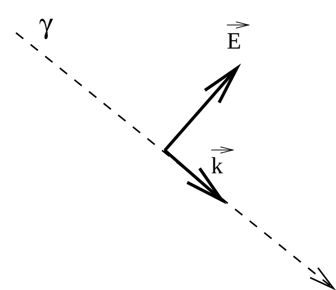

A system of coordinates with base vectors $\vec{u}$, $\vec{v}$ and $\vec{k}$ was built with:

$$\begin{aligned} \vec{u} &= (-k_y, k_x, 0)/\sqrt{k_x^2 + k_y^2} \qquad (7.1) \\ \vec{v} &= \vec{k} \times \vec{u} \end{aligned}$$

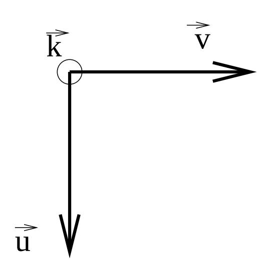

The polarization vector is generated in the transverse plane defined by $\vec{u}$ and $\vec{v}$.

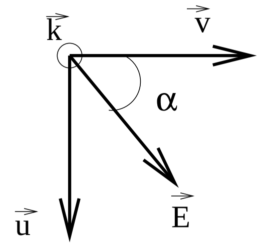

$$\begin{aligned} \vec{E} &= c_1\,\vec{u} + c_2\,\vec{v} \qquad (7.2) \\ c_1 &= \vec{E}\cdot\vec{u} = \cos\left(\frac{\pi}{2} - \alpha\right) = \sin\alpha \\ c_2 &= \vec{E}\cdot\vec{v} = \cos\alpha \end{aligned}$$

Therefore, α is randomly generated between 0 and 2π and the electric field is defined as

$$\vec{E} = \sin\alpha\;\vec{u} + \cos\alpha\;\vec{v}. \qquad (7.3)$$

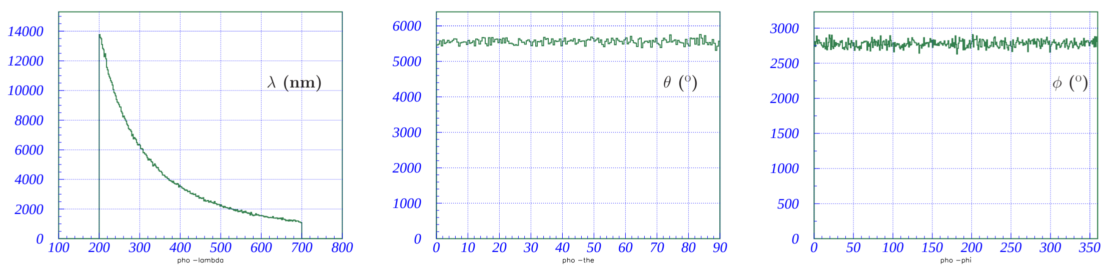

Figure 7.15: *Distributions of generated photon wavelength* (left), θ (middle) *and* ϕ (right).

7.6.1 Results

Detection efficiency

A reflectivity of 100% and a specularity of 100% were initially simulated for the shielding surface. The detection efficiency is defined as the fraction of the detected photons in any pixel of the PMT and is represented in Figure 7.16. The first panel shows the light-guide detection efficiency for all photons. The next panel represents the same detection efficiency for photons that enter the light-guide cell and are confined to its volume which means they do not touch the shielding. Comparing the first distribution with the second an increase of the detection efficiency is visible for higher incidence angles, as expected. This angular region is clarified in the third panel that shows the detection efficiency for photons that touched the shielding. The mean incident angle of this population is around 50$^{\rm o}$ and an efficiency increase of more than 4% is reached for this angle compared to the fully absorbing shielding.

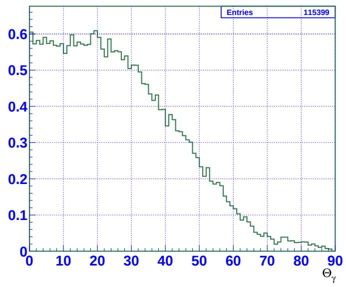

Figure 7.16: *Distributions of the light-guide detection efficiency versus the photon incident angle: for all the detected photons* (left), *for light-guide-confined photons* (middle) *and for photons reflecting on the shielding* (right). *An extreme shielding reflectivity of 100% and a specularity of 100% were considered.*

Following the distribution of the photons hitting the shielding will be looked in detail [Figure 7.16 (right)]. A fraction of 29% of the photons were shifted from one light-guide pipe to another (cross talk). Most of the photons that suffered cross talk have entrance angles in the light guide above 50° as shown in Figure 7.17 (right). Figure 7.17 (left) shows the photon's angle distribution entering the light guide and being detected in the same light-guide pipe.

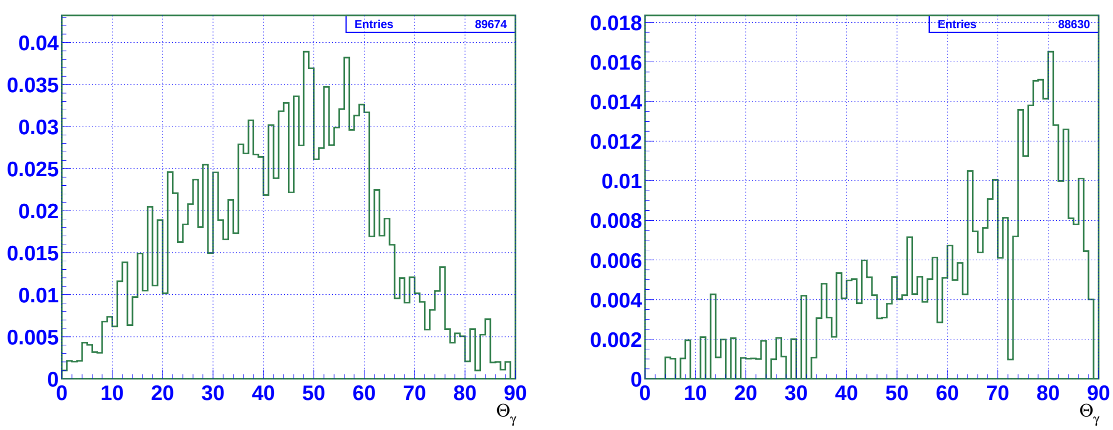

Figure 7.17: *Distributions of the light-guide detection efficiency versus the photon incident angle for photons reflecting in the shielding: photons that do not suffer cross-talk* (left), *photons suffering cross talk* (right). *A shielding reflectivity of 100% and a specularity of 100% were considered.*

The dependence of the light-guide efficiency with the shielding reflectivity and its specularity was evaluated. Figure 7.18 shows the variation of the detection ef-

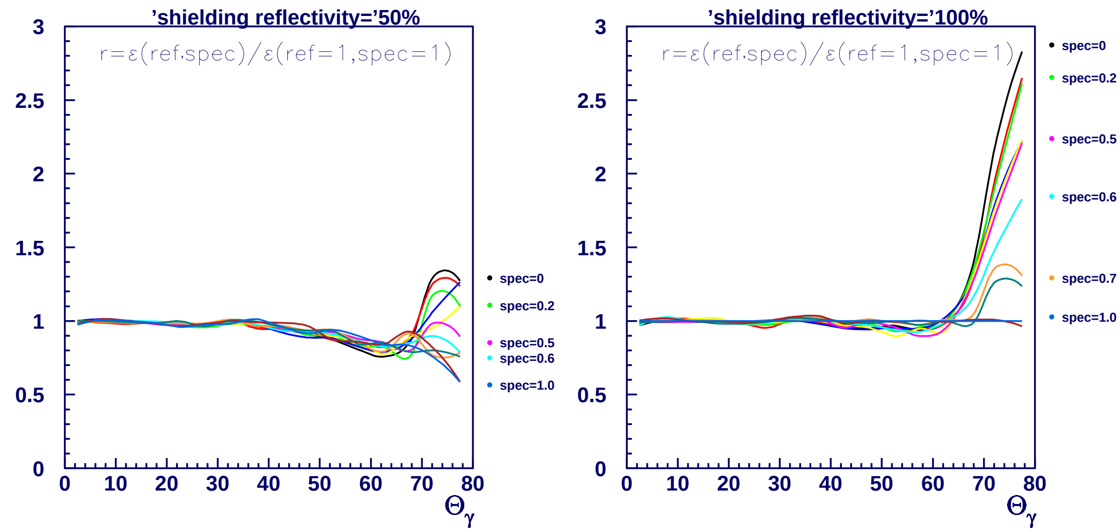

Figure 7.18: *Light-guide detection efficiency variation compared with a fully reflective and specular shielding: 50%* (left) *and 100%* (right) *reflectivity.*

ficiency when compared to the full reflective and specular case. The spectularity dependence is only relevant for large incident angles ($\theta_\gamma > 75°$). In particular, the higher detection efficiencies are obtained for the diffused case (specularity = 0). The dependence of the detection efficiency with the reflectivity is only relevant for angles greater than ∼50°. The higher is the reflectivity, the larger is the efficiency as can be seen in Figures 7.18 obtained with reflectivity 50% and 100% and specularity ranging from 0 to 1.

The photons incident angle on the top of the light guide can be reconstructed, Figure 7.19 (right) shows this reconstruction together with the simulated angle (left). The reconstructed angular distribution can not be used for the MC tunning, however its number N_{ring}^{SIM} can be used and compared with the data value N_{ring}^{DAT}. A scan on the parameter space of reflectivity and specularity was done and a χ^2 test was performed. Helium data from NaF run 557, which is a vertical run, were used. For these data the photon incident angle on the top of the light guide was $\theta_\gamma \sim 62^o$.

The estimator was built as expressed in equation 7.4 where $N_{ring}^{DAT} = \sum_{\theta_\gamma} N(\theta_\gamma)$

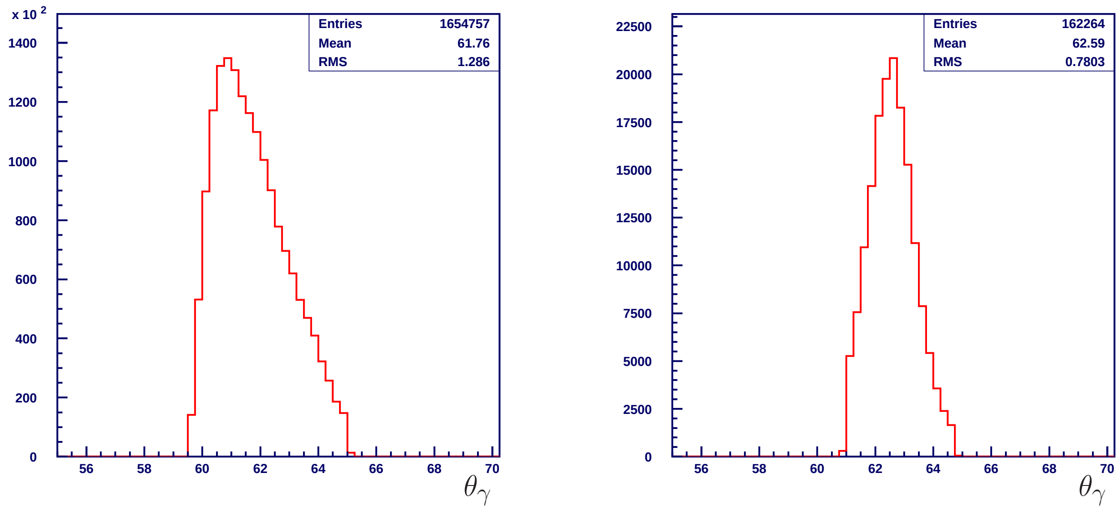

Figure 7.19: *Distribution of the photon incident angles at the top of the light guide generated by simulated, vertical, helium nuclei* (left) *and distribution of the reconstructed photon incident angle on top of the light guide for helium data collected in the 2003 beam test* (right). *The shielding was simulated with reflectivity and specularity 100%.*

and $N_{ring}^{SIM} = \sum_{\theta_\gamma} N(\theta_\gamma, ref, spec)$. $N(\theta_\gamma, ref, spec)$ will be explicitly written ahead.

$$\chi^2 = \frac{N_{ring}^{DAT} - N_{ring}^{SIM}(ref, spec)}{\sqrt{N_{ring}^{DAT}}} \tag{7.4}$$

The left-hand panel of Figure 7.19 shows the distribution of the photon incident angle on the top of the light guide $[N_0^{Basis}(\theta_\gamma)]$ extracted from simulation as mentioned above. Figure 7.20 (left) introduces the light-guide efficiency $\epsilon_0^{LG}(\theta_\gamma)$ for reflectivity one and specularity one. The distribution was fitted using a function $\frac{P_1}{1+\exp(P_2(x-P_3))}$ where $P_1 = 0.594 \pm 0.127$, $P_2 = 0.106 \pm 0.040$ and $P_3 = 46.6 \pm 7.6$. However due to a feature of the simulation the photon's angle at the light-guide entrance is only stored for those which entered the light-guide medium. According to Fresnel laws, part of the photons that cross an interface between two media with different dielectric properties are transmitted but another part are reflected. The percentage corresponding to each part depends on the incidence angle and the higher the angle of incidence the lower the transmission is. Figure 7.20 (right) shows a correction to this distribution which is the ratio between the number of photons detected inside and outside the light guide $\left(\frac{N_{inLG}(\theta_\gamma)}{N_{outLG}(\theta_\gamma)}\right)$ as function of the photon incident angle at

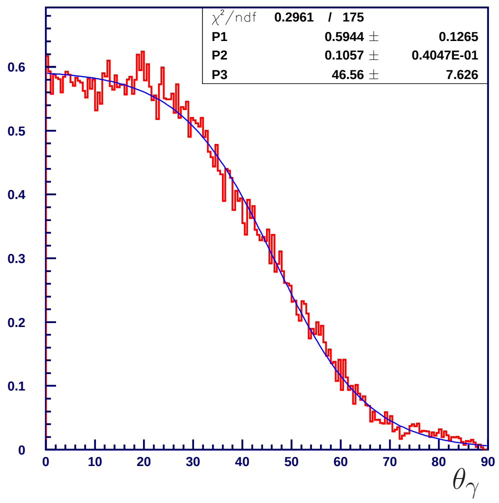

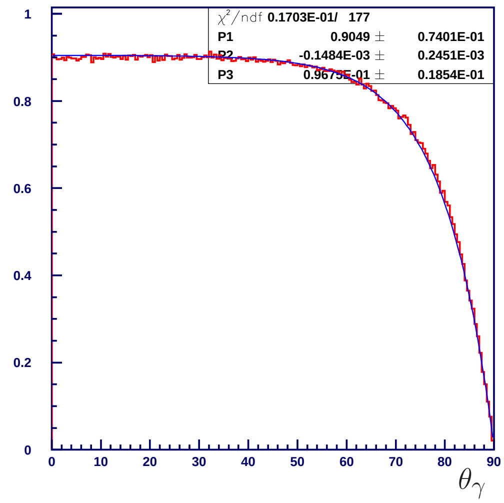

Figure 7.20: *Parametrization of the light-guide detection efficiency for a shielding reflectivity and specularity of 100%* (left). *Ratio between the number of photons detected inside and outside the light guide as function of the photon incident angle at its top* (right).

the top of the light guide. This is parametrized by the curve $P_1 - P_2 \exp(P_3 x)$ where $P_1 = 0.90 \pm 0.07$, $P_2 = -0.0001 \pm 0.0002$ and $P_3 = 0.10 \pm 0.02$. The counted number of photons at the light guide in the simulation will have to be corrected and the correction factor will appear as $corr = 1/\frac{N_{inLG}(\theta_\gamma)}{N_{outLG}(\theta_\gamma)}$.

Therefore $N(\theta_\gamma, ref, spec)$ is obtained as follows:

$$N(\theta_\gamma, ref, spec) = N_0^{Basis}(\theta_\gamma) \times \epsilon_0^{LG}(\theta_\gamma) \times r(ref, spec) \times \epsilon_{GEO} \times corr. \tag{7.5}$$

The reflectivity $r(ref, spec)$ is extracted from curves like the ones presented in Figure 7.18. The photon ring acceptance ϵ_{GEO} has to be taken into account because the observed rings are not completely contained generating a mean geometrical acceptance of 92%.

The result of the χ^2 test for the different reflectivity-specularity pairs tried is shown in Figure 7.21. The region of the expected minimum from light-guide standalone simulation is around 75% for the reflectivity. Different values of specularity lead to a minimum. This reflectivity value is slightly higher than the value of ~45% measured in laboratory.

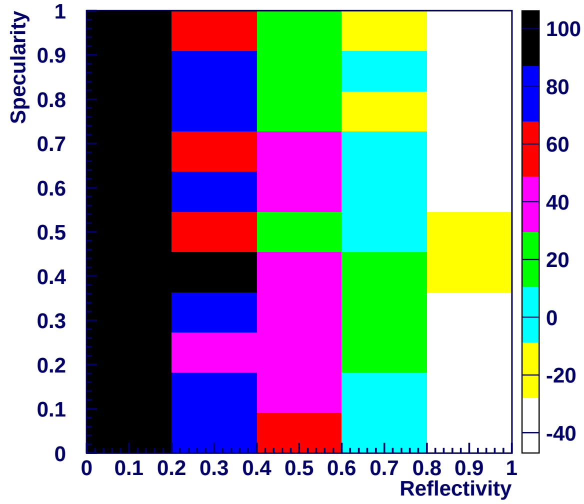

Figure 7.21: *χ^2 values as function of the specularity and reflectivity. The region of the expected minimum is around a reflectivity of 75%.*

The next step will be directly applying the simulated light-guide geometry used in the standalone simulation of the unit cell to the RICH simulation. Since the specularity seems to be degenerate this will be set close to the 66% measured in the laboratory.

The relative variation between collected and simulated data on the number of photoelectrons $\left(\frac{N_{pe}^{DAT}-N_{pe}^{SIM}}{N_{pe}^{SIM}}\right)$ and on the number of hits $\left(\frac{N_{hits}^{DAT}-N_{hits}^{SIM}}{N_{hits}^{SIM}}\right)$ for each set of shielding reflectivity and specularity values is summarized in the panels of Figure 7.22. The initial disagreement observed for simulated null reflectivity and null specularity is the first point marked upon both plots. Considering a reflectivity of 45% and a specularity of 60% the disagreement on the number of photoelectrons is reduced from 15% to 6.2% and the disagreement on the number of hits, from 16% to 8%. Increasing the reflectivity to higher values closer to the 75% that lead to the minimum values of the χ^2 test reduces the disagreement to values better than 4% in both cases. However an agreement is not yet reached. Higher reflectivity values were tried reducing the disgreement on the number of photoelectrons. The last two values have the simulation geometry improved: 1 mm of air was introduced between the housing and the light guide, which seems to be more realistic than having both pieces in direct contact. The relative variation on the number of photoelectrons for

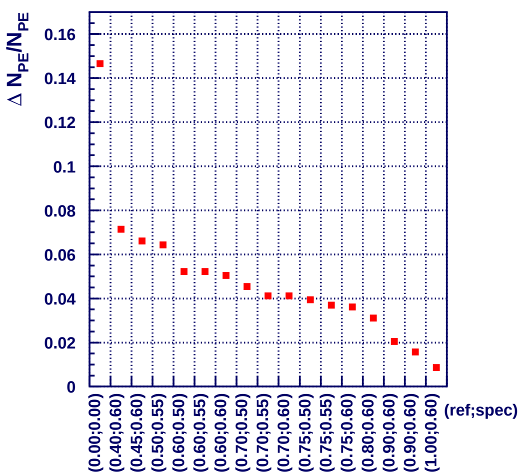

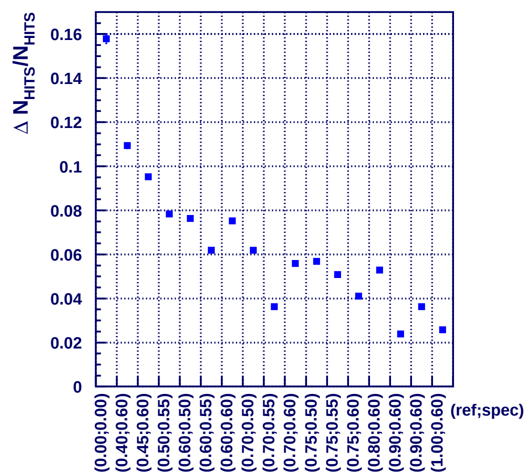

Figure 7.22: *Relative variation between collected and simulated data on the number of photoelectrons and on the number of hits for each set of shielding reflectivity and specularity values.*

the same reflectivity of 90% and specularity 60% improves from 2% to 1.6%. With a reflectivity 100% the agreement is at the level of 0.9%, however this reflectivity value is too high and not compatible with the 45% measured for the flight shielding. As mentioned before this material differs from the one used in the prototype but it was the only piece available.

7.7 Conclusions

Data acquired with the sodium fluoride radiator show a resolution on the reconstructed β for helium nuclei of $[\sigma_\beta \sim (3.28 \pm 0.02) \times 10^{-3}]$ which is compatible with the expected resolution from MC simulation.

For these runs, the Čerenkov rings were built from photons inciding the light guide at larger angles ($\sim 62^o$). The prototype data analysis for large photon incident angles on the light guide shows a data/MC discrepancy of the order of 15% on the number of photoelectrons. An incomplete description of the detection cell at the simulation level could be the reason since the reflectivity of the shielding was not considered and the housing volume was not introduced.

The light guide was extensively studied building a detailed standalone simulation of the detection cell. The shielding reflectivity and specularity values measured in the laboratory were introduced as well as the housing configuration and the corresponding reflectivity and specularity.

Data and MC agreement improves to a level better than 1% considering a shielding reflectivity of 100%. Nevertheless, this reflectivity value is not compatible with the 45% measured for the flight shielding. This material differs from the prototype one but it is the only one available to be measured.

Chapter 8

Mirror Prototype Studies

'...and if you're not good directly,' she added, 'I'll put you through into Looking-glass House. How would you like THAT?'

Alice quotation in Through the Looking Glass
by Lewis Carroll

8.1 Mirror Prototype

The RICH design includes a conical mirror to increase the detector's geometrical acceptance. A mirror prototype was included in the RICH prototype and its performance was studied during the 2003 beam test. A picture of the mirror prototype is shown in Figure 8.1 (left). This is a segment with 1/12 of the total azimuthal coverage. It has the same curvature as the final device and it is 22 cm high and 29.5 cm wide. A coating of silicon monoxide, SiO which presents a better reflectivity, was used while the final coating to be used in the flight piece is made of silica, SiO_2.

The purpose of these tests was to measure the mirror's reflectivity from data analysis and compare the measurements with the manufacturer data. The position of the mirror in the prototype was chosen in order to obtain a significant fraction of photons in the mirror. Figure 8.2 illustrates the established configuration while Figure 8.3 shows the scheme with the mirror limits represented in dashed, the mirror distance d is marked upon the figure.

Data collected with the mirror prototype are presented in Table 8.1. Different angles of the setup with respect to the beam line were used together with different

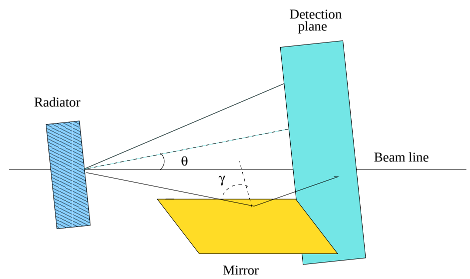

Figure 8.2: *Rotated setup with mirror prototype.*

Figure 8.1: *Mirror prototype.*

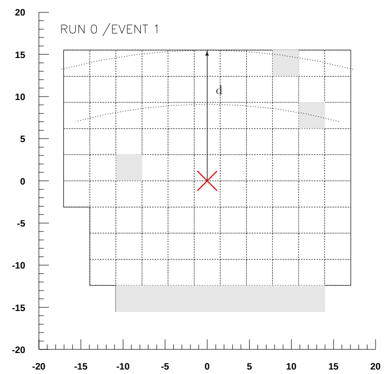

Figure 8.3: *Mirror prototype position.*

radiators and different mirror positions.

Mirror analysis					
Run Nb	A/Z	radiator	H (cm)	θ (°)	d (cm)
575	2	CIN105	42.3	15	15.5
579	2	MEC105	43.8	20	10.0
580	2	MEC105	38.65	20	10.0
581	2	MEC105	38.65	15	10.0
583	2	MEC105	38.65	10	10.1
584	2	MEC105	38.65	0	10.1
585	2	MEC103	42.3	0	10.1
586	2	MEC103	42.3	10	10.1
587	2	MEC105	42.3	20	10.2

Table 8.1: *Mirror data.*

Different particle angles together with slighly different mirror distances originate different acceptances for the reflected photon branches as can be observed in Figure 8.4. Data presented were collected using radiator MEC105. A maximum of 36% for mirror photon ring acceptance is reached for a setup rotated 20° with respect to the beam line. Figure 8.5 shows different Čerenkov rings for each of the inclinations mentioned.

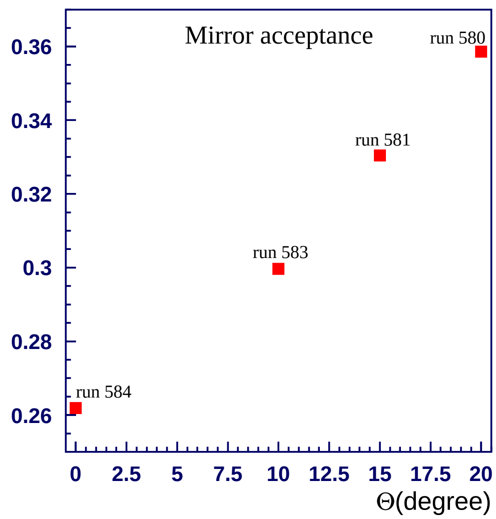

Figure 8.4: *Mirror coverage dependence with particle inclination for runs with MEC105.*

8.2 Velocity Measurement with Reflected Hits

The coordinates of the particle impact point (X, Y) and the velocity reconstruction are obtained through a three-parameter fit that returns the Čerenkov angle (θ_c). This track determination is done event by event since the fitcircle method is no longer applied for inclined events. The β reconstructed for helium events in CIN105 in a setup that includes the mirror are shown in Figure 8.6 (left). The present configuration generates events with 21% of the hits arising from reflected photons. A gaussian fit is applied to the distribution and a resolution $\sigma_\beta(Z=2) = (0.480 \pm 0.002) \times 10^{-3}$ is extracted. The same procedure is applied to the other charges, selected using scintillator information. The β resolution obtained is presented in Figure (8.6) (right). The function (4.37) is adjusted to the data points and the

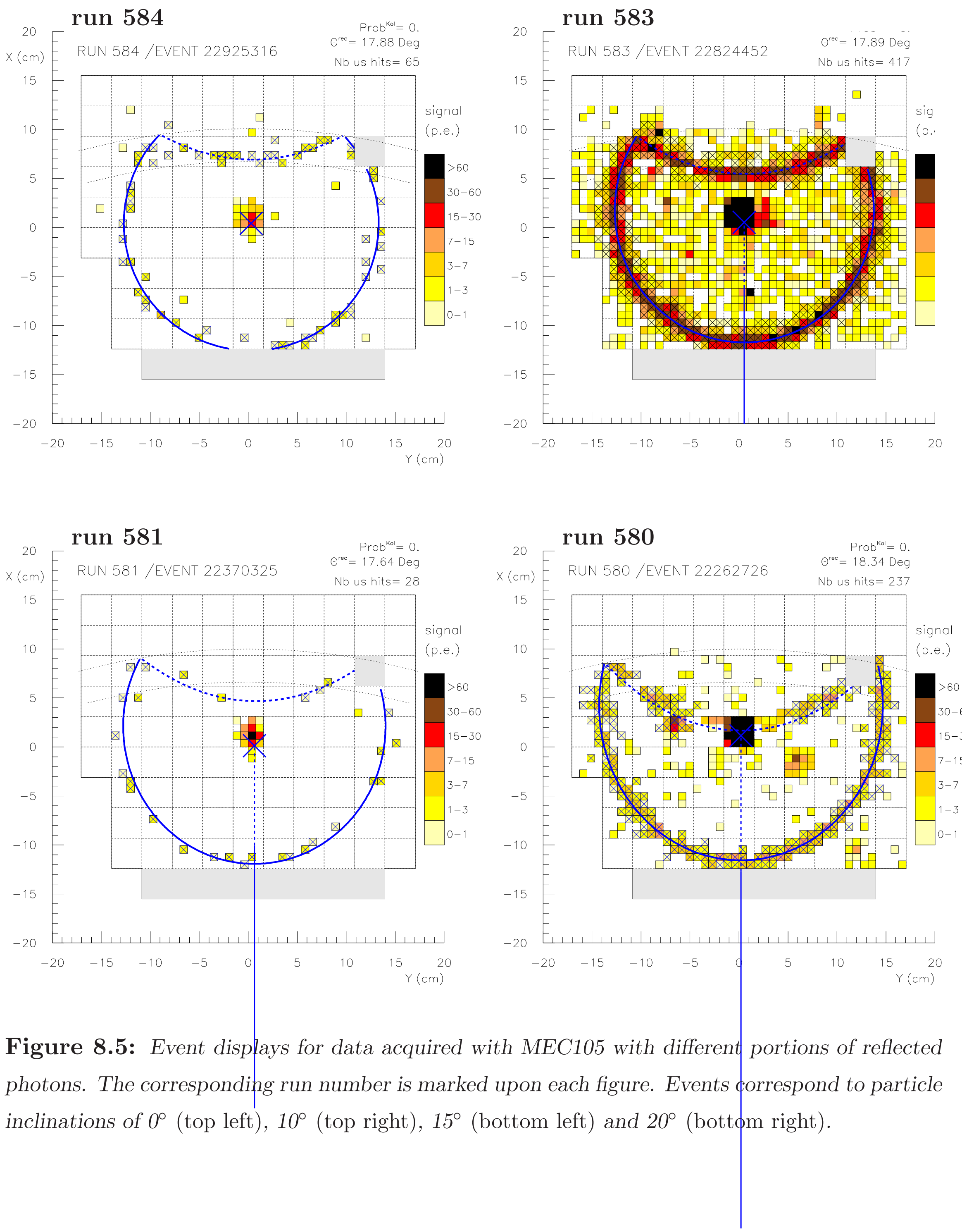

Figure 8.5: *Event displays for data acquired with MEC105 with different portions of reflected photons. The corresponding run number is marked upon each figure. Events correspond to particle inclinations of 0°* (top left)*, 10°* (top right)*, 15°* (bottom left) *and 20°* (bottom right).

resolution parameters $A = 0.956 \pm 0.004$ and $B = 0.079 \pm 0.002$ are obtained.

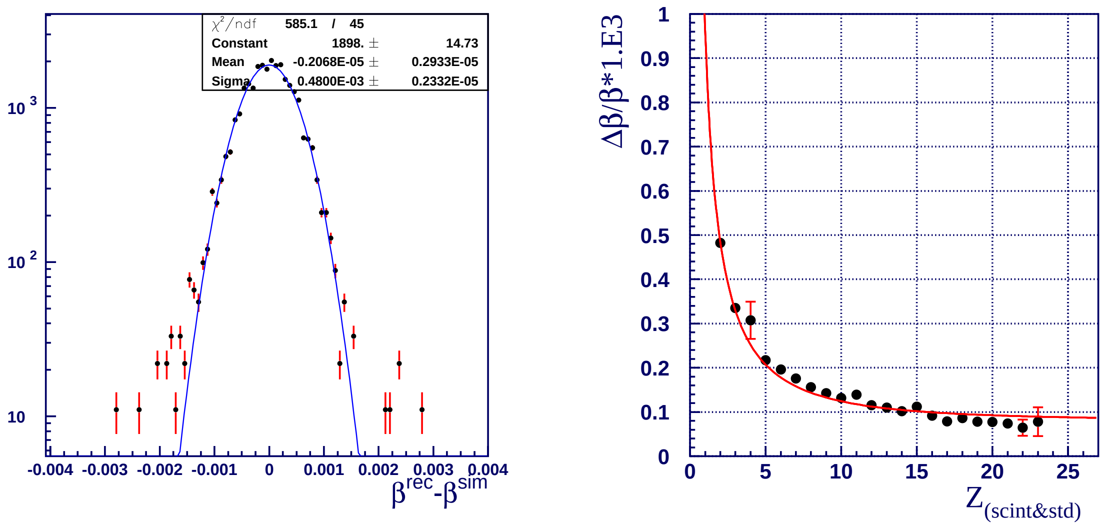

Figure 8.6: *Reconstructed β for helium events impinging in CIN105 radiator, (run 575)* (left). *Evolution of β resolution with charge obtained for the same radiator* (right).

To confirm that the presence of the mirror does not deteriorate the velocity, resolution the single-hit resolution for reconstructions using either only direct hits or only reflected hits was calculated. In order to confirm how it varies with the mirror acceptance this estimator was calculated for runs acquired with MEC105 with different particle inclinations. The same data deal with reflected branches which have the acceptances shown in Figure 8.4. Figure 8.7 shows the evolution of the single-hit resolution for Čerenkov ring reconstructions based only on hits coming from reflection or only on direct hits. The former reconstructions do not show deterioration, and in fact the resolution is even better, of the order of 3.4×10^{-3} while the latter reconstructions give a resolution that is slighly higher than 4.5×10^{-3} for the patterns with the maximum number of direct photons. This is expected due to the fact that reflected hits are associated to photons with longer photon arms, d (see section 4.2) which reduce the uncertainty in θ_c.

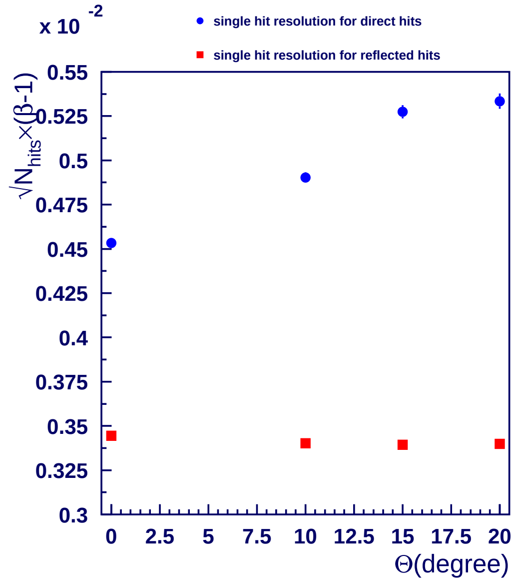

Figure 8.7: *Evolution of the single-hit resolution for a reconstruction using either only direct hits or only reflected hits, as function of particle inclination for MEC105.*

8.3 Charge Measurement

Figure 8.8 (left) shows the reconstructed charge spectrum using all the hits available in the Čerenkov patterns generated by 15° particles impinging in CIN105, 2.5 cm thick. The charge peaks are well separated along all the spectrum. Figure 8.8 (right) shows the helium peak reconstructed using all the hits of the event. The achieved resolution is of (0.1728 ± 0.0008) charge units.

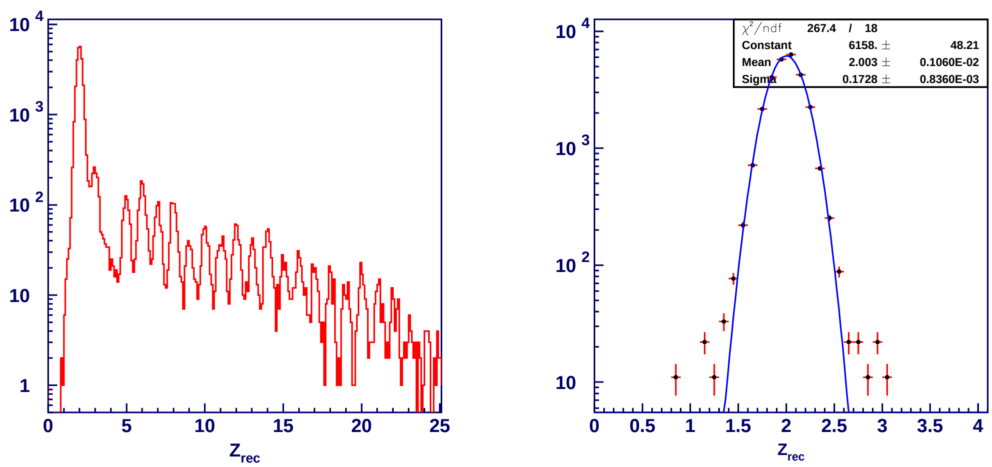

Figure 8.8: *Reconstructed charge* (left) *and reconstructed charge for helium events* (right) *generated by particles impinging in CIN105 radiator (run 575).*

8.4 Reflectivity Evaluation

Mirror reflectivity can be evaluated solving the system of equations 8.1 since the constant of proportionality is the same for both cases. To calculate the final quantity it is necessary to count the signal in each branch and evaluate the most significant efficiency factors involved in its detection which are the photon ring acceptance and the light guide efficiency since the photon's incident angle at the top of the light guide has different distributions for reflected and direct photons. There is no significant difference in the radiator efficiency between the two types of photons.

$$\begin{aligned} N_{pe}^{dir} &\propto N_{\gamma}^{rad} \cdot \varepsilon_{geo}^{dir} \cdot \varepsilon_{lg}^{dir} \\ N_{pe}^{ref} &\propto N_{\gamma}^{rad} \cdot \varepsilon_{geo}^{ref} \cdot \varepsilon_{lg}^{ref} \cdot \varepsilon_{mir} \end{aligned} \tag{8.1}$$

Therefore from equations 8.1 the mirror reflectivity (ε_{mir}) can be extracted to be:

$$\varepsilon_{mir} = \frac{N_{pe}^{ref}}{N_{pe}^{dir}} \frac{\varepsilon_{geo}^{dir}}{\varepsilon_{geo}^{ref}} \frac{\varepsilon_{lg}^{dir}}{\varepsilon_{lg}^{ref}} \tag{8.2}$$

The reflectivity will be evaluated based on data from run 575 where the radiator CIN105, 2.5 cm thick was used. Helium events were selected and the signal distributions for direct and reflected branches are shown in Figure 8.9.

The signal distribution for the direct branch was fitted with the function 6.9 introduced in section 6.4. Depending on the statistics the function $G_1(n)$ is replaced by a Poisson $P(n)$. Since the number of photoelectrons in the reflected branch is small (< 10 on average) a Poisson function is used. The final fitting function is given by the sum over all channels of the product function described and written as:

$$\begin{aligned} f(x; \mu, \sigma_{p.e.}, N_0) &= \sum_n P(n) G(x,n) = \\ &= N_0 \sum_{n=1}^{N_{p.e.}} \frac{\mu^n e^{-\mu}}{n!} \frac{1}{\sqrt{2\pi}} \frac{1}{\sqrt{n}\,\sigma_{p.e.}} \exp\left[-\frac{1}{2} \left(\frac{x-n}{\sqrt{n}\,\sigma_{p.e.}} \right)^2 \right] \end{aligned} \tag{8.3}$$

where the parameters to be determined are the gaussian normalization factor, N_0, the single photoelectron width, $\sigma_{p.e.}$, and the average number of photoelectrons, μ.

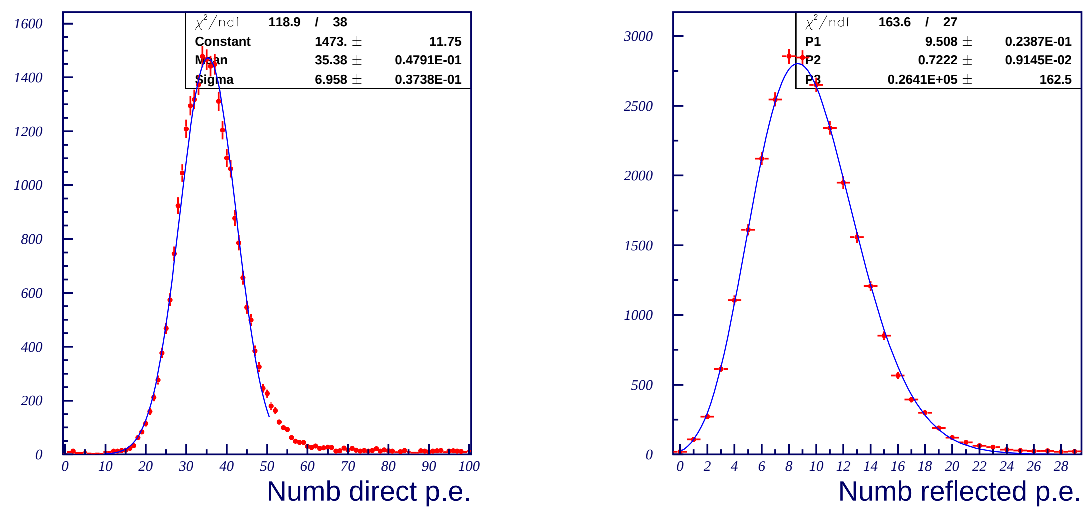

Figure 8.9: *Distributions of the number of photoelectrons measured in the direct* (left) *and reflected branches* (right) *for photon patterns generated by particles impinging in CIN105 radiator, 2.5 cm thick together with an expansion height of 42.3 cm (run 575).*

The Poisson function describes the statistical fluctuation related with the measurement while the gaussian describes the uncertainty of the instrumentation. The fit values obtained are presented in the statistical boxes of each plot. The average signal of the reflected hits is 9.51 ± 0.02 while the average signal of the direct hits is 35.38 ± 0.05. These values together with the efficiency factors are presented in Table 8.11.

The calculated reflectivity is $\varepsilon_{mir} \sim (75.1 \pm 0.2)\%$.

The estimated error only takes into account the statistical error. The most important sources of systematic uncertainties are the confusion of hits near the separation between the reflected and direct part (they can either be associated to one or another), the uncertainty in the mirror position which determines the fraction of reflected and direct ring and the fact that the photomultipliers limits most of the times are not coincident with the limits of the branch.

The manufacturer's reflectivity measurements according to photon wavelength are shown in Figure 8.12 (left). The values were obtained for different photon incident angles (15°, 30°, 45° and 60°). The run 575 from which the reflectivity was evaluated in the present work deals with photon incidences of ∼64°. The mean

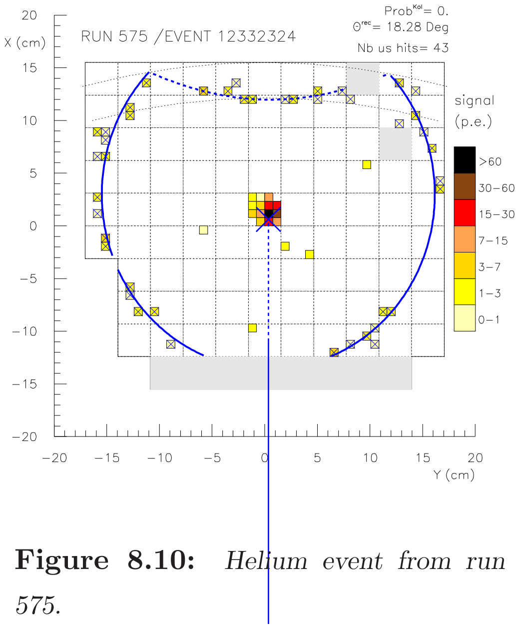

Figure 8.10: *Helium event from run 575.*

Run 575	Direct	Reflected
N_{pe}	35.38 ± 0.05	9.51 ± 0.02
ε_{geo}	$0.77090 \pm 3 \times 10^{-5}$	$0.70670 \pm 2 \times 10^{-5}$
ε_{lg}	$0.6254 \pm 7 \times 10^{-5}$	$0.20500 \pm 2 \times 10^{-4}$

Figure 8.11: *Factors involved in mirror reflectivity determination for run 575.*

wavelenght for the detected photons is $< \lambda >= 376.8\,\text{nm}$. For these incidences the evaluated reflectivity value is in agreement with the manufacturer measurements. In fact, the closest measured incidence is $\theta_\gamma = 60°$ and for $< \lambda >= 376.8\,\text{nm}$ the measured reflectivity is ∼75.8%. The reflectivity values for the mirror prototype are lower than the manufacturer measurements for the final mirror shown in Figure 3.19 (right) due to the different coating of both objects. The mirror prototype has a coating of SiO while the final mirror has a coating of SiO_2.

8.5 Conclusions

The main goals of the mirror data analysis were fulfilled. Different fractions of reflected photons were obtained displacing the mirror prototype from the lateral side of the detection matrix together with different setup rotations.

Velocity reconstruction was performed wih a three-parameter fit that gives the Čerenkov angle and the particle impact coordinates. The evolution of the reconstructed velocity resolution with charge was studied for a particular run with radiator CIN105 and its behaviour is in agreement with expectations.

Data do not show a visible degradation on reconstructions with reflected hits. In fact, the resolution is even better, being of the order of $\Delta\beta/\beta = 3.4 \times 10^{-3}$ while

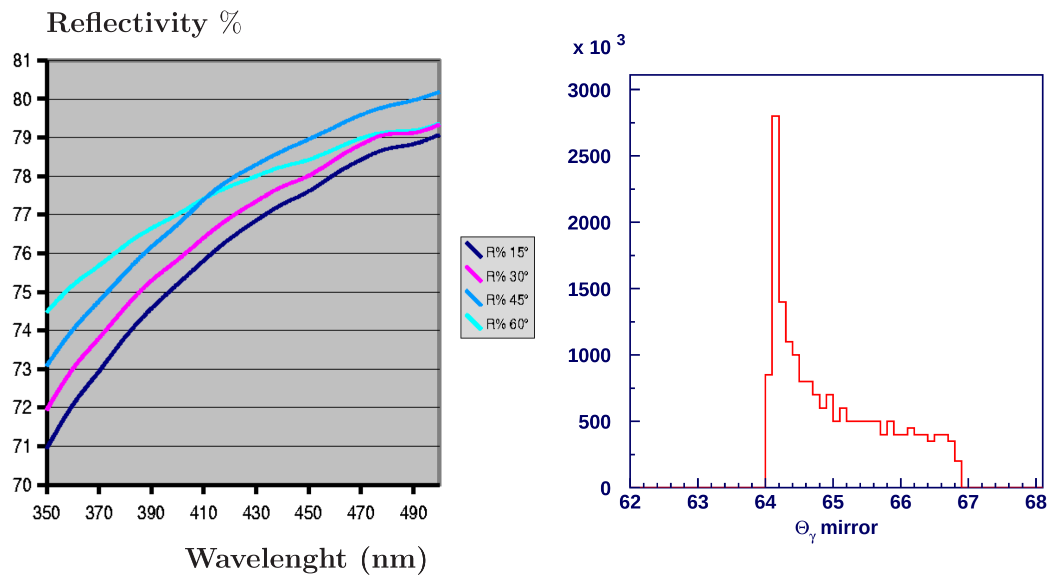

Figure 8.12: *Manufacturer measurements for prototype mirror reflectivity versus photon wavelength for different photon incident angles* (left). *Distribution of photon angles with respect to normal to the mirror surface at the incident point for run 575* (right).

reconstruction using only direct hits is slighly higher, $\Delta\beta/\beta = 4.5 \times 10^{-3}$. From the point of view of charge reconstruction with the same radiator, the reconstructed spectrum using all hits shows well separated charges with no significant degradation on the charge resolution.

Mirror reflectivity evaluation was done and the result obtained was cross-checked with the manufacturers' measurement. The result obtained $\varepsilon_{mir} \sim (75.1 \pm 0.2)\%$ is in good agreement with the measured values.

Chapter 9

RICH Assembly Status and Tests

The only source of knowledge is experience.

Albert Einstein

9.1 Introduction

The RICH is a complex detector and its long assembly process is finishing. This thesis could not be concluded without stating the detector's present situation. In the previous chapters beam test data were analyzed, which allowed to evaluate the prototype capabilities for velocity and charge measurements and to select the best radiator for the final RICH detector. The present chapter will briefly describe the RICH assembly status as well as the prior to assembly characterization tests of each element of the detector, in particular the functional tests of the detection cells.

9.2 RICH and AMS Assembly Status Overview

The RICH assembly started in September 2003 at CIEMAT in Spain and is foreseen to be finished before the end of 2007. Table 9.1 resumes the different tasks to fulfill or already fulfilled in the RICH assembly.

RICH Assembly tasks	**Date**
Unit cells assembly	$\surd$
LG assembly	$\surd$
LG wiring	$\surd$
Dallas sensor assembly	$\surd$
Shielding assembly	$\surd$
Grids assembly	$\surd$
Detector plane assembly in the main structure	$\surd$
Radiator plane assembly	$\surd$
Integration at CERN	January 2008

Table 9.1: *RICH and AMS assembly status.*

9.2.1 Unit cell assembly

The 680 unit detection cells introduced in subsection 3.3.3 were assembled before the end of 2005. The assembly procedure will be herein briefly described. First the front-end electronics is connected to each photomultiplier tube. Then the photomultiplier is surrounded by a polycarbonate housing which is fixed by Dow-Corning 93-500, a space-qualified optical silicone with insulator properties. The silicon is injected between the housing and the photomultiplier tube. The housing is the interface between the PMT and the walls of the shielding grid.

Meanwhile the 16 light guide pipes are glued. For a more complete description of this procedure see thesis [193]. A thin film of Dow-Corning is placed in the PMT window to guarantee the optical contact between the photomultiplier and the light guide. In addition, for a mechanical security reason, the light guide is mechanically attached through nylon wires to the photomultiplier housing.

Afterwards the shielding is installed and the Dallas thermal sensors (DTS)[1] are glued to it as close as possible to the photomultiplier. The purpose is to measure the temperature variations suffered by the detection plane during the mission. The idea is to correct the photomultipliers' gain variation due to the temperature fluctuation.

[1]All the AMS-02 subdetectors are equipped with thermal sensors DS18B20 produced by Dallas Semiconductor. They have a measuring precision of 0.5°C in the range [−10°C,+85°C].

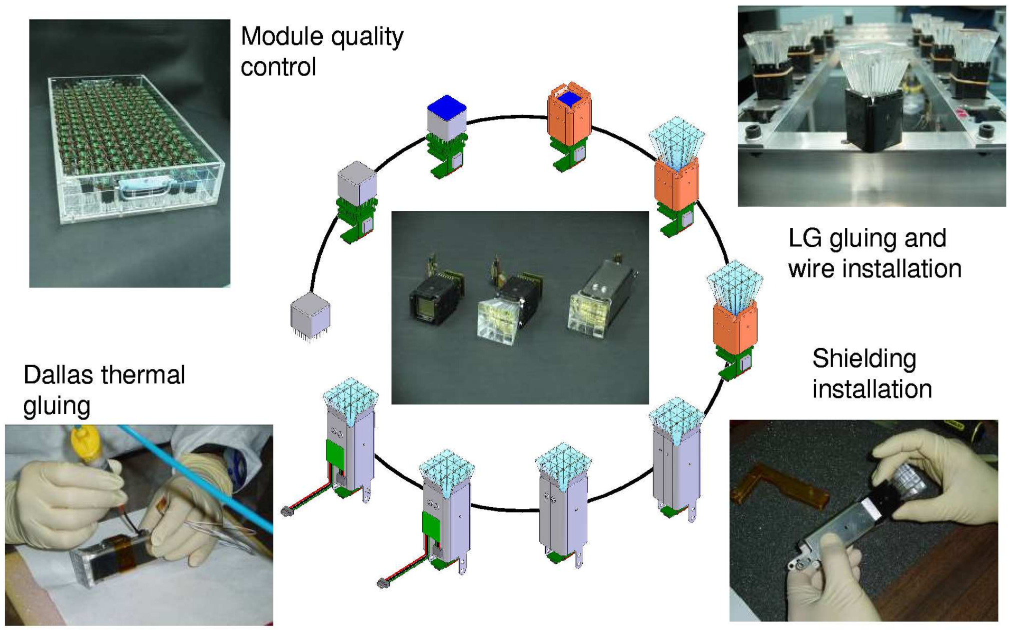

Figure 9.1: *Sequence of unit cell assembly.*

Figure 9.1 shows the complete sequence of the unit cell assembly.

The unit cells were subject to vibration tests and to thermal cycles. The purpose of the first tests is to ensure that the mechanics and the functionality of the unit cell are not affected during the launch. The vibration test was done at INTA[2], Spain using an array with 8 units subject to 6.8 g. No mechanical damages were observed and the photomultiplier gain was not affected. The thermal cycle tests were done at CIEMAT and consisted of 8 thermal cycles covering the temperature range from $-30\,°\mathrm{C}$ to $+55\,°\mathrm{C}$ during 6h20m. Each unit was recalibrated after those tests and the gains and pedestals remained essentially the same, with only 3 photomultipliers and 2 ASIC presenting a signal decrease.

9.2.2 Detection plane assembly

The detection cells are assembled in an octagonal, supporting structure made of aluminium with a central square for the insertion of the electromagnetic calorimeter. The detection plane is divided in eight different grids, four rectangular and four

[2]Instituto de Técnica Aeroespacial

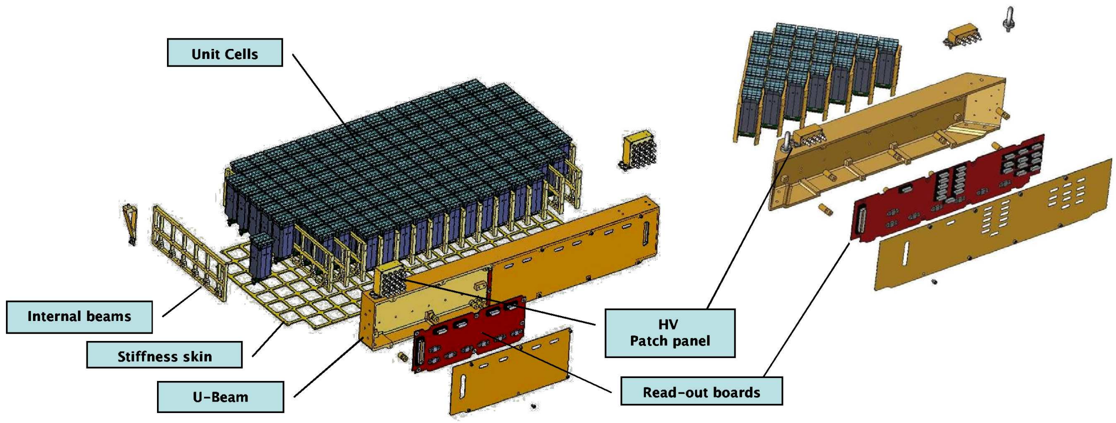

Figure 9.2: *Scheme of rectangular and triangular grids.*

triangular. The assemblage and cabling of each zone is done separately. The main elements of each grid are shown in Figure 9.2. Each set is assembled by successively placing internal beams and rows of unit cells [193] as depicted in Figure 9.3.

The internal cabling is done welding the HV cables to the corresponding PMTs and connecting the front-end electronics to the flexible kapton cable[3]. A stiffness skin is placed at the basis of the grid to reinforce the structure. The HV patch panel and the read-out boards are located in the external supporting structure.

All the grids have already been assembled and have been subject to a mechanical fit test to guarantee the insertion in the main structure, and functional tests at CIEMAT. Vibration and vacuum tests at INTA were done to grid G. After those new functional tests were performed.

[3]This cable transports the signal from the photomultipliers to a time memory integrated in the CDP (Common Digital Part), which is the electronic level above the front-end electronics.

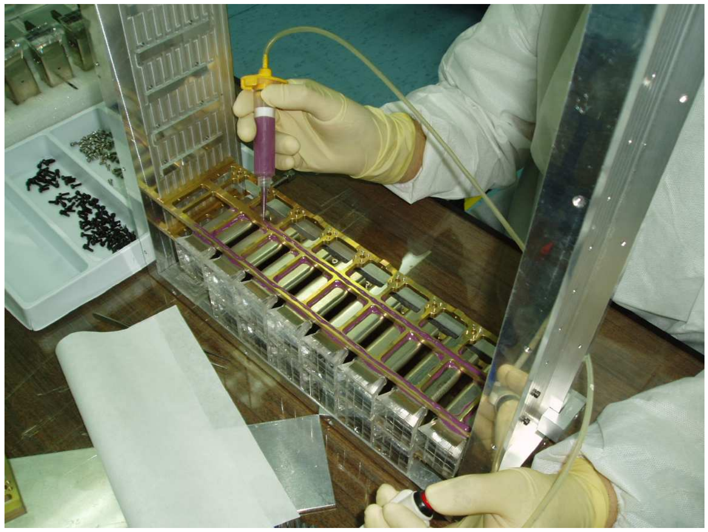

Figure 9.3: *Grid mechanical assembly.*

9.2.3 Radiator and mirror assembly

A first mechanical assembly trial of the RICH radiator has started at CIEMAT. The aerogel tiles are cut at the corners and black PORON foam is placed around each tile. Meanwhile the NaF cover is placed and bolted by 13 spacers and PORON foam is placed behind and around each tile. In addition, aerogel and NaF require a controlled dry environment. Due to this fact the radiator will be in a sealed container filled with neutral gas (nitrogen). The container should have venting capability to compensate atmospheric pressure variations during launch and landing. With this purpose venting valves are included and 2 TEDLAR/TEFLON bags ($0.6\,\ell$ each) are used.

The mirror is ready and prepared to be assembled. Before that a complete reflectivity mapping will be made.

9.3 The RICH System Characterization

9.3.1 Physical Motivations

To cover a wide range of charge in the RICH detector, as can be observed in section 6.5, a maximum systematic uncertainty of the order of 1-2% can be tolerated. The systematic origin in the beam test is attributed to the non-uniformities of the radiator since in each run the same particle inclination and velocity is obtained, leading to the same sample of PMTs being touched by the Čerenkov photons. This level of fully correlated systematic uncertainty seems to be unavoidable from beam test studies so the systematics value of 1-2% will be considered as the upper acceptable limit for the remaining contributions to the final uncertainty.

As explained in section 4.5, in the flight scenario, this systematic uncertainty in the charge measurement can arise from non-uniformities at the radiator level coming from spatial variations in the refractive index, tile thickness or clarity; from non-uniformities in the mirror reflectivity, in photon detection efficiency, which can take the form of a global photomultiplier gain variation due to temperature effects, a magnetic field perturbation or an intrinsic variation that arises from the different gains and quantum efficiencies; or from non-uniformities in the light guide or in the optical coupling between photomultipliers and light guides. Consequently, in order to keep the systematic uncertainty below that value a number of factors need to be measured and kept under control. Each of them will be analyzed in the next sections.

9.3.2 Radiator monitoring

The charge dependence with the refractive index of the aerogel tiles was deduced in subsection 4.5.1. It is expected that to contain the systematic uncertainty under 1%, the refractive index should not have a spread greater than 10^{-4}. The expected velocity resolution also imposes this value as the maximum acceptable variation on the refractive index. The charge dependence with the tile thickness and clarity were deduced in subsections 4.5.2 and 4.5.3, respectively. The variation allowed in the tile thickness is $\Delta H_{rad} \sim 0.4\,\mathrm{mm}$ while the maximum acceptable relative variation on the clarity is of the order of 3%. The constraints on the refractive index, tile thickness and clarity imply that these quantities have to be measured for each individual tile.

Aerogel tile characterization

Full maps of the aerogel tile thicknesses have been acquired at *Laboratoire de*

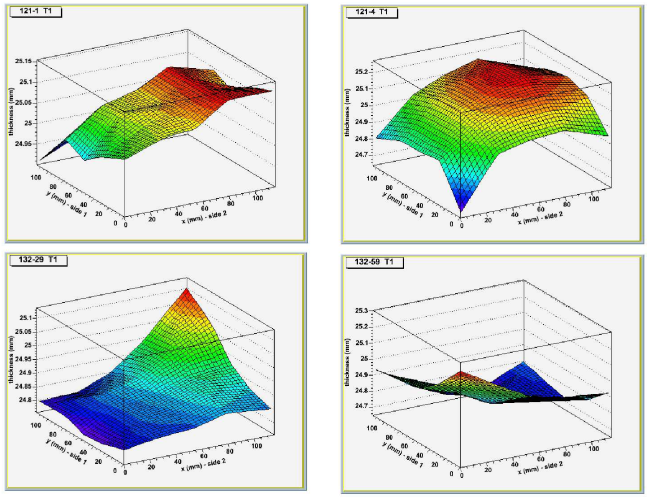

Figure 9.4: *Aerogel tile thickness maps* [194].

Physique Subatomique et de Cosmologie in Grenoble. LIP and *Universidad Nacional Autónoma de México* have also collaborated in the task. Figure 9.4 shows some thickness maps for four different aerogel tiles. These measurements will be extended to all tiles and the thickness for each tile coordinate will be introduced in the RICH simulation. The results are being organized in a database. The optical characterization of the aerogel is another important issue to control. It includes mapping the refractive index and the clarity within each tile. The refractive index determination was done using the method of gradient measurement thoroughly explained in [195]. Figure 9.5 shows an example of a refractive index map for one aerogel tile.

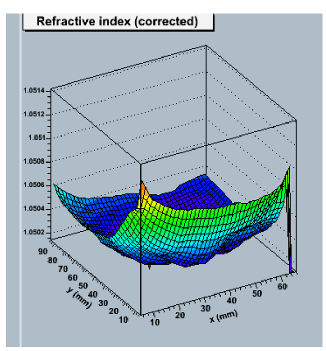

Figure 9.5: *Refractive index map of one aerogel tile.* [194]

The measurement performed in a set of 44 tiles provide the following statements:

- the refractive index variation between aerogel tiles is of the order of 1.2‰.
- the refractive index variation within a tile is of the order of 0.3‰.

Therefore, the need of characterizing the refractive index of the tile is clear.

The refractive index variation: physical implications

According to what was said in subsection 4.5.1 relative variations on the aerogel refractive index greater than 10^{-4} can be significant for isotopic mass separation with RICH in particular for beryllium isotope separation. Two simulations were done, one with the aerogel refractive index fixed at 1.050 and another with a random variation around the nominal value of $\Delta n \sim 1.6 \times 10^{-3}$, which is a conservative assumption. For the last one in order to save time and since the interest was to study the isotope mass separation in the upper limits of kinetic energy, only events with a momentum per nucleon greater than 5 GeV/c were simulated.

Simulation conditions:

- Simulated Setup:
  - Radiator: Novosibirsk aerogel
    * Tile radiator pitch = 11.4 cm
    * Refractive index = 1.050 fixed and with a random variation of $\Delta n \sim 1.6 \times 10^{-3}$
    * Clarity = $0.0052\,\mu\mathrm{m}^4\mathrm{cm}^{-1}$
  - Expansion height: 46.3 cm
  - Polyester foil: 1 mm thick
- Simulated events: $8.5{\times}10^5$ beryllium (^{9}Be and ^{10}Be).

The analysis of the simulated beryllium samples was done by R. Pereira [196] and both cases were compared to evaluate the random spread effect on the detector capabilities. The isotopic ratios were calculated for each kinetic energy bin since the mass resolution σ_m depends on β. This quantity as well as the separation power, already defined in Section 3.2, were also calculated and compared with the corresponding quantities evaluated from the simulation with no spread in the refractive index.

Figure 9.6 (left) shows the evolution of the reconstructed velocity resolution with the number of hits used both for the case using the nominal refractive index, represented by full dots, and considering the random spread in the refractive index, represented by squares.

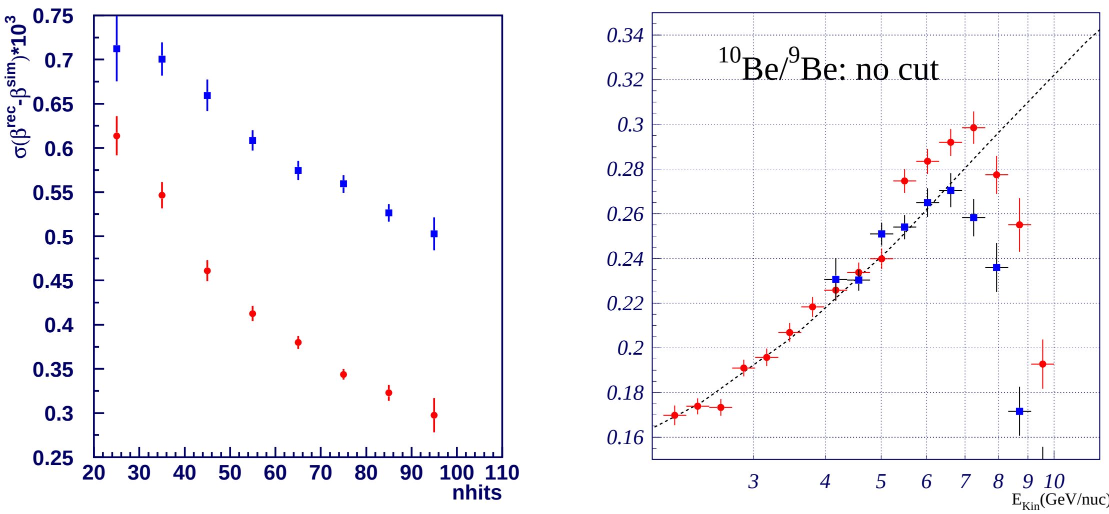

Figure 9.6: *Evolution of the reconstructed velocity resolution with the number of hits* (left). *Reconstructed isotopic ratios of beryllium versus the kinetic energy per nucleon. The plotted function is according to the Strong and Moskalenko model* [54] (right). *Both the nominal refractive index case (squares) and case of the random spread in the refractive index (full dots) are represented.*

Figure 9.6 (right) represents the isotopic ratios as function of the kinetic energy per nucleon for beryllium isotopes in the case of the simulated random variation in the refractive index. The plotted function describes the Strong and Moskalenko model [54], according to which all the beryllium isotopic abundances were simulated. Left-hand plot presents the beryllium isotopic ratios without any cut on the number of hits used in velocity reconstruction. Mass reconstruction fails when the ^{10}Be peak is 'hidden' under the large peak. The two peaks are mixed and the result of the mass fit does not provide us the correct ratio between the two isotopes. This happens when the separation between the two mass peaks falls to around $2\sigma_m$. Using all events mass reconstruction fails at ∼7 GeV/nucleon when previously this happened at 8 GeV/nucleon

Mass resolution gives a more reliable estimate for reconstruction capabilities because it is almost insensitive to the details of individual fits. Figure 9.7 (left) shows the mass resolution as function of the kinetic energy per nucleon. Using all the events the resolution curve in the case of a simulated random variation of n appears shifted with respect to the curve with a simulated fixed n by approximately one energy bin, whose width corresponds to a ∼10% of variation of the kinetic energy.

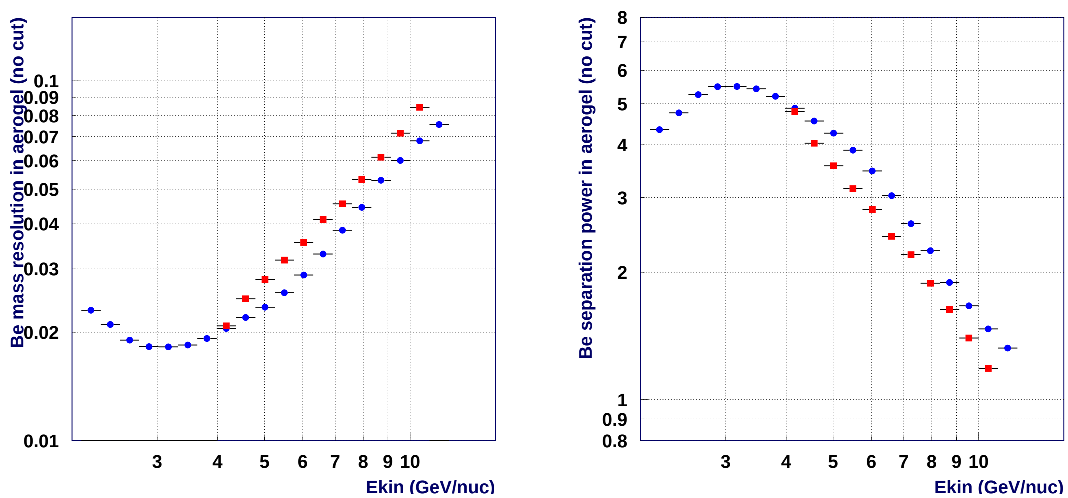

Figure 9.7: *Beryllium mass resolution* (left) *and separation power* (right) *as function of the kinetic energy per nucleon in the case of a simulated random variation of the refractive index (squares) compared with the case of a simulated fixed n (full dots).*

The separation power $\frac{\Delta m}{\sigma_m}$ is the number of mass sigma, σ_m, between the two mass peaks. Figure 9.7 (right) shows the separation power for the case of a simulated random variation of the refractive index (squares) compared with the case of a simulated fixed n (full dots). Assuming that the reconstruction fails when separation power reaches ∼2.5. The kinetic energy limit is now ∼6.6 GeV/nucleon while previously, with no variation in n, was ∼7.6 GeV/nucleon.

This simulation study confirms that a random spread in the aerogel refractive index or the order of $\Delta n \equiv 1.6\times10^{-3}$) does have an effect on the mass reconstruction. The kinetic energy limit for mass separation might decrease by $10-20\%$. In the case of ^{10}Be/^{9}Be, mass separation is feasible at least up to ∼7 GeV/nucleon.

9.3.3 Reflector monitoring

A precise map of the mirror reflectivity is needed since the reflected branch of the Čerenkov pattern is used in the particle charge calculation. The uncertainty in the reconstructed charge due to the uncertainty in the signal of the reflected hits can be derived from the following expression:

$$Z = N_0 \sqrt{N_{pe}} \tag{9.1}$$

where N_0 is the number of photoelectrons associated to the Čerenkov ring generated by a $Z = 1$ particle and N_{pe} is the total signal and is given by the sum of the number of photoelectrons associated to the direct and reflected branches. On the other hand the signal of the reflected hits is affected by the mirror reflectivity ε_{mir} which allows to write the following expression:

$$N_{pe} = N_{pe}^{dir} + N_{pe}^{ref} = \epsilon^{dir} N_{pe} + \varepsilon_{mir} \epsilon^{ref} N_{pe} \tag{9.2}$$

where ϵ^{dir} and ϵ^{ref} are the photon ring acceptances for the direct and reflected branches, respectively.

In the present situation it is assumed that the charge uncertainty is due to reflectivity variations, which affect the whole reflected branch in a correlated way. Performing the derivative of expression 9.1 leads to:

$$\Delta Z = \frac{1}{2} Z \frac{N_{pe}^{ref}}{N_{pe}} \frac{\Delta_{\varepsilon_{mir}}}{\varepsilon_{mir}} \tag{9.3}$$

Assuming the most conservative case which is of 100% reflected events ($N_{pe}^{ref} = N_{pe}$) and expecting a systematics on Z lower than 1% allows to conclude that $\frac{\Delta \varepsilon_{mir}}{\varepsilon_{mir}}$ should be lower than 1%.

Due to the spinning coating procedure in the mirror production, azimuthal (ϕ) non-uniformities in the reflectivity are expected to be highly suppressed, the dominant spatial contribution arising from vertical variations. However, a reflectivity map as function of $z - \phi$ coordinates will be obtained using the spectrophotometer

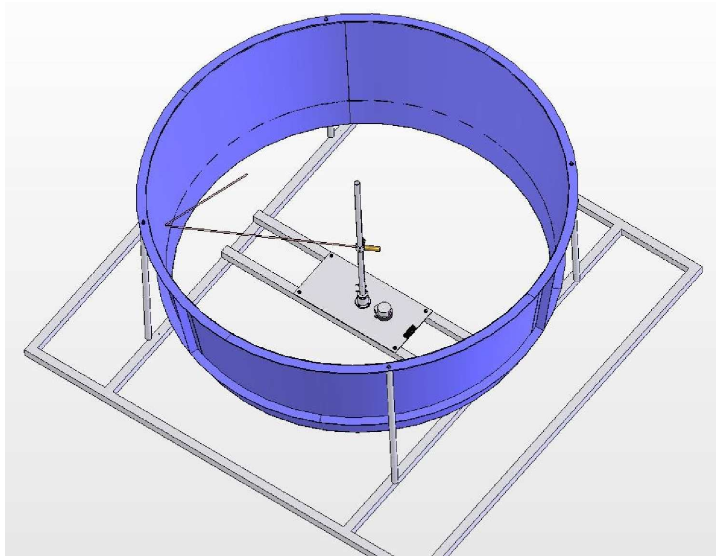

Figure 9.8: *Reflectivity measurement setup* [197].

Minolta CM-2600d [see Figure 7.12 (right)]. A semiautomatic setup has been designed to provide the position measurement with an accuracy $\sim$1 mm. The scheme of the setup is depicted in Figure 9.8. A rotating mast, placed at the center of the mirror, holds a laser point which flashes the target position on the reflector. Once the measurement is done the mast rotates 10° to the next ϕ position. When the ϕ scan is complete the pointer is manually fixed to a different height along the mast (step of 2 cm) for a new scan, now with a different z. The measurements will be done in a clean room at CIEMAT. These results will also be included in the database.

9.3.4 Detection matrix monitoring

One significant non-uniformity at the detection level is the intrinsic variation that arises from the different gains and quantum efficiencies of the photomultipliers. The right-hand panel of Figure 9.9 shows the distribution of the photocathode luminous sensitivity $S_k(A/lm) = \frac{I_k(A)}{\phi_e(lm)}$ extracted from the Hamamatsu datasheet for the photomultipliers of the rectangular grid G, depicted in Figure 9.11. The photocathode sensitivity S_k, which is directly related to the quantum efficiency, is the ratio of the cathode current I_k (subtracted the dark current) to the incident flux ϕ expressed in photometric units [lumen (lm)]. The measured values present a relative spread

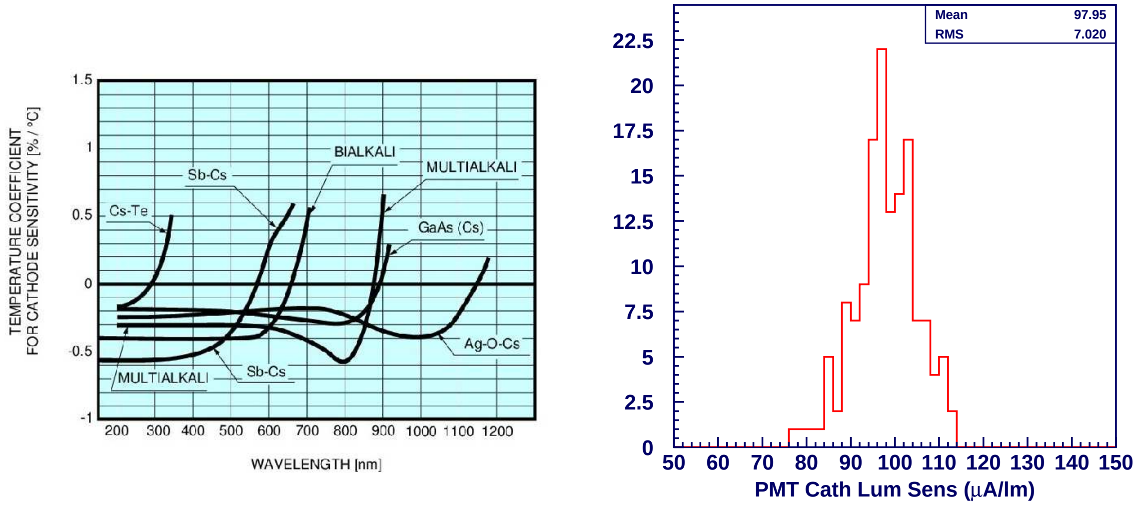

Figure 9.9: *Typical temperature coefficients for cathode sensitivity* [%/°C] *versus photon wavelength for different photocathode materials* [198] (left). *Cathode luminous sensitivity from the Hamamatsu datasheet for the 143 photomultipliers of grid G* (right).

$\sim$7% with the average $< S_k > \sim 97.95\,\mathrm{A/lum}$.

Assuming that in each photon ring generated by a particle with $\beta \simeq 1$ an average of $\sim$20 photomultipliers are touched the systematic effect due to the spread on the quantum efficiencies is of the order of $7\%/\sqrt{20} \sim 1.5\%$[4].

Another non-uniformity in the detection is a global photomultiplier gain variation due to temperature effects. The left-hand panel of Figure 9.9 introduces reference data on the temperature coefficient for the bialkali photocathode. This coefficient is $-0.4\%/°\mathrm{C}$ for the detected wavelengths. Therefore the temperature of the PMT-grid must be monitored at the degree level in order to correct gain variation due to temperature effects. Other non-uniformities can be observed in the light guide or in the optical coupling between photomultipliers and light guides. All these effects were already discussed in section 4.5 and lead to systematic uncertainties in the charge measurement.

In order to attain an accurate Z measurement, a precise knowledge ($< 7\%$) of the single Unit Cell photo-detection efficiency and gains is required. The intrinsic

[4]This effect was not present in the prototype since the beam was focused and consequently the same sample of photomultipliers was touched.

spread in PMT gains and quantum efficiencies (QE) − even more when additional elements are considered, i.e. light guide, glue − imply the need of a well-defined calibration and monitoring of the RICH detection cells. The idea is to map the different detection cells building a complete database with the measurements on pedestals, gains and relative quantum efficiencies. The functional tests were performed during the RICH assembly.

The results shown in this chapter were acquired in the first half of 2006 at CIEMAT in Madrid. LIP also collaborated on the measurement campaign for a short period.

Experimental Setup

All the optical and almost all the electronic devices used in the measurements for the characterization of the detection cells were placed inside a black box with dimensions $1140 \times 890 \times 720$ mm with a wall thickness of 20 mm. The box had a top door and lateral door that allowed an easier access to the devices. Figure 9.10 shows a picture of this box. Previous tests confirmed that this box is a light-tight container. All the aforementioned calibration tests were done with grid G.

An overview of the experimental setup used for the functionality tests is presented in Figure 9.11. The personal computer was placed upon the table while all the other devices were inside the box:

- grid G with 143 photomultipliers divided in 5 CDPs (Common Digital Part);
- integrated optical fibre system;
- port multiplexer which receives the signal from the parallel port and sends it to three boards that the port multiplexer is made and whose functions are:
  - trigger and fast trigger signal generation, busy generation;
  - Dallas temperature sensors readout;
  - direction of the control and reading commands between the acquisition cards;
- high voltage brick to feed the photomultipliers;

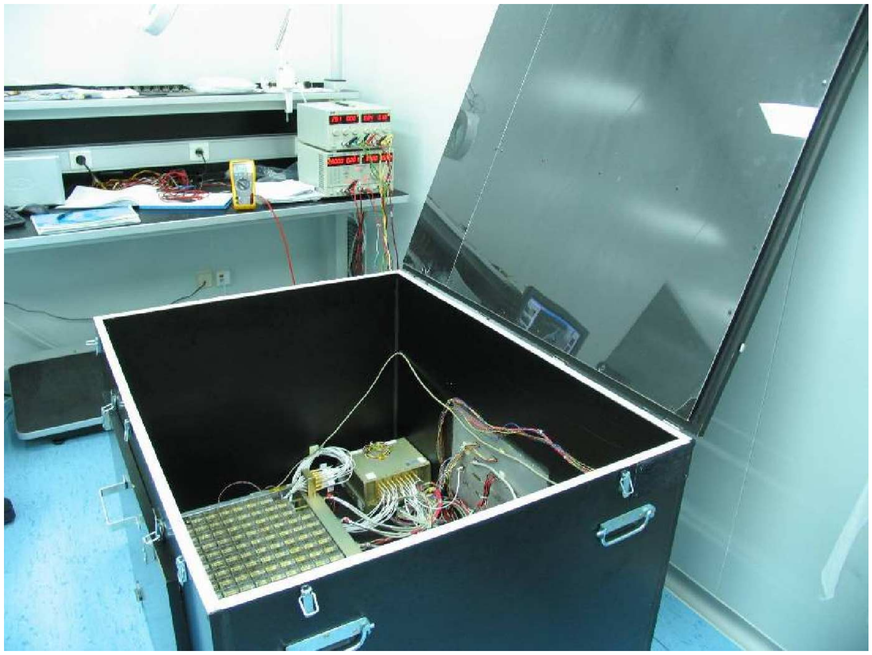

Figure 9.10: *Black box used in the functional tests* [199].

- a converter between AMSWire[5] and parallel port;
- JINF, which is a board including the connections with the 5 CDPs, the HV brick control using Lecroy protocol, the trigger and busy connection with the grid and the low voltage supplier.

Calibration method

All data can be characterized as acquired with no high voltage or with the nominal high voltage set at 800 V. The first type only provided the pedestal peak position and its width. The second type of data includes the so-called "dark runs", which consist of data acquired in the absence of light to simply measure the electronic noise (pedestals and dark current), and the LED runs which allowed to determine the gain through the use of the single photoelectron method as explained in Section 5.5 and the relative quantum efficiencies. The latter type of runs can also be used to characterize the pedestal.

[5]Communication protocol for data transmission

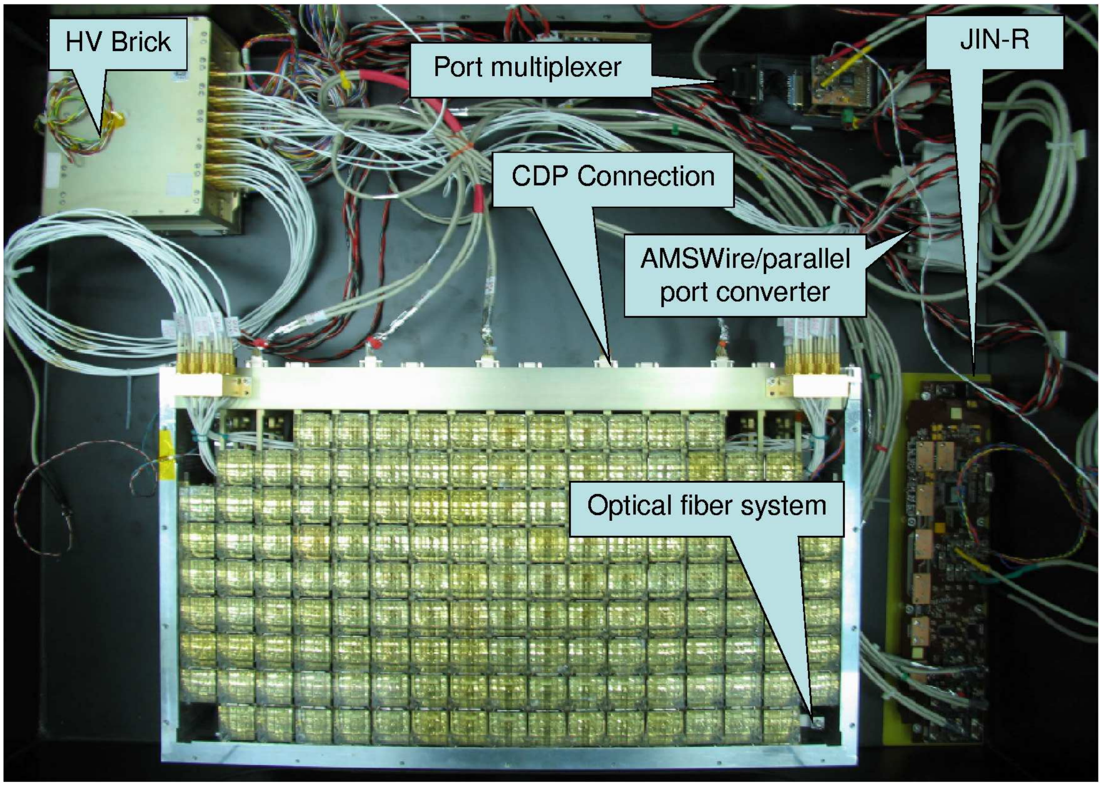

Figure 9.11: *Experimental setup used in the functional tests* [199].

The single-photoelectron method of determining the gains consists, as previously explained, in measuring the signal recoiled in the anode at very low levels of light, where the great majority of successes detected in the PMT were generated by only one incident photon. A fit to the signal using the biparametric function described in reference [189] allows to determine not only the gain but also the mean number of photoelectrons. Figure 9.12 shows a fit to the signal spectrum obtained in gain 5 using the aforementioned function.

The mean number of photoelectrons μ can also be straightforward derived from the number of events in the pedestal and the total number of events. In fact since the probability of not having any incident photon is given by

$$P_0 = e^{-\mu}, \tag{9.4}$$

the number of events in the pedestal is

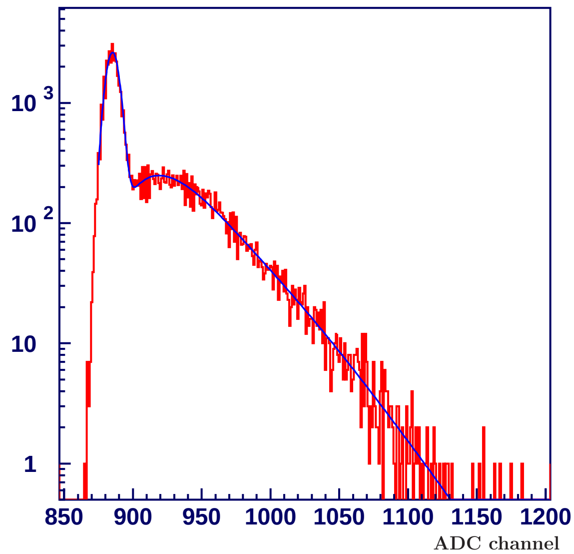

Figure 9.12: *Fit to the signal spectrum acquired in gain 5 of a certain PMT channel using a biparametric function to describe the single photoelectron response.*

$$N_{PED} = N_{TOT}\, e^{-\mu}, \tag{9.5}$$

which leads to a mean number of photoelectrons expressed as:

$$\mu = -\ln\left(\frac{N_{PED}}{N_{TOT}}\right). \tag{9.6}$$

The number of events in the pedestal is counted until the ADC position at pedestal peak position plus three standard deviations.

Results

Pedestal analysis

The pedestals for each PMT channel were acquired both with the high voltage switched off and on. No difference was observed between both measurements. First, the pedestal of each channel was fitted with an effective function given by the fit of two gaussian functions centered at the same mean value μ, with two widths σ_1

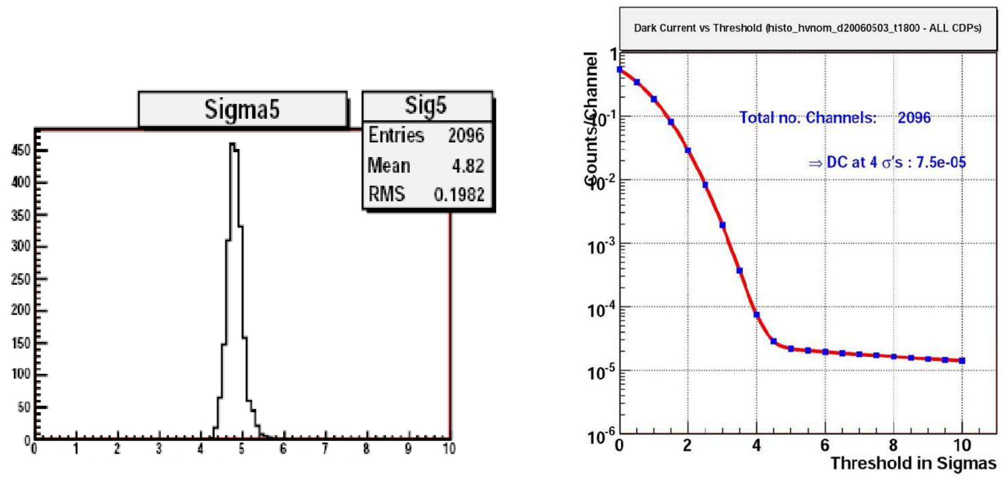

Figure 9.13: *Distributions for pedestal width* (left) *and dark current versus the number of standard deviations of the pedestal peak* (right) *of all channels of the 131 photomultipliers of grid G* [199].

and σ_2. Each gaussian is weighted by a factor that takes into account their relative populations. The effective function and the effective variance for the global fitting function can be written as it is explicit in equations 9.7.

$$\begin{aligned} F_{eff} &= \alpha G(\mu,\sigma_1) + (1-\alpha)G(\mu,\sigma_2) \\ \sigma^2_{eff} &= \alpha\sigma_1^2 + (1-\alpha)\sigma_2^2 \end{aligned} \tag{9.7}$$

Figure 9.13 (left) shows the pedestal width (σ_{ped}) acquired in gain 5 for all channels of 131 photomultipliers of grid G. The mean width is 4.8 ± 0.2 channels. The stability of the pedestal position and width were checked during a 25-day period and a stability within 1.5 ADC channels and 1% was measured, respectively.

The other factor to be controlled is the dark current. The dark current [200] is not, strictly speaking, a noise; however, noise that is associated with it does impose a limitation on the detection of very low energy radiation. The current that flows in the anode circuit when voltage is applied to a photomultiplier in total darkness has two components:

- a continuous one due to leakage on glass and insulation surfaces,

- an intermittent one, consisting of pulses of a few nanoseconds duration.

The effect of the various sources of dark current varies according to the operating and environmental conditions (applied voltage, gain, temperature, humidity, etc.), and also according to the tube's history (e.g. past storage and illumination conditions). Some of the sources are temporary in their effect, in which case the dark current eventually settles down to a stable level. Other sources are permanent, meaning they are independent of the history of the tube, like leakage currents, thermionic emission, field emission or background radiation.

As previously mentioned, the dark current was evaluated with the HV turned on. Figure 9.13 (right) shows the normalized distribution of the number of counts per channel within each fraction of the pedestal width. The dark current ratio for ADC channels positioned at a distance equal to the pedestal peak position plus $4\sigma_{ped}$ is $\sim 7.5 \times 10^{-5}$ which is a low value.

Gain calibration

The scheme established to perform gain calibration on the complete detection plane consists of an integrated LED-fibre system. Four fibres light the detector volume upwards from the detection plane and the light is reflected in the methacrylate layer placed at the radiator bottom. The reflected light uniformly illuminates the detector plane. The fibres run below the lower skin mentioned in subsection 9.2.2 to fibre connectors located in the octagonal structure. An external blue LED is optically coupled to the fibres. More technical details on this device are explained in Appendix B.

Each fibre system is placed in one corner of the ECAL hole as depicted in Figure 9.14 (left). This system was also conceived to be used when the magnet is switched on for a final calibration and following corrections to calibration constants. The concept design has been previously validated by the simulation software [201].

In the current tests using the grid G only one set of fibres is being used and its position is illustrated in Figure 9.11 (left). The distribution of the average number of photoelectrons as function of the PMT position in grid G is shown in Figure 9.14 (right). As expected, the photomultipliers closer to the fibre system see more light

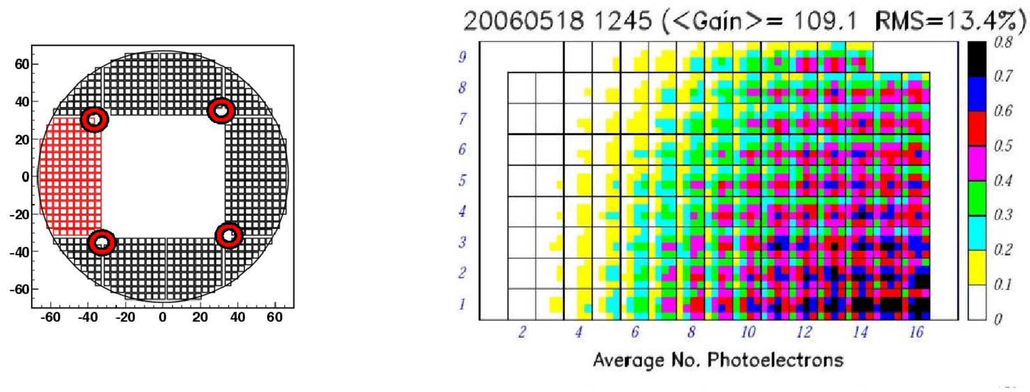

Figure 9.14: *Integrated optical fibre system location in the detection plane* (left) . *Spatial distribution of the mean number of photoelectrons observed by the PMTs in grid G considering a fibre location on the bottom right corner of the grid* (right). [199]

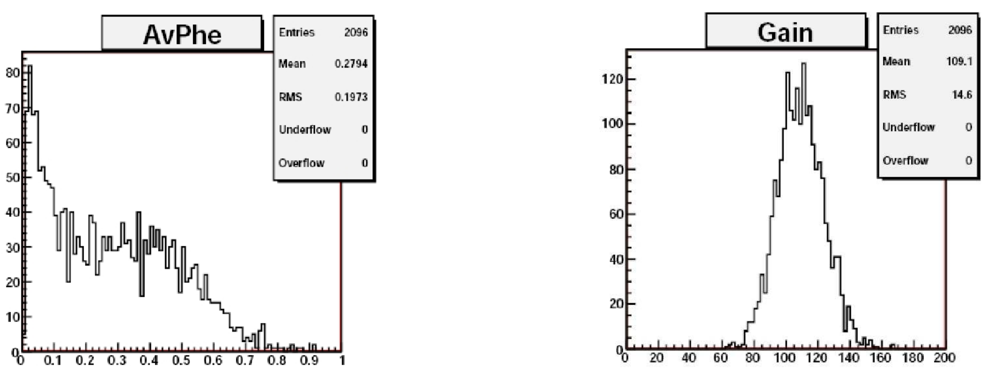

Figure 9.15: *Distributions of the average number of photoelectrons* (left) *and gains* (right) *for all the channels of the 131 PMTs calibrated in the grid G using the integrated optical fibre system.* [199]

than the others.

Figure 9.15 (left) introduces the measured average number of photoelectrons for all the channels of the 131 photomultipliers tested in grid G. The mean value is 0.28 and the spread is 0.20. Figure 9.15 (right) shows the distribution of the evaluated gain ($\times 5$) for the same channels. The mean value is 109 ADC counts with a spread of 15 ADC channels.

Since the previous illumination is not quite uniform, as proved in distribution of

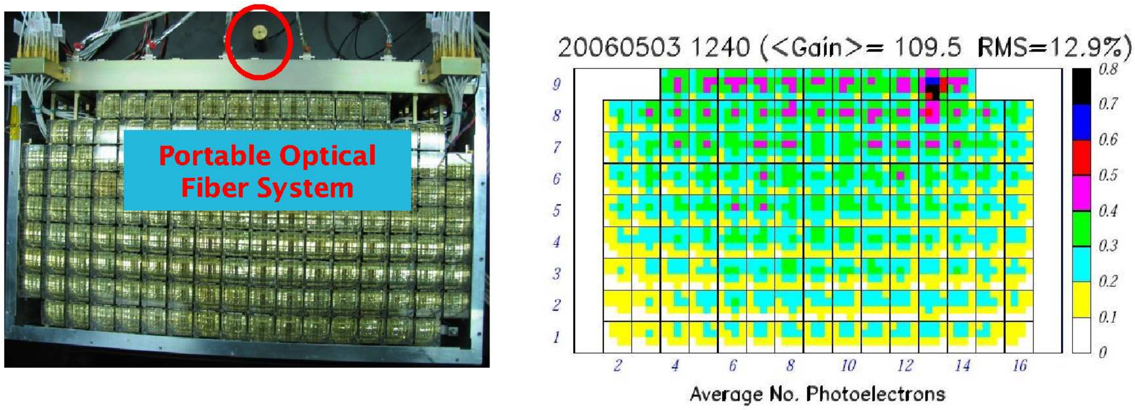

Figure 9.16: *Location of the portable optical fibre system in the detection plane* (left) . *Spatial distribution of the mean number of photoelectrons observed by the grid G PMTs considering a fibre location centred at the top of the grid* (right). [199]

Figure 9.14 (right), due to the location of the fibres a validation of the calibration was done using a portable optical fibre system. The new system is placed on the central top of grid G as illustrated in Figure 9.16 (left).

Figure 9.16 (right) introduces the new illumination map with the average number of photoelectrons as function of the PMT location. Figure 9.17 (left) shows the average number of photoelectrons for all the channels with the mean value of the distribution at 0.23 and a spread of 0.09, while the gain distribution is shown in the right-handed plot of the same figure. The average gain is centered at 110 ADC counts and the distribution presents a spread of 14 ADC channels. The results allow to conclude that gain calibrations are consistent for both illuminations and in both cases the calibration results are consistent with the values from the Hamamatsu database.

Gain stability was also studied during 15 days. The gain was proved to be stable within 1%.

PMT relative detection efficiency

The photoelectron detection efficiency for each photomultiplier was evaluated using a relative method. The relative efficiency will be defined as the ratio between the

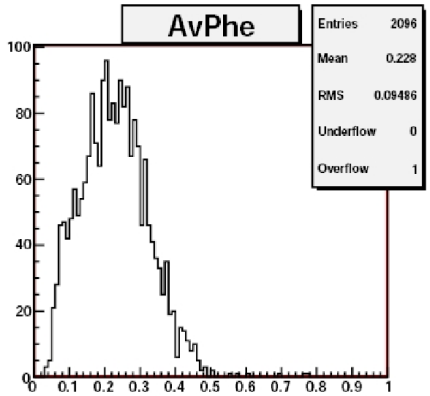

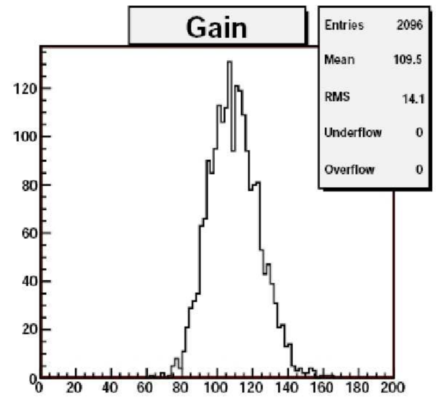

Figure 9.17: *Distributions of the average number of photoelectrons* (left) *and gains* (right) *for all the channels of the 131 PMTs calibrated in the grid G using the portable optical fibre system.* [199]

average number of photoelectrons for a given PMT and the average number of photoelectrons seen by a reference PMT. Thus the estimator can be expressed by relation 9.8:

$$Eff = \frac{\sum_{i=1,16} \mu(i)}{\sum_{i=1,16} \mu_{ref}(i)}. \tag{9.8}$$

According to what was said in Section 9.3.1 the detection efficiency should be known at the level of 7%. A unit-cell adapted LED system was used to perform the relative calibration of the unit cell response in terms of average photoelectron number. An LED was connected to four optical fibres, each of them attached to a unit like the one presented in the drawings of Figure 9.18 (left). From now on this measuring system will be called fibre stand system. Each of these units is adapted to the top of the light guide as depicted in the same scheme of the aforementioned figure. Figure 9.18 (right) shows the grid G with the four-fibre stand system. The system was first validated on a row of eight photomultipliers coupled to light guides (see presentation mentioned in [201]).

The experimental setup was the same used for pedestal and gain evaluation. A stable setup is required, this was proved to be the case by making repeated measurements of the amount of the detected light within 2%.

Since the four fibre stand devices do not give exactly the same amount of light to

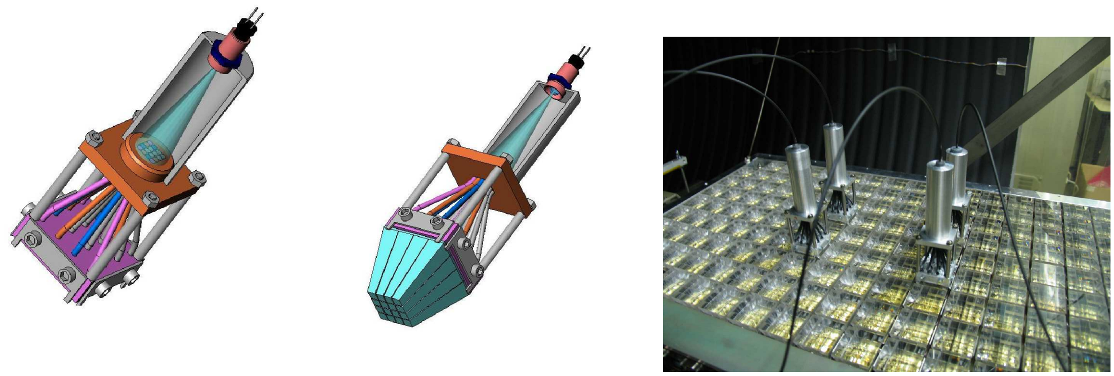

Figure 9.18: *Optical fibre stands system* (left). *Grid G with the optical fibre stands system* (right).

the unit cells and since it is necessary to obtain the relative efficiency with respect to the same reference for all the grid, the four devices should be intercalibrated. Therefore, the fibre stand devices were numbered as 1, 2, 3 and 4. Device 1 was taken as the reference calibration tool since it provides more light. Every measurement made with one of other devices is then divided by its correspondent made with device 1.

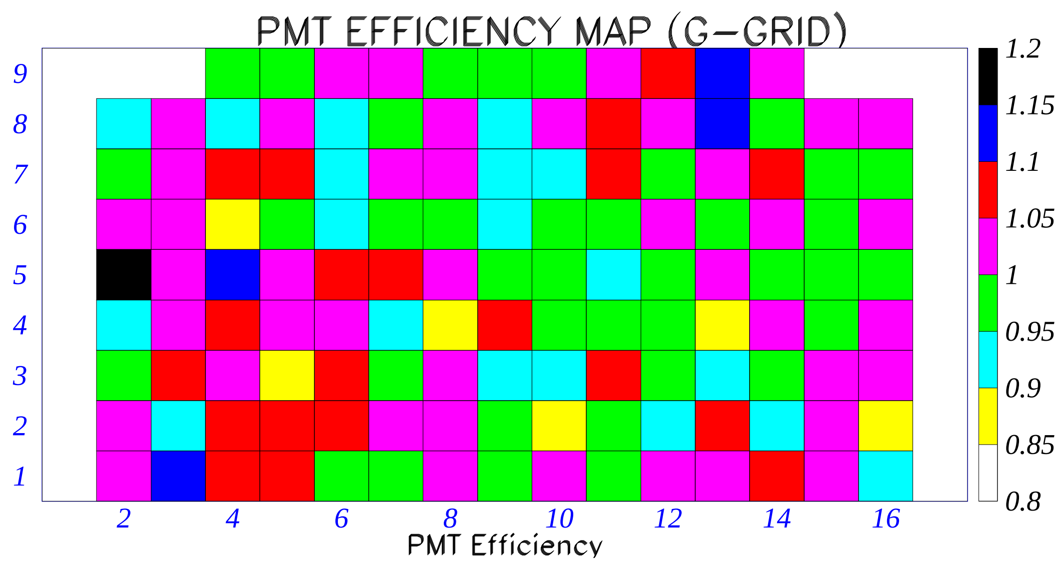

Figure 9.19: *PMT relative detection efficiency map for grid G* [199].

Figure 9.19 shows the mapping of the relative detection efficiency for grid G while Figure 9.20 (left) introduces the distribution of the same quantity, showing a

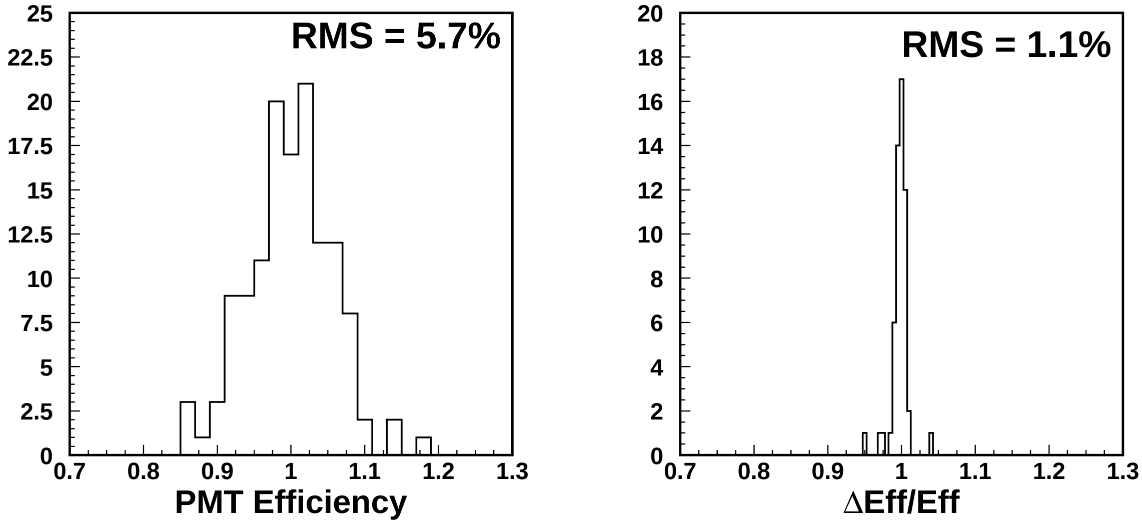

Figure 9.20: *Relative detection efficiency PMTs in grid G* (left). *Reproducibility of the relative detection efficiency* (right). [199]

spread of 5.7%. The measurement was done twice and Figure 9.20 (right) proves that the reproducibility of the measurement is within 1.1%.

All these efficiency values will be added to the database.

9.4 Conclusions

The RICH integration is almost completed. A detailed characterization of the detector plane parameters as well as the radiator tile refractive index and thickness variations were performed before the final assembly. The mirror reflectivity mapping will be also done.

The same calibration procedure, described here for grid G, was applied to the other grids and the results on the relative detection efficiency, pedestals and gain evaluation will be incorporated into the RICH database.

The RICH integration in the AMS spectrometer is scheduled to start in January of 2008.

Conclusions

AMS is a high energy particle detector developed to measure cosmic ray fluxes outside the Earth's atmosphere. It will be installed on the International Space Station and will stay there collecting data for at least 3 years. The instrument is equipped with a proximity focusing RICH detector based on a mixed radiator of aerogel and sodium fluoride, enabling velocity measurements with a resolution of about 0.1% for $Z = 1$ particles and extending the charge measurements up to the iron element.

Velocity reconstruction is made with a likelihood method. Charge reconstruction is made in an event-by-event basis. A complete description of both methods as well as simulation results were presented in this thesis. Evaluation of both algorithms on real data taken with in-beam tests at CERN, in October 2003 was done. These data were acquired using a prototype of the RICH built at LPSC. The detector design was validated and a refractive index 1.05 aerogel from Novosibirsk was chosen for the radiator, fulfilling both the demand for a large light yield and a good velocity resolution. Photon yield aerogel uniformity was estimated at the level of 1% while the aerogel refractive index uniformity is lower than 0.06×10^{-3}.

The sodium fluoride performance was also evaluated. The velocity reconstruction capabilities are according to expectations from MC simulation. Sodium fluoride data allowed to study the light guide detection behaviour for larger photon incident angles. A data/MC signal disagreement was detailed study through a dedicated light guide standalone simulation. The complete and correct description of the detection cell was updated in the RICH simulation.

A prototype of the mirror was used in the beam tests and its reflectivity was derived from data analysis. The obtained value is in good agreement with the optical measurement of the manufacturer. Data do not show a visible degradation on charge and velocity reconstructions with reflected hits.

Beam test data analysis concerning the charge reconstruction shows a systematic uncertainty of the order of 1%. In the flight scenarium this uncertainty appears due to non-uniformities at the radiator level, at the mirror surface leading to different reflectivity values or at the photon detection. In order to keep the systematic uncertainties below 1%, the aerogel tile thickness, the refractive index and the clarity should not have an unknown spread greater than 0.4 mm, 10^{-4} and 3%, respectively. The relative uncertainty on the reflectivity measurement should be controlled better than 1%. At the detection level a precise knowledge (<7% level) of the single unit cell photo-detection efficiency and gains is required.

A detailed characterization of the photomultipliers gains and pedestals as well as the relative detection efficiencies of the unit cells was done at CIEMAT. A complete map of the mirror reflectivity will be made at CIEMAT. The radiator tile thickness and refractive index mapping was performed at LPSC. All these measurements were (will be, in the case of reflectivity) done before the final assembly and will be added to the RICH database for a complete knowledge of their values at the simulation and reconstruction level.

The RICH detector is being constructed and its assembling to the AMS complete setup is foreseen to begin in January of 2008.

Appendix A

Fit to the Čerenkov ring signal

An efficient model to describe the distribution of the number of photoelectrons detected in the Čerenkov ring was previously applyed by R. Pereira and it is thoroughly explained in [191]. The Čerenkov signal associated to a ring is obtained from the signal counting within $\pm 3\sigma$ of the reconstructed pattern. Its description, can be done taking into account the different factors that contribute to it:

- statistical fluctuation;
- photomultiplier amplification:
  the uncertainty associated to the charge amplification in each dynode causes a natural spread on the photoelectron response.
- ring acceptance:
  the ring acceptance, corresponding to the fraction of detected photons, varies from event to event, as in the flight case;
- particle velocity:
  $$N_{pe} \propto \sin^2\theta_c \propto \left(1 - \frac{1}{\beta^2 n^2}\right); \tag{A.1}$$
- signal threshold:
  a minimal number of three hits is required to have a reliable reconstruction.

Therefore, the modulation function describing the ring signal, for a set of events, can be parametrized in terms of:

- the statistical distribution followed by the photoelectron signal population:

$$P(n,\mu) = \frac{e^{-\mu}\mu^n}{n!}. \tag{A.2}$$

The probability of getting n photoelectrons out of an expected number μ is given by a Poisson distribution $P(n,\mu)$. For large statistics, the distribution tends to a gaussian

$$P(n,\mu) = \frac{1}{\sqrt{2\pi}}\frac{1}{\sqrt{\mu}}\exp\left[-\frac{1}{2}\left(\frac{n-\mu}{\sqrt{\mu}}\right)^2\right]. \tag{A.3}$$

- the photomultiplier amplification: the photomultiplier anode signal depends on the number of photoelectrons (n) inciding in its cathode; its shape for any statistics of n photoelectrons can be derived from the photoelectron response of the photomultiplier. Figure A.1 shows the distributions f_n obtained for 3, 4, 5 and 6 photoelectrons. An accurate description of the single photoelectron spectrum is needed in case of a low mean number of photoelectrons μ; otherwise the single photoelectron response can be approximated by a gaussian with a width close to 0.7 p.e.

Hence, the signal function can be generically described in terms of a normalization factor A and a mean number of photoelectrons μ:

$$f(x;\mu) = A\sum_{n=3}^{\infty} P(n,\mu)f_n(x), \tag{A.4}$$

where the sum takes into account the applyed threshold ($n \geq 3$).

In case of collecting events with different ring acceptances (ϵ_i), the mean number ($\mu_i = \epsilon_i\mu_0$) of photoelectrons will change from event to event. Therefore, the ring signal distribution will be given by:

$$f(x;\mu_0) = A\sum_{n=3}^{\infty}\sum_{i} W_i P(n,\mu_i)f_n(x), \tag{A.5}$$

where W_i is the weight associated to the ring acceptance distribution of the events. Hence, the final signal distribution corresponds to a weighted sum of the different signal distributions for all the possible acceptances. For the aerogel 1.05 and sodium fluoride in the flight setup the distributions considered were the same introduced in Figure 4.27.

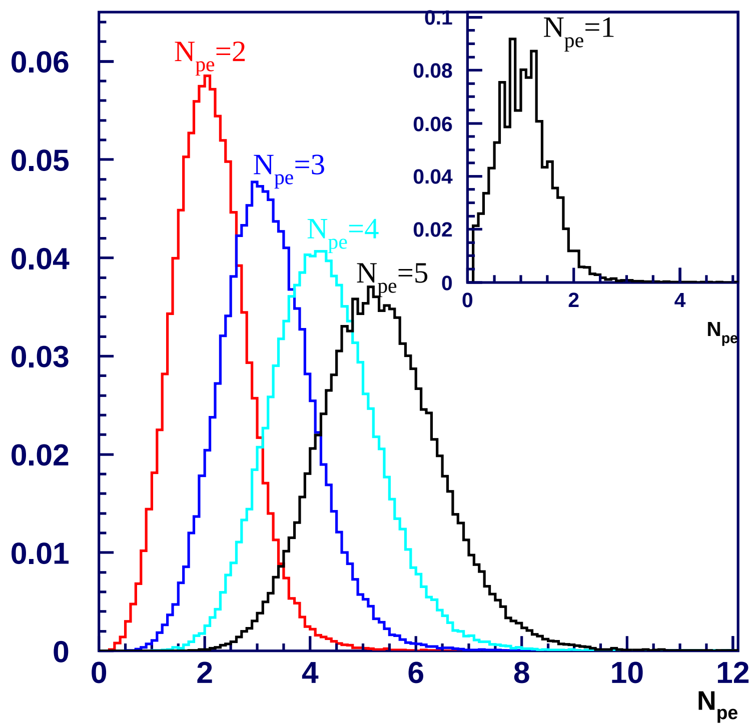

Figure A.1: *Expected signal distribution for 2, 3, 4 and 5 photoelectrons, extrated from prototype data acquired with CIN105.*

Finally, in case of dealing with a population of events generated by particles with different velocities the mean number of photoelectrons will change according to $\mu_j = W_j \mu_0 = \frac{n^2-1/\beta^2}{n^2-1}\mu_0$, where μ_0 is the number of hits foreseen for a photon ring acceptance of 100% and $\beta \simeq 1$ particles. In this case, the overall function is written as:

$$f(x;\mu_0) = A \sum_{n=3}^{\infty} \sum_{i} \sum_{j} W_{ij} P(n, \mu_{ij}) f_n(x), \tag{A.6}$$

with μ_0 the free parameter that gives the expected light yield for a 100% contained ring generated by $\beta \simeq 1$ particles. The weight W_{ij} is written as $\epsilon_i \frac{n^2-1/\beta^2}{n^2-1}$.

This method is used to fit the number of photoelectrons counted in the Čerenkov rings generated in the aerogel 1.05 and NaF radiators for $\beta \sim 1$ particles in the flight setup. Figure 4.21 shows this result for protons. The issue of particle velocity profile is naturally solved because only $\beta \sim 1$ particles were studied in the light yield studies performed in this thesis, so the ring signal estimation only has to deal with the other points.

Appendix B

LED characteristics

The LED used in the photomultiplier functionality tests for gain calibration and relative efficiency evaluation was a blue pulsed LED (Kingbright W53MBC) operating at 3.48 V with 3 filters to attenuate the light. The blue source colour devices are made with GaN on SiC Light Emitting Diode. The main characteristics are summarized in Table B.1. The left-hand distribution of Figure B.1 introduces the LED relative radiant intensity as function of the wavelength showing the peak of the spectral response at 430 nm, while the left-hand plot proves the good directionality of the same diode ($\pm 16°$).

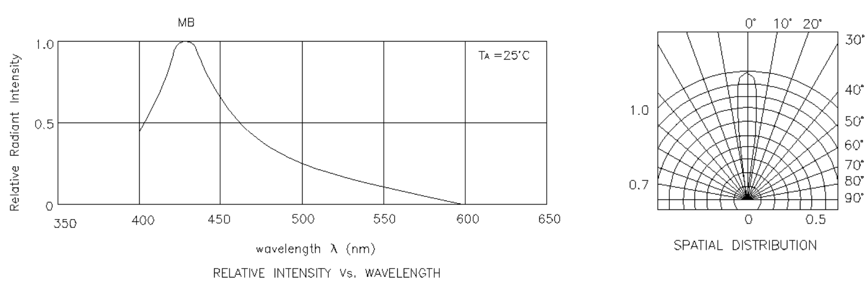

Figure B.1: *Relative Radiant Intensity* (left) *and directionality* (right) *for LED W53MBC from Kingbright.*

LED characteristics		
Material		Gallium nitride
Viewing Angle ($2\theta_{1/2}$)[1]		16°
Luminous Intensity [(a)]	Minimum	50 mcd
	Typical	150 mcd
Electrical/Optical characteristics @$\mathbf{T_A}$=25°C		
Peak Wavelength [(a)]		430 nm
Dominant Wavelength [(a)]		466 nm
Forward Voltage (V_F) [(a)]	Typical	3.8 V
	Maximum	4.5 V
Reverse Current (I_R) [(b)]	Maximum	10 μA
Absolute Maximum Ratings @$\mathbf{T_A}$=25°C		
Power dissipation		105 mW
DC Forward current		30 mA

[1] $\theta_{1/2}$ is the angle from optical centerline where the luminous intensity is 1/2 the optical centerline value.

Table B.1: *LED characteristics. Test conditions:* (a) I_F=*20 mA;* (b) V_R=*5 V.*

Bibliography

[1] M. Takeda *et al.* Energy determination in the Akeno Giant Air Shower Array experiment. *Astropart. Phys.*, (19):447–462, 2003.

[2] R. U. Abassi *et al.* A Study of the Composition of Ultra High Energy Cosmic Rays Using the High Resolution Fly's Eye. *ApJ.*, (622):910, 2005.

[3] P. Mantsch for the Pierre Auger collaboration. The Pierre Auger Observatory Progress and First Results. In *Proc. 29th Int. Cosmic Ray Conf.(Pune)*, volume 10, pages 115–124, August 2005.

[4] H. Ulrich *et al.* Composition and energy spectra of elemental groups around the knee: Results from KASCADE. In *Proc. 29th Int. Cosmic Ray Conf.(Pune)*, volume 6, pages 129–132, August 2005.

[5] A. Haungs *et al.* The KASCADE-Grande Experiment. In *Proc. 28th Int. Cosmic Ray Conf.(Tsukuba)*, volume 1, pages 985–988, August 2003.

[6] Nutter *et al.* Detection of cosmic-ray antiprotons with the HEAT-pbar instrument. In *Proc. 27th Int. Cosmic Ray Conf.(Hamburg)*, page 1691, August 2001.

[7] G. A. Nolfo *et al.* A measurement of the ^{10}Be/^{9}Be ratio above 1.0 Gev/nucleon: Results from the 1998 Flight of ISOMAX. In *Proc. 27th Int. Cosmic Ray Conf.(Hamburg)*, pages 1659–1663, August 2001.

[8] M. Boezio *et al.* The Cosmic-Ray Antiproton Flux between 3 and 49 GeV. *ApJ*, (561):787, 2001.

[9] The Bess collaboration. The BESS Program. *Nucl. Phys. B (Proc. Suppl.)*, 134:31–38, 2004.

[10] J. Wefel *et al.* The ATIC Science Flight in 2002-03: Description and Preliminary Results. In *Proc. 28th Int. Cosmic Ray Conf.(Tsukuba)*, volume 4, pages 1849–1852, August 2003.

[11] D. Müller *et al.* Measurements with TRACER: Discussion of Results and Future Prospects. In *Proc. 29th Int. Cosmic Ray Conf.(Pune)*, volume 3, pages 89–92, August 2005.

[12] E. S. Seo *et al.* The Recording Breaking 42-day Ballon Flight of CREAM. In *Proc. 29th Int. Cosmic Ray Conf.(Pune)*, volume 3, pages 101–104, August 2005.

[13] M. Boezio for the PAMELA collaboration. The PAMELA space experiment. In *Proc. 29th Int. Cosmic Ray Conf.(Pune)*, volume 10, pages 255–270, August 2005.

[14] AMS Collaboration. The Alpha Magnetic Spectrometer (AMS) on the International Space Station: Part I - results from the test flight on the space shuttle. *Physics Reports*, (366):331–405, 2002.

[15] I. Usoskin *et al.* Heliospheric Physics and Cosmic Rays. Lecture Notes, Fall term 2000, January 2001.

[16] Gaisser. *Cosmic Rays and Particle Physics*. Cambridge University Press, 1^{st} edition, 1990.

[17] S. Eidelman *et al.* Review of Particle Physics. *Physics Letters B*, 592:1+, 2004.

[18] H.V. Klapdor-Kleingrothaus *et al.* *Particle Astrophysics*. Institute of Physics Publishing, 1997.

[19] F. Barão. Results from the AMS precursor flight and prospects of AMS2. Presentation at Third International Workshop on New Worlds in Astroparticle Physics, September 2000.

[20] V. Ptuskin. Cosmic Rays: Origin, Propagation, and Interaction. In *Third International Workshop on New Worlds in Astroparticle Physics*, pages 46–65. World Scientific, 2000.

[21] V.L. Ginzburg and S.I. Syrovatskii. *The Origin of Cosmic Rays*. Pergamon Press, 1964.

[22] F.C. Jones and D.C. Ellison. The Plasma Physics of Shock Acceleration. *Space Science Rev.*, 58:pp. 259–346, 1991.

[23] Enrico Fermi. On the origin of the cosmic radiation. *Phys. Rev.*, 75(8):1169–1174, April 1949.

[24] A. R. Bell. The acceleration of cosmic rays in shock fronts. I. *MNRAS*, 182:147–156, January 1978.

[25] R. D. Blandford and J. P. Ostriker. Particle acceleration by astrophysical shocks. *ApJ*, 221:L29–L32, April 1978.

[26] T. J. Jones *et al.* The Identification of Infrared Synchrotron Radiation from Cassiopeia A. *ApJ*, 587:227–234, April 2003.

[27] V. Ptuskin. Supernova remnants as cosmic accelerators. In M. M. Shapiro *et al.*, editor, *Neutrinos and Explosive Events in the Universe*, pages 131–142, 2005.

[28] Esposito *et al.* EGRET Observations of Gamma-Ray Emission from Supernova Remnants. *Bulletin of the American Astronomical Society*, 28:861–+, May 1996.

[29] K. Koyama *et al.* Evidence for Shock Acceleration of High-Energy Electrons in the Supernova Remnant SN:1006. *Nature*, 378:255+258, November 1995.

[30] S. P. Reynolds. Synchrotron Models for X-Rays from the Supernova Remnant SN 1006. *ApJ*, 459:L13, March 1996.

[31] K. Koyama *et al.* Discovery of Non-Thermal X-Rays from the Northwest Shell of the New SNR RX J1713.7-3946: The Second SN 1006? *PASJ*, 49:L7–L11, June 1997.

[32] P. Slane *et al.* Nonthermal X-Ray Emission from the Shell-Type Supernova Remnant G347.3-0.5. *ApJ*, 525:357–367, November 1999.

[33] G. E. Allen *et al.* Evidence of X-Ray Synchrotron Emission from Electrons Accelerated to 40 TeV in the Supernova Remnant Cassiopeia A. *ApJ*, 487:L97+, September 1997.

[34] H. Muraishi *et al.* Evidence for TeV gamma-ray emission from the shell type SNR RX J1713.7-3946. *A&A*, 354:L57–L61, February 2000.

[35] F. Aharonian *et al.* Evidence for TeV gamma ray emission from Cassiopeia A. *A&A*, 370:112–120, April 2001.

[36] M. Simon. Propagation of Cosmic Rays in the Galaxy. In M. A. DuVernois, editor, *Topics in Cosmic-Ray Astrophysics*, volume 230 of *Horizons in World Physics*, pages 105–130. Nova Science Publishers, New York, NY, 2000.

[37] M. S. Longair. *High Energy Astrophysics vol 1,2*. Cambridge University Press, 1992.

[38] V.S. Berezinskii *et al.* *Astrophysics of Cosmic Rays*. North Holland, Amsterdam, 1990.

[39] D. Maurin. *Propagation des rayons cosmiques dans un modele de diffusion : une nouvelle estimation des parametres de diffusion et du flux d'antiprotons secondaires*. PhD thesis, Université de Savoie, 2001.

[40] M. Garcia-Munoz *et al.* Cosmic-ray propagation in the Galaxy and in the heliosphere - The path-length distribution at low energy. *ApJ*, 64:269–304, May 1987.

[41] A. Molnar *et al.* Test of the diffusion halo and the leaky box by means of secondary radioactive cosmic ray nuclei with different lifetimes. In *Proc. 28th Int. Cosmic Ray Conf. (Hamburg)*, 2001.

[42] T. Hams *et al.* ^{10}Be/^{9}Be ratio up to 1.0 Gev/nucleon measured in the ISOMAX 98 balloon flight. In *Proc. 27th Int. Cosmic Ray Conf. (Hamburg)*, 2001.

[43] N. E. Yanasak *et al.* Implications for Cosmic Ray Propagation from ACE Measurements of Radioactive Clock Isotope Abundances. In *Proc. 26th Int. Cosmic Ray Conf. (Salt Lake City)*, 1999.

[44] J. J. Connel. Galactic cosmic-ray confinement time: *Ulysses* high energy telescope measurements of the secondary radionuclide ^{10}Be. *ApJ*, 501:L59–L62, 1998.

[45] A. Lukasiak, *et al.* Voyager Measurements of the Mass Composition of Cosmic-Ray Ca through Fe Nuclei. *ApJ*, 488:454–461, 1997.

[46] M. E. Wiedenbeck *et al.* A Cosmic-Ray Age based on the abundance of ^{10}Be. *ApJ*, 239:L139–L142, 1980.

[47] M. Garcia-Muñoz *et al.* In *Proc. 17th Int. Cosmic Ray Conf. (Paris)*, volume 2, page 72, July 1981.

[48] V. L. Prischep and V. S. Ptuskin. Decaying nuclei and the age of cosmic rays in the galaxy. *Ap&SS*, (32):265, 1975.

[49] D. Maurin. Galactic cosmic ray nuclei as a tool for astroparticle physics. *Recent Research Developments in Astrophysics*, 2002.

[50] K. L. Stanek *et al.* Distance to M31 with the Hubble Space Telescope and Hipparcos Red Clump Stars. *ApJ*, 503:L131–L134, 1998.

[51] D. R. Alves. K-Band Calibration of the Red Clump Luminosity. *ApJ*, 539:732–741, 2000.

[52] V. L. Ginzburg *et al.* On the origin of cosmic rays: some problems of high-energy astrophysics. *Rev. Mod. Phys.*, 48:161–189, 1976.

[53] V. S. Ptuskin, *et al.* On using the weighted slab approximation in studying the problem of cosmic ray transport. *ApJ*, 465:972–981, 1996.

[54] A.W. Strong and I.V. Moskalenko. Propagation of Cosmic-Ray Nucleons in the Galaxy. *ApJ*, 509:212–228, December 1998.

[55] K. Beuermann, *et al.* Radio structure of the Galaxy - Thick disk and thin disk at 408 MHz. *A&A*, 153:17–34, 1985.

[56] J. Casaus on behalf of the AMS-02 Collaboration. Cosmic-ray Astrophysics with AMS-02. In *Proc. 28th Int. Cosmic Ray Conf.(Tsukuba)*, volume OG 1.5, pages 2149–2152, August 2003.

[57] R. Pereira *et al.* Isotope separation with the RICH detector of the AMS experiment. In *Fifth International Workshop on New Worlds in Astroparticle Physics*, pages 140–144. World Scientific, 2005.

[58] L. Arruda. Čerenkov Ring Acceptance in the RICH Detector of the AMS Experiment. Master's thesis, Instituto Superior Técnico, June 2003.

[59] D. Casadei. Esperimento AMS: problemi teorici e sperimentali nella ricerca di antimateria in raggi cosmici. Master's thesis, Univ. di Bologna, March 1998.

[60] L.J. Gleeson and W.I. Axford. Solar modulation for galactic cosmic rays. *ApJ*, 154:1011–1026, December 1968.

[61] Y. Asaoka. Measurements of Cosmic-ray Low-energy Antiproton and Proton Spectra in a Transient Period of the Solar Field Reversal. *Physical Review Letters*, 88:051101, 2002.

[62] http://www.ngdc.nasa.gov/seg/potfld/geomag.stml.

[63] M. Walt. *Introduction to Geomagnetically Trapped Radiation.* Cambridge University Press, 1^{st} edition, November 1994.

[64] E. P. Hubble. A relation between distance and radial velocity among extragalactic nebulae. *Publ. Nat. Acad. Sci.*, (15):168, 1929.

[65] A. A. Penzias and R. W. Wilson. A measurement of excess antenna temperature at 4080-mc/s. *ApJ*, (142):419–421, 1965.

[66] J. C. Mather *et al.* Early results from the Cosmic Background Explorer (COBE). *ApJ*, (354):L37, 1990.

[67] G. Gamow. The Origin of Elements and the Separation of Galaxies,. *Phys. Rev.*, (74):505, 1949.

[68] D. Pomarade. *Recherche d'antimatiere dans les rayons cosmiques de 10^{12} eV par la methode Artemis et interpretation du spectre des rayons cosmiques*. PhD thesis, Ècole Polytechnique, 1999.

[69] M. Yu. Khlopov. Physical Origin, Evolution and Observational Signature of Diffused Antiworld. *Astropart. Phys.*, 12:367, 2000.

[70] M. Yu. Khlopov, *et al.* Possible Origin of Antimatter Regions in the Baryon Dominated Universe. *Phys. Rev. D*, 62:083505, 2000.

[71] A. G. Cohen, *et al.* A Matter-Antimatter Universe. *ApJ*, 495:539–549, March 1998.

[72] Super-Kamiokande collaboration. Search for Proton Decay via $p \rightarrow e^+\pi^0$ in a Large Water Cherenkov Detector. *Phys. Rev. Lett.*, 81:3319–3323, 1998.

[73] F. Donato *et al.* Antiprotons from Spallations of Cosmic Rays on Interstellar Matter. *ApJ*, 563, December 2001.

[74] I. Moskalenko *et al.* Secondary Antiprotons and Propagantion of Cosmic-Rays in the Galaxy and Heliosphere. *ApJ*, 565, January 2002.

[75] E. A. Bogomolov *et al.* Balloon study of spectra and composition of singly-charged component of primary and secondary cosmic radiations, using magnetic spectrometer. In *Proc. 16th Int. Cosmic Ray Conf. (Kyoto)*, volume 330, 1979.

[76] A. Buffington *et al.* A Mesurement of the Cosmic-Ray Antiproton Flux and a Search for Antihelium. *ApJ*, 248, September 1981.

[77] F. W. Stecker *et al.* In *Proc. 17th Int. Cosmic Ray Conf. (Paris)*, volume 9, page 211, 1981.

[78] F. W. Stecker and A. W. Wolfendale. The case for antiparticles in the extra-galactic cosmic-radiation. *Nature*, 309:37, 1984.

[79] J. Silk. Cosmic-Ray Antiprotons as a Probe of a Photino-Dominated Universe. *Phys. Rev. Lett.*, 53(6):624–628, August 1984.

[80] Th. Kirn. Antimatter & Dark Matter Search. Trento meeting, November 2001.

[81] BESS Collaboration. Measurement of Low-Energy Cosmic-Ray Antiprotons at Solar Minimum. *Phys. Rev. Lett.*, 81:4052–4055, 1998.

[82] BESS Collaboration. Precision Measurement of Cosmic-Ray Antiproton Spectrum. *Phys. Rev. Lett.*, 84:1078–1081, 2000.

[83] BESS Collaboration. Precision Measurement of Cosmic-Ray Proton and Helium Spectra with the BESS Spectrometer. *ApJ*, 545:135, 2000.

[84] J. W. Bieber. Antiprotons at Solar Maximum. *Phys. Rev. Lett.*, 83(4):674–677, July 1999.

[85] S. C. Kappadath. *Measurement of the cosmic diffuse gamma-ray spectrum from 800 KeV to 30 MeV*. PhD thesis, University of New Hampshire, 1998.

[86] P. Sreekumar. EGRET Observations of the Extragalactic Gamma-Ray Emission. *ApJ*, 494:523–534, February 1998.

[87] Chong-Ming Xu, Xiang-Yu Wang, Xue-Jun Wu, and Yong-Heng Zhao. Is the 0.36-kev x-ray a sign of the existence of antimatter domains? *Chin. Phys. Lett.*, 16:232–234, 1999.

[88] Yu. V. Galaktionov. Antimatter in cosmic rays. In *Reports on Progress in Physics*, volume 65, page 1258. Institute of Physics Publishing, August 2002.

[89] M. Buénerd. AMS, a particle spectrometer in space. In *XXIV Symposium on Nuclear Physics*, Tasco, Mexico, January 2001.

[90] R. Battiston. Astro Particle Physics with AMS on the International Space Station. *Nuc. Phys. B (Proc. Suppl.)*, (113):9–17, 2002.

[91] A. H. Broeils *et al.* Extended rotation curves of spiral galaxies - Dark haloes and modified dynamics. *Mon. Not. R. Astr. Soc.*, 249:523–537, April 1991.

[92] L. Mosca. An Introduction to the direct detection of particle Dark Matter (WIMPS). In *Third International Workshop on New Worlds in Astroparticle Physics*, pages 189–200. World Scientific, 2000.

[93] N. Bahcall. Dark Matter. preprint Princeton Observ-P-693, November 1996.

[94] D. N. Spergel *et al.* Wilkinson Microwave Anisotropy Probe (WMAP) Three Year Results: Implications for Cosmology, astro-ph/0603449.

[95] G. Jungman *et al.* Supersymmetric Dark Matter. *Phys. Rept.*, (267):195–373, 1996.

[96] G. Servant *et al.* Is the Lightest Kaluza-Klein Particle a Viable Dark Matter Candidate? *Nucl. Phys.*, (B650):391–419, 2003.

[97] B. Serfass. Status of the Cryogenic Dark Matter Search (CDMS) Experiment. In *Rencontres de Moriond - Contents and Structures of the Universe La Thuile, Italy*, March 18-25 2006.

[98] H. Gast *et al.* Indirect dark matter search: Cosmic positron fraction measurement from 1-Gev to 50-Gev with AMS-01. *astro-ph/0605254*, 2006.

[99] P. Maestro. *Indirect search for dark matter by measurements of the cosmic ray positron spectrum with the AMS-02 experiment.* PhD thesis, Università Degli Studi Di Siena, 2003.

[100] M. A. DuVernois *et al.* Cosmic-Ray Electrons and Positrons from 1 to 100 GeV: Measurements with HEAT and Their Interpretation. *ApJ*, (559):296, 2001.

[101] J. J. Beatty *et al.* New Measurement of the Cosmic-Ray Positron Fraction from 5 to 15 GeV. *Phys. Rev. Lett.*, (93):241102, 2004.

[102] J. Alcaraz *et al.* Leptons in the near orbit. *Phys. Lett. B*, (484):10–22, 2000.

[103] E. Falcini. *AMS-02 dark matter search inspecting cosmic ray positron spectrum.* PhD thesis, Università Degli Studi di Siena, 2004.

[104] E. A. Baltz *et al.* The cosmic ray positron excess and neutralino dark matter. *Phys. Rev. D*, (65):063511, 2002.

[105] J. Pochon. *Mesures du spectre de positons cosmiques avec l'experience AMS-02 et recherche de signaux. exotiques*. PhD thesis, Université de Lion 1, 2005.

[106] J. Lavalle *et al.* Clumpiness of Dark Matter and Positron Annihilation Signal: Computing the odds of the Galactic Lottery. *A&A*, (462):827–840, 2007.

[107] V. Choutko. Cosmic Antiproton Spectrum Measurement Modelling with the AMS-02 Detector at ISS. *Nucl. Phys. B (Proc. Suppl.)*, 113:170–176, 2002.

[108] F. Donato *et al.* Antideuterons as a Signature of Supersymmetric Dark Matter. *Phys. Rev. D*, 62, April 2000.

[109] L. Bergstrom *et al.* Cosmic antiprotons as a probe for neutralino dark matter? *astro-ph/9906034*, June 1999.

[110] R. Duperray *et al.* Flux of light antimatter nuclei near Earth, induced by cosmic rays in the Galaxy and in the atmosphere. *Phys. Rev. D*, 71, April 2005.

[111] L. Bergström. Non-Baryonic Dark Matter - Observational Evidence and Detection Methods. *Rept. Prog. Phys.*, 63, 2000.

[112] L. Bergström. Spectral Gamma-ray Signatures of Cosmological Dark Matter Annihilation. *Phys.Rev.Lett.*, 87, 2001.

[113] P. Sreekumar. The Extragalactic Diffuse Gamma-Ray Emission. *ApJ*, 494:523–534, 1998.

[114] http://glast.gsfc.nasa.gov/.

[115] http://www-glast.slac.stanford.edu/software/is/glast_lat_performance.htm.

[116] R. Battiston *et al.* The Gamma Ray Detection Capabilities of the Alpha Magnetic Spectrometer. *Astropart. Phys.*, 13:51, 2000.

[117] G. Lamanna. High-energy gamma-ray detection with the Alpha Magnetic Spectrometer on board the International Space Station. *Nucl. Phys. B (Proc. Suppl.)*, 113:177, 2002.

[118] G. Lamanna. High Energy Gamma-ray Detection with AMS-02 operating as e^+e^- pair spectrometer. *AMS-Note 2003-03-03.*

[119] G. Choutko *et al.* Cosmic photon and positron spectra measurements modelling with the AMS-02 detector at ISS. *Int. J. Mod. Phys. A*, 17:1817–1828, 2002.

[120] A. Jacholkowska *et al.* An indirect dark matter search with diffuse gamma rays from the Galactic Center with the Alpha Magnetic Spectrometer. *Phys. Rev.*, D74:023518, 2006.

[121] I. Sevilla Noarbe. *El experimento AMS-02 como observatorio de rayos gamma desde la Estación Espacial Internacional.* PhD thesis, Universidad Complutense de Madrid, 2006.

[122] S. Di Falco. Indirect dark matter search with AMS-02. In *Rencontres de Moriond - Contents and Structures of the Universe La Thuile, Italy.*

[123] L. Girard. *Gamma Detection with AMS-02.* PhD thesis, Université de Savoie, 2004.

[124] J. K. Daugherty *et al.* Gamma Ray Pulsars: Emission from Extended Polar Cap Cascades. *ApJ*, 458:287, 1996.

[125] R. W. Romani. Gamma-Ray Pulsars: Radiation Processes in the Outer Magnetosphere. *ApJ*, 470:469, 1996.

[126] AMS collaboration. AMS on ISS - Construction of a particle physics detector on the International Sapce Station. *to be submitted to Nucl. Instrum. and Meth. B.*

[127] J. Alcaraz *et al.* Search for Antihelium in Cosmic Rays. *Phys. Lett. B*, (461):387–396, 1999.

[128] J. Alcaraz *et al.* Cosmic Protons. *Phys. Lett. B*, (490):27–35, 2000.

[129] J. Alcaraz *et al.* Protons in Near Orbit. *Phys. Lett. B*, (472):215–226, 2000.

[130] J. Alcaraz *et al.* Helium in Near Orbit. *Phys. Lett. B*, (494):193–202, 2000.

[131] http://ams.cern.ch/ams/ams homepage.html.

[132] J. Olzem for the AMS-02 TRD Collaboration. Construction of the AMS-02 Transition Radiation Detector for the International Space Station. In *Proc. 29th Int. Cosmic Ray Conf.(Pune)*, volume 3, pages 285–288, August 2005.

[133] D. Casadei on behalf of the AMS-02 TOF Collaboration. The AMS-02 Time of Flight System. final Design. In *Proc. 28th Int. Cosmic Ray Conf. (Tsukuba)*, volume 4, pages 2169–2172, August 2005.

[134] R.H. McMahon *et al.* The Alpha Magnetic Spectrometer Superconducting Magnet. In *Proc. 29th Int. Cosmic Ray Conf.(Pune)*, volume 9, pages 303–306, August 2005.

[135] C. Lechanoine-Leluc on behalf of the AMS Tracker collaboration. The AMS-02 Tracker. In *Proc. 29th Int. Cosmic Ray Conf.(Pune)*, volume 9, pages 299–302, August 2005.

[136] F. Cadoux *et al.* The AMS-02 electromagnetic calorimeter. *Nucl. Phys. B (Proc. Suppl.)*, 113:159–165, 2002.

[137] A. Monfardini *et al.* AMICA, an astro-mapper for AMS. *Astroparticle Physics*, 25:355, 2006.

[138] C. Grupen. *Particle Detectors*. Cambridge University Press, 1^{st} edition, 1996.

[139] R. Fernow. *Introduction to Experimental Particle Physics*. Cambridge University Press, 1^{st} edition, 1990.

[140] T. Ypsilantis and J. Seguinot. Theory of ring imaging cherenkov counters. *Nucl. Instrum. and Meth. A*, 343:30–51, 1994.

[141] J. Seguinot. Les Compteurs Cherenkov: Applications et limites pour l'identification des particules developpements et prespectives. Presented at 1988 Joliot-Curie School, Maubuisson, France, Sep 26-30, 1988.

[142] P. A. Čerenkov . Visible Radiation Produced by Electrons Moving in a Medium with Velocities Exceeding that of Light. *Phys. Rev.*, 52:378, 1937.

[143] I. M. Frank and I. J. Tamm. Coherent Radiation of Fast Electrons in a Medium. *Dokl. Academie des Sciences de l'URSS*, 14:107–113, 1937.

[144] P. Marmier and E. Sheldon. *Physics of Nuclei and Particles Vol. 1.* Academic Press, New York, 1^{st} edition, 1969.

[145] J.V. Jelley. *Cherenkov Radiation and its Applications.* Pergamon Press, New York, 1958.

[146] E. Nappi and J. Seguinot. Ring imaging Cherenkov detectors: The state of the art and perspectives. *Riv. Nuovo Cim.*, 28:1–130, 2005.

[147] http://wwwae.ciemat.es/ams.

[148] M. Buénerd. The RICH counter of the AMS experiment. *Nucl. Instrum. and Meth. A*, 502:158–162, 2003.

[149] P. Carlson *et al.* A RICH counter for identifying antiprotons and light isotopes in the cosmic radiation. *Nucl. Instrum. and Meth. A*, (343):198–202, 1994.

[150] G. Barbiellini *et al.* Performance of the CAPRICE RICH detector during the 1994 balloon flight. *Nucl. Instrum. and Meth. A*, (371):169–173, 1996.

[151] http://www.notz-plastics.ch/docseng/hesa.htm.

[152] E. Nappi. Aerogel and its applications to RICH detectors. *Nuclear Physics B Proceedings Supplements*, 61:270–276, February 1998.

[153] M. Cantin *et al.* Silica Aerogels used as Čerenkov Radiators. *Nucl. Instrum. and Meth.*, (118):177, 1974.

[154] H. Jackson. The HERMES dual radiator RICH: Performance and impact Theory of ring imaging Cherenkov counters. *Nucl. Instrum. and Meth. A*, 553:205–209, 2005.

[155] S. Easo. Overview of LHCb RICH detector development. *Nucl. Instrum. and Meth. A*, 553:333–338, 2005.

[156] D. Barancourt *et al.* The AMS-01 Aerogel Threshold Cherenkov counter. *Nucl.Instrum.Meth. A*, 465:306–317, 2001.

[157] A. Danilyuk *et al.* Recent results on aerogel development for use in Cherenkov counters. *Nucl. Instrum. and Meth. A*, 494:491–494, 2002.

[158] A. Barnyakov *et al.* Development of aerogel Cherenkov detectors at Novosibirsk. *Nucl. Instrum. and Meth. A*, 553:125–129, 2005.

[159] P. Aguayo *et al.* Prototype study of the Cherenkov imager of the AMS experiment. *Nucl. Instrum. and Meth. A*, 560(2):291–302, May 2006.

[160] M. Brassed. *Handbook of Optics*. McGraw Hill, 1995.

[161] P. Wang *et al.* Optical Investigations of Silica Aerogels. *Journal of Non-Crystalline Solids*, 145:141–145, 1992.

[162] R. De Leo *et al.* Chromatic aberration and foward scattering of light in silica aerogel. *Nucl. Instrum. and Meth. A*, 457:52–63, January 2001.

[163] E. Lanciotti. *Estudio de las capacidades del detector RICH de AMS mediante el análisis de los datos de un prototipo en un haz de iones*. PhD thesis, Universidad Complutense de Madrid, 2006.

[164] Hamamatsu photonics (http://www.hamamatsu.com).

[165] L. Gallin-Martel *et al.* A 16-channel analog integrated circuit for PMT pulse processing. *IEEE Transactions on nuclear science*, 49(4):1798–1801, August 2002.

[166] http://wwwae.ciemat.es/∼delgadom/richsim/.

[167] J. Borges. Velocity Reconstruction with the RICH detector of the AMS experiment. Master's thesis, Instituto Superior Técnico, January 2004.

[168] A. Keating. Reconstrução da carga eléctrica de partículas cósmicas no detector RICH da experiênia AMS. Master's thesis, Instituto Superior Técnico, May 2002.

[169] F. Barão, L. Arruda *et al.* Cerenkov angle and charge reconstruction with the RICH detector of the AMS experiment. *Nucl. Instrum. and Meth. A*, 502:310–314, 2003.

[170] Glen Cowan. *Statistical Data Analysis.* Oxford University Press, 1998.

[171] J. Casaus. The AMS RICH detector. *Nucl. Phys. B-Proc Sup*, (114):259–273, 2002.

[172] C. Delgado *et al.* The AMS-RICH prototype: test beam results. In *IEEE Transactions on Instrumentation and Measurement*, to be published.

[173] C. Delgado. *Medida de la velocidad de mounes y nucleos ligeros con un prototipo del contador RICH del experimento AMS.* PhD thesis, Universidad Autonoma de Madrid, 2003.

[174] http://www.mew.co.jp/e-index.html.

[175] http://www.catalysis.nsk.su/.

[176] L. Gallin-Martel *et al.* The read-out electronics of the AMS prototype RICH detector. *Nucl. Instrum. and Meth. A*, 504(1):273–275, May 2003.

[177] *Model S9007 DAQ Board for AMS/PAMELA experiment.* Technical Information Manual Rev 0 CAEN, 2000.

[178] *APEX 20K Programmable Logic Device Family.* Altera datasheet, November 1999. ver 2.05.

[179] *AD7476/AD7477 1 MSPS, 12-/10 Bit ADCs in 6-Lead SOT-23PEX 20K Programmable Logic Device Family.* Analog Devices datasheet, 2000.

[180] http://www.ni.com/labview.

[181] J. Marín *et al.* Operation of the Electronics for the AMS-02 RICH Detector Protoype. Informe Técnico CIEMAT, 1011, December 2002.

[182] M Buénerd and I Efthymiopoulos. A High Energy Secondary Beam of Ion Fragments for Instrumental Tests at CERN. April 2003.

[183] M Buénerd *et al.* Fragments from the CERN SPS Pb Ions as a Test Beam for the AMS RICH. internal note, May 2002.

[184] R Pereira *et al.* Scintillator calibration for the October 2003 AMS prototype test at CERN. internal note, November 2005.

[185] B. Alpat *et al.* Charge determination of nuclei with the AMS-02 silicon tracker. *Nucl. Instrum. and Meth. A*, 540(1):121–130, March 2005.

[186] http://ams.bo.infn.it/tofbeamtest2003.html.

[187] http://www.crystran.co.uk/.

[188] C. Palomares. Prototype Calibration. oral communication in the AMS-RICH meeting in Madrid, February 2004.

[189] M. Aguillar *et al.* Parametric Model for the Response of a Photo-multiplier Tube. Informe Técnico CIEMAT, 1058, May 2005.

[190] http://paw.web.cern.ch/paw/.

[191] R Pereira *et al.* In-beam aerogel light yield characterization for the AMS/RICH detector. internal note in preparation.

[192] http://www.konicaminoltaeurope.com/fileadmin/user_upload/Products/Industrial_Products/PDFs/en/CM2600d.pdf.

[193] A. Torrentó. *Contrucción y pruebas del detector de radiación Čerenkov (RICH) del experimento AMS.* PhD thesis, Univ. de La Laguna, May 2007.

[194] M. Buénerd. The AMS-RICH aerogel tiles characterization - Status report. oral communication in the AMS-RICH meeting in Madrid, March 2007.

[195] M Buénerd *et al.* Note sur les mesures de déviation par un gradient d'indice. internal note in preparation.

[196] L. Arruda. Effect of refractive index random spread on isotope separation with the AMS RICH. oral communication in the AMS-RICH meeting in Madrid, March 2006.

[197] J. Casaus. Mirror reflectivity mapping. oral communication in the AMS-RICH meeting in Madrid, May 2007.

[198] J. Casaus. Systematics on the AMS-RICH Charge Determination. oral communication in the AMS-RICH meeting in Madrid, April 2005.

[199] J. Berdugo. RICH Status Report. oral communication in the TIM meeting at CERN, July 2006.

[200] Photonis. *Photomultiplier tubes*, 2002.

[201] J. Casaus. Preflight PMT Calibration tools: Feasibility Studies. oral communication in the AMS-RICH meeting in Madrid, July 2005.